Melanin Nanoparticles as a Potential Iron Chelation Therapy for Women with Beta Thalassemia during Pregnancy

Nahla Bakhamis

Linacre College

Nuffield Department of Women's and Reproductive Health

University of Oxford

Thesis submitted for the degree of

Doctor of Philosophy

Michaelmas Term 2022

Word count: ~ 48000

Abstract

The main challenges in developing medications that are safe to use during pregnancy is to minimize foetal exposure to the drug, which has become increasingly challenging with the increased prevalence of chronic conditions among young women. In beta thalassemia, patients can now survive beyond puberty and achieve pregnancy. β-TM pregnancies, however, are at high risk of maternal morbidity due to the complication of iron overload. Current chelation medications are withheld during pregnancy as they can cross the placenta causing potential risk to the foetus. This thesis addressed this complicated challenge in which a chelation agent needs to be retained in the maternal circulation and not cross the placenta. Previous experiments in iron-overloaded mice have shown that melanin nanoparticles can effectively chelate iron. Since the interaction between nanoparticles and cells/tissues is determined by particle characteristics and functionalization that can manipulated at synthesis, it was hypothesized that a melanin nanoparticulates with appropriate characteristics could be restricted from movement across the placenta, and safely used to treat the mother. A library of melanin nanoparticles of different sizes was established, and functionalized. This was followed by particle characterization and imaging. Functional analysis confirmed that particles were able to chelate iron more effectively than the iron chelator desferroxamine at the same concentration. Haemocompatibility testing found that the particles did not cause red cell haemolysis or blood clots. Moreover, it was determined that a cut off size of 200 nm can be restricted from passing across the placental barrier in an *in vitro* model using a human choriocarcinoma cell line and *ex vivo* human placental perfusion. Finally, physiological changes during pregnancy such as the decrease in plasma albumin concentrations can alter the

volume of distribution as well as the transport of drugs. Proteomics analysis was used to identify nanoparticle binding proteins in the serum from pregnant women, non-pregnant women, and women with beta thalassemia. 43 significantly different proteins between the three serum groups were identified, followed by the gene ontology analysis of cellular components that revealed the mediation of biological identity of the bio-inspired melanin in the biological system.

‘We must protect pregnant women through research not from research’

Dr. Diana Bianchi

SWHR 2020

Pregnant individuals are medically complex not vulnerable!

SWHR 2020

Acknowledgements

First and foremost, I would like to express my sincerest thanks to my supervisor Prof. Helen Townley for giving me the opportunity to join her lab and carry out this research. I am immensely grateful for her constant support, mentorship, kindness, and inspiration throughout this journey. Thank you, Helen!

I must thank my secondary supervisor Prof. Jane Hirst who inspired me with her clinical experience and always offered her help whenever I needed. I also appreciate the support of Prof. Manu Vatish for allowing me to use the perfusion facility in his lab, and the guidance I received from his team; Neva, Shuhan, Tolu, and Prassana.

I am extremely grateful to all past and current members of the Townley lab for the warm welcome, lab pizzas and outing; Ben, Chengchen, Emma, Laura S, Hakmin, Molly, and Morgan. Thanks to Ben for offering help with his engineering experience. Chengchen for our endless discussions in the lab; whenever I wanted to brainstorm, your brain was the one to pick. I was fortunate enough to be surrounded by a genuinely kind and amazing group of scientists at the science park; the “Farmhouse dwellers”, you made our lunch time and afternoon teas the most enjoyable. Thanks for all the fun virtual games and pop quizzes during the quarantine!

To all the friends I met in Oxford; Maryam, Alaa, Cheryl, Hala, Lucia, Sara, and Sally, for the home cooked meals, picnics, chocolates, coffee hunts, libraries, and dinners. Special thanks to Cheryl and Maryam, for our adventurous trips when most needed. Thanks to all people at Linacre community, and my network in Oxford who made my Oxford experience so special. To the ladies who made me feel home away from home, Maryam, Hadeel, Abeer, Ayda, Layla, and Lama, Thank you!

Couldn’t help but to thank my support system, my friends back home, Ghada, Fadwa, and Sara T for the constant encouragements and pep talks that kept me moving forward.

I would like to express my deepest gratitude to my family, my parents for always believing in me and for the endless love, and support. To my sisters, Sara, Nora, and Rana, I could never imagine how tough it is being unable to be around through your significant journeys, I love you!

Finally, thanks to all the women who donated their blood or placenta, your generosity is greatly appreciated. Thanks to the midwives Linda, Fenella, and Lotoyah for organizing and delivering the placentas to the lab, especially during the time of Covid. Special thanks to King Saud University for awarding me the scholarship to pursue this DPhil and for the funding and support for the research without which this work would not have been possible.

List of publications & awards

Research output

Published papers

Panicos Shangaris, Stavros P Loukogeorgakis, Sindhu Subramaniam, Christina Flouri, Laurence H Jackson, Wei Wang, Michael P Blundell, Shanrun Liu, Simon Eaton, Nahla Bakhamis, Durrgah Latchumi Ramachandra, Panayiotis Maghsoudlou, Luca Urbani, Simon N Waddington, Ayad Eddaoudi, Joy Archer, Michael N Antoniou, Daniel J Stuckey, Manfred Schmidt, Adrian J Thrasher, Thomas M Ryan, Paolo De Coppi, Anna L David. In Utero Gene Therapy (IUGT) Using GLOBE Lentiviral Vector Phenotypically Corrects the Heterozygous Humanised Mouse Model and Its Progress Can Be Monitored Using MRI Techniques. Sci Rep 9, 11592 (2019).

Unpublished Manuscript

Nahla BAKHAMIS, Toluwalase AWOYEMI, Manu VATISH, Helen E TOWNLEY. Melanin nanoparticles as a safe and effective iron chelation therapy for pregnant beta thalassemia.

Presentations at national and international conferences

Nahla Bakhamis & Helen Townley. Melanin nanoparticles for safe and effective iron chelation therapy for Beta-thalassemia during pregnancy. 42nd Annual Pregnancy Meeting. Society of Maternal-Fetal Medicine (SMFM). Orlando, Florida, USA 2022. (Oral presentation)

Nahla Bakhamis & Helen E Townley. Melanin-like nanoparticles exhibit a potential chelation therapy for iron-overload in β-thalassemia women during pregnancy. The

6th Nano-Boston Conference, Boston, Massachusetts, USA 2020. (Poster presentation)

Nahla Bakhamis & Helen Townley. Toward a safe and effective chelation therapy for β-thalassemia women during pregnancy. Oxford MSD 2019. (Poster presentation)

Awards

NWC Boston Student and Fellowship Award. Boston 2020

Linacre college travel award, Oxford 2019.

Excellence DPhil research rewards. Saudi Arabia cultural bureau. London 2019/2021/2022

Contents

Abstract 2
Acknowledgements 6
List of publications & awards 8
Research output 8
Contents 10
List of tables 15
List of figures 16
ABBREVIATIONS 19

CHAPTER 1. GENERAL INTRODUCTION 22

1.1 Thalassemia overview 22
1.1.1 Disease heterogenicity and pathophysiology 23
1.2 Beta thalassemia 24
1.2.1 Epidemiology, management, and survival 26
1.2.2 Iron overload 28
1.2.3 Iron chelation 31
1.3 Pregnancy in b-thalassemia 33
1.3.1 Fertility in beta-thalassemia 33
1.3.2 High risk pregnancy 33
1.3.3 Pregnancy and iron markers 35
1.3.4 Iron chelation during pregnancy 35
1.4 Drug development in pregnancy 37
1.5 The nanoparticle approach 38
1.5.1 Nanoparticle properties and biological interaction 39
1.5.2 Studies of nanoparticle interactions with the placenta 40
1.5.3 Melanin nanoparticles 43
1.6 Model system to study the transfer of nanoparticles across the placenta 44
1.6.1 Membrane structure of mammalian placenta 44
1.6.2 The human placenta 46
1.6.3 Transport mechanism of the human placenta 47
1.6.4 The possible transport mechanisms of nanoparticles 50
1.6.5 Model systems to study drug transport across the placenta 50
1.7 Protein corona 52
1.8 Thesis aims and hypothesis 55

CHAPTER 2. SAMPLES RECRUITMENTS AND PROCESSING 57

2.1 Overview 57
2.2 Patients and ethical approval 57
2.3 Information on samples and patient characteristics 58
2.4 Inclusion and exclusion criteria 58
2.5 Limitations on recruitment 59
2.6 Sample processing and storage 59
2.7 Introduction to and clarification of nomenclatures and terminologies used in this thesis 60
2.8 Fundamental theories and practical explanation behind the methods used in particle imaging 61

CHAPTER 3 SYNTHESIS, CHARACTERIZATION & POST SYNTHESIS MODIFICATION OF POLY-DOPAMINE MELANIN NANOPARTICLES 63

3.1 Abstract: 64
3.2 Introduction: 65
3.2.1 Melanin 65

3.2.2 Melanin nanoparticles ... *66*
3.2.3 PEGylation of nanoparticles ... *67*
3.2.4 Rhodamine dye as a fluorescent label ... *68*
3.2.5 Aims: ... *68*
3.3 Materials and Methods: ... 69
3.3.1 Melanin nanoparticles synthesis ... *69*
3.3.2 Size Control ... *70*
3.3.3 Hydrodynamic Diameter ... *70*
3.3.4 Zeta potential ... *70*
3.3.5 Transmission Electron Microscopy (TEM) ... *71*
3.3.6 Scanning Electron Microscopy (SEM) ... *71*
3.3.7 Size Distribution ... *71*
3.3.8 PEGylation of melanin nanoparticles ... *71*
3.3.9 Confirmation of PEGylation ... *72*
3.3.10 Stability of PEGylated particles. ... *72*
3.3.11 Post functionalization of with Rhodamine-B ... *72*
3.3.12 Statistical Analysis ... *73*
3.4 Results: ... 73
3.4.1 Synthesis of Melanin Nanoparticles ... *73*
3.4.2 Hydrodynamic Diameter ... *74*
3.4.3 Zeta potential ... *75*
3.4.4 Transmission and Scanning Electron Microscopy ... *76*
3.4.5 Size distribution ... *77*
3.4.6 Confirmation of PEGylation ... *78*
3.4.7 Stability at 37°C ... *80*
3.4.8 Post functionalization of MNP and MNP-PEG with Rhodamine B ... *81*
3.4.9 Summary of key characteristics of particles ... *82*
3.5 Discussion: ... 83
3.5.1 MNP synthesis and size control ... *83*
3.5.2 Characterization of the water soluble MNPs ... *84*
3.5.3 Surface functionalization ... *86*
3.5.4 Strength and limitations ... *87*
3.6 Summary: ... 87

CHAPTER 4 FUNCTIONAL ANALYSIS: THE EFFICACY OF POLY-DOPAMINE MELANIN NANOPARTICLES IN CHELATING IRON AND REDUCING LABILE IRON POOL ... 88

4.1 Abstract ... 89
4.2 Introduction ... 90
4.2.1 Overview ... *90*
4.2.2 LIP (labile iron pool): Chelatable iron ... *90*
4.2.3 Chelation therapy: attempts on overcoming challenges in current iron chelation therapy ... *91*
4.2.4 Poly-dopamine melanin nanoparticles as an iron chelator ... *92*
4.2.5 Calcein fluorescence for measurement of the LIP ... *92*
4.2.6 HepG2 cell line ... *93*
4.2.7 Aims ... *93*
4.3 Materials and Methods: ... 94
4.3.1 Determining the efficacy of MNPs in binding iron and the effect of MNP size ... *94*
4.3.2 Determining the effect of incubation time on particle efficacy in chelating iron ... *95*
4.3.3 Determination of PEGylation effect on particle efficacy in chelating iron ... *95*
4.3.4 HepG2 cell culture ... *96*
4.3.5 Determination of MNPs effect in reducing labile iron pool in HepG2 by calcein assay and flow-cytometry ... *96*

4.3.6 Quantification of cell iron content and protein determination *97*
4.3.7 Statistical analysis *97*
4.4 Results: 98
4.4.1 Efficacy of the synthesized particles in chelating iron; size and concentration comparison *98*
4.4.2 Effect of the incubation time on iron binding efficacy *99*
4.4.3 Effect of PEGylation on the efficacy of the synthesized particles in chelating iron *100*
4.4.4 Determination of MNPs effect in reducing labile iron pool in HepG2 cells *101*
4.4.5 Quantification of HepG2 cells iron content before and after iron chelation *103*
4.5 Discussion: 104
4.5.1 Efficacy of the synthesized particles in chelating iron *104*
4.5.2 MNPs effect in reducing labile iron pool in HepG2 cells *106*
4.5.3 Strength and limitations *107*
4.6 Summary: 108

CHAPTER 5 HAEMOCOMPATIBILITY INVESTIGATION OF MELANIN NANOPARTICLES AND IMPROVEMENT BY SURFACE FUNCTIONALIZATION WITH PEG 109

5.1 Abstract 110
5.2 Introduction 111
5.2.1 Overview *111*
5.2.2 Background *111*
5.2.3 Erythrocytes haemolysis *111*
5.2.4 Coagulation testing *112*
5.2.5 Aims *114*
5.3 Materials and Methods 115
5.3.1 Determination of erythrocytes haemolysis *115*
5.3.2 Clotting time (CT); determination of clotting activity of melanin nanoparticles *116*
5.3.3 Prothrombin time *117*
5.3.4 Statistical analysis *117*
5.4 Results 118
5.4.1 Determination of RBC haemolysis *118*
5.4.2 Clotting time dependence on the window size *118*
5.4.3 Prothrombin Time *121*
5.5 Discussion 122
5.5.1 Erythrocyte haemolysis *122*
5.5.2 Coagulation testing *124*
5.5.3 Strength and limitations *125*
5.6 Summary 126

CHAPTER 6. INVESTIGATION OF MELANIN NANOPARTICLE TRANSPORT ACROSS CELL MODEL OF THE PLACENTAL BARRIER 127

6.1 Abstract 128
6.2 Introduction 130
6.2.1 Overview *130*
6.2.2 Human choriocarcinomic cell BeWo *130*
6.2.3 BeWo syncytial fusion *131*
6.2.4 Aims *131*
6.3 Materials and Methods 133
6.3.1 BeWo cell culture *133*
6.3.2 Setting up transwell model with BeWo cell lines *133*
6.3.3 Hormonal assay; hCG-β ELISA *133*
6.3.4 Characterization of monolayer formation and BeWo syncytial fusion *135*
6.3.5 Nanoparticles translocation across BeWo cell line *137*

6.3.6 Statistical analysis *138*
6.4 Results 139
6.4.1 Secretion of hCG *139*
6.4.2 Confirmation of monolayer formation and BeWo syncytial fusion in transwell model *140*
6.4.3 The passage of MNPs across BeWo cell layer in a transwell model is size dependence *141*
6.4.4 Comparison of the passage of MNPs and polystyrene beads across BeWo cell barrier in a transwell model; effect of material *142*
6.4.5 PEGylation limits the passage of MNPs across BeWo cell layer in a transwell model *144*
6.4.6 Increasing concentration has no effect on passage of MNP-PEG across BeWo cell barrier in a transwell model. *145*
6.5 Discussion 148
6.5.1 BeWo hormonal secretion, syncytial fusion, and integrity of monolayer *148*
6.5.2 Transport of MNP across BeWo cell layer *150*
6.5.3 Effect of PEGylation on particle transport across BeWo *151*
6.5.4 Effect of concentration on particles transport across BeWo *151*
6.5.5 Strength and limitations *152*
6.6 Summary 152

CHAPTER 7. INVESTIGATION OF MELANIN NANOPARTICLE TRANSPORT USING AN *EX VIVO* HUMAN PLACENTAL PERFUSION SYSTEM 153

7.1 Abstract 154
7.2 Introduction 155
7.2.1 Overview *155*
7.2.2 Ex vivo human placental perfusion *155*
7.2.3 Criteria for successful perfusion *155*
7.2.4 Antipyrine *156*
7.2.5 Aim *156*
7.3 Materials and Methods 157
7.3.1 Physical examination *157*
7.3.2 Perfusion media *157*
7.3.3 Perfusion equipment *157*
7.3.4 Perfusion procedure; setting up the system *160*
7.3.5 Nanoparticle transport *161*
7.3.6 Permeability of the maternal-foetal barrier *161*
7.3.7 Integrity of the maternal-foetal barrier *161*
7.3.8 Viability of the placental tissue; hCG *162*
7.3.9 Criteria for a successful perfusion; checkpoints thought perfusion *162*
7.3.10 Accumulation of melanin nanoparticles in placental tissue *162*
7.3.11 Statistical analysis *163*
7.4 Results 165
7.4.1 Selection of successful perfusions *165*
7.4.2 Confirmation of successful perfusion *167*
7.4.3 Transport of melanin and polystyrene nanoparticles *169*
7.4.4 Viability of the placental tissue; hCG *170*
7.4.5 Assessment of accumulation of melanin nanoparticles in the placental tissue *170*
7.5 Discussion 171
7.5.1 Validity, adequacy, and integrity of the perfusion *171*
7.5.2 Transfer of nanoparticles across the placental barrier *173*
7.5.3 Strength and limitations *174*
7.6 Conclusion 175

CHAPTER 8. INVESTIGATING PROTEIN BINDING TO MELANIN NANOPARTICLES; FORMATION OF PROTEIN CORONA 176

8.1 Abstract 177
8.2 Introduction 178
8.2.1 Overview *178*
8.2.2 Personalized (disease specific) corona *178*
8.2.3 Protein binding and drug transfer across the placenta *179*
8.2.4 Aims *180*
8.3 Materials and methods 181
8.3.1 Sample processing *181*
8.3.2 SDS-PAGE *181*
8.3.3 Zeta potential *181*
8.3.4 Proteomics analysis *182*
8.4 Results 186
8.4.1 Determination of protein corona formation using SDS-PAGE *186*
8.4.2 Zeta potential before and after particle incubation *186*
8.4.3 Proteomics analysis *189*
8.5 Discussion 200
8.5.1 Strength and limitations *202*
8.6 Summary 203
CHAPTER 9. CONCLUSION AND FUTURE PERSPECTIVES 204
9.1 Summary of the main finding of the thesis 204
9.2 Contribution to the field and clinical implications 207
9.3 Experimental consideration 208
9.4 Impact of Covid-19 on this thesis 209
9.5 Future perspectives and research directions 210
References 213
Appendix I 225
Melanin nanoparticles characteristics *225*
Appendix II 227
Appendix IIl 230
Appendix IV 232

List of tables

Table 1.1 Features of currently approved iron chelators..... 32

Table 1.2 FDA classification of drugs during pregnancy.....36

Table 1.3 Size dependant transfer across the placental barrier of different models..... 42

Table 1.4 Model system to study drug interaction and transport across the placenta.....51

Table 3.1 Synthetic Parameters of Melanin Nanoparticles..... 70

Table 3.2 Summary of key particles characteristics..... 82

List of figures

Figure 1.1 Schematic representation of α and β globin gene clusters.....22

Figure 1.2 Developmental regulation of Human Hb and the shifting of beta globin locus.....25

Figure 1.3 Thalassemia distribution in the UK (2021).....27

Figure 1.4 Primary and secondary iron overload in β-thalassemia.....30

Figure 1.5 Recent data for medicines in pregnancy.....37

Figure 1.6 Nanoparticles interaction at maternal foetal interphase.....38

Figure 1.7. Zeta Potential of nanoparticles.....40

Figure 1.8. Schematic representation of membrane structure of mammalian placentae.....45

Figure 1.9. Schematic representation of haemochorial placental barrier.....45

Figure 1.10. Structure of human term placenta.....48

Figure 1.11. Schematic representation of the transport mechanism of human placenta.....49

Figure 1.12 Kinetic formation of protein corona; Vorman effect.....53

Figure 1.13 Surface PEGylation minimises corona formation on nanoparticle surfaces.....54

Figure 2.1. Post transfusion sample processing.....60

Figure 2.2. Diagram of SEM and ETEM.....62

Figure 3.1 Pathway of Eumelanin and Pheomelanin synthesis.....66

Figure 3.2 Schematic representation of melanin nanoparticles synthesis.....69

Figure 3.3 Melanin Nanoparticles Synthesis.....73

Figure 3.4 Hydrodynamic diameter of melanin nanoparticles.....74

Figure 3.5 Zeta potential of melanin nanoparticles.....75

Figure 3.6 Transmission and scanning electron microscopy imaging.....76

Figure 3.7 Size distribution of melanin nanoparticles.....77

Figure 3.8 FTIR Confirmation of PEGylation.....78

Figure 3.9 Zeta potential of PEGylated nanoparticles.....79

Figure 3.10 Stability of MNP and MNP-PEG at 37°C.....80

Figure 3.11 Fluorescence labelling of MNP-PEG with Rhodamine.....81

Figure 4.1 Graphical Summary of the Iron Binding Method.....95

Figure 4.2 Ability of MNPs to chelate iron.....98

Figure 4.3 Effect of time on MNPs ability to chelate iron.....99

Figure 4.4 Effect of PEGylation on MNPs ability to chelate iron……100

Figure 4.5 Fluorescence quenching of calcein AM……101

Figure 4.6 The effect of MNPs in reducing labile iron pool in HepG2 cells……102

Figure 4.7 Iron quantification in HepG2 cells before and after iron chelation……103

Figure 5.1 Stages of Haemostasis……113

Figure 5.2. Coagulation cascade……114

Figure 5.3 Graphical Summary of the haemolysis assay……115

Figure 5.4 Graphical Summary of clotting activity analysis of melanin nanoparticles……116

Figure 5.5 Haemolysis assay……119

Figure 5.6. Coagulation assay……120

Figure 5.7 Prothrombin Time……121

Figure 6.1 Graphical Summary of Traswell model setting up with BeWo cell lines……134

Figure 6.2 Graphical Summary of Characterization of monolayer formation and BeWo syncytial fusion……136

Figure 6.3 Graphical Summary of nanoparticle transportation across BeWo cell barrier……138

Figure 6.4 Level of hCG hormone in culture media of BeWo cells……139

Figure 6.5 Confirmation of monolayer and BeWo syncytial fusion……140

Figure 6.6 Fluorescence staining for barrier integrity; Confirmation of monolayer and BeWo syncytial fusion……141

Figure 6.7 MNPs passage across BeWo cell barrier or acellular control in a transwell model……143

Figure 6.8 Comparison of the passage of MNPs and Polystyrene beads across BeWo cell barrier in a transwell model……144

Figure 6.9 Passage of MNP-PEG across BeWo cell barrier or acellular control in a transwell model……146

Figure 6.10 Effect of concentration on the passage of MNP-PEG across BeWo cell barrier or acellular control in a transwell mode……147

Figure 7.1 Physical examination of collected placentae……158

Figure 7.2 Placental perfusion system……159

Figure 7.3 Cannulation of the perfused lobe……160

Figure 7.4 Workflow of the ex vivo placental perfusion and checkpoints to insure successful perfusions……164

Figure 7.5 Selection of successful perfusions……166

Figure 7.6 Permeability of the maternal-foetal barrier; measurement of Antipyrine concentration……167

Figure 7.7 Integrity of the maternal-foetal barrier; measurement of volume loss thought perfusion……168

Figure 7.8 Trans-placental transport of melanin nanoparticles in an ex vivo human placental perfusion……169

Figure 7.9 Viability of the placental tissue; hCG production……170

Figure 8.1 Schematic representation of personalized corona depending on serum profile of different conditions……179

Figure 8.2 Graphical abstract for methods used in this chapter……182

Figure 8.3 Formation of Protein corona; SDS-PAGE……187

Figure 8.4 Zeta potential before and after corona formation……188

Figure 8.5 The effect of plasma alterations mediated by different groups; healthy, pregnant and thalassemia on the corona composition formed attached on the surface of MNPs……191

Figure 8.7 Gene ontology cellular component enrichment analysis of MNP corona……192

Figure 8.7 Gene ontology pathway and process enrichment analysis of MNP corona……193

Figure 8.8. The effect of plasma alterations mediated by different groups; healthy, pregnant and thalassemia on the corona composition formed attached on the surface of polystyrene particle..196

Figure 8.9 Gene ontology pathway and process enrichment analysis of polystyrene corona……197

Figure 8.10 The effect of particle material on corona composition mediated by different groups; healthy, pregnant and thalassemia……198

Figure 8.11 The effect of PEGylation on corona composition mediated by different groups; healthy, pregnant and thalassemia……199

Figure 9.1 Graphical summary of the key findings of the thesis……206

ABBREVIATIONS

AAG	α1-acid glycoprotein
aPTT	Activated partial thromboplastin time
ATP	Adenosine 5′-triphosphate
CA	Cooly's anaemia
cAMP	Adenosine 3',5' –cyclic monophosphate
CT	Clotting time
DFO	Deferoxamine
DFP	Deferiprone
DFX	Deferasirox
DHI	Dihydroxyindole
DIA	Data-independent acquisition
DLS	Dynamic light scattering
DMEM	Dulbecco's Modified Eagles Medium
DMSO	Dimethyl sulfoxide
E-cad	E-cadherin
ELISA	Enzyme-Linked Immunosorbent assay
ELT	Eltrombopag
Em	Emission
Ex	Excitation
FBS	Fetal bovine serum
FDA	Food and Drug Association
FDR	False Discovery Rate
$FeSO_4$	Ferrous sulfate
FTIR	Fourier transform infrared spectroscopy
GI	Gastrointestinal
GO	Gene ontology
GRAS	Generally regarded as safe
Hb	Haemoglobin protein

HCD	Higher-energy C-trap dissociation
hCG	Human chorionic gonadotropin
HEPES	4-(2-hydroxyethyl)-1-piperazineethanesulfonic acid)
HPLC	High-performance liquid chromatography
HR	Haemolysis ratio
IAA	Iodoacetamid
ID	Initial dose
IR	Infra-red
IUGR	Intrauterine growth retardation
IV	intravenous injection
LC	Liquid chromatography
LCR	Locus and locus control regions
LIP	Labile iron pool
MBR	Match Between Runs
MNPs	Melanin nanoparticles
MSN	Mesoporous silica nanoparticles
mPEG	Methoxy-polyethylene glycol
MRI	Magnetic resonance imaging
MS	Mass spectrometry
MW	Molecular weight
NaOH	Sodium hydroxide
NCE	Normalized collision energy
Ns	Non-significant
NTBI	Non–transferrin-bound iron
OD	Optical density
PBPK	Physiologically based pharmacokinetic
PBS	Bhosphate buffer saline
PCA	Principal component analysis
PD	Pharmacodynamics
PEG	Polyethylene glycol

PEI	Polyethylenimine
PGD	Preimplantation genetic diagnosis
pH	Potential of hydrogen
PK	Pharmacokinetics
PLGA	Poly(lactic-co-glycolic acid)
PT	Prothrombin time
RBCs	Red blood cells
ROS	Reactive Oxygen Species
SD	Standard deviation
SDS-PAGE	Sodium dodecyl-sulfate polyacrylamide
SEM	Scanning electron microscopy
β-TM	Beta thalassemia major
STC	Syncytiotrophoblast
S-TRAP	Suspension Traps
TCEP	Tris Carboxy Ethyl Phosphene
TDI	Target Discovery Institute
TEAB	Triethylammonium bicarbonate buffer
TEER	Trans-epithelial electrical resistance
TEM	Transmission electron microscopy
Tf	Transferrin
TFA	Trifluoroacetic acid
UHPLC	Ultimate
UK	United Kingdom
ZO-1	Zonula occludens-1

Chapter 1. General introduction

1.1 Thalassemia overview

Hemoglobinopathies are the most common hereditary disorders with 300,000 to 500,000 cases born annually worldwide, with thalassemia comprising 17 % of the total (Halim-Fikri et al., 2022; The Lancet Global, 2022). The term thalassemia refers to a monogenic disorder characterized by suppressed synthesis or complete absence of alpha (α) or beta (β) polypeptide chains of the haemoglobin protein (Hb) due to missense/non-sense or frameshift mutations of the genes controlling the structure of haemoglobin chains (Figure 1.1). This results in decreased Hb concentration, microcytosis and anaemia with diverse clinical severities depending on allelic heterogeneity and the modifier genes (Stephanou et al., 2019).

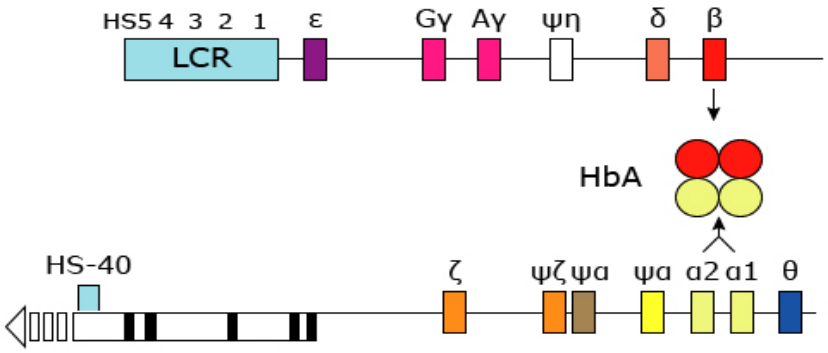


Figure 1.1 Schematic representation of α and β globin gene clusters.

Schematic representation of the chromosomal location of alpha globin gene cluster (αglobin, chromosome 16p) in the upper panel, and beta globin gene cluster (ß-globin, chromosome 11p) in the lower panel. These illustrate globin genes position, locus control region (LCR) for the ß-gene cluster and hypersensitivity sites for ß-globin gene clusters (HS 1 to 5) and α-gene cluster (HS-40). The genes that remain active in the ß-globin cluster throughout postnatal life are from left to right: G-gamma (G- ɣ), A-gamma (A- ɣ), delta (δ), and beta (ß) globin. The genes that active after birth in the α-gene clusters are from left to right: alpha-2 (α-2) and alpha-1 (α-1). Adult hemoglobin (hemoglobin A (HbA)) is a be heterotetramers molecule that made up of 2 α and 2 β globin chains and is shown between the two panels (Soni, 2021).

1.1.1 Disease heterogenicity and pathophysiology

Although the clinical spectra are different according to the affected genes, the underlaying pathology of most types of thalassemia is similar. This is characterized by low levels of Hb synthesis and compromised red blood cells (RBCs) because of the homotetramer structure formed from an excess of the unaffected globin chain. The unaffected globin homotetramer structure is formed when there is suppressed production of the other globin chain. The β homo-tetra-mers (α-thalassemia) in general are more stable than α homo-tetra-mers (β-thalassemia) and is the most common inherited disorder of haemoglobin (Kidd et al., 2001).

Alpha thalassemia is characterized by supressed production of α globin chains from the foetal stage of life (Figure 1.2). In homozygous α thalassemia (--/--), a complete absence of α chain leads to an excess of gamma (γ) chain forming an unstable γ_4 Hb (Bart's Hb) that is incapable of oxygen transfer. Foetuses with Bart's Hb die intrauterine or soon after birth due to severe anaemia, cardiomegaly, and hydrops fetalis (Kidd et al., 2001). HbH (α-/--) however, also called β_4, is formed when there is insufficient synthesis of the α chain resulting in anaemia ranging from a mild to transfusion dependent anaemia according to the phenotypic variability (Chui et al., 2003). Finally, the α thalassemia trait (α^0(αα/--) or α^+ (α/-,αα)) is characterized by mild hypochromic microcytic anaemia where the silent carriers (α^+) are capable of normal Hb production but the α^0 (αα/--) Hb synthesis is unbalanced resulting in RBC haemolysis and iron overload (Higgs and Weatherall, 2009).

Beta thalassemia, however, is extremely heterogenous in both genotype and phenotype and is characterized by shorter RBCs lifespan resulting in severe

haemolysis and a 20- to 30-fold increase in erythropoiesis (Rund and Rachmilewitz, 2005).

1.2 Beta thalassemia

The clinical heterogenicity of β-thalassemia depends on the nature of the mutation and the proximity of the gene regulatory elements, specifically the locus control regions (LCR) (Figure 1.2) (Hanscombe et al., 1991; Li et al., 2002). More than 200 thalassaemic mutations have been identified (Rachmilewitz and Giardina, 2011) that result in decreased production (β^{+}, β^{++}) or complete absence (β^{0}) of β-globin. Mutations in one allele (a heterogenous mutation) are asymptomatic with slightly altered laboratory values. Mutation in both alleles results in clinical manifestation ranging from an asymptomatic carrier state, to sporadic transfusion dependant thalassemia (β-thalassemia intermedia), chronic transfusion-dependent thalassemia (β-thalassemia major (β-TM) also called Cooly's anaemia (CA), (β^{0}/β^{0} or (β^{0}/β^{+})) (Danjou et al., 2011).

Patients with β-thalassemia intermedia in general have later clinical onset and milder anaemia that does not severely affect the quality of life in the first few years but can be complicated if left untreated. Therefore, a blood transfusion will be required at some point in the patient's life (Camaschella and Cappellini, 1995; Danjou et al., 2011).

Patients with β-TM however, are symptomatic at infancy or early childhood during the shift from foetal to adult Hb (Figure 1.2) and present with severe hypochromic microcytic anaemia. This is characterized by damaged RBCs, severe homolysis and ineffective erythropoiesis (Danjou et al., 2011). Patients are highly dependent on blood transfusions that are typically combined with iron chelation therapy to prevent

the complications of iron overload that includes cardiac morbidity, liver disease, and endocrine dysfunction.

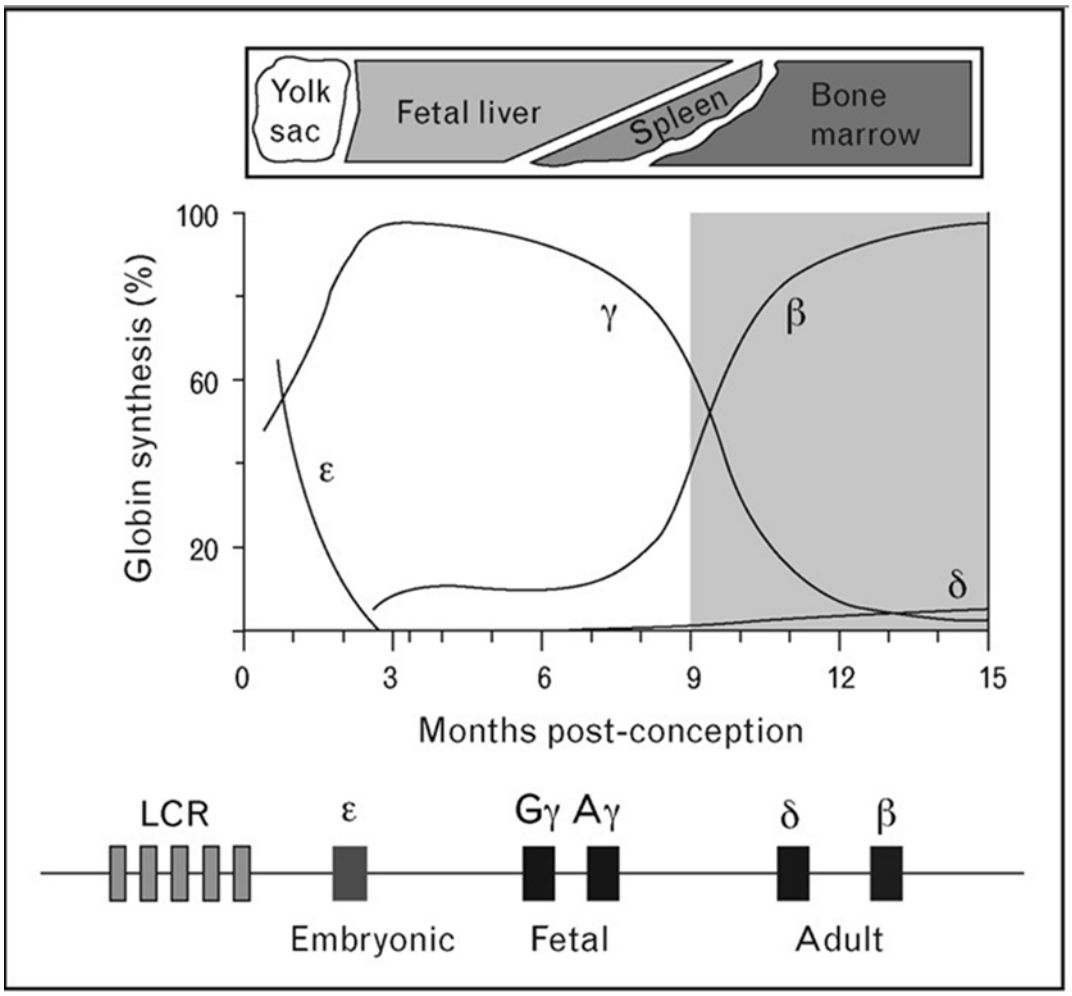


Figure 1.2 Developmental regulation of Human Hb and the shifting of beta globin locus.

Top: Two switches occur during human development of β globin: the shift from embryonic (2 α, 2 ε) to foetal globin chain (2 α, 2 γ), and the shifting from the major sites of haematopoiesis to the bone marrow around birth from foetal globin (2 α, 2 γ) to adult globin (2 α, 2 β). Even the second switch starts soon after birth, it takes almost a year for a full replacement. Bottom: Schematic representation of β-globin locus and locus control regions (LCR) which regulates the level of β globin expression. Image acquired from: Wolters Kluwer Health, Inc. Licensed under Copyright Clearance Center's, License number 5423330958010. Copyright © 2022 Wolters Kluwer Health, Inc. and/or its subsidiaries. All rights reserved.

1.2.1 Epidemiology, management, and survival

Historically, the highest prevalence (2.5 % to 25 %) of β-thalassemia was in the Mediterranean region, the Middle East, and Southeast Asia, and the lowest rates in Northern Europe and North America (Colah et al., 2010). But due to migration patterns, β-thalassemia is increasingly more common in Western Europe and North America (Kattamis et al., 2020). In the United Kingdom (UK) for example, 17 % of Cypriot immigrants after the 1960s civil war were carriers of the disease; which increased the prevalence to 7 per 1000 neonates (Kattamis et al., 2020). Similarly, in the United States (US) the incidence and prevalence of β-thalassemia has markedly increased over the past 50 years due to immigration as well as an increase in the adoption rates from endemic countries such as China (Sayani and Kwiatkowski, 2015). Although birth rate has decreased in the general population, it remains relatively high among the high-risk group (Figure 1.3).

While numbers of β-thalassemia patients have increased in many countries, the survival rates have also improved into adulthood due to blood transfusion and iron overload management (Figure 1.3) (Rund and Rachmilewitz, 2005). The implementation of comprehensive prevention programmes, population screening, premarital screening, genetic counselling, prenatal and preimplantation genetic diagnosis (PGD), stem cell and gene therapy, offered information and therapy choices to the high-risk and affected individuals. However, many obstacles affect the efficacy of these measures and limited the benefits of the new therapies. Stigmatization and legislation of pregnancy termination of affected foetuses, cultural and religious considerations, financial burdens of PGD, stem cell transplantation and gene therapy as well as the difficulty in finding a matching donor, are barriers to changing the status quo of transfusion therapy combined with iron chelation in

the management and treatment of β-thalassemia (Figure 1.3) (Kattamis et al., 2020; Modell et al., 2001; Saffi and Howard, 2015).

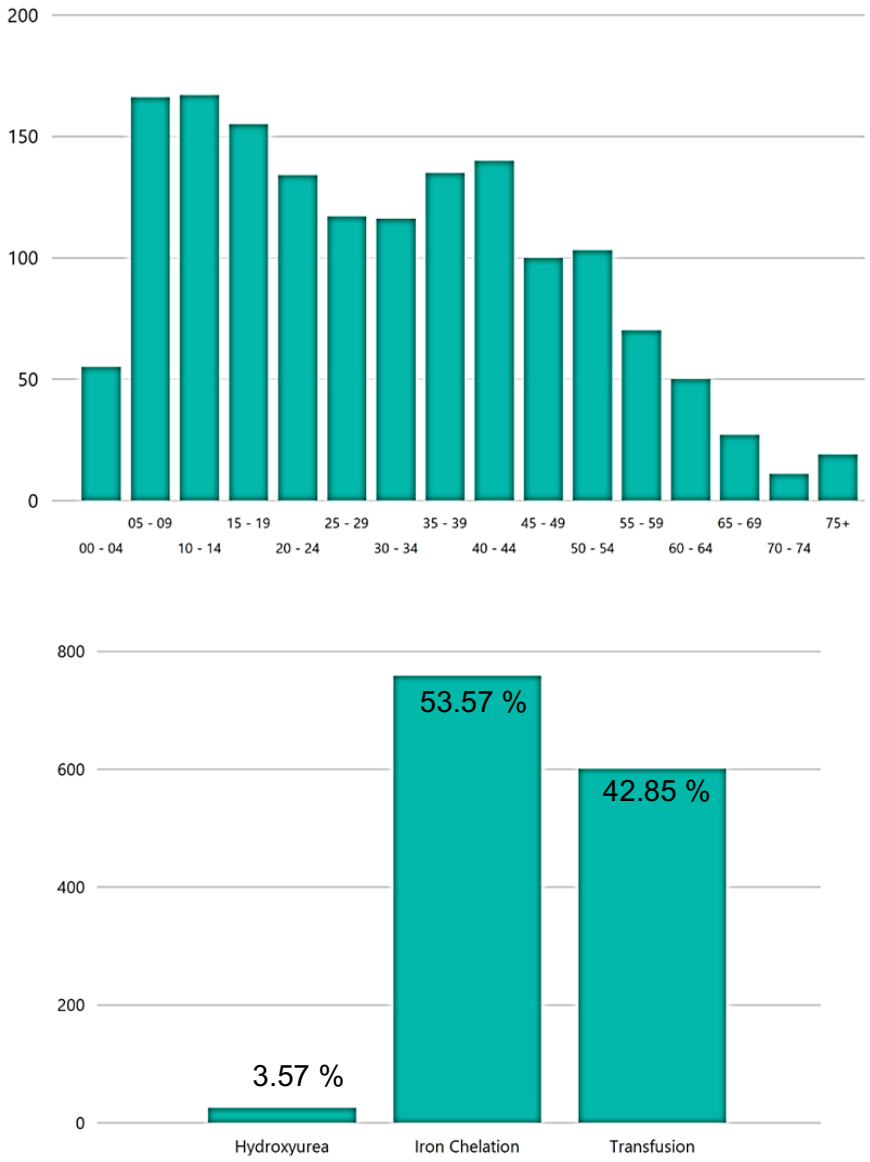


Figure 1.3 Thalassemia distribution in the UK (2021).

Thalassemia distribution by (top) age group showing that most thalassemia patients are within the childbearing age, and (bottom) therapy type showing that iron chelation is the most common therapy followed by blood transfusion which can eventually leads to chelation therapy. Data obtained from the National Haematology Registry report 2021.

1.2.2 Iron overload

Iron overload is the main cause of the mortality and morbidity associated with thalassemia. Both transfusional iron overload and excess gastrointestinal absorption are contributary (Rund and Rachmilewitz, 2005).

Free iron is potentially extremely toxic to cells because it donates electrons to oxygen resulting in the formation of reactive radicals (Hamilton and Kizhakkedathu, 2015; Wang and Pantopoulos, 2011). Under normal physiological conditions, iron is often complexed with iron binding proteins such as transferrin (Tf) in plasma or ferritin, the main iron storage molecule within the cells which maintain Fe^{3+} in a redox inert state (Wang and Pantopoulos, 2011). In the case of iron overload, iron overwhelms the iron-carrying capacity of plasma Tf. The resulting non-transferrin bound iron (NTBI) in plasma is deposited in organs like the liver, spleen, myocardium of the heart and endocrine organs. This forms a toxic redox active intracellular labile iron pool (LIP) that reacts with cellular hydrogen peroxide and ultimately causes severe tissue damage through oxidation reactions by increasing cellular reactive oxygen species generation in a process called the Fenton reaction. Consequently, there can be an increased risk of heart failure, liver cirrhosis and cancer, diabetes, arthritis, and gonadal dysfunction (Crichton, 2001; Murphy and Oudit, 2010; Wang and Pantopoulos, 2011). This is because humans lack the ability to off-load excess iron since they do not possess any regulated mechanisms for iron excretion from the body (Wang and Pantopoulos, 2011).

The human body contains 3.5 to 5 grams of iron exist and recycled in forms of haemoglobin, myoglobin, intracellular storage in liver, spleen, bone marrow and macrophages (Hamilton and Kizhakkedathu, 2015). Although the process of iron regulation, metabolism, and storage is highly evolved in humans, there is no

physiological pathway to effectively excrete iron. This poses a major challenge in beta thalassemia, where levels of iron are markedly increased due to several aetiologies including haemolysis (ineffective erythropoiesis that releases iron into the circulation), blood transfusions, and increased dietary iron absorption due to increased hepcidin expression (Rund and Rachmilewitz, 2005).

Hepcidin is a small peptide that inhibits intestinal iron absorption. Iron status affects hepcidin expression where its level is normally increased with elevated levels of iron while a decreased level is shown with low iron intake. In beta thalassemia, patients present with extremely low levels of hepcidin despite the marked increase in total body iron leading to an increase in iron absorption. The ethology is not fully understood; however, it is suggested that presence of hormonal factors or stimuli caused by RBC haemolysis in patient serum play a major role in the down regulation of hepcidin in beta thalassemia. This conclusion was drawn when patient serum was found to inhibit hepcidin messenger RNA expression in the HepG2 cell line (Weizer-Stern et al., 2006), and in a mouse models of beta thalassemia (Nicolas et al., 2002).

Blood transfusions are used to ameliorate anaemia secondary to ineffective erythropoiesis in patients with β-thalassemia, which results in apoptosis of the immature erythrocytes. Ineffective erythropoiesis in turn induces an increase in gastro-intestinal iron absorption to approximately 3 to 4 times greater than normal (Pippard et al., 1979). As a result, non-transfusion dependent patients can accumulate 2-5 grams annually leading to a primary iron overload state (Hamilton and Kizhakkedathu, 2015; Pippard et al., 1979). This rate of iron accumulation is doubled in transfusion dependent thalassemia (Mariani et al., 2009) since each unit of RBCs contains approximately 250 mg of iron (Hoffbrand et al., 2012) leading to

a secondary iron overload state. It was found that an iron accumulation rate of 0.2-0.4 mg /kg /day developed if the patient received a blood transfusion more than twice a year (Hershko et al., 2005; Hoffbrand et al., 2012), causing severe tissue damage and ultimately organ dysfunction and failure of the heart, liver and endocrine glands (Figure 1.4). Cardiac events due to iron overload are still the primary cause of death in patients with β-thalassemia (Modell et al., 2000; Olivieri, 1999).

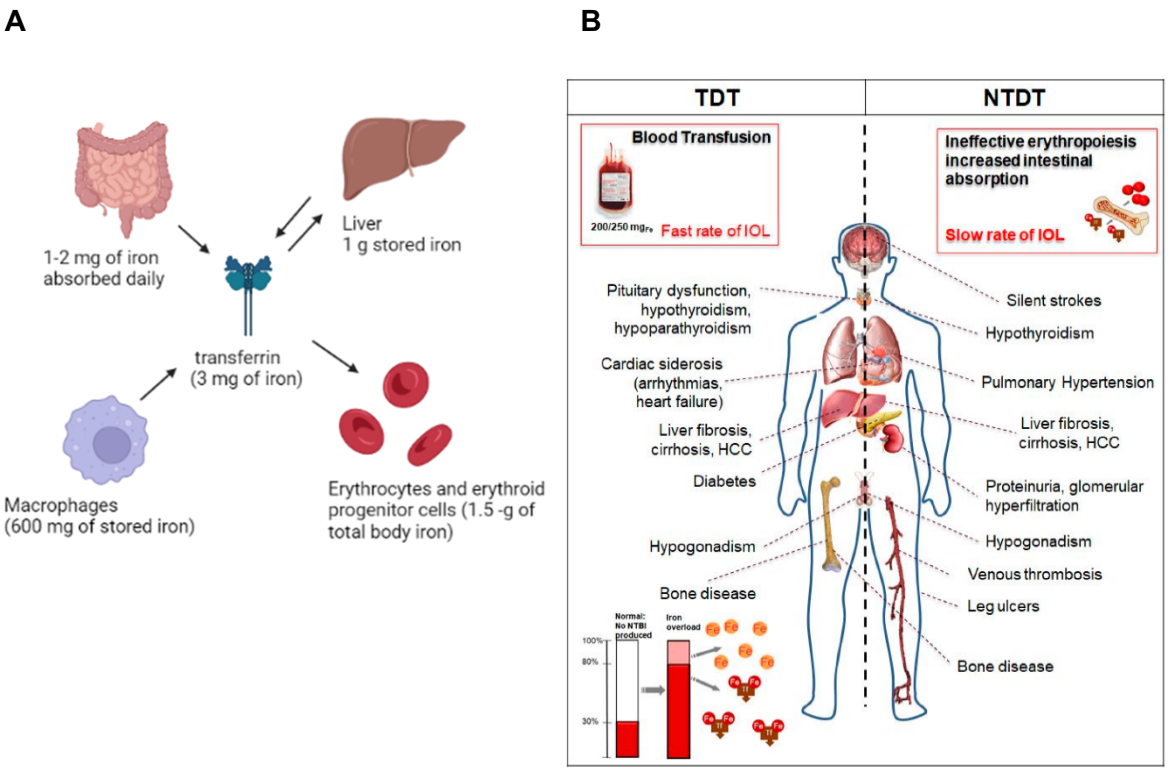


Figure 1.4 Primary and secondary iron overload in β-thalassemia.

(A) Iron recycling and distribution in the body. Erythrocytes obtain iron from the diet. Macrophages obtain iron from phagocytosis of senescent RBCs and release iron into the circulation where it binds to transferrin. Transferrin then delivers iron to the bone marrow to generate new RBC, or to the liver the main iron storage site. Image created with BioRender.com. (B) Iron overwhelms the iron-carrying capacity of plasma transferrin and generate redox active forms causing tissue iron overload in vital organs. This can be a primary condition due to increased intestinal absorption of iron or secondary to repeated blood transfusions. IOL: iron overload, TDT: transfusion-dependent thalassemia, NTDT: non-transfusion-dependent thalassemia, HCC: hepatocellular carcinoma, NTBI: non-transferrin-bound iron, Fe: iron, Tf: transferrin (Pinto and Forni, 2020).

1.2.3 Iron chelation

The risk of death due to iron overload was decreased when deferoxamine (DFO) was first introduced in the late 1960s, followed by the oral iron chelation agents deferiprone (DFP) and deferasirox (DFX), in 1999 and 2006, respectively (Borgna-Pignatti et al., 2004; Kattamis et al., 2020). The process of chelation reduces the amount of excess iron and protects the cells from oxidative damage.

DFO is the most commonly used chelator and considered the gold standard of chelation therapy for over 40 years (Kwiatkowski, 2011). DFO however, is hardly the ideal chelator since it has a short *in vivo* half-life of 20 minutes and requires a subcutaneous infusion dose of 40-60 mg/kg for 8-12 hours/day for 5 to 7 days per week. Moreover, prolonged treatment with DFO has been associated with severe toxicity (Table 1.1) (Olivieri et al., 1992; Porter et al., 1998).

Difficulties associated with DFO have led to a search for new orally active iron chelators such as DFP and DFX which have number of advantages over DFO, but were found to be extremely toxic and may worsen hepatic fibrosis in the long term (Table 1.1), (Olivieri, 1999). Because treatment with one chelator does not adequately control body iron in a substantial proportion of patients, a combination of DFP and DFO was also introduced for more effective therapy (Rund and Rachmilewitz, 2005).

Overall, although adequate blood transfusions with appropriate control of iron levels improved survival, data suggests that treatment is often insufficient, and complications are common. It is estimated that around 20 % of patients are inadequately chelated and approximately 3000 of these patients die annually due

to the complications of iron overload (Hamilton and Kizhakkedathu, 2015; Kattamis et al., 2020).

	Deferoxamine (DFO)	***Deferiprone (DFP)***	***Deferasirox (DFX)***
Route *of Administration*	subcutaneously or IV	Oral	Oral
half-life	Short (20 min), requires continuous infusion (all day)	Moderate: at least 3 times/day	8-6 hours once daily
Cost	Moderate	Moderate	Unaffordable to low income countries
Toxicity	Neurotoxicity, ocular and auditory toxicity, bone deformities, Growth retardation and Local reactions	Joint pain, GI upset, Agranulocytosis and neutropenia embryotoxicity, teratogenicity,	Ocular and auditory toxicity, GI upset hepatitis, rash
Recommended dose	20-50 mg/kg/day Over 8-12 hrs for 5-7 days/week	75–100 mg/kg/ 3 times/day	20–40 mg/kg/day

Table 1.1. Features of currently approved iron chelators.

Data from (Hamilton and Kizhakkedathu, 2015; Hoffbrand et al., 2012; Kwiatkowski, 2011).
GI: Gastrointestinal, IV: intravenous injection

1.3 Pregnancy in β-thalassemia

1.3.1 Fertility in beta-thalassemia

Women with beta-thalassemia usually suffer from hypogonadotropic hypogonadism (HH) associated with primary or secondary amenorrhea, delayed puberty, or infertility. This is thought to be mainly due to direct or indirect effects of iron overload on the hypothalamic-pituitary-ovarian axis and the female reproductive system. The direct effect is due to iron accumulation in the in the pituitary gland which affects its size and function, while the indirect effect is assumed to be mostly due to iron induced oxidative stress (Castaldi and Cobellis, 2016; Roussou et al., 2013).

Transfusion dependent beta thalassemia patients often develop pituitary iron overload in the first decade of life leading to a significant volume loss in the second decade. This reduction in volume is mostly irreversible in severe cases (Castaldi and Cobellis, 2016). Iron toxicity to the anterior pituitary leads to reduced synthesis of gonadotropin secretion resulting in a reduced ovarian antral follicle pool and ovarian volume (Castaldi and Cobellis, 2016). Thalassemia women were shown to have a considerably lower ovarian volume and lower antral follicle count compared to normal controls (Singer et al., 2011), probably due to a lack of gonadotropin stimulation attributed to iron toxicity to ovarian tissue.

Oxidative stress has been shown to accelerate follicle aging (Tarin, 1996). Women with beta thalassemia were shown to have lower antioxidant capacity represented by low levels of ascorbic acid (Singer et al., 2011), which play a role in oocyte development. In another study, patients were presented with high redox activity in the ovarian follicular fluid (Reubinoff et al., 1996). It was suggested that iron-induced radical production contributes to ovarian tissue injury. This could possibly affect

fertility status not only by accumulating in the endocrine organs, but also indirectly by affecting other organs associated with metabolism of hormones and serum antioxidants such as liver and pancreas (Castaldi and Cobellis, 2016; Roussou et al., 2013). Cases with amenorrhea were not directly correlated with free iron but were associated with cardiac iron overload and other endocrinopathies (Singer et al., 2011).

1.3.2 High risk pregnancy

Currently, most women with β-TM can survive beyond puberty and achieve pregnancy (Origa and Comitini, 2019; Sorrentino et al., 2020). This is largely due to the marked improvement in managing iron overload and the assisted reproductive technologies. Pregnancy planning however, is essential in both spontaneous and suspected pregnancies to minimize complications in women with β-thalassemia. Cardiac and liver functions, iron status and medication review should be monitored from pre-conception to post-partum to ensure optimal outcomes (Nourollahpour Shiadeh et al., 2020; Origa and Comitini, 2019; Petrakos et al., 2016; Vlachodimitropoulou et al., 2018).

During normal pregnancies, there is a 50 % increase in cardiac output associated with significant structural changes due to increased demands to both the mother and the foetus (Robson et al., 1989; Robson et al., 1987). In the thalassemia population, cardiac complications remain the leading cause of death which are exacerbated during pregnancy (Petrakos et al., 2016; Sorrentino et al., 2020).

While chronic transfusion is required to maintain sufficient haemoglobin levels (10g/dL) essential for normal foetal growth (Origa and Comitini, 2019; Petrakos et al., 2016), it can exacerbate haemosiderosis in women with a pre-existing iron-

overload status. As a consequence, the increased oxidative stress of pregnancy leads to organ damage, including endocrine abnormalities, liver complications and heart failure (Petrakos et al., 2016). It has been concluded that the overall prevalence of miscarriage and foetal loss among women with β-thalassemia is between 9 to 33.3 % (Nourollahpour Shiadeh et al., 2020). A multidisciplinary team approach of obstetricians, cardiologists and haematologists with emphasis on continuity of care is required to maintain a thalassemia pregnancy (Nourollahpour Shiadeh et al., 2020; Origa and Comitini, 2019; Vlachodimitropoulou et al., 2018).

1.3.3 Pregnancy and iron markers

Unlike normal pregnancies where women are usually vulnerable to iron deficiency, pregnancy has no impact on lowering iron in women with thalassemia (Scotet et al., 2018; Sorrentino et al., 2020; Vlachodimitropoulou et al., 2018). Significant increases in serum ferritin and liver iron loading were reported in 11 out of 14 pregnant β-thalassemia women in North London Hospital. Consequently, a complication with intrauterine growth retardation (IUGR) (n =2), pre-eclampsia and gestational diabetes (n=4) was also reported (Thompson et al., 2013; Vlachodimitropoulou et al., 2018). In another study, 19 out of 48 women required chelation that was complicated with spontaneous abortion, preterm delivery, and IUGR (Roumi et al., 2017). Preterm delivery and severe neonatal complications were reported in children exposed to DFO in foetal life (Sorrentino et al., 2020).

1.3.4 Iron chelation during pregnancy

While iron overload may threaten the mother's life even long after delivery, iron chelation therapy is normally stopped during pregnancy and three months prior to conception. This is because currently used chelators can cross the placenta causing

potential risk to the foetus (Cassinerio et al., 2017; Origa and Comitini, 2019; Vlachodimitropoulou et al., 2018). Teratogenic effects, delayed ossification, and skeletal anomalies have been observed in foetal mice and rabbits exposed to DFO and DFX (Origa and Comitini, 2019). Therefore, during pregnancy DFO and DFP are classified by the Food and Drug Association as category C, and DFX as category D (Table 1.2).

Ceasing medication puts the mother at increased risk of new onset endocrine disorders such as diabetes mellitus, hypothyroidism and hypoparathyroidism (RCOG, 2014) and deteriorate cardiac and hepatic iron loading. Severe hepatic fibrosis was reported in thalassaemic patients attributed to the fact that the patients stopped chelation treatment with DFX during pregnancy. All women with increased risk of liver fibrosis had a preterm delivery (Diamantidis et al., 2016). In another study, diabetes developed or worsened, cardiac issues including atrial fibrillation, peripartum ventricular dysfunction and arterial enlargement developed during pregnancy and after delivery (Thompson et al., 2013).

	Animal Studies	**Clinical Studies**
Category A	No risk	No risk
Category B	No risk	No data
Category C	Adverse effect of foetus (teratogenic or embryocidal)	Limited or no controlled studies
Category D	Positive evidence of human foetal risk	
Category X	Contradicted	

Table 1.2. FDA classification of drugs during pregnancy

1.4 Drug development in pregnancy

Although more women are being included in clinical research and trials, mostly by accidently being pregnant during the trials, the inclusion of pregnant and lactating women in drug research and clinical trials remains limited. The classification of pregnant women as vulnerable has led to the lack of motivation to include or conduct research specific for this population. As a result, for 40 years, only two drugs have ever been developed specifically for pregnancy related conditions (Ren et al., 2021; Spencer et al., 2022; Wise, 2022).

This is a great challenge in current obstetrical pharmacology, particularly in recent years with an increased prevalence of chronic and pre-existing conditions among women of childbearing age who require to continue their medications when they are pregnant or lactating. Around 3 out of 4 women take some form of medication during pregnancy, or breastfeeding (McClatchey et al., 2018). Most of these medications do not have appropriate labelling for use during pregnancy because they had not been appropriately evaluated at the research stage and may have a significant adverse effects (Figure 1.5) (Ren et al., 2021). Thus, there is an increased need for drug developmental research that are specifically designed for pregnant women.



Figure 1.5 Recent data for medicines in pregnancy. *(Ren et al., 2021)*

1.5 The nanoparticle approach

The main challenge in developing medications that are safe to use in pregnancy is to minimize foetal exposure to the drug. Many of the clinically used drugs are small molecular weight (MW) of less than 1000 g/mol (Syme et al., 2004). The small molecules can easily cross the placenta causing potential risk to foetus. Nanoparticle medications may overcome this challenge because they can be engineered otherwise by manipulating particle properties that determine their interaction with the placenta (Figure 1,6).

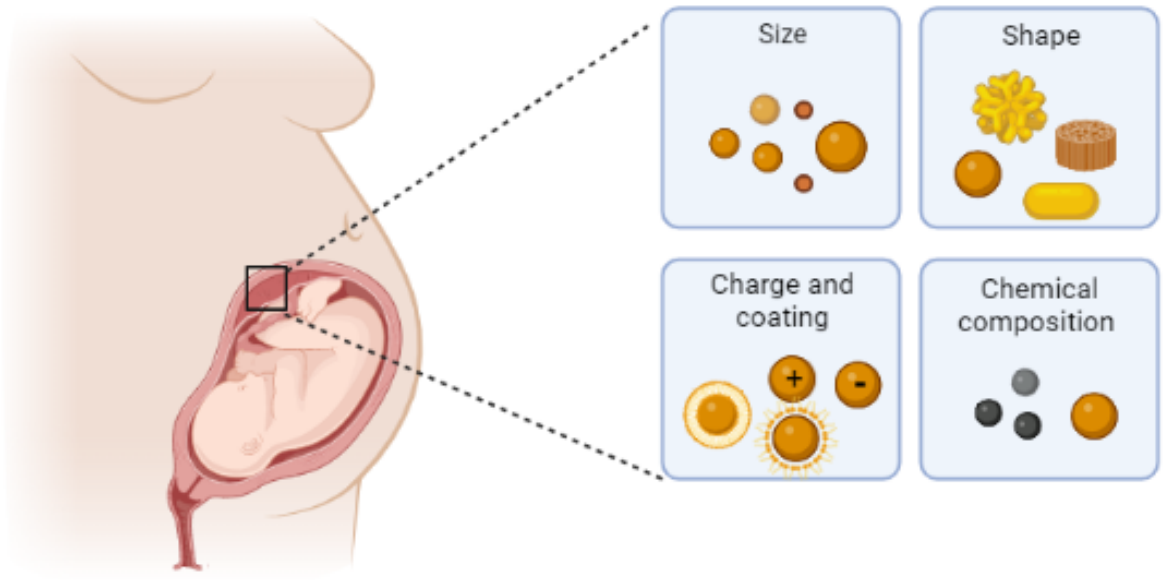


Figure 1.6 Nanoparticles interaction at maternal foetal interphase.

Figure illustrating the nanoparticle characteristics that affect their interaction with the human placenta at the maternal-foetal interphase. These characteristics include particle size, particle shape, chemical composition, and surface charge/functionalisation of the particles. Image created with BioRender.com.

1.5.1 Nanoparticle properties and biological interaction

Nanoparticles were originally defined as any particle of less than 100 nm diameter. The term nanoparticles, however, is currently used in the literature for any particle shape with dimensions of less than 1000 nm.

The interaction of nanoparticles with most cells and tissues is determined by their intrinsic characteristics and functionalization. These factors include particle size, shape, surface charge, and coating. Rod-shaped silica and gold nanoparticles, for example, have a significantly higher cellular uptake than core/shell and hollow particles (Bartczak et al., 2012).

The size of the particles strongly affects their cellular uptake rate and mechanism of action. While particles larger than 500 nm could be taken up by active transfusion mechanisms (trans-cellular passage) such as phagocytosis and macrophages, smaller particles of less than 25 nm enter the cells through passive diffusion including para-cellular passage, and passage between the cells (Herd et al., 2013; Zhao and Stenzel, 2018). It was found that the optimal size for cellular uptake of gold nanoparticles using Hela cell lines was 50 nm diameter (Chithrani et al., 2006).

Another critical factor that determines cellular interaction with nanoparticles is the surface charge. Positively charged particles can be easily taken up by the cells since the cell membrane is negatively charged (Zhang et al., 2017). Zeta potential, the potential at the interface of the electric double layer formed at the solid-liquid interface between the particle and the liquid dispersion (Figure 1.7), plays a significant role in particle stability. Zeta potential values of less than ± 20 mV indicates incipient and moderate stability while values greater than ± 20 mV indicates good and excellent stability.

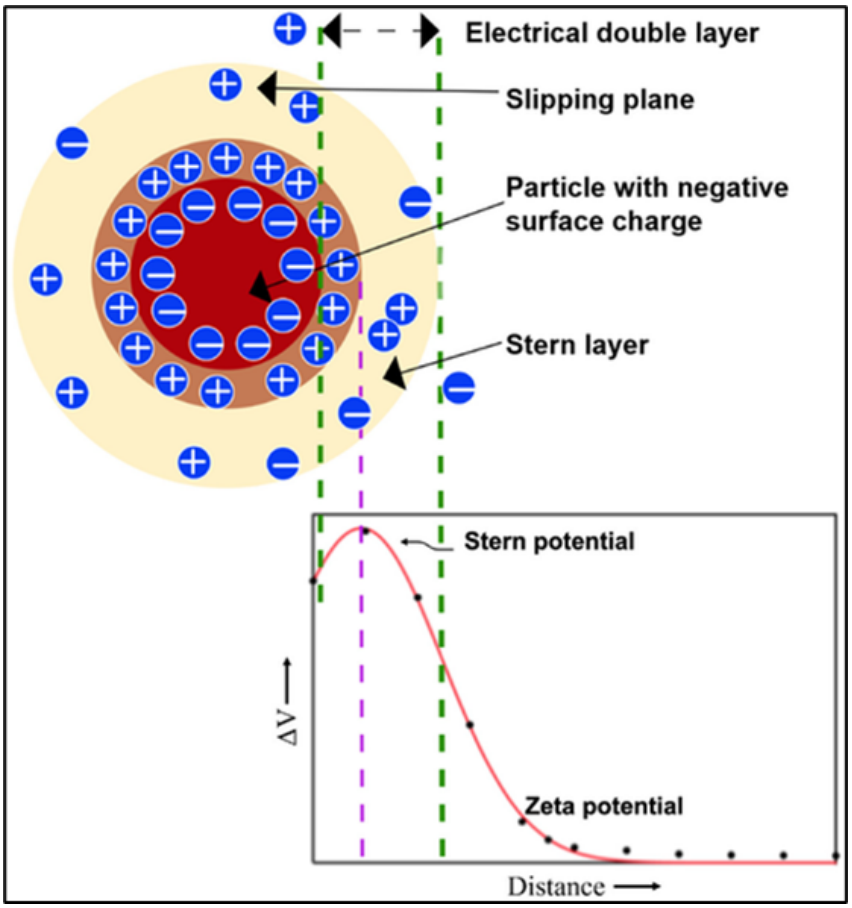


Figure 1.7. Zeta Potential of nanoparticles.

When charged particles are in a liquid solution, they attract oppositely charged particles to their surface forming a layer of tightly bound ions and an outer layer of loosely bound ions at the solid-liquid interface. The particle and its double electric layer move through the solution as one unit. Zeta potential is the potential at the interface of this unit and the medium and it determines the stability/aggregation status of the particle in the liquid. Adapted from (Lunardi et al., 2021).

1.5.2 Studies of nanoparticle interactions with the placenta

The chemical characteristics of the particles influence their biological interactions with the placenta (Figure 1.6). Studies of particle translocation across the placenta using different types of nanoparticles have identified a trend towards particle size being the major factor that affects translocation (Muoth et al., 2016). This was

observed with interactions of silica, gold, polystyrene, and liposomes across both mice and human placental models (Aengenheister et al., 2018b; Cornford et al., 2016; Huang et al., 2015; King and Muller, 2016; Myllynen et al., 2008; Poulsen et al., 2015; Semmler-Behnke et al., 2014; Wick et al., 2010; Yamashita et al., 2011). Almost in all these studies smaller particles tend to transfer across the placenta; with a different cut off according to particle material (Table 1.3). Thus, it is challenging to draw a conclusion on size-dependent transfer across the particles.

While particle size highly affected their transfer across the placental barrier, surface charge was also seen to influence this crossing. In general, negatively charged particles are less likely to interact with placental tissue (Zhang et al., 2017). The transfer of plain polystyrene particles of 50 nm with a zeta potential of -19.8 ± 4.02 mV was significantly higher than carboxyl functionalized (-34.7 ± 7.12 mV) polystyrene of the same size in an *ex vivo* human placental model (Grafmueller et al., 2015). Similarly, a charge dependent transfer of gold nanoparticles with different surface functionalization with ferritin (-1.6 mV) or citrate (-17 mV) was seen with the least negative charge being the highest transfer in murine pregnancy (Yang et al., 2012). However, this is not always the case; a higher transfer with more negative charge was seen in a transwell model of BeWo cells using iron oxide nanoparticles (Correia Carreira et al., 2015), Poly(lactic-co-glycolic acid) (PLGA) nanoparticles (Ali et al., 2013) and polystyrene (Kloet et al., 2015). This could be due to particle agglomeration which may block their transfer across the transwell pores. On the other hand, a similar trend was seen in a mice model using 70 nm silica nanoparticles with different charges (Yamashita et al., 2011).

Particle type	Size	Crossed the placenta	Experimental Model
Silica	70 nm	Yes	Mice
	300 nm	No	Mice
	1000 nm	No	Mice (Yamashita et al., 2011)
	25 and 50 nm Rhodamine labelled	Yes	*Ex vivo* human placenta (Poulsen et al., 2015)
Gold	1.5 nm	Yes	Rat
	18 nm	No	Rat
	80 nm	No	Rat (Semmler-Behnke et al., 2014)
	3 nm PEG	Yes	*Ex vivo* human placenta (Aengenheister et al., 2018a)
	10 nm PEG	No	*Ex vivo* human placenta (Myllynen et al., 2008)
	30 nm PEG	No	*Ex vivo* human placenta (Myllynen et al., 2008)
Liposomes	75-100 nm	Yes	Mice (Cornford et al., 2016)
	200 nm	No	*Ex vivo* human placenta (King and Muller, 2016)
Polystyrene	20-500 nm	Yes	Mice (Huang et al., 2015)
	50-240 nm	Yes	*Ex vivo* human placenta
	500 nm	No	*Ex vivo* human placenta (Wick et al., 2010)

Table 1.3. Size dependant transfer across the placental barrier of different models. *PEG: polyethylene glycol; is a protein conjugate often to improve particles' safety and stability. Further explained in section 3.2.3.*

1.5.3 Melanin nanoparticles

Melanin is a biological pigment that is widely distributed in living organisms. The various biological functions of melanin include coloration, ultraviolet photoprotection and thermoregulation. Melanin binds to iron in nature to protect the cells from the Fenton reaction, and oxidative stress (Hong and Simon, 2007). These properties, as well as the intrinsic biocompatibility of melanin, are attractive for many biological and medical applications (Ju et al., 2011; Park et al., 2019; Zhang et al., 2015).

Melanin nanoparticles (MNPs) are bio-inspired water-soluble melanin nanomaterials that mimic the physical and chemical properties of the biological pigment eumelanin and combine the excellent properties of melanin and nanoparticles including biocompatibility and easy degradation (Ju et al., 2011; Park et al., 2019; Zhang et al., 2015). Biomedical applications of melanin nanoparticles show promising results in UV-protected materials *in vitro* (Huang et al., 2017), photothermal cancer therapy *in vivo* (Liu et al., 2013), magnetic resonance imaging (MRI) (Lin et al., 2015), intracellular imaging (Amin et al., 2017), and *in vivo* iron chelation (Zhang et al., 2016).

MNPs have been used to chelate iron in cancer cells (Perring et al., 2018) and used in a mouse model of iron overload (Yan et al., 2016; Zhang et al., 2016). The first application of MNPs in iron overload therapy was reported in mice by Yan and colleague who showed that MNPs were more efficient and had a favourable safety profile and longer circulation half-life compared to DFO (17 hours in mice compared to 5 minutes DFO) (Yan et al., 2016). This can decrease the frequency and total dosage needed for iron overload treatment. When tested in a mice model of iron overload, melanin nanoparticles significantly improved the therapeutic effect at a

low dose (30-100 mg/kg) compared to a higher dose (750 mg/kg) of DFO (Yan et al., 2016).

1.6 Model system to study the transfer of nanoparticles across the placenta

To study the transfer of substances from mother to foetus it is important to understand the complex structure of the placenta which enables a link between maternal and foetal blood while maintaining physical separation to protect the foetus from xenobiotics that may presents in the maternal blood. The main function of the placenta is to transfer oxygen and nutrients from the mother to the foetus and aid in the removal of foetal waste to maternal circulation. The placenta also plays an important role in hormonal secretions and the synthesis of peptides and steroids to ensure a successful pregnancy (Syme et al., 2004).

1.6.1 Membrane structure of mammalian placenta

Placental structure varies remarkably among species and is classified according to the number of layers between the mother and the foetus. There are three major types; epitheliochorial (cow, pig and horse), endotheliochorial (cat and dog), and haemochorial (human and rodents) (Figure 1.8) (Enders and Blankenship, 1999; Syme et al., 2004).

Since these membranes affect the ability by which certain molecules can cross the placenta, one might be tempted to consider that exchange across the endotheliochorial placenta is much less efficient than that across the human placenta. However, other features of the placental structure make up for the extra layers in the diffusion barrier. Moreover, species with similar barriers vary in the actual ultrastructure of the placenta (Figure 1.9), thus the study of transplacental

transport in animal models is not an ideal representation for human pregnancy (Enders and Blankenship, 1999; Kulvietis et al., 2011; Syme et al., 2004).

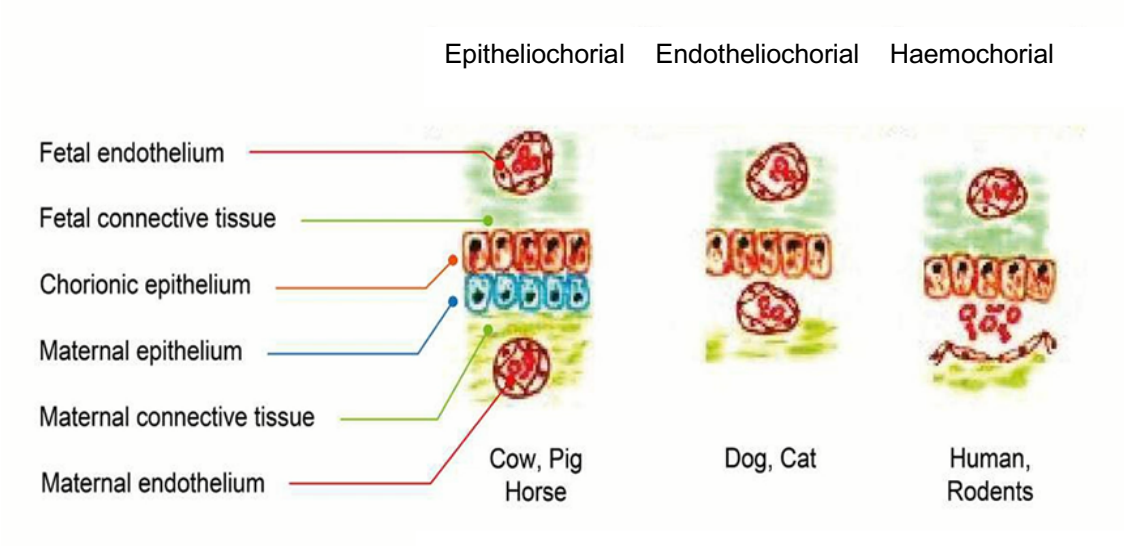


Figure 1.8. Schematic representation of membrane structure of mammalian placentae. Adapted from www.vivo.colostate.edu

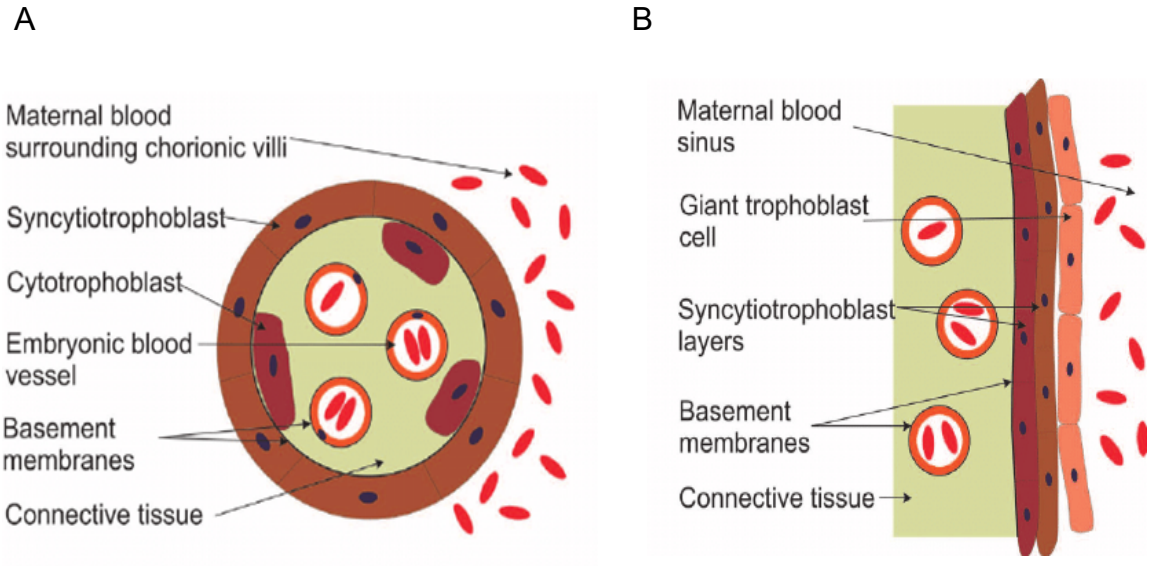


Figure 1.9. Schematic representation of haemochorial placental barrier.

Representation of the placental barrier In (A) human and (B) mice (Kulvietis et al., 2011).

1.6.2 The human placenta

In humans, the placenta is formed from both foetal tissue (chorionic plate and chorionic villi) and maternal tissue (*decidual basalis* of the uterus, remodelled from the endometrium at site of placental attachment). The placenta is divided by the decidual septa into separate functional units called cotyledons. Each cotyledon contains a villous tree (branched from the umbilical vein and arteries) bathed in the maternal blood within the intervillous space. The whole unit is limited between the basal decidua on the maternal side and the chorionic plate on the foetal side (Figure 1.10 A) (Holder et al., 2021; Kulvietis et al., 2011; Rote et al., 2010; van der Aa et al., 1998; Zhang et al., 2019).

The placental villi are the functional areas of exchange where the maternal and foetal tissues are separated by the placental barrier. The barrier consists of a capillary endothelium (containing the central foetal capillary in direct contact with foetal blood), villous stroma (containing fibroblasts and macrophages), and an outer trophoblast layer. The trophoblast layer consists of inner cytotrophoblast cells and outer multinucleated syncytiotrophoblast layer (formed from fused cytotrophoblast) which is in direct contact with maternal blood (Figure 1.10 A and B) (Jones and Fox, 1991; Midgley et al., 1963; van der Aa et al., 1998; Zhang et al., 2019). Thus, for substances to reach the foetal circulation they must cross several layers of the barrier and basement membranes. The syncytiotrophoblast is an important layer of the barrier that expresses certain transporters and prevents harmful substances from transfer to the foetus (Holder et al., 2021) and is considered as the rate limiting barrier of the human placenta.

As pregnancy progresses, a reduction in the thickness of the barrier is observed because the cytotrophoblast layer becomes relatively sparser and thinner at term but it maintains its structural integrity (Mori et al., 2007; van der Aa et al., 1998). This reduction in thickness, as well as the enlarged surface area of the barrier late in pregnancy, results in higher permeability enabling efficient nutrient transport in parallel to the increasing demand of the developing foetus (van der Aa et al., 1998).

1.6.3 Transport mechanism of the human placenta

Since the placenta plays an important role as a pipeline between the mother and the foetus, a wide range of transport mechanisms exist to allow movement of substances needed for the development of the foetus. Transport mechanisms of the human placenta involve passive transport, active transport, facilitated diffusion, phagocytosis, and pinocytosis (Figure 1.11) (Syme et al., 2004; van der Aa et al., 1998; Zhang et al., 2019).

Most pharmacologically active drugs that can cross the placenta move *via* passive diffusion. Factors affecting transport of components by passive diffusion include the concentration gradient between the maternal and foetal circulations, barrier thickness, surface area of transport, and the physiochemical properties of the drug. Drugs and other chemicals that are favoured by this transport mechanism are of low molecular weight (> 500 Da), lipophilic, and have a low degree of ionization (Audus, 1999; van der Aa et al., 1998) e.g. urea, gases.

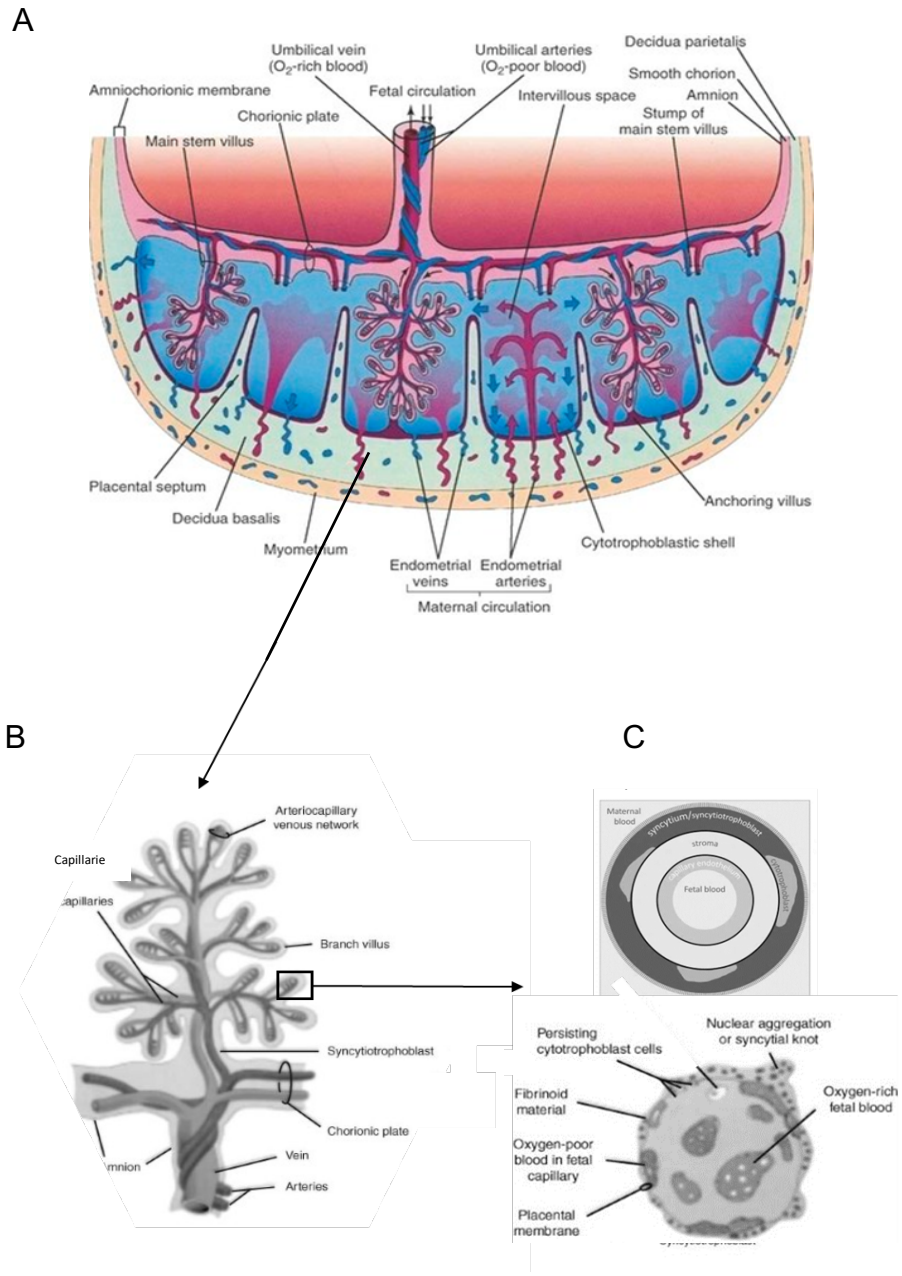


Figure 1.10. Structure of human term placenta.

(A) Schematic drawing of a transverse section of a human term placenta. (B) Schematic drawing of the structure of a human placental villus tree. (C) Schematic drawing of a cross section through a placental villus at term. (Holder et al., 2021; Syme et al., 2004).

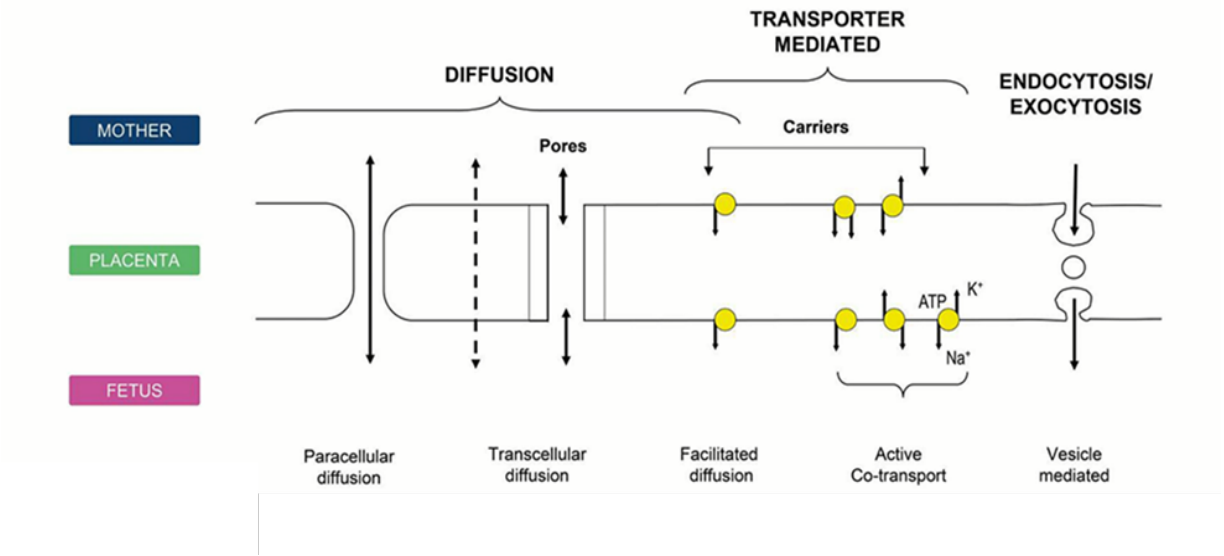


Figure 1.11. Schematic representation of the transport mechanism of human placenta.

Adapted from ***www.vivo.colostate.edu***

Facilitated diffusion is a carrier mediated transfusion mechanism that does not require energy and substances are transported through pores that exist in the membrane layers between the mother and the foetus (Syme et al., 2004). Active transport, however, is a carrier mediated transfusion that needs a transporter proteins and additional energy source such as Adenosine 5′-triphosphate (ATP) or sodium to provide energy (Syme et al., 2004; van der Aa et al., 1998). These transporters are present in the cell membranes and occurs at every single membrane that exists between the mother and the foetus.

Phagocytosis or pinocytosis routes of transfer are mainly for large or highly charged molecules like immunoglobulins. In this situation the molecules are taken into the vesicle, transported across the cells, and then released from the vesicle at the opposite side of the placenta (van der Aa et al., 1998; Zhang et al., 2019). Pinocytosis and phagocytosis, however, are considered too slow to have any significant effect on foetal drug concentration (Rubinchik-Stern and Eyal, 2012).

1.6.4 The possible transport mechanisms of nanoparticles

Data from *in vivo* mouse studies have found that placental channels allow nanoparticles of less than 25 nm in diameter to cross the placenta *via* passive diffusion (Chu et al., 2010). In *ex vivo* human placental perfusion studies it has been shown that silica (Poulsen et al., 2015) and polystyrene particles (Wick et al., 2010) of up to 50 nm were able to quickly cross the placenta. It was suggested from the perfusion profile that these small particles crossed the placenta *via* passive diffusion (Wick et al., 2010; Zhang et al., 2019).

In general, large particles are mainly taken up *via* phagocytosis (Zhang et al., 2019). It was found in a mouse study that particles of around 1 to 2 μm in diameter were taken up by the peritoneal macrophages (Liu et al., 2009). Phagocytes in placental trophoblasts play a significant role in tissue remodelling during trophoblastic invasion of the decidua but exhibit lower phagocytic activity than conventional macrophages (Choy and Manyonda, 1998; Orendi et al., 2011). It has not yet been investigated whether larger particles can be taken up the placental trophoblasts *via* phagocytosis.

1.6.5 Model systems to study drug transport across the placenta

The study of transplacental transport of drugs in pregnant women is restricted due to ethical considerations. Furthermore, animal models are not ideal representations of human pregnancy due to anatomical, morphological, and functional differences (Enders and Blankenship, 1999; Kulvietis et al., 2011; Syme et al., 2004). Thus, a variety of *in vitro* and human *ex vivo* models have been established to study the transport of substances across the placenta (Table 1.4).

Model type	Advantages	Disadvantages
Cell culture models		
Isolated primary trophoblast (villous and extravillous trophoblasts)	Can be isolated at any stage of gestation	Lack of proliferation in culture Absence of cell interactions STC not available for many passages Difficult to establish a monolayer
Placental explants	Any stage of gestation Cell-to-cell interaction	Limited lifetime STC might be damaged
Human placental choriocarcinoma cell lines; BeWo, JAR and JEG-3	Share many properties with villus trophoblast in terms of morphology, biological markers, and hormonal secretions. Replicate rabidly Commonly used for placental barrier and transport studies.	Easily contaminated
***Ex vivo* placental perfusion**		
	Maintain whole organ complexity and blood flow (close resemble the in vivo situation) Easily available	Only full-term placenta Maternal side can be damaged during delivery Limited lifetime

Table 1.4. Model system to study drug interaction and transport across the placenta.

STC ; syncytiotrophoblast. (Levkovitz et al., 2013; Orendi et al., 2011; Syme et al., 2004).

1.7 Protein corona

The surface of all materials has a higher free energy than the same bulk material, including nanosized materials. Therefore, when nanoparticles are exposed to a complex biological system, they progressively and selectively adsorb biomolecules to their surface to lower their surface energy and enhance dispersion (Kharazian et al., 2016; Monopoli et al., 2012; Nel et al., 2009). This biomolecule shell around the particles is called a “protein corona” and could consequently replace the biological identity of the particles. This can then determine their physiological responses including biodistribution, cellular uptake, transport, toxicity, and overall fate in the biological system (Gruber et al., 2020; Partikel et al., 2019; Yoshida et al., 2015).

Formation of a protein corona is a very dynamic, competitive, and time dependent process. It is determined by particle-to-protein binding affinity and protein-to-protein interactions. Low affinity proteins with high abundance in serum, such as albumin, bind first but are then replaced by higher affinity proteins with lower abundance and slower kinetics (i.e., apolipoproteins and immunoglobulins). Proteins with high binding affinity form a layer of “hard corona” that binds tightly to the particle surface; but this is not completely irreversible. Proteins with lower binding affinity bind loosely to the particle surface or on top of the hard corona forming another layer called the “soft corona” that is rapidly exchangeable. However, the corona does not completely mask the particle or its functional groups (Kharazian et al., 2016; Nel et al., 2009). It was shown from several examples of unmodified particles in biological media that the hard corona exchanges slowly over hours, while rapid exchange of the soft outer layer is expected to be within seconds (Milani et al., 2012) (Figure 1.12).

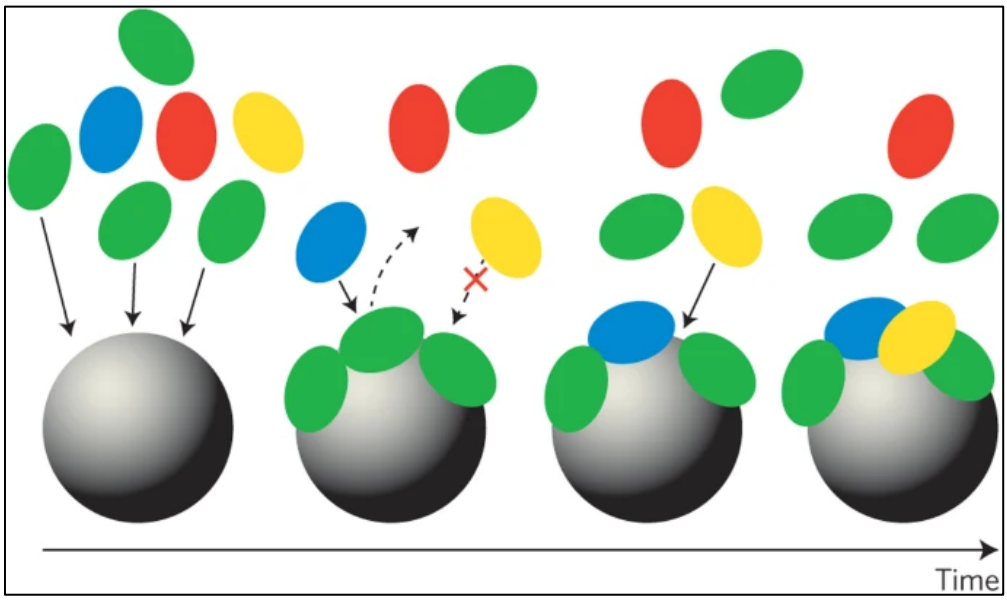


Figure 1.12 Kinetic formation of protein corona; Vorman effect.

When nanoparticles are exposed to a complex biological fluid, proteins with the highest association rate (green) attach first to the surface and are subsequently replaced by a higher affinity molecules (blue) that arrives later. These molecules may have a lower association rate but longer residence time. This is then followed by the adsorption of molecules that have low affinity (yellow) to the particles but higher affinity for protein-to-protein interaction with the green and blue proteins attached to the surface. Some molecules (red) do not attach at all. Figure adapted from Monopoli et al., (2012).

There are certain parameters that determine the structure, composition, and thickness of the protein corona. These parameters are generally related to the nanoparticle characteristics such as size, charge, chemical composition, surface properties, shape, angle of curvature, and dispersion. Hydrophobic nanoparticles, for example, adsorb twice as many proteins as hydrophilic nanoparticles (Aggarwal et al., 2009; Kharazian et al., 2016).

Other factors that govern corona composition are those related to the biological environment such as protein concentration, temperature, and disease status (Hajipour et al., 2015; Kharazian et al., 2016; Partikel et al., 2019).

Pre-coating and surface functionalization of nanoparticles are the most common strategies used to avoid corona formation. Various molecules and polymers such as poloxamine, poloxamer, dextran, and PEG have been used to minimize particle interactions with proteins and minimize the amount of protein adsorbed to its surface. The effect of each has been well summarized by Aggarwal et al (2009). Surface PEGylation is the most common method used for particle opsonization and escape from the immune system. However, although the use of PEG can reduce particle interaction with the surrounding proteins, it can't fully avoid corona formation on the particles (Gref et al., 2000) (Figure 1.13).

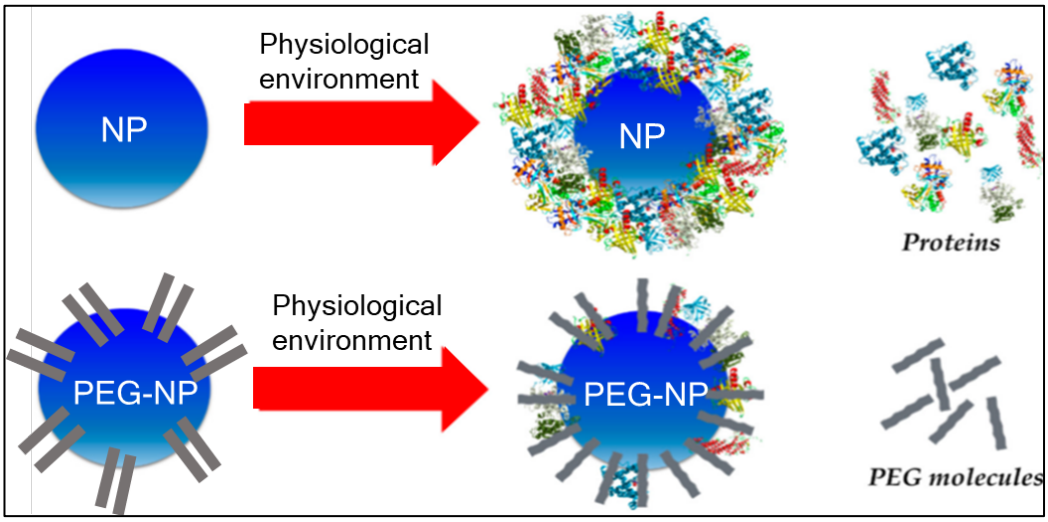


Figure 1.13 Surface PEGylation minimizes corona formation on nanoparticle surfaces. *When nanoparticles are exposed to a biological environment, they adsorb proteins to their surface to lower their surface energy forming a shell of protein corona. Particles PEGylation were found to decrease the amount of adsorbed proteins to the surface.(García-Álvarez and Vallet-Regí, 2021).*

1.8 Thesis aims and hypothesis

Women with β-thalassemia have a high-risk pregnancy owing to the complications of iron toxicity. Iron chelation therapy, however, is mostly withheld during pregnancy due to the increased risk of teratogenic effect to the developing foetus. This is because currently used chelators are small molecular weight that can cross the placenta. Physicians and healthcare providers as well as pregnant and lactating women are facing the dilemma and challenge when making real-time decisions about whether to delay medication with increased risk of maternal morbidity, or to take the medication with increased risk of major congenital malformations. Therefore, a chelation agent is needed for use during pregnancy that is retained in maternal circulation and minimizes foetal exposure. One potential solution is to use a nanoparticle chelator. By manipulating the physical and chemical properties of the particles, foetal exposure to the drug can be minimized. With a capability of melanin to chelate iron, it was hypothesized that melanin nanoparticles with appropriate characteristics could be restricted from movement across the placenta, and safely used to treat the mother.

The main aims of this thesis are:

1. To synthesize a library of melanin nanoparticles of different sizes followed by characterization and post synthesis modifications. This was due to the fact that the interaction of nanoparticles with mice and human placentae was found to mainly affected by particle size.
2. To evaluate the functional analysis of the synthesized particles on their efficacy in chelating iron *in chemico,* and to reduce intracellular labile iron

pool (the chelatable iron) *in vitro* using a hepatocellular carcinoma cell line where the largest iron pool is deposited.

3. To investigate the haemolytic activity and haemocompatibility of the synthesized melanin particles by evaluating their coagulation and haemolytic toxicity.
4. To establish which, if any, of the synthesized particles pass through the placental barrier *in vitro* using a transwell assay with the BeWo choriocarcinomic cell line representing the rate limiting barrier of the maternal-foetal interphase.
5. To test the translocation of candidate particles in a perfused human placenta *ex vivo*.
6. To investigate protein binding to the particles and differential expression after incubation with serum from three different groups: healthy non-pregnant women, healthy pregnant women, and women with beta thalassemia, using a deep proteomic analysis and gene ontology analysis of identified clusters.

Chapter 2. Samples recruitments and processing

2.1 Overview

This chapter describes the sample recruitments utilised in this thesis. Details of sample collection, ethical approvals, and limitations of recruitments are presented in this chapter. Detailed analysis, processing with a description of the statistical tools employed will be described in each of the results chapters where these samples were used.

2.2 Patients and ethical approval

Donated blood and placentae were used in several investigations included in this thesis. Before donation, all women were given a participant information sheet concerning the nature of the research and provided written informed consent if they agreed to donate their blood or placentae. Oxford University Hospitals, NHS Foundation Trust pre-approved the study (Oxford Research Ethics Committee C (REC ref no. 07/H0606/148 and 07/H0607/74). Only pregnant women undergoing elective caesarean sections were selected from the maternity ward at the Women's centre, John Radcliffe Hospital, Oxford. Blood samples from healthy control (non-pregnant) women (n=6), and blood and placentae samples from healthy pregnant women (n=6) were collected at the Women's centre, John Radcliffe Hospital (Oxford, UK). Blood samples from women with thalassemia (n=4) were collected at the haematology department at the Churchill Hospital (Oxford, UK). The ethical

approval involved studying pre-eclampsia (or toxaemia of pregnancy) as well as conditions, which predispose to preeclampsia (such as beta thalassemia and gestational diabetes).

2.3 Information on samples and patient characteristics

Samples were collected from females who are within their childbearing age. Blood samples were collected in sodium citrate tubes. Control samples were defined as samples collected from healthy non-pregnant women at time of collection. Healthy pregnant samples are defined as samples collected from healthy women with non-complicated pregnancies. Thalassemia samples was defined as samples collected from women with thalassemia pre-iron chelation therapy. Non-identifying information was collected about women whose samples were used in this thesis.

2.4 Inclusion and exclusion criteria

Collected placentae were deemed eligible if they met the inclusion criteria:

1. Donor was able and willing to give informed consent.
2. Collected from women who had healthy non-complicated pregnancy and underwent an elective caesarean section at term.
3. Were delivered immediately to the lab and perfused within 10 to 20 minutes of delivery.
4. Passed the checkpoints of successful perfusion (Karttunen et al., 2015; Wick et al., 2010): leak of perfusion was < 3 mL/hour, Antipyrine concentration reached equilibrium between the maternal and foetal side within 2-3 hours, and a foetal pH of between 7.2 and 7.4.

Samples were considered ineligible if any of the following applied:

1. Unable to give informed consent.
2. Placentae collected from women who had complicated pregnancy, gestational diabetes, or pre-eclampsia.
3. Placentae collected after normal delivery.
4. Placentae collected from women who delivered pre-term.
5. Placentae that were not processed within 20 minutes after delivery or that did not pass the checkpoints.

2.5 Limitations on recruitment

The recruitment of blood and placentae was hindered by the interruption due to the covid-19 pandemic and the subsequent suspension with limited access to sample collection. Collection of samples was also paused during the update of the tissue collection protocol approval. Moreover, demographic difficulties in getting thalassemia samples in Oxford has also affected the sample collection process.

2.6 Sample processing and storage

Blood samples were immediately processed as described in the results chapters. Placental samples were perfused within 20 minutes of delivery. Biopsies were collected from a control lobe and a perfused lobe prior to perfusion (t_0) and after a duration of 6 hours perfusion (t_1). Biopsies were stored at −80 °C for further analysis of accumulated particle concentrations and hormonal analysis (Ali et al., 2021; Wick et al., 2010). Maternal and foetal perfusate were collected at each time point in separate tubes and centrifuged twice at 1500 g for 10 minutes at 4°C, followed by centrifugation at 10,000 g for 20 minutes to collect the particles and stored for further analysis (Figure 2.1).

2.7 Introduction to and clarification of nomenclatures and terminologies used in this thesis

The upper limit of nanosized material is still a matter of debate, the conventional terminology of a nanomaterial was defined as particles of any shape with dimensions of less than 100 nm. However, the term nanoparticles (the use of prefix "nano") is currently accepted and widely used for dimensions smaller than 500 nm (Vert et al., 2012), and occasionally for particles less than 1000 nm. In this thesis, 50.12 ± 6.15 nm MNPs were referred to as 'small' or '50 nm' particles, 194.11 ± 9.51 nm MNPs were referred as 'medium' or '200 nm' particles, and 504.84 ± 10.91 nm MNPs were referred as 'large' or '500 nm' particles.

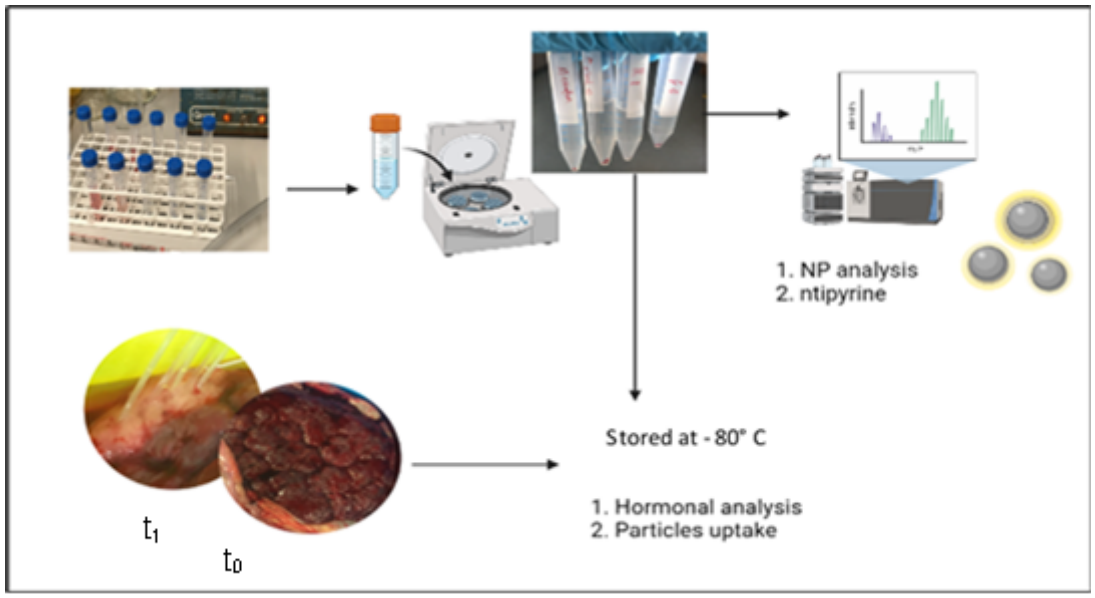


Figure 2.1. Post transfusion sample processing.

Perfusate were collected at each time point for a duration of 6 hours perfusion, centrifuged at 1500 g for 10 minutes at 4°C, followed by centrifugation at 10,000 g for 20 minutes to collect the particles. Samples were then stored for nanoparticle analysis or antipyrine analysis. Biopsies were collected control lobe and perfused lobe before (t_0) and after (t_1) perfusion.

2.8 Fundamental theories and practical explanation behind the methods used in particle imaging

Synthesized melanin particles of up to 200 nm were imaged using the transmission electron microscopy (TEM) and Scanning electron microscopy (SEM) was used to image larger 500 nm particles for practical reasons. In TEM, an image is created by the transmission of electrons produced from an electron gun and passing through the sample (figure 2.2). Thus, it gives information on the inner structure and morphology of the samples. TEM magnification is more than 50 million times making it suitable for small particles. SEM creates an image by detecting reflected or knocked-off electrons giving surface information about the sample (Figure 2.2). SEM spatial resolution is limited, and magnification is only up to 1-2 million times.

TEM is more powerful than SEM by providing information of the inner structure of the particles, thus, 50 nm and 200 nm MNPs were sent for TEM images (Solid Mechanics and Material Engineering Group, Department of Engineering science, University of Oxford). However, the size of the particle should be big enough to accommodate the transmitted electron beam. It was advised by the TEM service provider that if 500 nm MNPs were photographed by SEM, it would provide better images than TEM. Therefore, I was trained to use SEM for the 500 nm particles imaging.

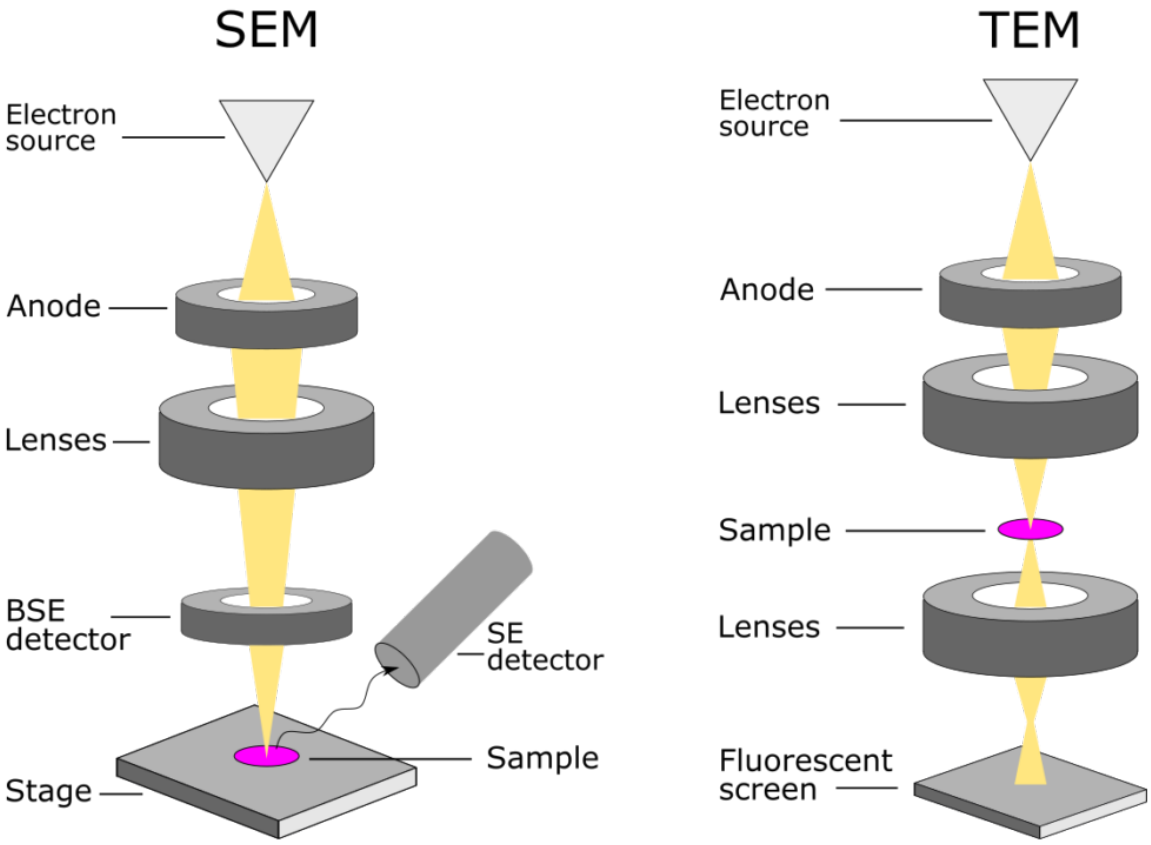
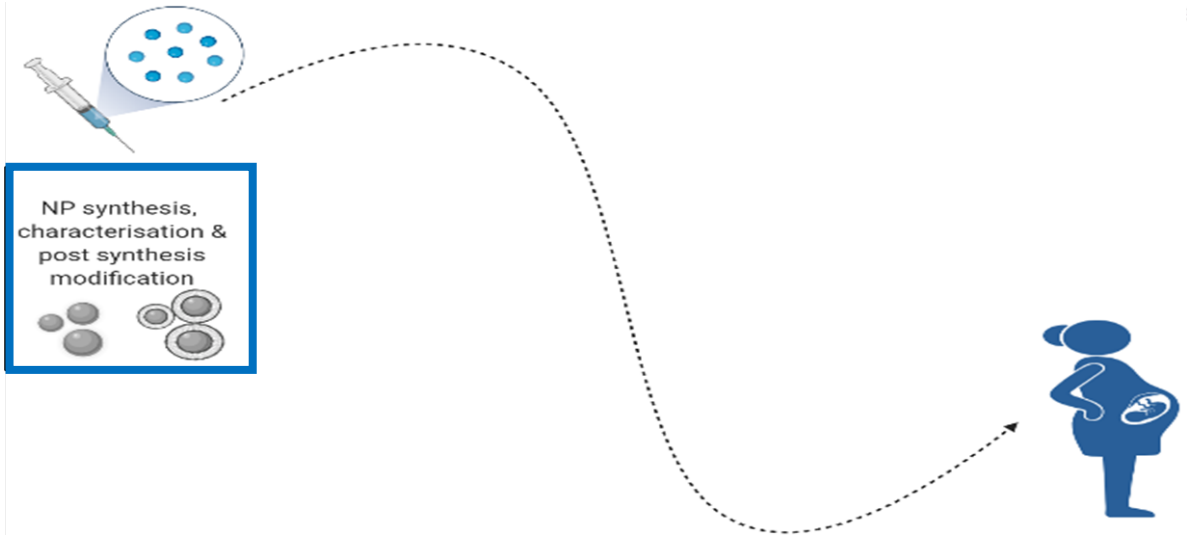


Figure 2.2. Diagram of SEM and TEM.

Diagram of Scanning electron microscopy (SEM) and transmission electron microscopy (TEM) showing the main components; electron source, series of electromagnetic and electrostatic lenses to control the shape and trajectory of the electron beam and Electron apertures. All of these components are housed inside a chamber that is under high vacuum.

https://anapath.ch/electron-microscopy-2/

Chapter 3 Synthesis, characterization & post synthesis modification of poly-dopamine Melanin nanoparticles



3.1 Abstract:

Background: The interaction between nanoparticles and cells/tissues is determined by particle characteristics and functionalization. Carefully manipulating these factors at the synthesis stage is important since it affects the biological activity and therapeutic efficacy of the particles.

Objectives: The aim of this chapter was to synthesize, characterize, and functionalize a library of three different sizes of melanin nanoparticles to test their interaction with the placenta.

Methods: Poly(dopamine) melanin nanoparticles were synthesized by hydroxylation of dopamine hydrochloride in an alkaline solution, different sizes were achieved by controlling the pH of the mixture. This was followed by characterization for zeta potential and morphology using TEM and SEM. Particles were then PEGylated and fluorescently labelled with Rhodamine B.

Results: Sizes of synthesized particles were 50 ± 10 nm diameter, 200 ± 20 nm diameter and 500 ± 10 nm diameter. TEM and SEM images determined particle morphology and surface structure and they appeared as roughly spherical with a smooth surface. Zeta potential of the particles ranged from -26 mV to -32 mV at pH 7 indicating good stability. PEGylated particles remained stable for more than 24 hours when incubated under physiological conditions.

Conclusion: Since particle size was the main factor that affect their interaction with the placenta, there different sizes of MNP was carefully designed and achieved. The synthesized particles showed excellent stability. The negative charge could in theory help in their restriction from crossing the placenta which will be tested later in this thesis.

3.2 Introduction:

3.2.1 Melanin

The melanin pigments are produced in a specialized group of cells known as melanocytes. Because melanin is an aggregate of smaller component molecules, there are different types of melanin with different proportions and bonding patterns of these component molecules. There are three different types of melanin in humans; neuromelanin which is the only type produced by specific populations of neurons in the brain, pheomelanin (red or yellow melanin), and eumelanin (brown or black melanin). They differ not only in colour but also in the size, shape, and packaging of their granules (Slominski et al., 2004). Both pheomelanin and eumelanin are derived via a tyrosinase-dependent pathway that involves the compulsory hydroxylation step of tyrosine to dopaquinone where the two pathways diverge (Figure 3.1). The individual melanocytes synthesize both eumelanin and pheomelanin with different ratios determined by variables such as the expression of pigment enzyme expression and the availability of tyrosine (Lin and Fisher, 2007).

Natural melanin can be obtained by separation and purification of melanin pigment from its biological environment (Zeise et al., 1992), however, there is no standardized method proven not to alter its physiochemical properties (Caldas et al., 2020). Moreover, natural melanin has a large size, and irregular shape. It is insoluble in most solvents other than strong alkaline solutions (d'Ischia et al., 2009) limiting applications in biological and medical fields.

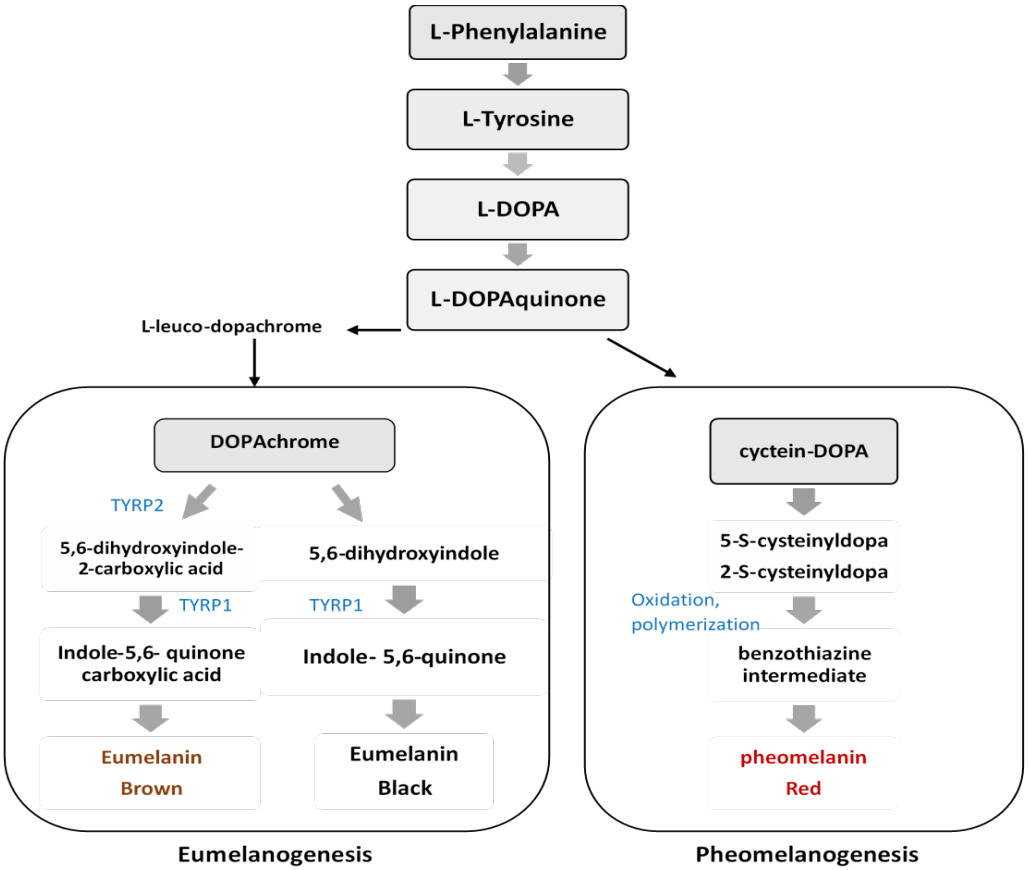


Figure 3.1 Pathway of Eumelanin and Pheomelanin synthesis.

Biosynthesis of eumelanin and pheomelanin start with the cyclisation by tyrosinase to L-Dopaquinone. The two pathways are then diverged. Dopaquinone can react with cysteine through two pathways to benzothiazines and pheomelanins. Eumelanin is derived from two separate pathways: brown and black eumelanin after the conversion of dopaquinone to leucodopachrome. Tyrosinase-related proteins TRP1 and TRP2 enzymes are essential for eumelanogenesis. Pheomelanin is derived from conjugation by thiol-containing cysteine or glutathione. Figure adapted from (Serre et al., 2018).

3.2.2 Melanin nanoparticles

Synthesis of melanin-like nanomaterial was inspired by melanogenesis in nature and has been achieved with melanin natural precursors or by enzymatic

crosslinking *in vitro*. Among the many precursors to synthesize melanin, dopamine is preferred for the preparation of synthetic melanin because it can be non-enzymatically cross-linked to 5,6-dihydroxyindole (DHI) under relatively moderate conditions (e.g., mildly basic pH 8.5) and the presence of dissolved oxygen in the aqueous reaction solution (Ju et al., 2011; Perring et al., 2018; Zhang et al., 2015). Poly-dopamine melanin provides the physical and chemical properties of natural melanin and contains various functional groups allowing multifunctional coatings (Ju et al., 2011). The initial synthesis of poly-dopamine melanin mimetic nanoparticles was achieved by Ju et al (2011) by hydroxylation of dopamine hydrochloride in alkaline solution.

The average diameter of the nanoparticles was around 100 nm in most studies. MNPs could be synthesized to give a broad range of sizes. Controlling the diameter of poly-dopamine melanin nanoparticles depends on parameters that influence the spontaneous oxidation rate of Dopamine.

3.2.3 PEGylation of nanoparticles

Polyethylene glycol is a type of protein polymer conjugate that has been used to improve safety and stability of many therapeutics without negatively affecting the drug bioactivity. PEG is classified by the FDA as generally regarded as safe (GRAS) category with the first PEGylated product approved in 1990 (Suk et al., 2016). PEG is highly soluble in water as it is an amphiphilic polymer that has both hydrophilic and hydrophobic parts (Parrott and DeSimone, 2012). It is also known to increase systemic circulation time and decrease immunogenicity of drugs (Nel et al., 2009; Parrott and DeSimone, 2012; Suk et al., 2016).

PEG coating of nanoparticles prolonged their circulation time by shielding the surface from aggregation, opsonization, and phagocytosis. PEGylation has been widely used in nanoparticle formation since the FDA approval of the first PEGylated nanoparticles (Doxil) in 1995, where PEGylation increased the drug circulation life by 90 % (Suk et al., 2016).

The surface of melanin nanoparticles could be effectively modified by methoxy-polyethylene glycol (mPEG) and this was found to improve their dispersion stability and circulation time as reported in the literature (Ju et al., 2011; Zhang et al., 2016; Zhang et al., 2015).

3.2.4 Rhodamine dye as a fluorescent label

Rhodamine is a water-soluble fluorescent xanthene dye. Both Rhodamine B and Rhodamine 123 have been used in labelling nanoparticles for cellular tracking (Amin et al., 2017; Craparo et al., 2021). The use of Rhodamine provided a narrow fluorescent excitation and emission peaks when used to label melanin nanoparticles (Amin et al., 2017). Wider peaks may interfere with other co-staining dyes that may be used for *in vitro* studies.

3.2.5 Aims:

1. To synthesize a library of melanin nanoparticles of different sizes.

2. To characterise synthesized particles.

3. Post-synthesis modifications and surface functionalization of the synthesized particles.

3.3 Materials and Methods:

3.3.1 Melanin nanoparticles synthesis

The synthesis method of the 200 nm MNPs was adapted from (Perring et al., 2018) i.e., the hydroxylation of dopamine hydrochloride in an alkaline solution. Briefly, 180 mg of Dopamine hydrochloride (Sigma-Aldrich, Gillingham, UK) was dissolved in 90 ml ddH_2O, followed by addition of 760 µl of 1 M sodium hydroxide (NaOH) solution while vigorously stirring. The mixture was aged for 5 hours at 50°C. Particles were then retrieved by centrifugation at 18016 g for 20 minutes and washed twice with ddH_2O. To remove large materials, centrifugation was repeated at 17699 g for 10 minutes (Figure 3.2).

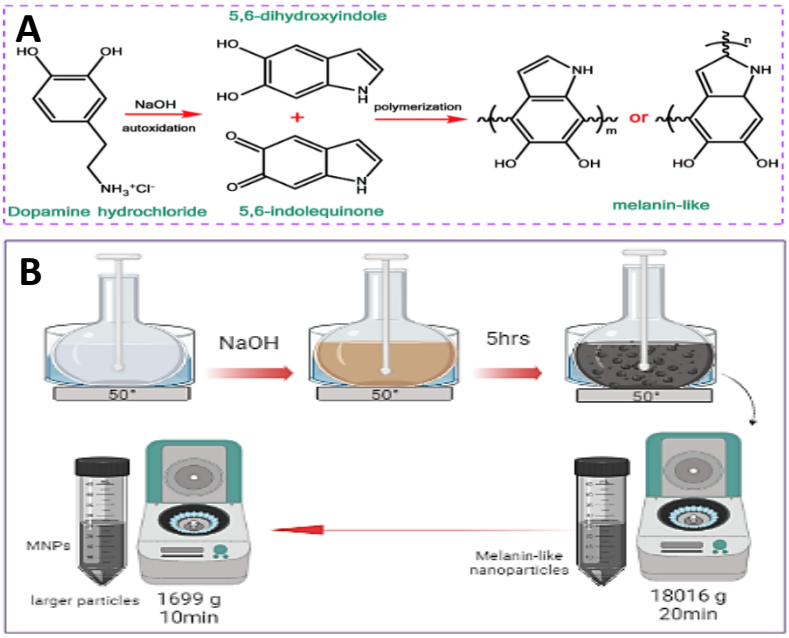


Figure 3.2 Schematic representation of melanin nanoparticles synthesis

(A) Melanin-like structure is produced by hydroxylation of dopamine hydrochloride followed by polymerization. (B) Synthesis of MNPs involves dissolving dopamine hydrochloride in deionized water under vigorous stirring at 50°C. Adding an alkali changed the colour from pale yellow to dark brown; the sample was aged for 5 hours followed by centrifugation to collect the nanoparticles. Image created with BioRender.com.

3.3.2 Size Control

From the standard synthetic conditions described in section 3.3.1 for the synthesis of 200 nm diameter MNPs, other size particles were synthesized by optimizing the dopamine to water ratio and pH of the mixture by adding 950 µl and 670 µl of 1 M NaOH for the synthesis of 50 nm and 500 nm diameter particles, respectively (Table 3.1).

	50 nm diameter	200 nm diameter	500 nm diameter
Dopamine/ Water ratio	2	2	4
1 M NaOH (µl)	950	760	670
Temperature	50°C	50°C	50°C
Time (hours)	5	5	5

Table 3.1 Synthetic Parameters of Melanin Nanoparticles

3.3.3 Hydrodynamic Diameter

The Hydrodynamic diameter of MNPs was measured using a disc centrifuge (DC 24000; CPS Instruments Europe) operated at maximum speed (28,978 g). To stabilize the particle sedimentation within the disc centrifuge, a density gradient was built up using increasing concentrations of 8 % (w/v) and 24 % (w/v) sucrose solution. A 100 µl MNP suspension was injected for size measurement and calibrated against a calibration standard of known diameter of 0.46 µm PVC (CPS Instruments, Europe).

3.3.4 Zeta potential

To measure the zeta potential of melanin nanoparticles, particles diluted in ddH_2O were injected into a disposable folded capillary cell (Malvern, Worcestershire, UK) ensuring no air bubbles were formed by turning the cell upside down, injecting the sample into the middle of the cell, then turning the cell again and inject the rest of

the sample. Surface zeta potential was then measured using zetasizer ZS90 (Malvern Panalytical, Malvern UK).

3.3.5 Transmission Electron Microscopy (TEM)

Preparation of 50 nm and 200 nm MNPs for TEM imaging entailed dispersion of the particles in ethanol followed by dropping the solution into holey carbon coated TEM grids (Agar Scientific, Stansted, UK). MNPs were then sent to the Solid Mechanics and Material Engineering Group, Department of Engineering science, University of Oxford and imaged by TEM using JEOL-2100 (JEOL-Japan). Image analysis was then performed using Gatan 3.

3.3.6 Scanning Electron Microscopy (SEM)

SEM imaging was used for the 500 nm MNP. MNPs were first dry-cast overnight on a carbon adhesive disc followed by a sputter-coating with 3 nm Au-Pd with primary energy of 15 kV. SEM imaging was then performed using a Carl Zeiss Evo LS15 VP-SEM.

3.3.7 Size Distribution

Distribution of nanoparticle sizes was calculated by measuring at least 50 particles per field in the Carl Zeiss Evo LS15 VP-SEM and by Malvern Zetasizer Nano ZS instrument.

3.3.8 PEGylation of melanin nanoparticles

The PEGylation method was adapted from (Zhang et al., 2016). In brief, particles were incubated with mPEG-5000 (Sigma-Aldrich, Gillingham, UK) at pH 10 for 12 hours at room temperature with vigorous stirring, followed by high-speed

centrifugation (12879 g) for 20 minutes. To remove the unreacted PEG, the mixture was washed with ddH_2O three times.

3.3.9 Confirmation of PEGylation

MNP and MNP-PEG were first freeze-dried overnight. Infra-red (IR) analysis (Varian Excalibur) was then used to confirm PEGylation. Absorption spectra were obtained at 25°C using 4 cm^{-1} resolution using synthetic melanin powder (MP Biomedicals, UK) as a reference control. A second analysis was performed to confirm PEGylation by zeta potential. MNPs and MNP-PEG were measured as described in section 2.4.4.

3.3.10 Stability of PEGylated particles

The stability of MNPs and MNP-PEG was compared by dissolving the particles in phosphate buffer saline (PBS) with 10 % Foetal bovine serum (FBS) at 37°C for 24 hours. The particle sizes were checked every two hours using Malvern Zetasizer Nano ZS instrument and a disposable capillary cell ensuring no air bubble was formed.

3.3.11 Post functionalization of with Rhodamine-B

To track melanin nanoparticles that may cross the placenta, an aliquot of the particles was labelled with Rhodamine B. *In situ* fluorophore modification of MNPs and MNP-PEG was performed following the method described in (Amin et al., 2017) by including 50 µg mL^{-1} Rhodamine B (Sigma-Aldrich, Gillingham, UK) during synthesis (as per sections 2.4.1, 2.4.2 and 2.4.8). To remove loosely bound dye, samples were centrifuged and washed with ddH_2O.

3.3.12 Statistical Analysis

GraphPad Prism 8.0.2 (San Diego, California, USA) software was used for statistical analysis of the data. Data were compared using One-way Anova or t-test. Data are presented as mean ± SD, statistical significance was defined as $P < 0.05$.

3.4 Results:

3.4.1 Synthesis of Melanin Nanoparticles

Water soluble Melanin-like nanoparticles were synthesized by hydroxylation of dopamine hydrochloride with NaOH in deionized water for five hours at 50°C under vigorous stirring. The colourless solution of dopamine hydrochloride turned orange/ yellow as soon as NaOH was added and then gradually turned dark brown. The nanoparticles were then easily obtained after two centrifugation steps (Figure 3.3 A and B). The reaction pathway is schematically illustrated in (Figure 3.2).

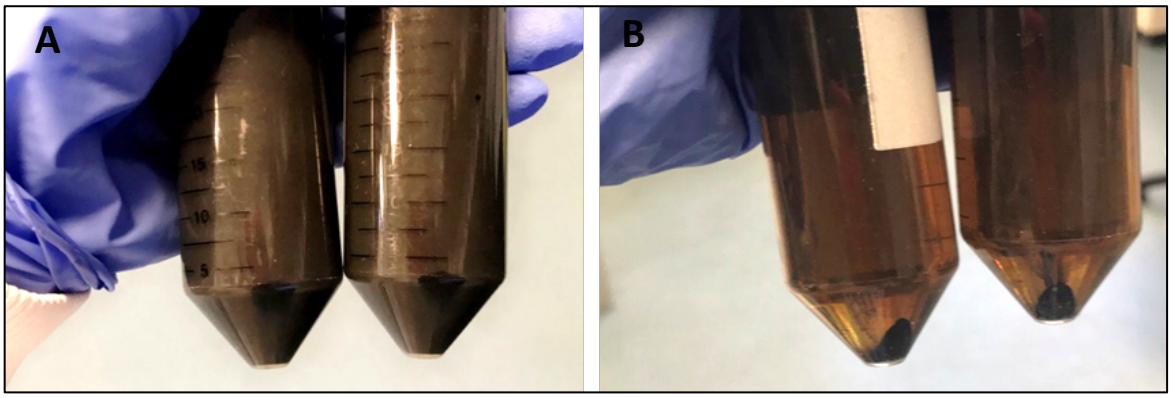


Figure 3.3 Melanin Nanoparticles Synthesis.

(A) 50 ml falcon tubes showing melanin nanoparticle pellet after centrifugation at 1699 g (B) 50 ml falcon tubes showing a pellet of melanin nanoparticles after centrifugation at 18016 g.

3.4.2 Hydrodynamic Diameter

The hydrodynamic diameter of three different sizes of synthesized melanin nanoparticles was measured using CPS disc centrifuge. This is based on the principle of differential (small size separated from whole size) sedimentation, whereby particles in a fluid settle under the influence of gravitational force. CPS results shows three different sizes of the particles with peaks at 60 nm, 250 nm, and 650 nm diameter (Figure 3.4).

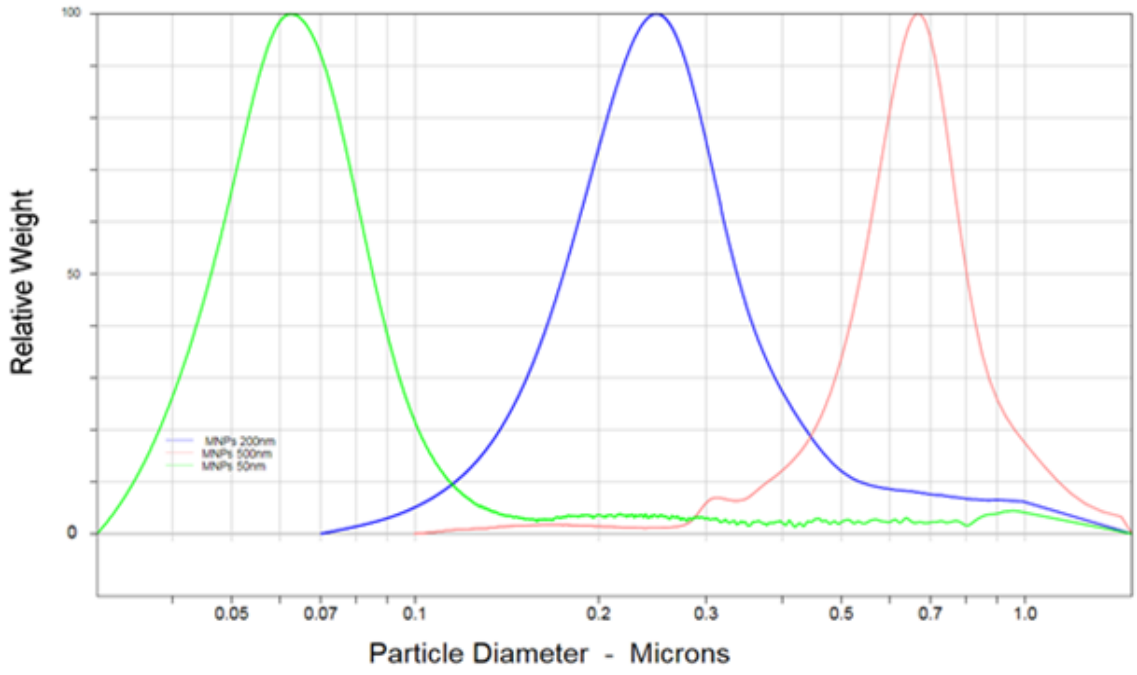


Figure 3.4 Hydrodynamic diameter of melanin nanoparticles

CPS disc centrifuge results showing the hydrodynamic diameter of three different sizes melanin nanoparticles peaked at 60 nm (green), 250 nm (blue) and 650 nm (red). Size was calibrated against a calibration standard of known size of 0.46 µm diameter PVC.

3.4.3 Zeta potential

The zeta potential is a strong indicator of nanoparticle stability in a dispersion fluid and thus determines whether the particles within a liquid will tend to aggregate or not. Particles with zeta potential more positive than approximately + 20 mV, or more negative than approximately – 20 mV indicates good stability (Figure 3.5A). Melanin nanoparticles showed a good stability at pH 7 with zeta potential ranging from -26 mV to -32 mV (Figure 3.5B).

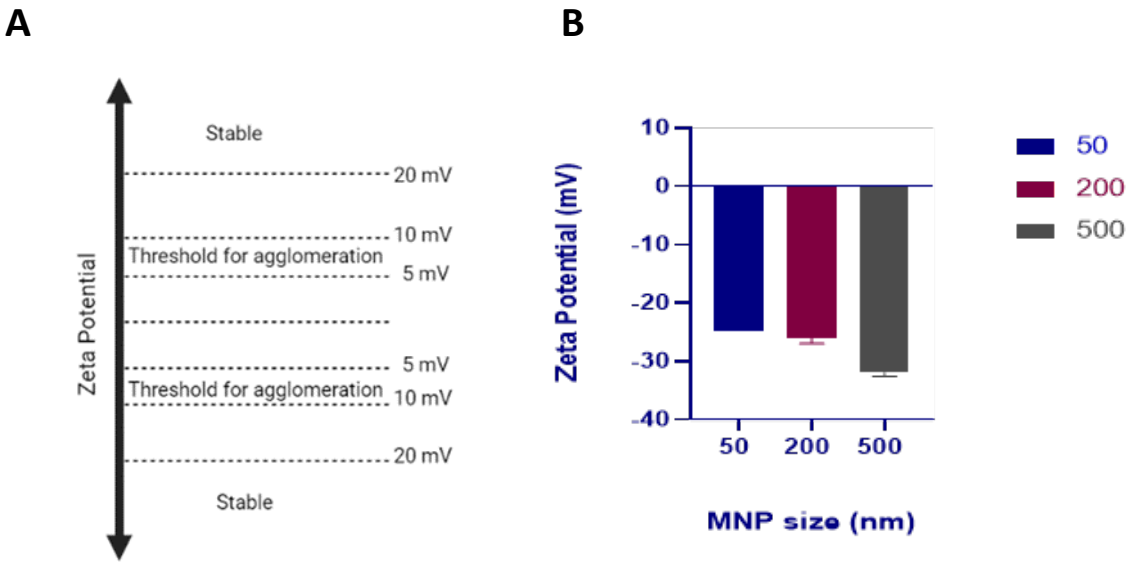


Figure 3.5 Zeta potential of melanin nanoparticles.

Interpretation of zeta potential values in assessing nanoparticles stability where particles greater than ± 20 mV are considered stable (A). Bar chart representing zeta potential of 50 nm (blue), 200 nm (red) and 500 (grey) nm diameter melanin nanoparticles dispersed in ddH_2O and measured by zetasizer using disposable folded capillary cell ensuring no air bubbles were formed (B). Data shows mean ± SD (n=3).

3.4.4 Transmission and Scanning Electron Microscopy

TEM and SEM images confirmed the synthesis of three different sizes of melanin nanoparticles with mean diameters of 50 nm (Figure 3.6 A and B), 200 nm (Figure 3.6 C and D), or 500 nm (Figure 3.6 E). The particles appear roughly spherical in shape and with a smooth surface. SEM was only used for the 500 nm diameter particles for practical reasons (section 2.8).

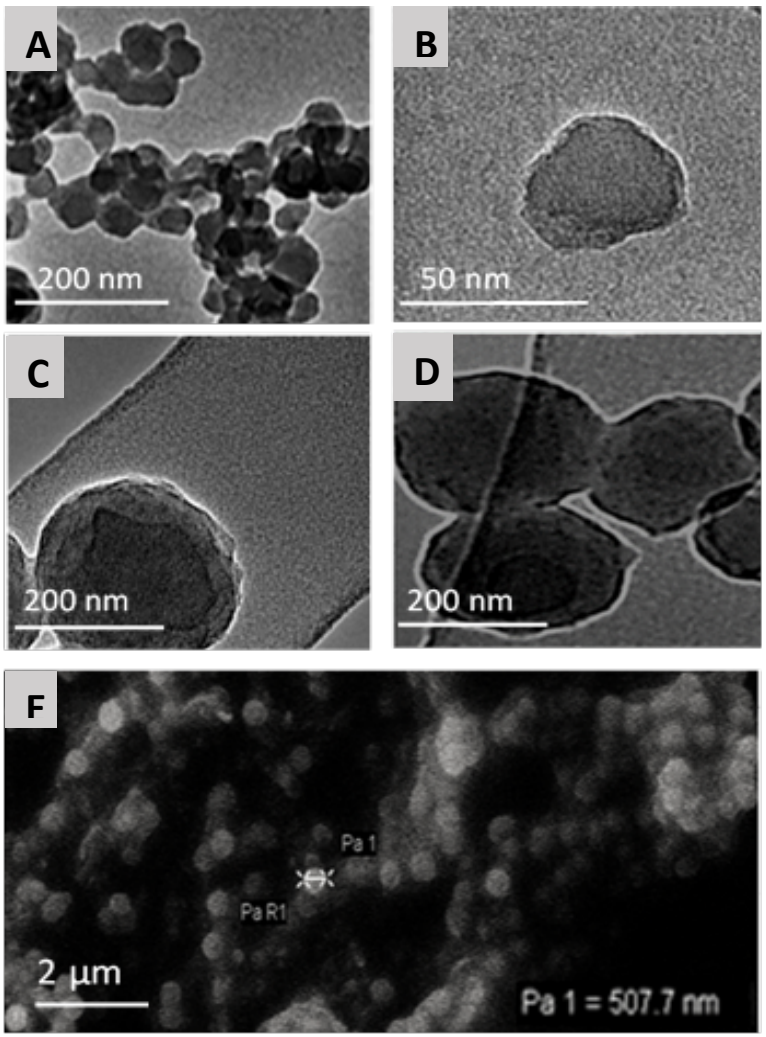


Figure 3.6 Transmission and scanning electron microscopy imaging.

TEM images of (A&B) 50 nm diameter, (C&D) 200 nm diameter melanin nanoparticles, and (E) SEM image of 500 nm diameter melanin nanoparticles. TEM images were performed by Dr. Chechen Duan at the (Solid Mechanics and Material Engineering Group, Department of Engineering science, University of Oxford).

3.4.5 Size distribution

Size distribution of melanin nanoparticles was 50.12 ± 6.15 nm diameter 194.11 ± 9.51 nm diameter and 504.84 ± 10.91 nm diameter obtained by measuring at least 50 particles per field (Figure 3.7 A, B and C).

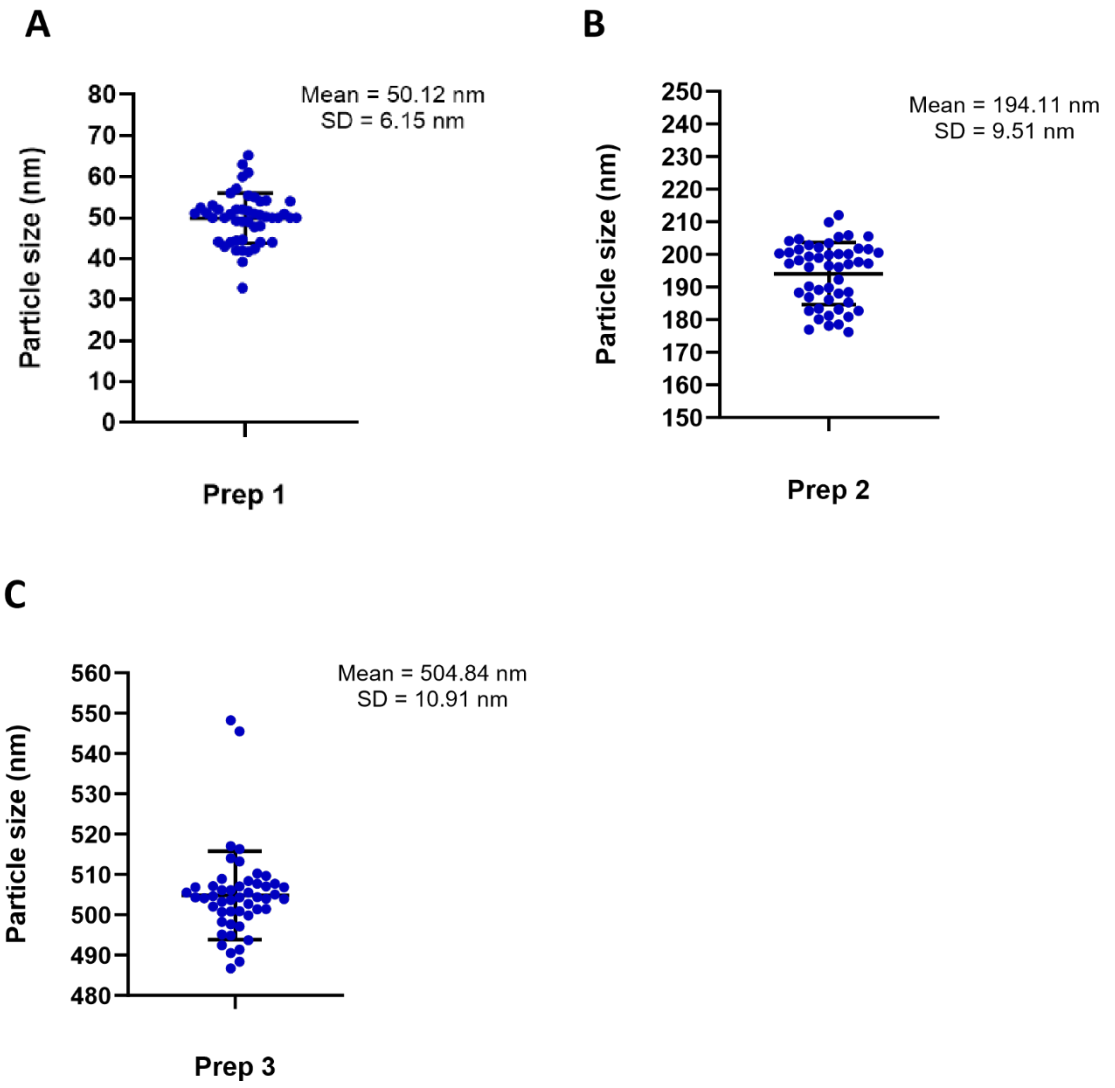


Figure 3.7 Size distribution of melanin nanoparticles.

Size distribution of melanin nanoparticles; (A) 50.12 nm (B) 194.11 nm, and (C) 504.84 nm diameter determined by measuring at least 50 particles per field.

3.4.6 Confirmation of PEGylation

The attachment of melanin nanoparticles to PEG was confirmed by infrared spectroscopy (IR) where MNP-PEG showed peaks representing MNP (3201 cm^{-1}), PEG (2883 cm^{-1}) and MNP-PEG (3151 and 2880 cm^{-1}) (Figure 3.8). A second assessment of PEGylation was performed by zeta potential whereby the PEGylated particles showed a higher zeta potential compared to the non-PEGylated particles (Figure 3.9) indicating shielding of the negatively charged MNPs.

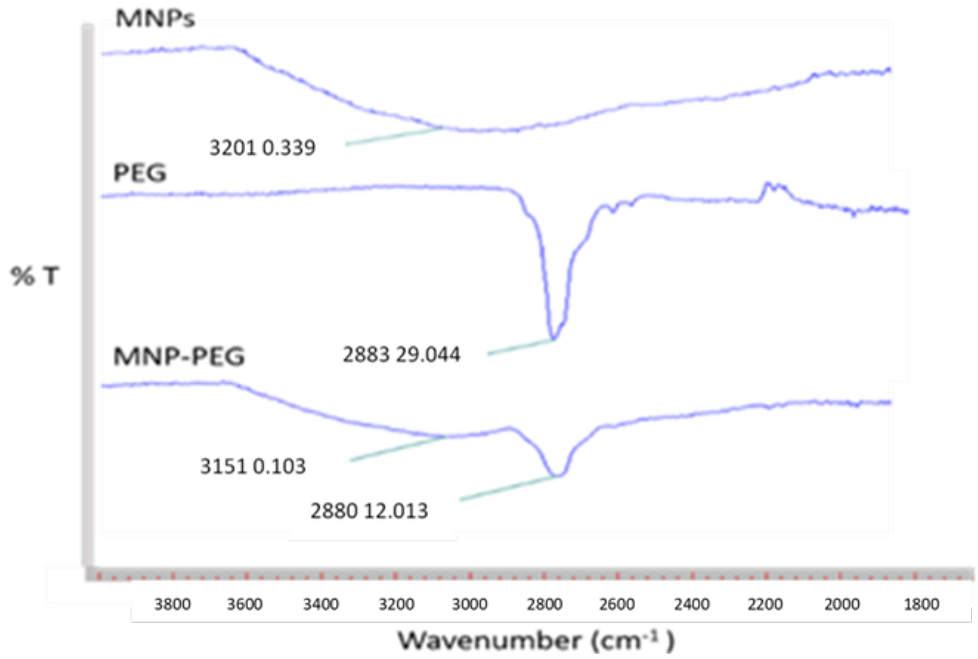


Figure 3.8 FTIR Confirmation of PEGylation.

Fourier transform infrared spectroscopy (FTIR) to confirm melanin nanoparticles PEGylation. Absorption spectra were obtained at 25°C using 4 cm^{-1} resolution using synthetic melanin powder, %T = percentage transmittance.

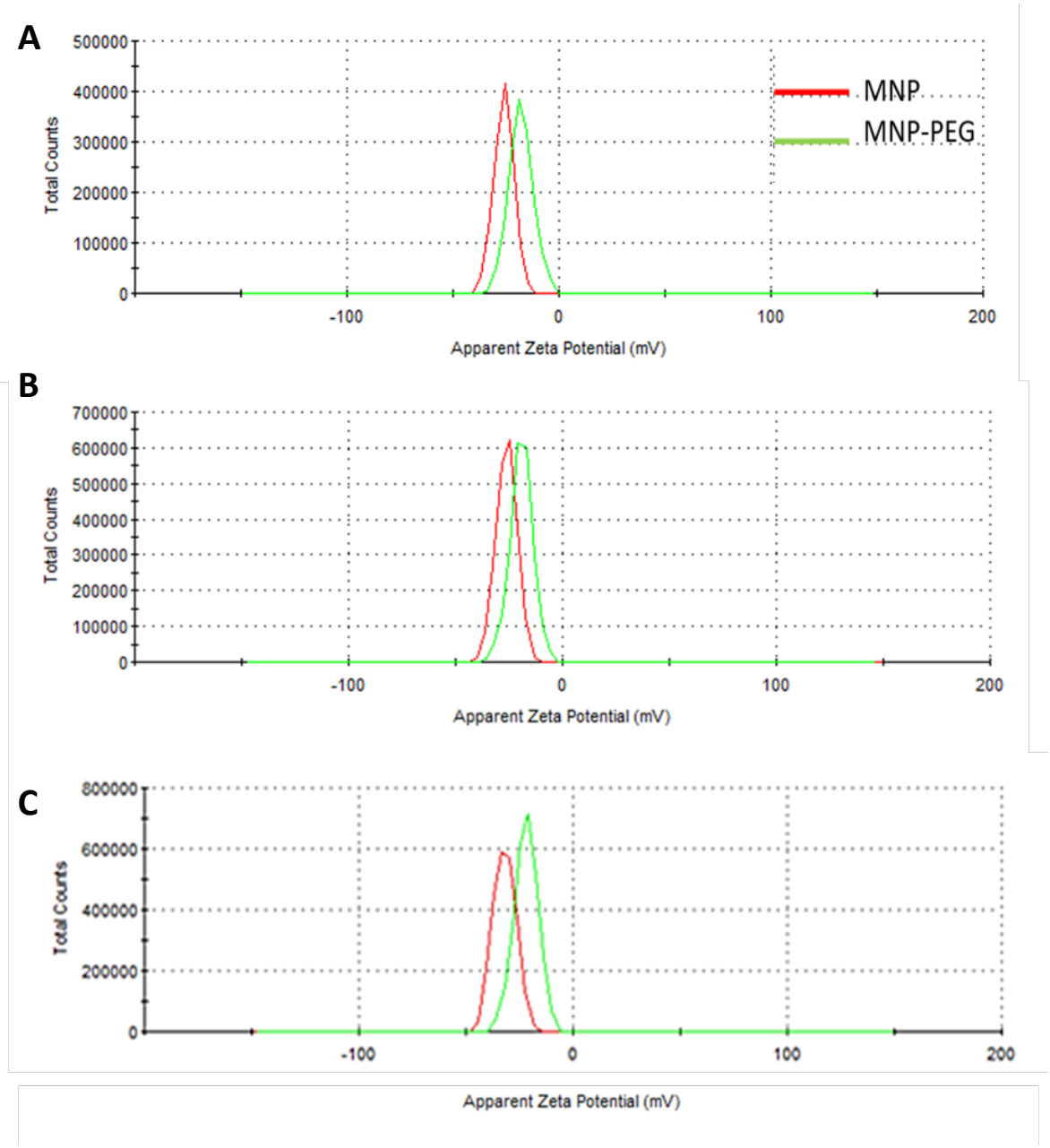


Figure 3.9 Zeta potential of PEGylated nanoparticles.

Zeta Potential of melanin nanoparticles before (red) and after (green) PEGylation of (A) 50 nm diameter, (B) 200 nm diameter and (C) 500 nm diameter, measured using zetasizer ZS90 (n=3).

3.4.7 Stability at 37°C

The stability of MNP and MNP-PEG were compared by incubating the particles at 37°C for 24 hours. Before PEGylation, MNPs appeared to be stable for about 18 hours before they start to visibly aggregate, while PEGylated MNPs remained stable for 24 hours (Figure 3.10 A). The size of both MNPs and PEGylated MNPs was also measured before and after incubating the particles at 37°C showing a slight increase in MNP sizes (Figure 3.10 B).

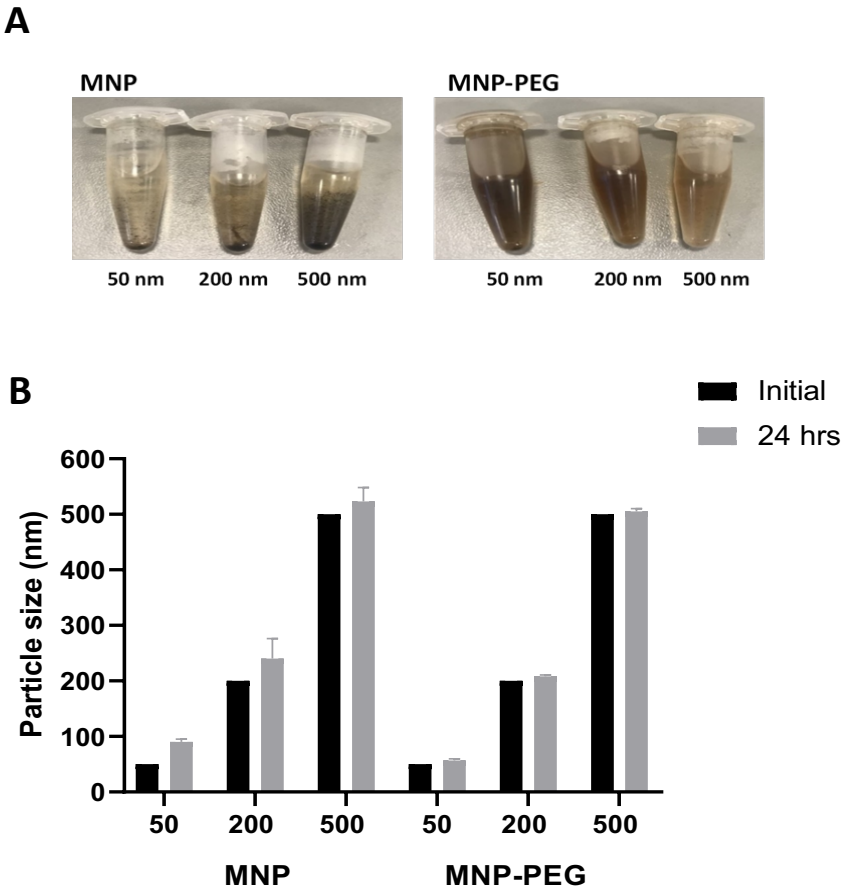


Figure 3.10 Stability of MNP and MNP-PEG at 37°C.

(A) Representative images showing tubes containing 50 nm diameter, 200 nm diameter, or 500 nm diameter MNP and MNP-PEG after incubation at 37°C. (B) Diameter of MNP and MNP-PEG before and after incubation at 37°C. Data shows mean ± SD (n=3).

3.4.8 Post functionalization of MNP and MNP-PEG with Rhodamine B

An aliquot of both MNPs and PEGylated MNPs were labelled with fluorescent Rhodamine B to be able to track the particles across the placental tissue. Fluorescence labelling was achieved after *in situ* incorporation of Rhodamine B during synthesis (Figure 3.11 A) as described in 3.4.11. After three washing steps, the fluorescence intensity of an increasing concentration of labelled particles was measured in a plate reader using Excitation 488 nm/ Emission 525 resulting in a linear relationship between concentration and fluorescence (Figure 3.11 B).

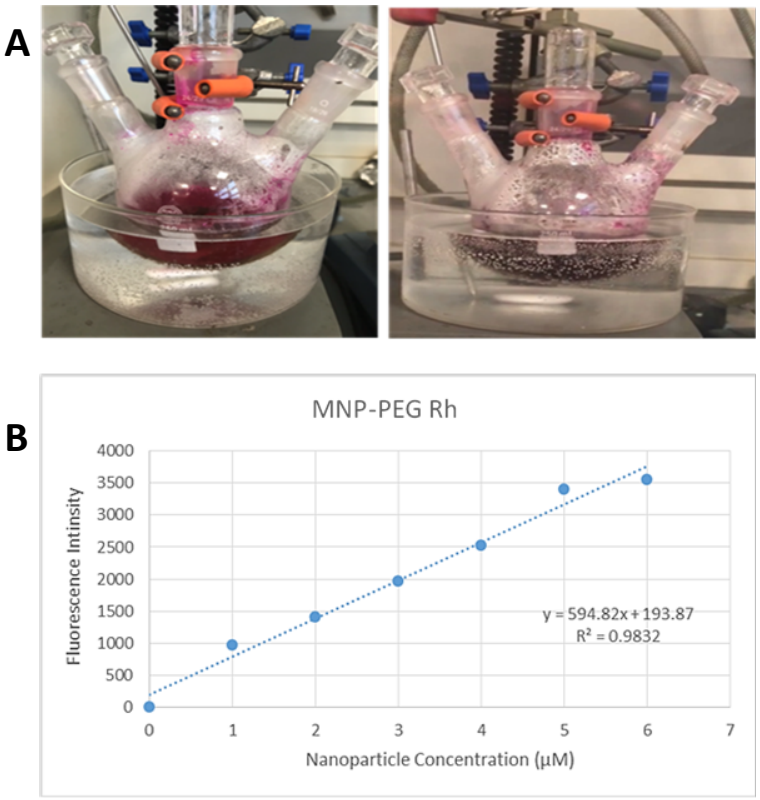


Figure 3.11 Fluorescence labelling of MNP-PEG with Rhodamine

(A) In situ incorporation of Rhodamine B during MNP synthesis; (Left) starting point, (Right) slightly darker after 1 hours. (B) A linear curve of an increasing concentration of Rhodamine labelled melanin nanoparticles.

3.4.9 Summary of key characteristics of particles

Characteristics of the three differently sized synthesized melanin nanoparticles and their post synthesis modification are summarized in table 2.2.

Melanin nanoparticle	Size 1	Size 2	Size 3
Hydrodynamic diameter peak	60 nm	250 nm	650 nm
Size as determined by TEM/SEM	50 nm	200 nm	500 nm
Size distribution	50 ± 10 nm	200 ± 20 nm	500 ± 10 nm
Zeta potential	- 26 ± 0.25 mV	-27 ± 1 mV	-32 ± 1 mV
Stability at 37°C	18 hours	20 hours	20 hours
Surface modification	PEGylation		
Stability at 37°C after PEGylation	24 hours		
Fluorescence functionalization	Rhodamine B		

Table 3.2: Summary of key particles characteristics

3.5 Discussion:

3.5.1 MNP synthesis and size control

To overcome the insolubility of natural melanin which limits biological application, synthetic dopamine melanin nanoparticles which have a more favourable profile were used. Melanin nanoparticles are water-soluble, degradable, and mimic the chemical and physical property of natural melanin (Park et al., 2019; Zhang et al., 2015).

Whilst the dopamine self-oxidation induced polymerization method was used to synthesise the poly-dopamine nanoparticles (Figure 3.2 A and B), the exact mechanism of polymerization has not been determined yet (Wu and Hong, 2016). Dopamine can spontaneously oxidise to 5,6-dihydroxyindole (DHI) in the presence of oxygen (Ju et al., 2011).

Size of poly-dopamine melanin nanoparticles decreases as the amount of NaOH increases (Ju et al., 2011), thus, in this chapter, preparation of three different sizes of MNPs was achieved by controlling the pH of the mixture as displayed in Table 3.1. The preparation of 200 nm diameter MNPs was carried out following the standard conditions (Ju et al., 2011; Perring et al., 2018). However, to have different MNP sizes, optimizing the amount of NaOH via several experimental trials to reach the 50 nm diameter and 500 nm diameter was performed. Size range of particles was carefully designed since it affects their clearance, uptake, and circulation time. It was found that particles smaller than 10 nm exhibit a high renal clearance (Alexis et al., 2008; Longmire et al., 2008) while phagocytosis is the main uptake of particles larger than 500 nm (Zhao and Stenzel, 2018). The hepatic system represents the primary role of clearance for particles that do not undergo renal clearance and thus

can rapidly eliminate particles of a size range between 10-20 nm (Longmire et al., 2008). Therefore, to achieve adequate retention time, longer circulation, and therapeutic efficacy, particle size and/or surface modification are key factors in particle bio-distribution.

Since nanoparticle interaction with the placenta can be affected by their size, the range of sizes in this thesis was chosen according to reports in the literature regarding the interaction of other types of nanoparticles (silica, gold, polystyrene, and liposomes) with mice and human placenta (Aengenheister et al., 2018b; Cornford et al., 2016; Huang et al., 2015; King and Muller, 2016; Myllynen et al., 2008; Poulsen et al., 2015; Semmler-Behnke et al., 2014; Wick et al., 2010; Yamashita et al., 2011). The diameter of the synthesized particles was then confirmed by measuring the hydrodynamic diameter (Figure 3.4) then the actual size and size distribution by TEM and SEM (Figure 3.6 and 3.7); 50 ± 10 nm diameter, 200 ± 20 nm diameter and 500 ± 10 nm diameter.

3.5.2 Characterization of the water soluble MNPs

The synthesized particles of chosen size were then characterized using DLS, Zeta potential and TEM/SEM imaging to measure size/size distribution, zeta potential, dispersion stability, and morphology characteristics.

The hydrodynamic diameter of the particles was measured using a disc centrifuge which is based on the principle of differential sedimentation. When a dispersed particle moves through a liquid medium, an electric layer adheres to its surface, known as hydrodynamic diameter. Therefore, it is mostly above the primary diameter of that measured with electron microscopy. The thickness of the layer

depends on several factors, such as the electrical conductivity of the liquid and it determines the dispersion status of the particles in a liquid solution.

The morphological characteristics of the particles was determined by TEM and SEM imaging and appeared roughly spherical with a smooth surface (Figure 3.6). MNPs were synthesized using the bottom-up technique which depends on the thermodynamic energy of the particles, thus the yield particles tend to be spherical to minimize the interfacial energies (Liu et al., 2012). The bottom-up technique is cost effective and provides a higher yield of nanoparticles. Although advanced fabrication techniques allow the generation of non-spherical particles, traditional spherical shape nanoparticles are most used in biological applications. Since scalability is an important parameter for clinical translation, a key characteristic of scalable technique is simplicity, reproducibility, and high throughput offered by high yield methods.

Because most melanin granules are insoluble in water, dispersion of the synthesized melanin is very critical to be applied in biomedical research. Zeta potential determines the particle dispersion stability in fluid (Kaur et al., 2017), and the synthesized poly-dopamine melanin particles were negatively charged with a zeta potential ranging from -26 to -32 mV at pH 7 (Figure 3.5) indicating good stability. As such, MNPs remained stable for up to 20 hours when incubated at 37°C (Figure 3.10 A), and further improved after PEGylation (Figure 3.10 B). The negatively charged particles may also limit their uptake/interaction with the placenta allowing longer circulation time.

3.5.3 Surface functionalization

PEGylation, the use of polyethylene glycol as a conjugate polymer, is a polymerization method that has been used for decades in biomedical and pharmaceutics applications to improve the safety and stability of drugs (Suk et al., 2016). PEGylated MNPs showed characteristic spectral peaks of PEG at 2883 cm^{-1} and MNPs at 3201 cm^{-1} (Figure 3.8) in agreement with Ju et al. (2011). The zeta potential of MNP-PEG was higher than the unreacted particles (Figure 3.9) which also confirms PEGylation.

While non-PEGylated MNPs were partially precipitated out from PBS/FBS solution in about 20 hours, PEGylated particles remained stable under physiological conditions even after 24 hours incubation (Figure 3.10 A and B). PEGylation of melanin nanoparticles was shown to increase their stability in liquids (Ju et al., 2011; Zhang et al., 2015) and systemic circulation time *in vivo* (Zhang et al., 2016) which increases their potential use in biomedical applications. PEGylation has also been found to significantly limit placental uptake and trans-placental passage in an *ex vivo* human placental perfusion of liposomal doxorubicin (Valero et al., 2017). Thus, PEGylation may also help in restricting the movement of the synthesized MNPs which is the aim of this thesis and will be tested in later chapters.

Fluorescence labelling of melanin nanoparticles has previously been achieved with thiol-containing poly-methacrylic acid polymer conjugated with Alexa Fluor 488 dye as a linker to label poly dopamine capsules (Chen et al., 2014). However, the approach of cross-linking and conjugation requires multiple steps, limiting the labelling efficiency. Other related work focuses on the synthesis of fluorescent melanin-like nanostructures by H_2O_2 oxidation resulted in broad fluorescent excitation and emission spectral peaks (Lin et al., 2015; Zhang et al., 2012). Wider

peaks may interfere with other co-staining dyes that may be used for *in vitro* studies. When melanin nanoparticles were labelled with Rhodamine using an *in situ* fluorophore modification approach, narrow fluorescent excitation and emission peaks were generated (Amin et al., 2017). Thus, to be able to track the particles in an *in vivo* human placenta, particles were fluorescently labelled with Rhodamine B (Figure 3.11 A). Rhodamine functionalization was confirmed by a linear relationship between concentration and fluorescence when different concentration of functionalised MNPs were tested in a plate reader at Excitation 488 nm/ Emission 525 (Figure 3.11 B).

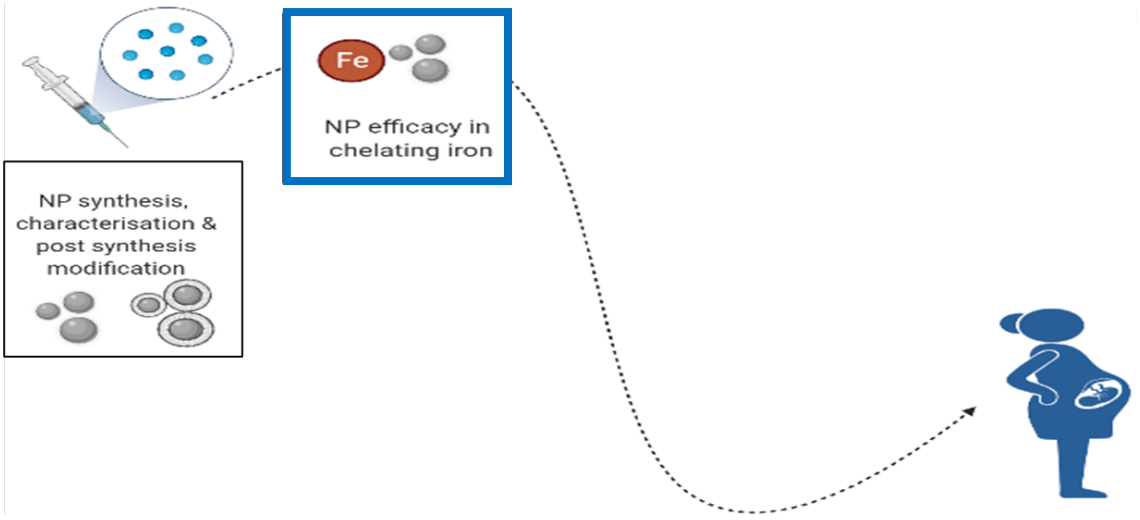
3.5.4 Strength and limitations

Natural melanin is poorly soluble in water and most solvents. The synthesized poly-dopamine melanin nanoparticles were water soluble and showed good dispersion stability with a zeta potential ranging from -26 to -32 mV at pH 7. PEGylated particles remained stable for more than 24 hours in a physiological condition which increases their potential use in biomedical applications.

3.6 Summary:

This chapter presents the synthesis, characterization, and post-synthesis modification of three different sizes of poly-dopamine melanin nanoparticles. Results demonstrate synthesis of spherical MNPs of 50 ± 10 nm diameter, 200 ± 20 nm diameter and 500 ± 10 nm diameter that was confirmed with TEM and SEM images. The negatively charged PEGylated particles were stable for more than 24 hours under physiological conditions. Since the interaction of nanoparticles with the human placenta was mainly affected by particle size, it was hypothesized that synthesized particles would be restricted from movement across the placenta.

Chapter 4 Functional analysis: The efficacy of poly-dopamine melanin nanoparticles in chelating iron and reducing Labile Iron Pool



4.1 Abstract

Background: The limitations of current chelation therapy, such as the short half-life, widespread toxicity, and insufficiency, means there is interest in developing better iron chelation options. It is suggested that the use of high MW chelators such as nanoparticles could reduce the undesirable limitations. Moreover, nanoparticles with appropriate characteristics could be restricted from movement across the placenta making them safe for use during pregnancy, unlike current chelators.

Objectives: The aim of this chapter was to test the iron chelation efficacy of the three different sizes of synthesized and functionalized melanin nanoparticles prepared in chapter 3.

Methods: Colorimetric assay was used to test the functionality of MNPs to chelate iron. Calcein assay and flow-cytometry were used to assess their ability to reduce the labile iron pool *in vitro* using hepatocellular carcinoma cell line HepG2.

Results: Results showed that melanin nanoparticles could chelate iron to a maximum adsorption of 14 +/- 0.25 mM of iron/g of material; significantly higher efficacy than DFO of the same concentration. Surface modification with PEG did not limit particles' ability in chelating iron. MNPs were also shown to reduce the LIP in iron loaded HepG2 cells with higher efficacy than DFO.

Conclusion: All three different sizes of MNP were more effective in chelating iron compared to DFO, likely due to the increased surface area of nanoparticles. This could help in reducing dose and frequency of medication administration.

4.2 Introduction

4.2.1 Overview

Chapter 3 presented the preparation and characteristics of three different sizes of poly-dopamine melanin nanoparticles and their surface functionalization. Here, the ability of the synthesized MNPs and MNP-PEG to chelate iron and their efficacy compared to the currently used chelators was demonstrated.

4.2.2 LIP (labile iron pool): Chelatable iron

LIP is defined as the intracellular, nonprotein bound iron that can promote the production of ROS via the Fenton reaction resulting in oxidative cell damage when exceeding cellular defence capacity, as associated with iron overload. Various cells contain a transient cytosolic iron pool that is likely bound to low MW intracellular chelates, such as citrate (Espósito et al., 2002; Wang and Pantopoulos, 2011), organic anions, surface components of membranes or extracellular matrix (Espósito et al., 2002). It acts as an intermediate or transitory pool between extracellular iron and the cellular iron associated with proteins. Efficient regulatory homeostatic mechanisms (largely centred in the liver) are triggered by fluctuations of the cytosolic iron under moderate iron loading to adjust iron absorption and recycling accordingly. However, massive iron loading overwhelms the homeostatic mechanism and results in an uncontrollable iron expansion that ultimately leads to organ dysfunction *via* oxidative reactions (Hamilton and Kizhakkedathu, 2015). This cytosolic LIP mirrors the cellular iron content and can be monitored *in situ* by fluorescence sensors such as calcein (Breuer et al., 2008). The LIP comprises chelatable iron that can be targeted by chelation agents to protect the cells against oxidative damage (Breuer et al., 2008; Wang and Pantopoulos, 2011).

4.2.3 Chelation therapy: attempts on overcoming challenges in current iron chelation therapy

Iron chelation therapy involves the use of chelators that can bind to iron under physiological conditions to form a non-toxic complex which is ultimately excreted from the body in faeces or urine. The process thereby reduces the amount of iron and protects the cells from oxidative damage. The limitations of currently used iron chelators (Origa, 2017), has generated an interest to overcome these limitations in developing better iron chelation options (Table 1.1) (Cohen et al., 2003; Hamilton and Kizhakkedathu, 2015; Hoffbrand et al., 2012; Porter et al., 1998; Shangaris et al., 2019).

The main challenges of the currently approved small MW chelators are the widespread toxicity and rapid elimination. It is suggested that high MW chelators such as polymeric chelators or polymeric nanocarriers would overcome systemic toxicity and improve pharmacokinetics (Hamilton and Kizhakkedathu, 2015). Several studies have investigated modifying DFO properties (Hallaway et al., 1989; Liu et al., 2016b; Rossi et al., 2009; Wang et al., 2018). Although, conjugating DFO with polymers indicated unique advantages over unconjugated small MW DFO, most have not been tested for efficacy *in vivo* and none have advanced to the clinic likely due to their biodistribution patterns, toxicity, and elimination pathways. Attempts to encapsulate DFO into liposomes has been unsuccessful as it sequesters the DFO only initially with a non-ideal release profile which may still cause systemic toxicity (Hamilton and Kizhakkedathu, 2015). It is vital that chelators are safe to use, easily reproduced on a large scale and suitable for clinical use. Moreover, the use of the low MW chelator during pregnancy is not recommended

due to possible risk to the foetus (Origa, 2017), increasing demands for alternative treatment options for this group of patients.

4.2.4 Poly-dopamine melanin nanoparticles as an iron chelator

When tested in a mice model of iron overload, melanin nanoparticles significantly improved the therapeutic effect with significantly lower dose (30-100 mg/kg) compared to DFO (750 mg/kg). This is due to the increase of surface area of nanoparticles. Melanin nanoparticles were also found to exhibit a relatively longer circulation time *in vivo* (17 hours in mice compared to 5 minutes DFO) (Yan et al., 2016).

In chapter 3, it was found that synthesized MNPs were stable for a maximum of 20 hours at 37°C, and a prolonged stability time of more than 24 hours was seen when MNPs were PEGylated (Figure 2.11) which may in turn have a relatively longer circulation life *in vivo.* Melanin nanoparticles used in the mice study were prepared from pristine melanin granules with an ultra-small size of 4.9 nm. In this chapter, efficacy of the synthesized poly dopamine melanin of 50, 200 nm and 500 nm diameter to chelate iron in comparison to DFO was tested.

4.2.5 Calcein fluorescence for measurement of the LIP

Detection of the LIP is based on the principle of tracing iron chelation either by the recovery of the fluorescence signal that has been quenched by complexing of iron to a fluorescent metal sensor or by the inhibition of ROS formation. Calcein, is a fluorescent chelator that undergoes a stoichiometric fluorescence quenching upon binding to LIP. This fluorescence quenching can fully reverse by scavenging iron with competing chelators such as DFO or MNPs. Thus, the calcein assay can be

used to monitor efficacy and affinity of a candidate chelator to bind to the LIP (Ali et al., 2003; Breuer et al., 2008; Espósito et al., 2002).

4.2.6 HepG2 cell line

HepG2 cells are derived from a hepatocellular carcinoma and can initiate iron loading by progressively increasing iron (Mariani et al., 2009; Mehta and Sharp, 2020). The largest chelatable iron pools are within hepatocytes where 70 % of iron is in deposits (Hamilton and Kizhakkedathu, 2015; Vlachodimitropoulou et al., 2017). Thus, HepG2 cells are useful for the investigation of the protective and therapeutic efficacy of iron chelators.

4.2.7 Aims

1. To establish efficacy of iron chelation of the three different size MNPs in comparison to the commonly used chelator DFO.

2. To investigate the effect of PEGylation on particle ability to chelate iron.

3. To establish MNPs and MNP-PEG ability to chelate intracellular labile iron pool.

4.3 Materials and Methods:

4.3.1 Determining the efficacy of MNPs in binding iron and the effect of MNP size

Assessment of iron binding to MNPs was carried out using a colorimetric assay. In brief, a final concentration of 1 mM MNP of 50 nm, 200 nm, or 500 nm diameter or 1 mM DFO (Sigma-Aldrich. Gillingham, UK) was incubated with 1, 3, or 4 mM ferrous sulfate ($FeSO_4$; Sigma-Aldrich. Gillingham, UK) for 24 hours at 37°C. The mixture was then centrifuged at 20,124 g for 3 minutes and supernatant containing the unbound iron was then collected and further incubated with 1/10 volume sodium acetate buffer (prepared with equal volumes of 6 M acetic acid and 5 M NaOH) for 10 minutes at room temperature. Hydroxylamine (10 µl; Sigma-Aldrich, Gillingham, UK) was then added and incubated for 10 minutes followed by the addition of 100 µl phenathroline (0.1 wt %) (Sigma-Aldrich, Gillingham, UK) for the colour reaction to take place. All samples were then transferred to a 96 well plate and the absorbance was measured at 450 nm in a plate reader (Magellan Infinite M200) against a standard calibration curve of $FeSO_4$ ($R^2 = 0.99$). The method is illustrated in Figure 4.1.

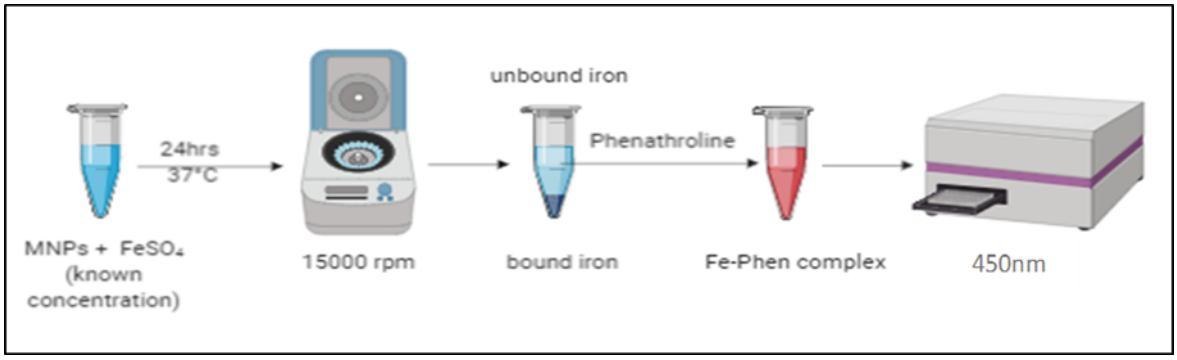


Figure 4.1 Graphical Summary of the Iron Binding Method.

Different concentrations of MNPs or DFO were incubated with equal amount of $FeSO_4$ at 37°C for 24 hours. The mixture was then centrifuged at 20,124 g for 3 min before the supernatant containing the unbound iron was collected and incubated with phenathroline for 20 min to allow the colour reaction take place. The absorbance was measured at 450 nm against a standard calibration curve. Image created with BioRender.com.

4.3.2 Determining the effect of incubation time on particle efficacy in chelating iron

To determine the effect of incubation time on particle efficacy in chelating iron, the experiment was carried out as explained in 4.3.1. 50 nm diameter, 200 nm diameter and 500 nm diameter MNPs or DFO were incubated with 4 mM $FeSO_4$ for 24 and 48 hours at 37°C.

4.3.3 Determination of PEGylation effect on particle efficacy in chelating iron

To assess the effect of PEGylation on iron binding ability of MNPs, the experiment was carried out as explained in 4.3.1 using 50 nm diameter, 200 nm diameter and 500 nm diameter PEGylated or non-PEGylated particles of equal concentrations with 4 mM $FeSO_4$.

4.3.4 HepG2 cell culture

HepG2 cells (from Dr.Ricky Bogal, University of Birmingham) were used for experiments in this chapter. Cells were expanded and frozen stocks were made within a few passages of receipt. Early passages were then thawed and used for this experiment. HepG2 cells were cultured in Roswell Park Memorial Institute (RPMI) media and supplemented with 10 % (v/v) FBS, 2 mM L-glutamine, 100 U/mL penicillin, and 0.1 mg/mL streptomycin (All Sigma-Aldrich, Gillingham, UK). Cells were incubated at 37 °C/ 5 % CO_2 and passaged when confluent.

4.3.5 Determination of MNPs effect in reducing labile iron pool in HepG2 by calcein assay and flow-cytometry

The ability of MNPs and MNPs-PEG to reduce the intracellular labile iron pool was tested with a calcein assay using flow-cytometry. HepG2 cells were first seeded in a 12 well plate, and iron loading was achieved after treating the cells with FBS and holo-transferrin 2% (v/v) (Sigma-Aldrich. Gillingham, UK) to allow intracellular iron transfer or with 200 µM iron from ferric ammonium citrate (Sigma-Aldrich, Gillingham, UK) for 24 hours as described by Mehta & Sharp 2020 and Vlachodimitropoulou et al., 2017. Cells were then incubated with an equal concentration of DFO, MNP, MNP-PEG or PBS for 1 hour. After washing the cells twice with PBS, a 2 µl of 50 µM Calcein (Cambridge Bioscience Ltd, UK) was added to a 1 mL cell suspension (0.1-5 x 10^6 cells/ml) and incubated for 15-20 minutes at 37°C. Cells were then washed twice and analysed by flow-cytometry for a minimum of 10,000 events. Data were analysed using FlowJo v.10 (BD Biosciences, UK).

4.3.6 Quantification of cell iron content and protein determination

The amount of iron in HepG2 cells before and after chelation was quantified by employing calcein as a fluorescent probe for the labile iron pool in the cell lysate as described in (Ali et al., 2003) and (Perring et al., 2018). Briefly, HepG2 cell suspension was placed on a hot plate of 95°C for 15 minutes then sonicated for 2 minutes using a VibraCell probe. Cell suspension was then centrifuged at 12,000 rpm for 5 minutes to remove cell debris. Supernatant (80 µl) was added to a 96-well plate containing 80 µl of 2 M calcein, 20 µl of 500 mM 4-(2-hydroxyethyl)-1-piperazineethanesulfonic acid) (HEPES) (pH 7.4) and 20 µl ddH_2O, in triplicate repeats. The plate was then placed in a moisturised environment at 37°C for 20 minutes. The fluorescence was then determined at Ex. 485 nm/Em. 515 nm in a plate reader (Magellan Infinite M200) against iron standard. Next, to reverse iron-induced calcein fluorescence quenching, 5 µl of 1 mM DFO was added to two of the three repeats and incubated at 37°C for 10 minutes. The fluorescence was then measured at the same wavelength and the difference in fluorescence reading with or without DFO was taken as specifically proportional to the LIP.

The amount of iron was reported as iron/ mg of protein determined by Bradford assay of the cell lysate. Bio-Rad protein assay reagent was used as per manufacturer's instructions. Absorbance was measured at 595 nm

4.3.7 Statistical analysis

GraphPad Prism 8.0.2 (San Diego, California, USA) was used for statistical analysis of the data. One-way Anova or multiple t -test was used for comparison between the data. Data are presented as mean ± SD, statistical significance was defined as $P < 0.05$.

4.4 Results:

4.4.1 Efficacy of the synthesized particles in chelating iron; size and concentration comparison

The ability of MNPs to chelate iron was investigated using a colorimetric assay by incubating MNPs or DFO in a solution with increasing amounts of iron, at 37° for 24 hours (Figure 4.1). It was found that MNPs of all sizes were able to chelate iron with a maximum adsorption of 14 +/- 0.25 mM of iron/g of material; significantly higher than DFO at the same concentration (Figure 4.2).

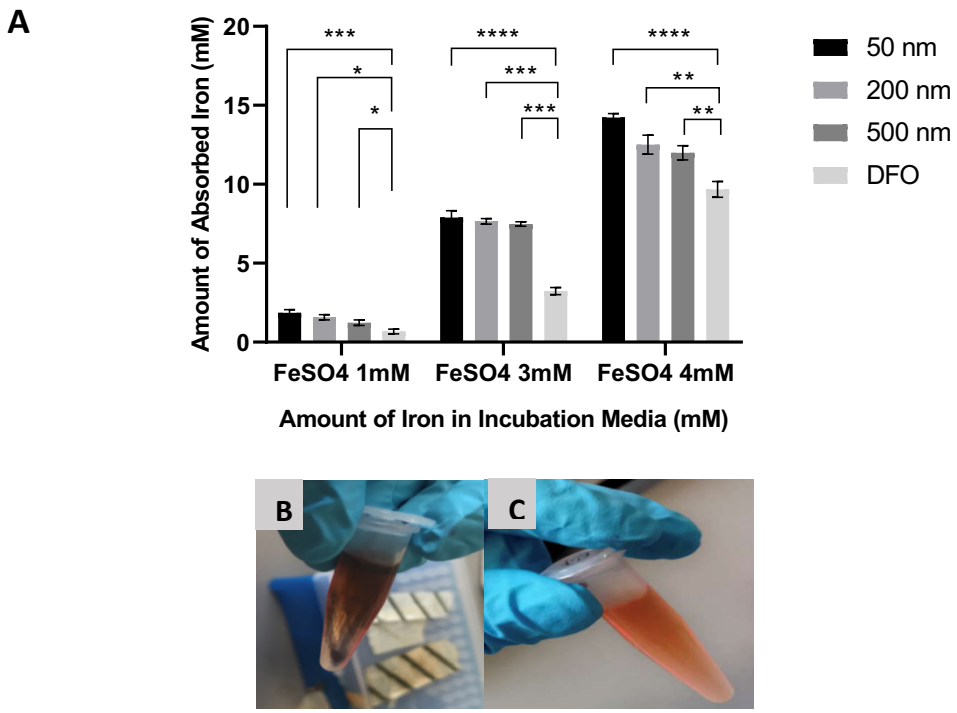


Figure 4.2 Ability of MNPs to chelate iron.

*(A) Comparison of iron chelation by 50 nm diameter, 200 nm diameter, 500 nm diameter MNPs and DFO, in iron containing media of 1 mM to 4 mM. Data shows mean ± SD after multiple t-test (n=3); *p ≤ 0.05, **p ≤ 0.01***p ≤ 0.001, ****p ≤ 0.0001. Eppendorf tubes representing MNPs (B) before and (C) after adding phenathroline for the colour change to take place.*

4.4.2 Effect of the incubation time on iron binding efficacy

To assess the effect of time on particles efficacy in chelating iron, 50 nm diameter, 200 nm diameter, 500 nm diameter MNPs or DFO where incubated in a solution with 4 mM of iron, at 37° for 24 and 48 hours. There was no significant increase in the amount of adsorbed iron when particles were incubated for longer (Figure 4.3) indicating that they had reached their maximum saturation capacity.

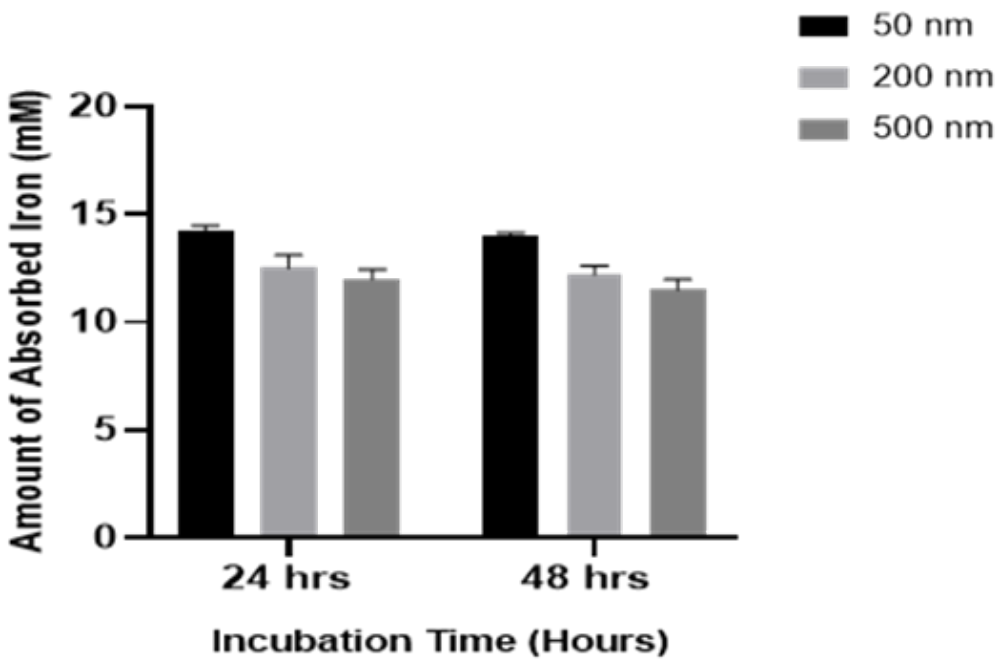


Figure 4.3 Effect of time on MNPs ability to chelate iron.

Graph to show a comparison of iron chelation in the 50 nm diameter, 200 nm diameter and 500 nm diameter MNPs after incubation with 4 Mm $FeSO_4$ for 24 or 48 hours. Data shows mean ± SD (n=3).

4.4.3 Effect of PEGylation on the efficacy of the synthesized particles in chelating iron

One limitation of PEGylation is decreasing efficacy of therapeutics and biological activity. To investigate the effect of PEGylation on particle efficacy in chelating iron, 50 nm diameter, 200 nm diameter and 500 nm diameter PEGylated, or non-PEGylated particles of equal concentrations were incubated with 4 mM $FeSO_4$. Particle ability to absorb iron was not significantly decreased after surface modification with PEG (Figure 4.4).

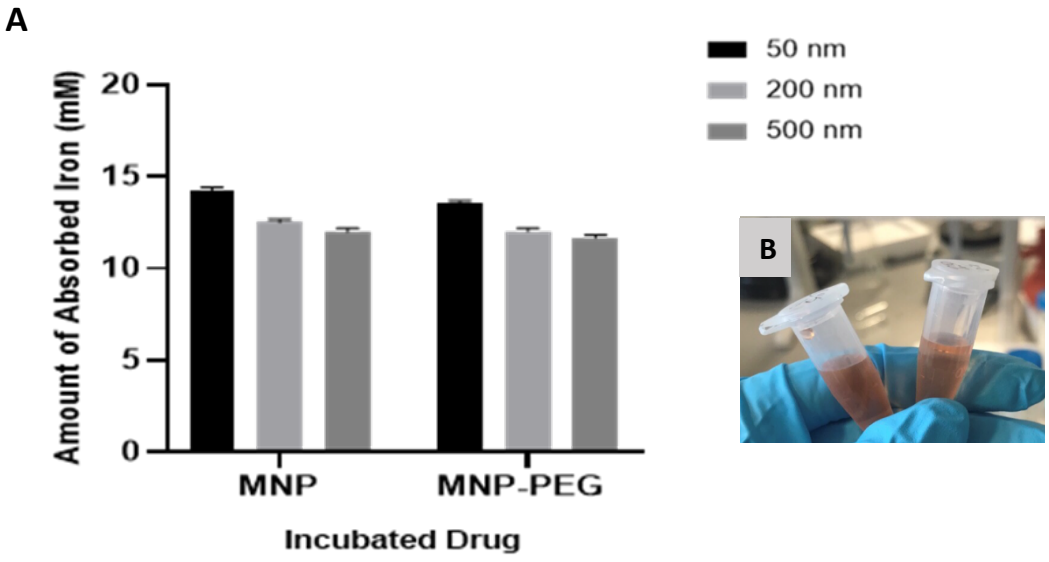


Figure 4.4 Effect of PEGylation on MNPs ability to chelate iron.

(A) Graph to show a comparison of iron chelation in 50 nm diameter, 200 nm diameter and 500 nm diameter particles which are either uncoated, or surface modified with PEG. Data shows mean ± SD (n=3). (B) Eppendorf tubes representing the colour change after adding phenathroline to MNP (left) and MNP-PEG (right).

4.4.4 Determination of MNPs effect in reducing labile iron pool in HepG2 cells

HepG2 cells are useful for the investigation of the protective and therapeutic effect of iron chelators (Hamilton and Kizhakkedathu, 2015; Mehta and Sharp, 2020; Vlachodimitropoulou et al., 2017). Iron loading of HepG2 was achieved by progressive increase of iron and determined with calcein assay and flow cytometry. Calcein is non-fluorescent and membrane permeable, and once inside the cell, it hydrolysis to give a fluorescent signal. The fluorescence intensity of calcein was decreased by the intracellular LIP and reversed by adding an iron chelator (Figure 4.5). Successful iron loading of HepG2 cells was confirmed by a reduced calcein fluorescence intensity compared to cells that were not treated with iron (Figure 4.6 A). This fluorescence intensity of calcein was reversed after incubation with DFO (Figure 4.6 B) or with 50 nm diameter, 200 nm diameter or 500 nm diameter MNPs (Figure 4.6 C-E) which indicates that MNPs are binding to the LIP.

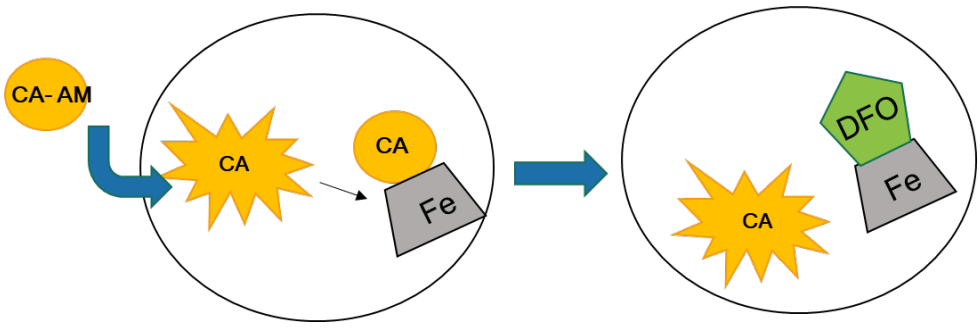


Figure 4.5 Fluorescence quenching of calcein AM.

A schematic diagram illustrating the principal of Calcein AM assay. Clacein AM hydrolysis inside the cell giving a fluorescent signal. The fluorescent signal of Calcien is then quenched when bind to the labile iron pool but reversed after adding a chelation agent.

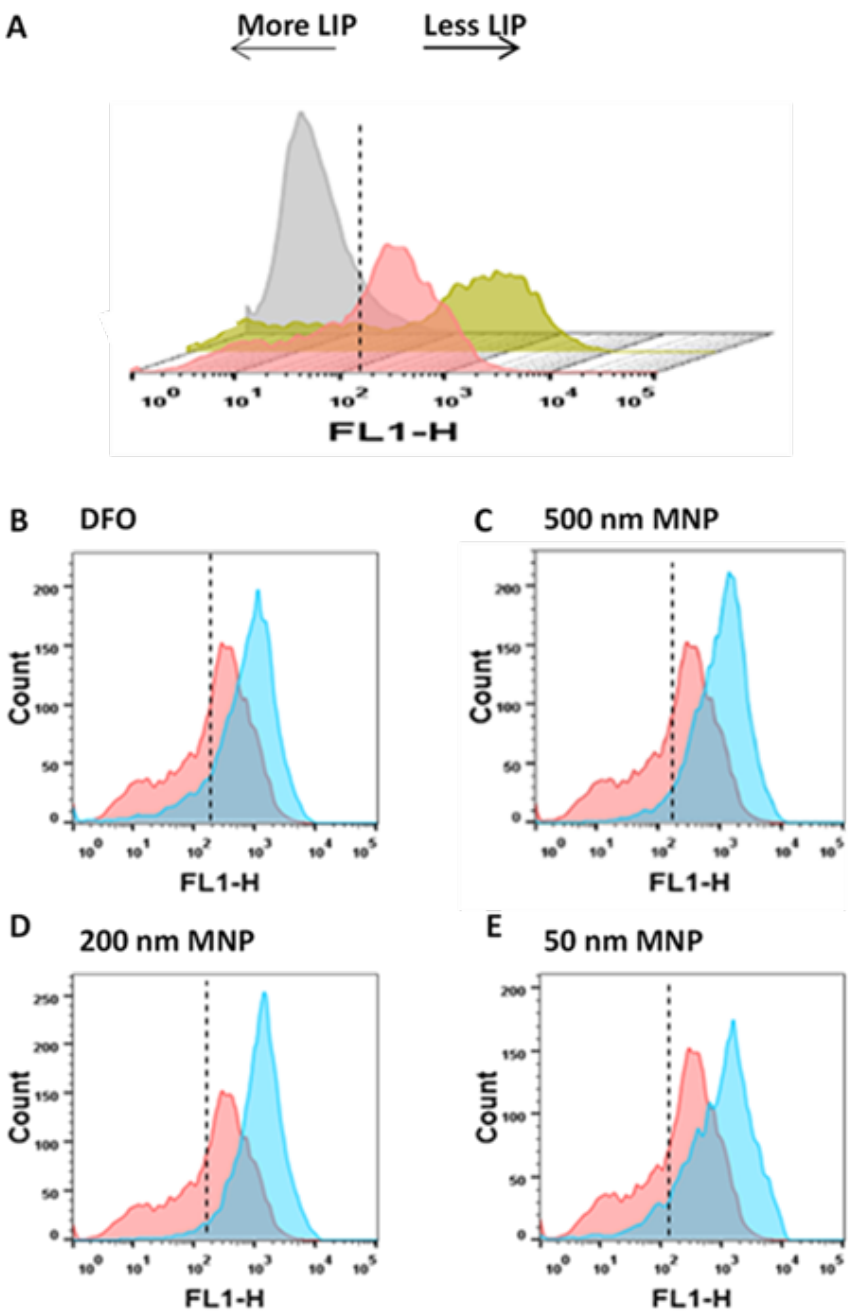
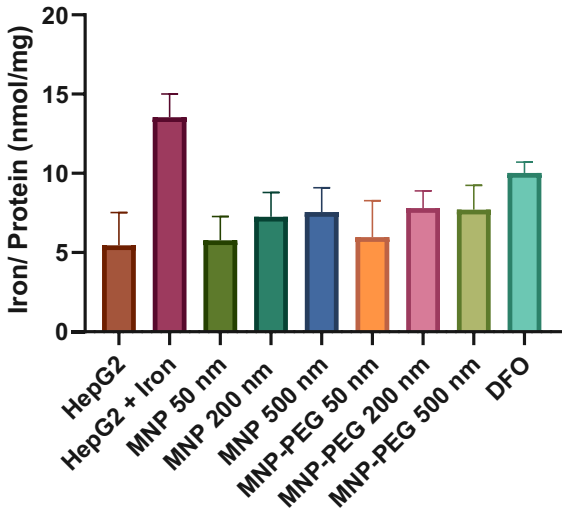


Figure 4.6 The effect of MNPs in reducing labile iron pool in HepG2 cells.

Flow cytometry analysis showing (A) a histogram of control unstained HepG2 cells (grey), iron loaded HepG2 cells stained with calcein (pink) control HepG2 cells stained with calcein (green). B-E shows the Labile iron pool (LIP) in HepG2 cells before (red) and after (blue) incubation with (B) DFO, (C) 50 nm, (D) 200 nm and (E) 500 nm MNP. (n=3). FL1-H: fluorescence intensity.

4.4.5 Quantification of HepG2 cells iron content before and after iron chelation

To quantify the amount of iron in HepG2 cells before and after chelation, a calcein assay was used, and calculated per mg of protein. Results show that the amount of iron adsorbed by MNPs was higher than that adsorbed with DFO of the same concentration. The level of iron in the iron loaded HepG2 cells incubated with melanin nanoparticles was returned to the normal levels before iron loading induced, indicating that the essential iron required for differentiation was not reduced (Figure 4.7).



Significant pairs	P value
HepG2 vs HepG2 + iron	0.0052
HepG2 + iron vs MNP 50 nm	0.0030
HepG2 + iron vs MNP 200 nm	0.0067
HepG2 + iron vs MNP 500 nm	0.0080
HepG2 + iron vs MNP-PEG 50 nm	0.0086
HepG2 + iron vs MNP-PEG 200 nm	0.0053
HepG2 + iron vs MNP-PEG 500 nm	0.0087
HepG2 + iron vs DFO	0.0190

Figure 4.7 Iron quantification in HepG2 cells before and after iron chelation

A bar chart representing iron content in HepG2 cells (nmol) per mg of protein before and after incubating the cells with DFO and MNPs (n=3). A table represent significant pairs after multiple t-test (n=3).

4.5 Discussion:

Current iron chelation therapy requires daily administration of the maximum tolerated dose to ensure adequate treatment (Cohen et al., 2003; Hamilton and Kizhakkedathu, 2015; Hoffbrand et al., 2012; Porter et al., 1998; Shangaris et al., 2019). However, treatment with current chelators is often insufficient in many cases, mainly due to short half-life and off-target toxicity (Hamilton and Kizhakkedathu, 2015; Kang et al., 2019). Moreover, these small MW chelators are toxic to the developing foetus if used during pregnancy. Thus, chelators that are less toxic and more efficient in removing iron and prevent iron overload complications are needed. It is well established that the use of high MW chelators such as polymers and nanoparticles could reduce the undesirable limitations associated with DFO (Hamilton and Kizhakkedathu, 2015). Since poly-dopamine melanin provides the physical and chemical properties of natural melanin including the chelation of iron, the aim of this chapter was to investigate the efficacy of the synthesized MNPs and MNP-PEG in chelating iron and reducing the toxic LIP *in vitro*. Results of this chapter showed that MNPs of all sizes could bind to iron with more affinity and efficacy than DFO of the same concentration (Figure 4.2) and reduce the LIP in HepG2 (figure 4.6 and figure 4.7). This efficacy in biding to iron was not affected when the particles were PEGylated (Figure 4.4).

4.5.1 Efficacy of the synthesized particles in chelating iron

To achieve effective iron chelation therapy for the treatment of iron overload, an equal or greater amount of iron to that accumulated due to transfusion therapy should be removed. This requires the chelator to have certain features; firstly, the ability of a chelator to remove a significant amount of iron at relevant concentration

to minimize toxic side effects. The ultra-small size of nanoparticles represents a high surface to volume ratio thus, the synthesized MNPs provided an excellent iron binding capacity at all three sizes with a maximum adsorption of up to 14 mM of iron/g of material, significantly higher than DFO of the same concentration (figure 4.2). This property of nano-sized chelators has significantly improved safety *in vivo.* It was found that a single dose of a 1550 mg kg^{-1} nano chelator yielded no evidence of tissue damage in the histological analysis of spleen, kidney and lung tissues compared to DFO which showed several toxicities even at a lower dose (Kang et al., 2019).

Yan et al., (2016) have investigated the appropriate treatment dose with other size melanin nanoparticles in a mouse model of iron overload in which one dose of 35 mg/kg MNPs was able to remove a relatively higher amount of iron compared to 750mg/kg of DFO at five doses. Iron removal was significantly higher when one dose of 100mg/kg of MNPs was used (Yan et al., 2016). Melanin nanoparticles used in the mice study were around 5 nm which is much smaller than the prepared poly-dopamine melanin nanoparticles used in this chapter. Thus, a higher concentration of the synthesized particles may be needed for *in vivo* applications. Nonetheless, when mice were exposed to increasing levels of MNPs from 50 to 500 mg/kg, unlike DFO, no signs of unhealthy conditions were seen nor abnormality in histology of tissues from heart, liver, spleen, lung, kidney, and pancreas (Yan et al., 2016) suggesting the safety of MNPs even at higher concentration.

Secondly, an ideal chelator should have the ability to bind to non-transferrin binding iron over a relatively long period of time to ensure adequate coverage and thus reduce the amount of iron that would ultimately accumulate in tissues (Hamilton and Kizhakkedathu, 2015). It was shown in chapter 3 that MNPs were stable in a

physiological condition for a maximum of 20 hours when incubated at 37°C (Figure 3.10). MNP-PEG remained stable even after 24 hours which may in turn have a relatively longer circulation life *in vivo.* When MNP-PEG of smaller size were applied in a mouse model of iron overload, it remained in the circulation for 17 hours, compared to DFO which was cleared after 5 minutes (Yan et al., 2016)

One drawback of PEGylation however, is the decrease or loss of biological activity as shown in PEGylated enzymes and antibodies which is probably due to interference in receptor binding (Parrott and DeSimone, 2012). Herein, the effect of PEGylation on the particles' efficacy in chelating iron was investigated. Figure 4.4 shows that surface modification with PEG did not significantly limit the ability of the particles in adsorbing iron. Similar findings were reported where PEGylated particles were able to chelate a significantly higher amount of iron than DFO (Yan et al., 2016). Although PEGylation has improved biocompatibility of DFO with HUVECs cells where around 90 % viability was achieved compared to DFO alone which resulted in cell death at low concentration (3 μM), PEG-DFO has not been tested for efficacy (Hamilton and Kizhakkedathu, 2015).

These two factors of a nanoparticle chelator may lower the required dosage quantity and frequency, this could in turn, reduce toxicity.

4.5.2 MNPs effect in reducing labile iron pool in HepG2 cells

The cell damage associated with iron overload is due to excessive levels of cell LIP that promotes the production of ROS. The largest LIP is within hepatocytes where more than 70 % of body iron is deposited (Hamilton and Kizhakkedathu, 2015; Vlachodimitropoulou et al., 2017). In this chapter, iron binding properties of the synthesized particles to mobilize intracellular iron in hepatocellular carcinoma cell

lines was investigated. HepG2 cells were used because they can initiate an iron overload status by progressive increase of iron making them useful for the investigation of a therapeutic effect of iron chelator (Mariani et al., 2009; Mehta and Sharp, 2020). Cellular iron loading in HepG2 cells was confirmed (figure 4.6 A) in parallel to previous studies where treatment of HepG2 cells with higher concentrations of holo-transferrin increased iron levels with no noticeable alterations in cell morphology (Mariani et al., 2009; Mehta et al., 2016; Mehta and Sharp, 2020). Results in this chapter also showed that MNPs were able to reduce LIP in an iron loaded cells with higher efficacy compared to DFO (figure 4.7). Iron levels in the iron loaded HepG2 cells incubated with MNPs were returned to the normal pre-iron loading levels, indicating that it did not affect essential iron required for differentiation. Attempts in reducing LIP in hepatocytes was achieved with Eltrombopag (ELT) which reduced LIP in HuH7 cell lines by 6.9 %. However, it was less effective than DFO of similar concentration (Vlachodimitropoulou et al., 2017). This could be due to the rapid metabolism of ELT which may decrease efficacy.

4.5.3 Strength and limitations

Results in this chapter showed that MNPs poses three key features of an ideal iron chelator. The removal of a significant amount of iron (higher than DFO) at low concentration, the reduction of LIP in HepG2, and over 20 hours stability at 37°C (tested in chapter 3) which may mirror a longer circulating time *in vivo*. These characteristics show the superiority of MNPs over DFO as an iron chelator.

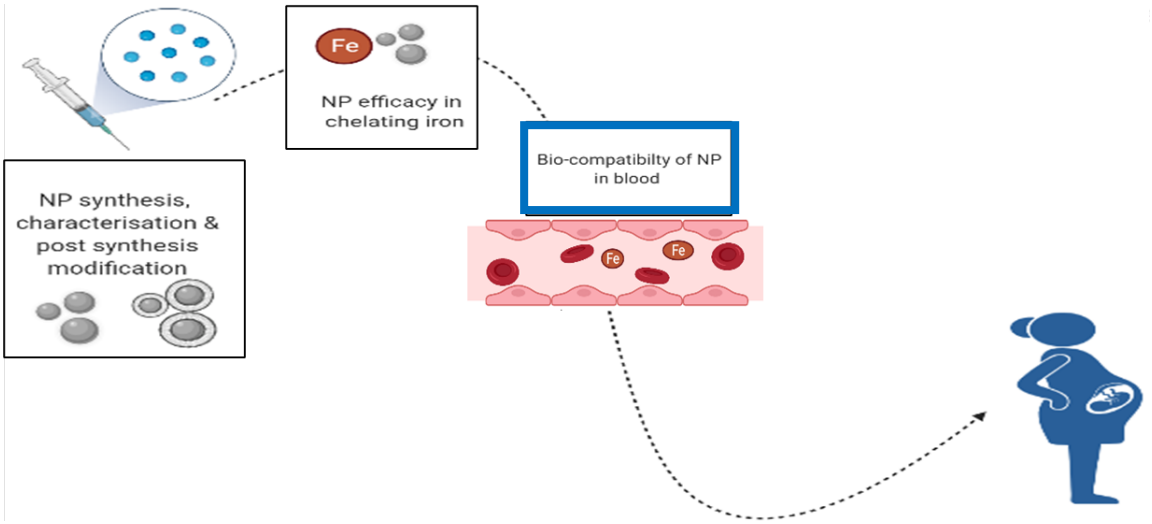
Although selectivity of MNPs toward chelating iron over other metals ions was not measured in this thesis due to the timeline of the DPhil, it is supposed that in iron overload conditions the probability of iron chelation is more predominant than other metals since the concentration of iron is much higher. Also, even if chelation of other

metals is a chance, like in the case of DFO and DFP where lower zinc levels were reported, the levels of zinc remain within the normal reference range (Caldas et al., 2020). This is probably due to the predominance of iron in comparison to zinc in iron overload individuals. Lastly, selectivity of iron binding using other sizes of pristine melanin nanoparticles were tested by other group and showed that a large amount of iron was chelated (over 50 µg/ml) while binding to other metals was almost negligible (less than 4 µg/ml) (Yan et al., 2016) and may not consider clinically significant. Thus, iron selectivity of MNPs was not tested.

4.6 Summary:

This chapter showed superior efficacy of the synthesized poly-dopamine melanin nanoparticles over DFO in chelating iron and reducing the LIP in HepG2 cell lines at relevant concentration. The mechanism of reducing the LIP in HepG2 is unknown. Particles' PEGylation, did not affect their chelation efficacy and would allow longer circulation time *in vivo*. These findings may provide a promising clinical advancement for chelation therapy.

Chapter 5 Haemocompatibility investigation of melanin nanoparticles and improvement by surface functionalization with PEG



5.1 Abstract

Background: Melanin nanoparticles show promising results in a wide variety of biomedical applications, but there is only limited data on their behaviour in blood.

Objectives: The aim of this chapter was to investigate the haemocompatibilty of the synthesized MNPs and MNP-PEG.

Methods: Haemolysis and coagulation assays were used to assess haemocompatibilty of melanin nanoparticles.

Results: Results here showed that melanin nanoparticles were compatible with RBCs with less than 5 % haemolysis at a concentration of 250 μm. Although administration of higher concentration (1 mM) could possibly approach 10 % haemolysis, the ratio is considered generally compatible. In coagulation assays the clotting time and prothrombin time were significantly shorter with 50 nm particles compared to controls. Clotting activity of the 50 nm however was within the acceptable limits.

Conclusion: Haemolysis and coagulation activities of Melanin nanoparticles were within the acceptable limit.

5.2 Introduction

5.2.1 Overview

For *in vivo* applications MNPs will be injected into the circulation, therefore it is important to achieve blood compatibility. The aim of this chapter was to investigate haemocompatibility of the synthesized particles *in vitro* by testing their haemolytic and clotting activity. Improvement of haemocompatibility by surface functionalization with PEG has also been analysed.

5.2.2 Background

Evaluating the quality, safety and efficacy of nanomaterials and the understanding of the requirements related to the impact of the specific properties of nanomaterials on the quality and safety of a medication is the key for smooth translation into clinical applications. A robust standard *in vitro* blood compatibility test can enable detection of adverse effects in blood. Therefore, further improvements at the early developmental stage of nanomaterial preparation can be achieved.

5.2.3 Erythrocytes haemolysis

Haemolysis is defined as an alteration, dissolution, or destruction of the erythrocyte membrane resulting in the release of haemoglobin into the plasma. The released haemoglobin can result in undesirable medical conditions, including anaemia, jaundice, kernicterus, and acute renal failure (Amin and Dannenfelser, 2006). Thus, haemolytic potential of a candidate pharmaceutical must be tested.

Data from the literature shows that *in vitro* results generated by the dynamic method are in agreement with *in vivo* results (Amin and Dannenfelser, 2006; Krzyzaniak et al., 1997). This indicates that the potential to induce intravascular haemolysis after injection of a candidate drug can be determined *in vitro*.

Current guidance considers formulations with a haemolysis ratio of < 10 % to be non- haemolytic while values > 10 % indicate a risk of haemolysis and incompatibility; and therefore cannot be used for medical applications (Amin and Dannenfelser, 2006; Guo et al., 2021; Jiang et al., 2019).

5.2.4 Coagulation testing

A thrombus is normally formed in the blood vessel of a living person after an endothelial injury to minimize blood loss and maintain regular blood volume. On the other hand, a clot is a blood coagulum that develops outside of a blood vessel, or inside a blood vessel in a post-mortem state. It is important to highlight that coagulation events *in vitro* and *in vivo* are not identical (Winter et al., 2017). Thus, it is vital to assess coagulation *in vivo* prior to clinical applications.

Haemostasis is defined as the mechanism that leads to cessation of bleeding from a blood vessel (LaPelusa A, 2022). Coagulation is frequently divided into three stages; primary haemostasis which involves construction of the blood vessels and a temporary platelet plug. To stabilize the temporary platelet plug, a secondary haemostasis (also called coagulation) occurs in multi steps that ultimately ends with a formation of a fibrin (a stable clot) (Figure 5.1). The last stage of haemostasis fibrinolysis; a remodelling of the fibrin clot into the same kind of tissue that was there before the injury (LaPelusa A, 2022; Winter et al., 2017). In vitro coagulation however, involves the intrinsic, common, and extrinsic pathways as illustrated in Figure 5.2 (Winter et al., 2017).

Testing for coagulation involves functional assays that evaluate clotting rate formation starting after activation of the cascade. This includes clotting time (CT), prothrombin time (PT) and activated partial thromboplastin time (aPTT). CT and

aPTT measure the intrinsic and common pathways while PT measures the extrinsic and final common pathways (Jiang et al., 2019; Urbán et al., 2019; Winter et al., 2017).

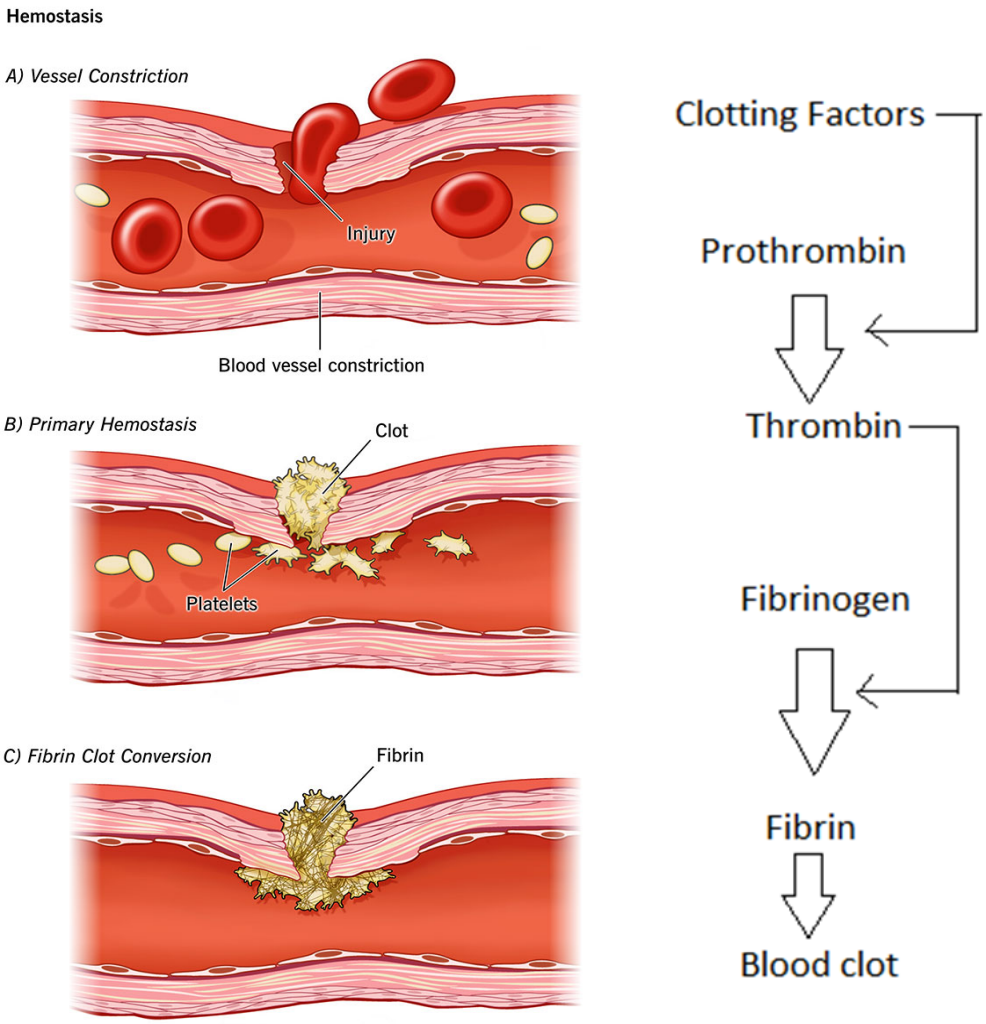


Figure 5.1 Stages of Haemostasis.

Haemostasis process involves three main stages: vessel construction to form temporary platelets plug, followed by a primary haemostasis which involves a formation of a fibrin clot, and a remodelling of the fibrin clot to tissues. *Adapted from* www.my.clevelandclinic.org

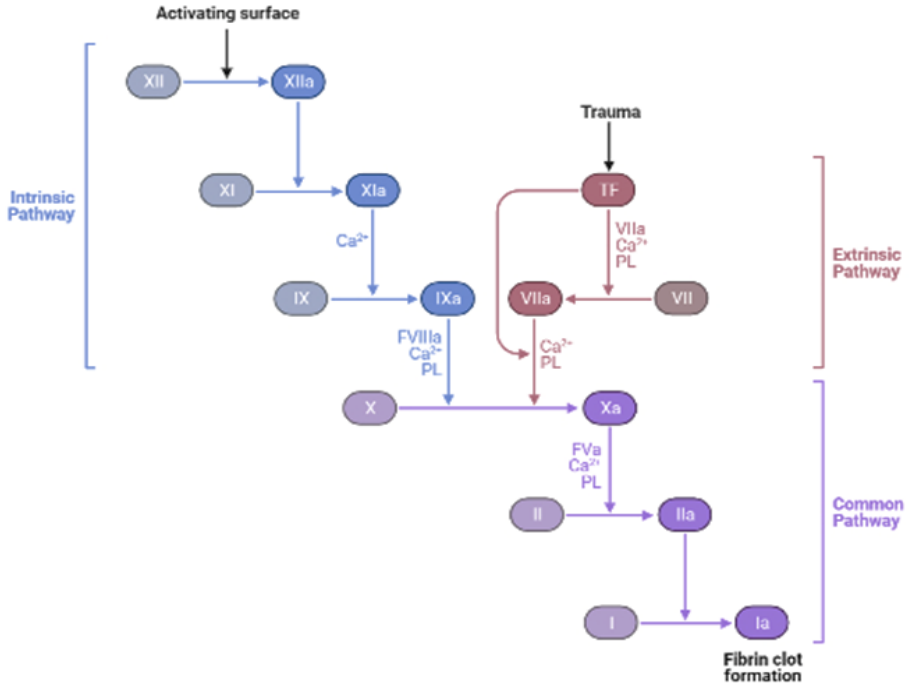


Figure 5.2. Coagulation cascade.

Coagulation cascade refers to a serious of steps that occur during a formation of blood clot *after injury by activating a cascade of proteins called clotting factors. This involves the intrinsic pathway that is activated endothelial collagen and the extrinsic pathway that is activated through tissue factors. Both intrinsic and extrinsic pathways result in activation of factor X leading into the common pathway which ends with converting fibrinogen into fibrin to form a stabilized blood clot. Image created with BioRender.com.*

5.2.5 Aims

1. To investigate the haemolytic activity of the synthesized melanin particles of all sizes.
2. To investigate clotting activity of the synthesized melanin nanoparticles of all sizes.
3. To determine PEGylation effect on improving haemocompatibility of the particles.

5.3 Materials and Methods

5.3.1 Determination of erythrocytes haemolysis

To measure the rate of haemolysis, RBCs were first suspended in PBS (1:10) and incubated for 1 hour at 37°C with equal amounts of (i) a positive control Triton X-100 (Sigma-Aldrich. Gillingham, UK), (ii) a negative control PBS, (iii) 250 µM MNP, (iv) 1 mM MNP, (v) 250 µM MNP-PEG, or (vi) 1 mM MNP-PEG. The mixture was then centrifuged to pellet, and the supernatant was transferred to a 96-well plate to measure the absorption of the released haemoglobin at 595 nm (Figure 4.3). Haemolysis ratio was then calculated as: [HR (%) = ($OD_{test} - OD_{negative\ control}$)/ ($OD_{positive\ control} - OD_{negative\ control}$)].

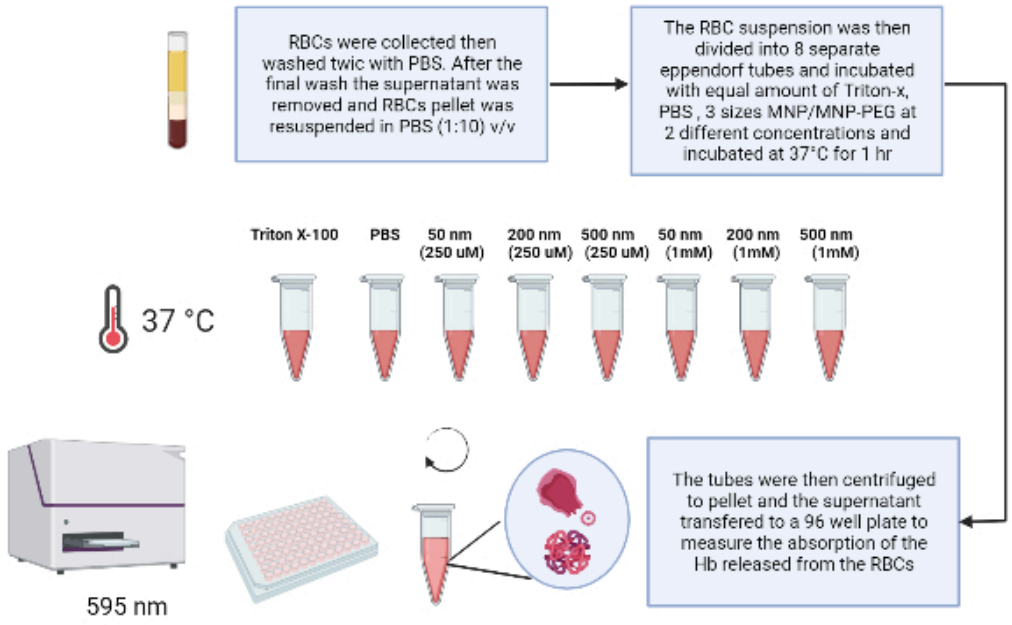


Figure 5.3 Graphical Summary of the haemolysis assay.

Two different concentrations of MNP or MNP-PEG were incubated with RBCs suspension (1:10 v/v) alongside positive control Triton X-100 and negative control PBS for 1 hour at 37°C before measuring the haemoglobin released from the red blood cells. Image created with BioRender.com.

5.3.2 Clotting time (CT); determination of clotting activity of melanin nanoparticles

For clotting time analysis, 1 ml blood was collected and incubated in a glass tube with Polyethylenimine (PEI) (Sigma-Aldrich. Gillingham, UK), PBS, MNP, or MNP-PEG for 5 minutes at 37 °C. All the tubes were then placed in a water bath at 37°C and inclined up to 180° every 15 seconds. Clotting time was recorded when the blood stopped flowing in the tube (Figure 5.4).

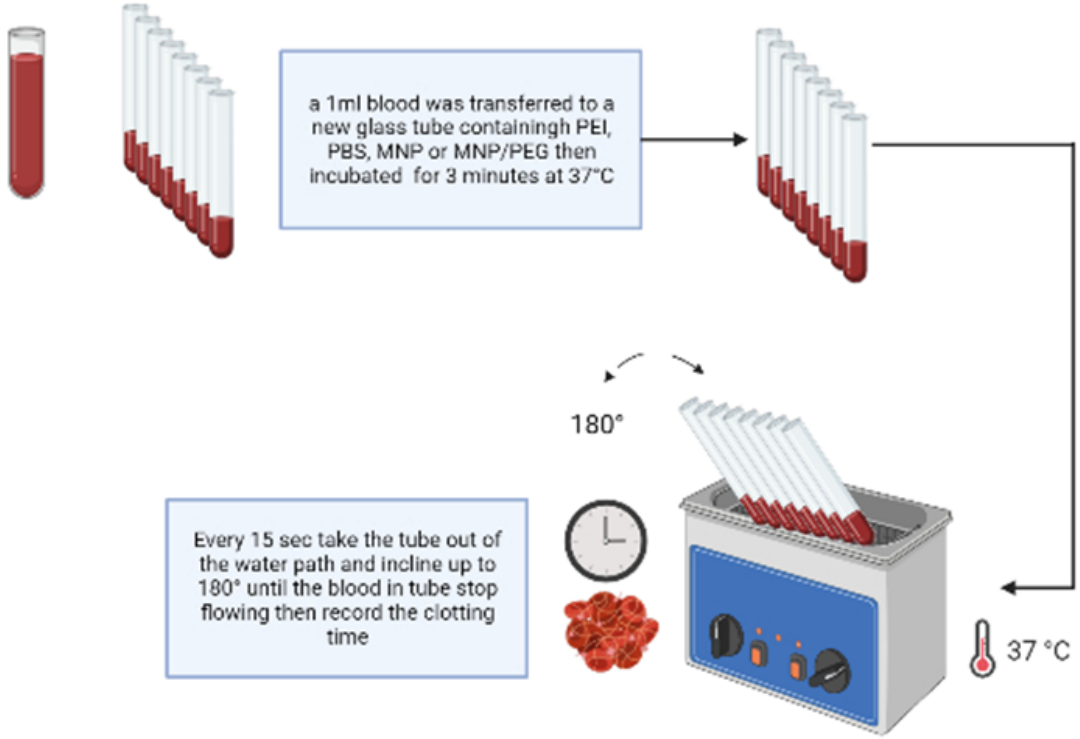


Figure 5.4 Graphical Summary of clotting activity analysis of melanin nanoparticles. *In vitro intrinsic pathway initiated by the contact of glass with the blood converting factor XII to factor XIIa. Image created with BioRender.com.*

5.3.3 Prothrombin time

PT was adapted from (Jiang et al., 2019; Yang R, 2022). Briefly, citrated blood was collected and centrifuged at 2500 g for 5 min at 4 °C to collect the platelet plasma. Plasma was then transferred to new tubes containing PBS, MNP or MNP-PEG and incubated at 37°C for 30 minutes. This was followed by the addition of 500 µL of a 25 mM calcium chloride solution. A stopwatch was started as soon as the calcium chloride was added. The time taken from the addition of calcium chloride to the formation of fibrin clot was recorded.

5.3.4 Statistical analysis

GraphPad Prism 8.0.2 (San Diego, California, USA) software was used for statistical analysis of the data. Data were compared using One-way Anova or multiple t-test. Data are presented as mean ± SD, statistical significance was defined as $P < 0.05$.

5.4 Results

5.4.1 Determination of RBC haemolysis

MNPs and MNP-PEG were tested for their interaction with RBCs, and the haemolysis ratio was calculated after measuring the absorbance of haemoglobin released from the cells (Figure 5.3). It is shown here that all three sizes of MNPs and MNP-PEG were compatible with RBCs and induced less than 5 % haemolysis at a concentration of 250 μm. Although this ratio was increased at higher concentrations (1 mM), where particles could possibly approach 10 % haemolysis (generally compatible). Surface functionalization with PEG significantly decreased the haemolysis ratio of 500 nm particles to around 5 % (Figure 5.5).

5.4.2 Clotting time dependence on the window size

Clotting time is a blood test that directly reflects the haemostasis (Chen et al., 2016) and was determined as described in figure 5.4. No significant differences in clotting time were seen with the 200 nm or 500 nm MNPs or MNP-PEG compared to controls, indicating a good compatibility. Even though clotting time was significantly shorter regarding the 50 nm particles compared to a blank control or PBS, it was within the normal clotting time in a glass tube i.e., 6 minutes. Surface modification with PEG shows no significant differences in clotting time compared to non-PEGylated MNPs of all sizes (Figure 5.6).

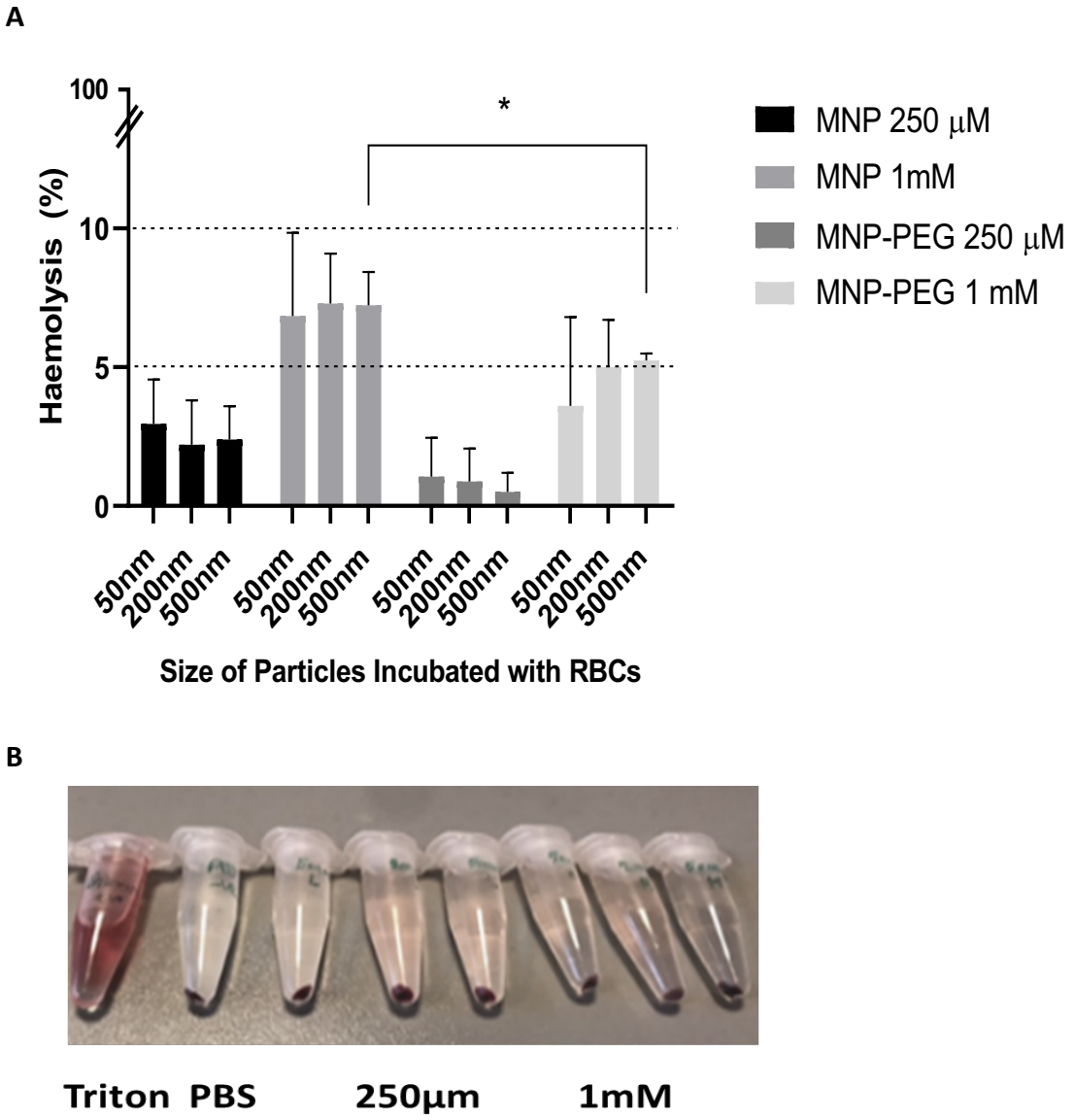


Figure 5.5 Haemolysis assay.

*Haemolysis assay was performed after incubating MNPs-MNP-PEG with RBCs suspension at 37°C for 1hr, then measure the Haemoglobin absorption released from the cells. (A) Haemolysis ratio was calculated [HR (%) = (OD $_{test}$ – OD $_{negative\ control}$)/ (OD $_{positive\ control}$ – OD $_{negative\ control}$)]. The horizontal dashed lines represent the compatible (5%) and significant (10%) haemolysis thresholds. (B) Eppendorf tubes represents haemolysis induced by (left to right) the positive control Triton, the negative control PBS, 250 μM and 1mM MNP. Data shows mean ± SD (n=3). *p≤ 0.05 after multiple t-test.*

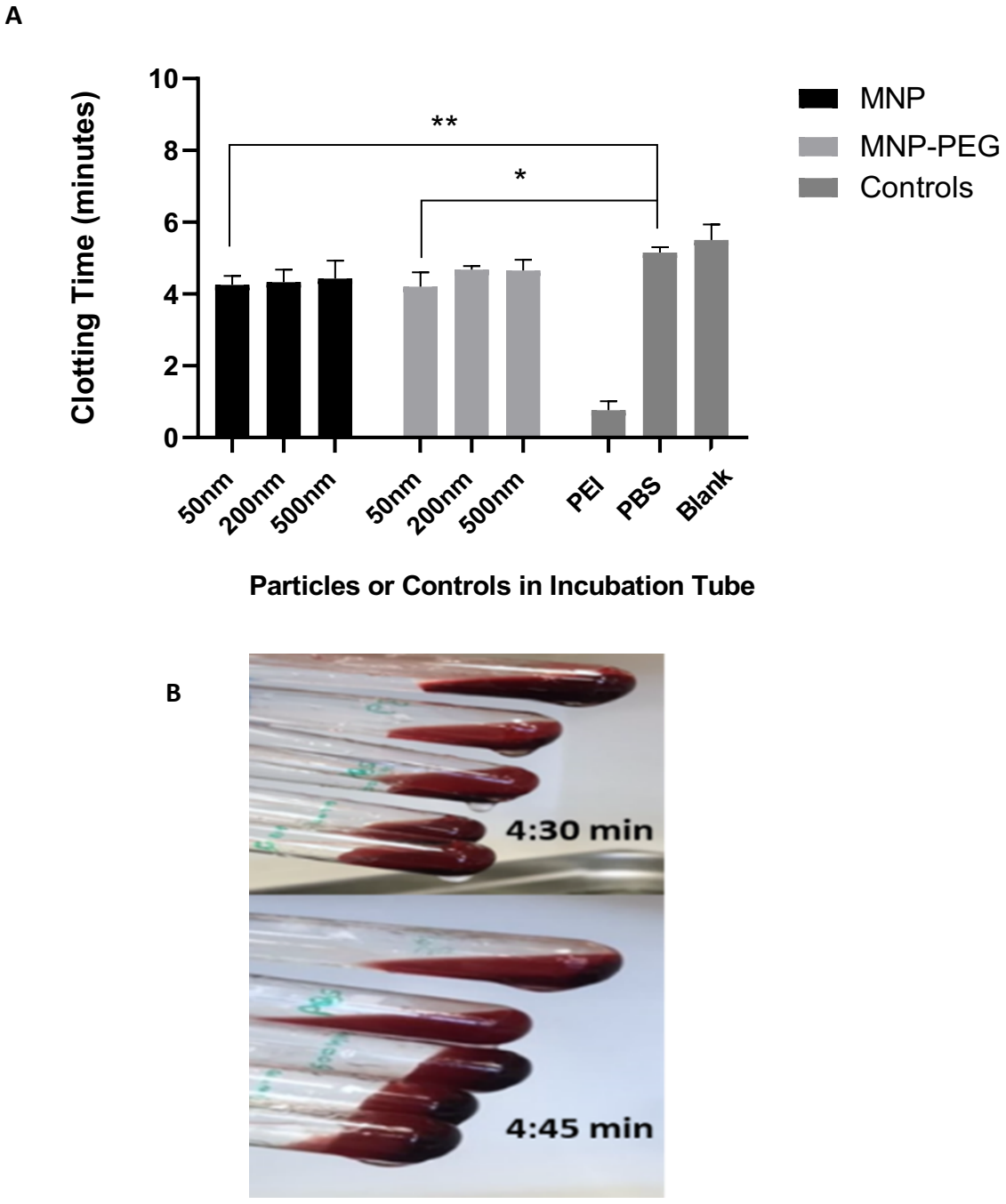


Figure 5.6. Coagulation assay.

*(A) Graph shows blood clotting time after incubation with three different sized MNPs or MNP-PEG, PEI was used as positive control and PBS as negative control. (B) Glass tubes represents clotting time of (top to bottom) Blank, PBS, MNP sized 50, 200 and 500 nm at 4:30 min (top image) and 4:45 min (bottom images). Data shows mean ± SD (n=3). *p≤ 0.05; **p ≤ 0.01after multiple t-test.*

5.4.3 Prothrombin Time

The prothrombin assay is used to measure extrinsic coagulation (Jiang et al., 2019). Results showed no significance difference in PT time of 200 nm and 500 nm MNP or MNP-PEG in comparison to control. PT of the 50 nm MNP was significantly shorter than the control tube with PBS but still within the normal range (between 10 to 13 seconds). No significant difference was observed after PEGylation (Figure 5.7).

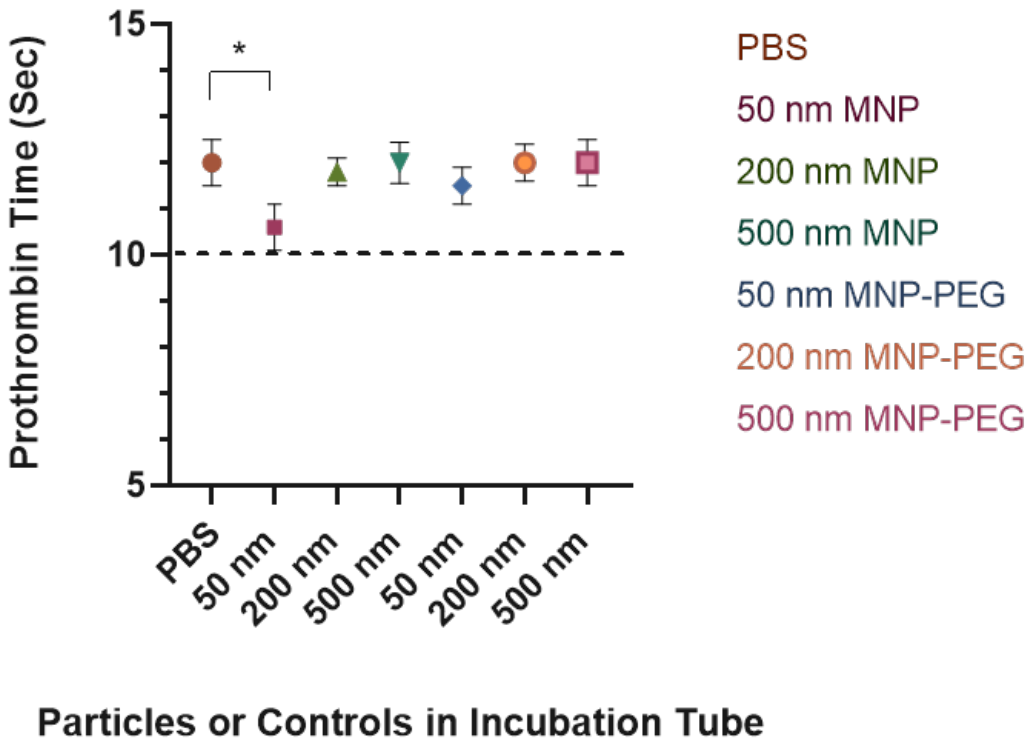


Figure 5.7 Prothrombin Time.

*Graph shows prothrombin time after incubation with three different sized MNPs or MNP-PEG and control PBS. Data shows mean ± SD (n=3). *p≤ 0.05 after multiple t-test.*

5.5 Discussion

For *in vivo* applications, melanin nanoparticles would be injected into the systemic circulation, which requires that they do not produce adverse effects in blood. Although melanin nanoparticles have been studied in different biomedical applications (Amin et al., 2017; Huang et al., 2017; Lin et al., 2015; Liu et al., 2013; Zhang et al., 2016), there is no sufficient data on their blood compatibility. Haemocompatibility is the measure of the damaging effects resulting from interaction of compounds with the blood; including whether they can cause thrombosis or destruction of the RBCs (Gorbet and Sefton, 2004). The aim of this chapter was to investigate the haemocompatibility of the synthesized MNPs and MNP-PEG with haemolysis and coagulation assays. Results of this chapter demonstrate that interaction of melanin nanoparticles were compatible with RBCs with less than 5 % haemolysis at a concentration of 250 µM. Although particles could possibly generate 10 % haemolysis at an increased concentration (1 mM), this haemolysis ratio however is considered generally compatible and meets the requirements of the haemolysis test for medical materials (Jiang et al., 2019). In terms of the coagulation analysis (CT and PT), only the 50 nm particles induced a significantly shorter clotting time and prothrombin time compared to a blank control or PBS, but it still was within the normal reference ranges (figure 5.6 and figure 5.7).

5.5.1 Erythrocyte haemolysis

Haemolysis refers to the rupture and release of haemoglobin from RBCs into the plasma. Standard test methods for analysis of haemolytic properties of nanoparticles *in vitro* should be considered in toxicological studies (Guo et al., 2021; Krzyzaniak et al., 1997). Thus, a haemolysis assay was used to evaluate *in vitro*

blood compatibility of melanin nanoparticles (figure 5.3). The haemolytic effect of Triton-X 100 is often used as an evaluation control standard for haemolysis assays.

Exposure to any medication can cause RBC haemolysis even in normal adults, and this may potentially result in vascular irritation, phlebitis, anaemia, jaundice, and acute renal failure (Amin and Dannenfelser, 2006; Krzyzaniak et al., 1997). Therefore, testing for haemolytic potential of candidate drug is recommended by the FDA standard regulation for biological drug evaluation. The haemolysis ratio reflects the interaction of materials with blood cells. A haemolysis rate of less than 5 % is ideal. The material also considered 'generally compatible' if the haemolysis rate generated was less than 10 %, while a haemolysis rate higher than 10 % indicates significant haemolysis that is not compatible and cannot be used for medical applications (Amin and Dannenfelser, 2006; Guo et al., 2021; Jiang et al., 2019).

Haemolysis results in this chapter showed that MNPs were compatible with RBCs generating less than 5 % haemolysis (figure 5.5). This compatibility may be attributed to the negative charge of MNPs, an important property of nanoparticles in terms of blood compatibility. Many cationic nanoparticles were found to be toxic due to the interaction with the negatively charge RBCs (Guo et al., 2021).

On the other hand, the percentage of RBC haemolysis is positively correlated with the concentration; mesoporous silica nanoparticles (MSN) showed low RBC haemolysis at a concentration below 500 mg/ml but obvious haemolysis was found at a concentration of 500 mg/ml (He et al., 2010). Here, MNPs did not generate significant RBC haemolysis (more than 10 %) even at a concentration of 1 mM (figure 5.5).

Morphological factors such as size and shape of the particles also plays an important role in the blood compatibility. Smaller sizes have a higher tendency to combine with RBC membranes and have a higher haemolytic activity than larger particles (Guo et al., 2021; Nimtrakul et al., 2019).

Modification with PEG is a commonly used strategy to improve nanoparticle properties which also applied to blood compatibility by shielding the particles surface from contact with nearby surfaces. In a haemolytic study of silica nanoparticles, it was found that unmodified MSN showed higher haemolytic activity than PEGylated MSN (Chen et al., 2019). It was also found in another study that there was no visible haemolysis on RBCs targeted by PEG-MSN (Liu et al., 2016a). In this chapter, results demonstrate that PEGylation of 500 nm MNPs had significantly reduced haemolytic activity (figure 5.5).

5.5.2 Coagulation testing

Blood coagulation is a multistep process leading to the conversion of soluble fibrinogen to insoluble fibrin. *In vitro* coagulation assessment of melanin nanoparticles was tested as described in figure 5.4. The results indicate that no blood clot was generated by the particles where no significant difference in clotting time or prothrombin time was shown with the 200 nm or 500 nm MNPs, or MNP-PEG compared to controls. Although clotting time was significantly shorter with smaller particles (50 nm) compared to a blank control or PBS, it was within the normal clotting time in glass tube; 6 minutes (figure 5.6). The compatibility of melanin nanoparticles with blood is mainly attributed to their biological nature. It was found from data extracted from both *in vitro* testing and *in vivo* applications of nanoparticles that blood incompatibilities were most frequently reported for

inorganic nanoparticles with thrombosis being the main adversity associated blood toxicity reported with these nanoparticles (Urbán et al., 2019).

Moreover, charge is one of the important factors influencing the effect of nanoparticles on blood components. In the study by Svirshchevskaya *et al*., (2016), all positively charge derivatives activated platelet aggregation while the negatively charge derivatives were compatible with blood components in this study (Svirshchevskaya et al., 2016). This is most likely due to the interaction with the negative charge on platelets. The positive charge may interact with blood components and interfere with the coagulation cascade (Guo et al., 2021).

PEGylation strategy has an excellent effect on improving the blood compatibility of nanoparticles. It is known that PEGylated particles hardly cause platelet adhesion or activation which means it will not cause blood clotting (Guo et al., 2021). However, it was found in here that surface modification with PEG has no significant effect in improving blood compatibility of MNPs (figure 5.5 and figure 5.6).

5.5.3 Strength and limitations

To our knowledge, no study has investigated the compatibility of melanin nanoparticles with blood. The haemolytic activity of 200 nm MNP was previously studied in our lab (Perring et al., 2018). This chapter provided information of the haemolytic and clotting activity of 50 nm, 200 nm, and 500 nm MNPs and MNP-PEG. The *in vitro* blood compatibility testing enables detection and early elimination of undesired materials that induced blood adverse events at the developmental stage.

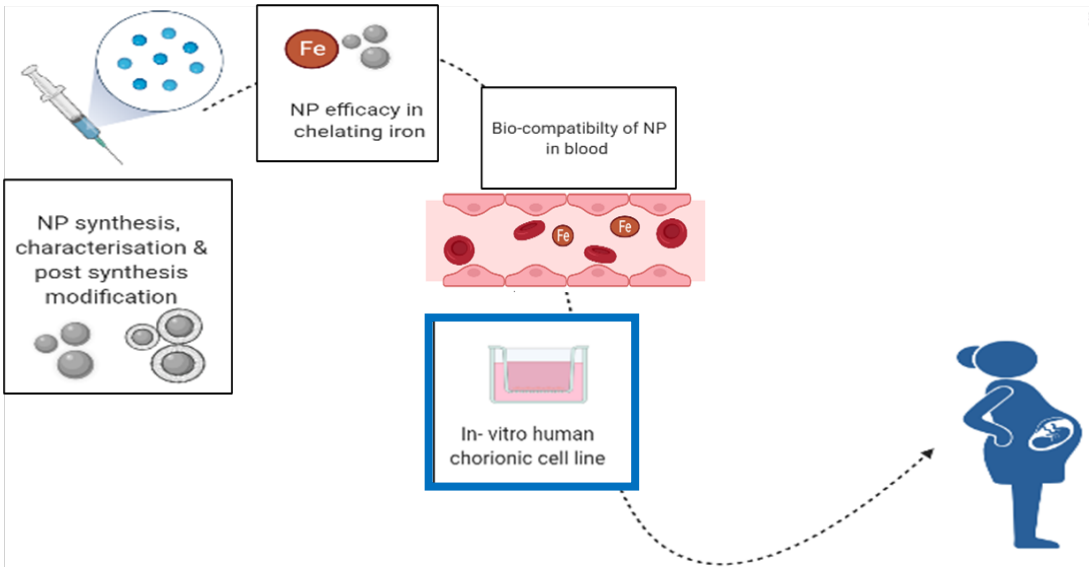
Although the use of coagulation assays *in vitro* is recommended by many guidelines for blood compatibility, it is not recommended by the international organization for

standardization (ISO 10993-4) (ISO, 2017); since they assess coagulation in isolation, whereas *in vivo* these pathways are closely interlinked. Therefore, *in vivo* assessment of melanin nanoparticles is recommended for future work.

5.6 Summary

This chapter presents the compatibility of all size melanin nanoparticles with blood. Results indicates that melanin nanoparticles were compatible with RBCs with an acceptable haemolysis ratio. Clotting activity of melanin nanoparticles depends on the window of size, while 200 nm and 500 nm are more compatible with RBCs 50 nm particles generated of shorter clotting time. This however was within the acceptable limits suggesting good blood safety.

Chapter 6. Investigation of melanin nanoparticle transport across cell model of the placental barrier



6.1 Abstract

Background It was found from the literature that for most types of nanoparticles, particle diameter was the most important parameter for their interaction with the placental tissue.

Objectives The main aim of this chapter was to identify the cut off size of melanin nanoparticle translocation across BeWo cells in an *in vitro* transwell model with the three different sized particles as an indication for how they would interact with a human placenta.

Methods After setting up the transwell system and a monolayer of BeWo choriocarcinomic cells was confirmed, a library of 50.12 ± 6.15 nm, 194.11 ± 9.51 nm, and 504.84 ± 10.91 nm MNPs or MNP-PEG or 250 µM of 47 nm, 200 nm or 490 nm polystyrene beads were tested for their translocation across the BeWo cell layer (n=3). This was followed by investigation of the effect of particle concentration on their translocation across the barrier (n=3).

Results: BeWo cells formed a confluent monolayer on the transwell membrane on day 4 post seeding as confirmed by transport restriction of the negative control FITC-Dextran (40kDa) and by the staining of tight junction proteins ZO-1 and adherent junction protein E-cad. The 50 nm MNPs were not restricted from movement across the BeWo cell barrier, while 200 nm were significantly retained, and 500 nm were completely restricted from movement across the barrier. Surface modification with PEG had a significant effect on reducing translocations of the smaller particles (50 nm), and completely blocked the 200 nm from movement across the barrier. Increasing concentration of the particles had no effect on their translocation across the BeWo cell layer.

Conclusion: Translocation of melanin nanoparticles across the BeWo cell barrier layer appeared to mostly depends on the size of the particles. The cut off size of particle restriction from movement across the barrier was 200 nm MNP-PEG which will be tested in an *ex vivo* human placental perfusion in the next chapter.

6.2 Introduction

6.2.1 Overview

In chapter 3, three differently sized melanin nanoparticles were synthesized and functionalized with PEG. The size range was carefully chosen according to what was reported in the literature with other types of nanoparticles. In this chapter, the three sized MNP and MNP-PEG were tested for their movement across an *in vitro* model of the placental barrier using a BeWo choriocarcinomic cell line in a transwell model. This would be used to determine a candidate size for the *ex vivo* human placental study in the next chapter.

6.2.2 Human choriocarcinomic cell BeWo

The BeWo cell line is derived from a human choriocarcinoma and was originally isolated in 1968 by Pattillo and Gey (Pattillo and Gey, 1968). BeWo cells are known to form a confluent polarized monolayer in a short time; unlike isolated primary trophoblast cells which poorly proliferate in cell culture. They are preferred over other choriocarcinomic cell lines because they are the best at forming syncytia, and resemble transfer ratios similar to *ex vivo* studies (Poulsen et al., 2009; Rothbauer et al., 2017). BeWo cells also demonstrate hormonal secretion properties and represent the rate limiting barrier of maternal exchange (Drwal et al., 2018). Overall BeWo cells have been widely used to investigate the transport of multiple nutrient and chemical compounds giving results that are in agreement with those demonstrated from clinical effects *in vivo* (Moe et al., 1994; Rytting and Audus, 2005; Schmid et al., 2003; Shah et al., 1999; Takahashi et al., 2001; Way et al., 1998).

6.2.3 BeWo syncytial fusion

Human trophoblast differentiation is characterized by the formation of the syncytiotrophoblast through intercellular fusion of the relatively undifferentiated, mitotically active cytotrophoblasts (Midgley et al., 1963). This intercellular fusion is crucial for placentation and foetal growth (Msheik et al., 2019). The syncytiotrophoblasts become a continuous epithelial layer throughout pregnancy and are located at the villous surface of the placenta where essential foetal nutrients must cross this placental barrier to reach the foetal circulation. The trophoblast derived choriocarcinoma cell line BeWo shares the morphological and biochemical characteristics of villous trophoblasts mimicking the *in vivo* syncytialization of placental villous trophoblast (Gauster and Huppertz, 2010; Rote et al., 2010). These cells however show low spontaneous fusion rates compared to *in vivo*, but can be boosted if treated with adenosine 3',5' –cyclic monophosphate (cAMP), or forskolin for the expression of syncytin-1 which is involved in trophoblast fusion (Orendi et al., 2010; Wice et al., 1990).

6.2.4 Aims

1. To establish which, if any, of the synthesized melanin nanoparticles of 50 nm, 200 nm, and 500 nm in diameter pass through the placenta in an *in vitro* transwell model with BeWo choriocarcinomic cell line.

2. To study the effect of surface functionalization with PEG on particles transfer across BeWo in a transwell model.

3. To investigate the effect of size and concentration of the particle transfer across a BeWo cell barrier in a transwell model.

6.3 Materials and Methods

6.3.1 BeWo cell culture

BeWo b30 cells (Caltag Medsystems; Cat. # C003002) were used for experiments in this chapter. Cells were expanded, and frozen stocks were made within a few passages of receipt. Early passages were then thawed and used for experiments. BeWo cells were cultured in complete Dulbecco's Modified Eagles Medium – high glucose (DMEM): F12-K media and supplemented with 10 % (v/v) FBS, 2 mM L-glutamine, 100 U/mL penicillin, and 0.1 mg/mL streptomycin (All Sigma-Aldrich, Gillingham, UK). Cells were incubated at 37 °C/ 5 % CO_2 and passaged when confluent. In some experiments, cells were treated with 50 μM forskolin (Sigma Aldrich, Gillingham, UK) to induce differentiation.

6.3.2 Setting up transwell model with BeWo cell lines

A 3.0 μm pore polycarbonate insert transwell plate (Scientific Laboratory Supplies Limited, WILFORD) was used for this study. BeWo cells were seeded in the apical chamber (transwell insert) of the transwell plate at a seeding density of $1x10^5$ cells/cm^{-2} in 0.5 mL phenol-red-free media. In the basal chamber, 1.5 mL phenol-red-free media was added, and the entire plate was incubated at 37°C and 5% CO_2 to achieve equilibrium. Characterization of monolayer development was carried out after a 24 hours incubation (Figure 6.1).

6.3.3 Hormonal assay; hCG-β ELISA

Secretion of Human chorionic gonadotropin hormone (hCG) in the culture media of BeWo cells grown on a 96 well plate or the apical chamber of transwell model was determined to assess cell functionality. hCG-β Enzyme-Linked Immunosorbent assay (ELISA) (Sigma Aldrich, Gillingham, UK) was performed daily on 50 μl

samples diluted in 100 µl sample buffer in duplicate alongside standards, following the manufacture instructions. Readout was performed using a plate reader (Magellan Infinite M200) and concentrations were calculated against a standard plot formulated after subtraction of the background blank media.

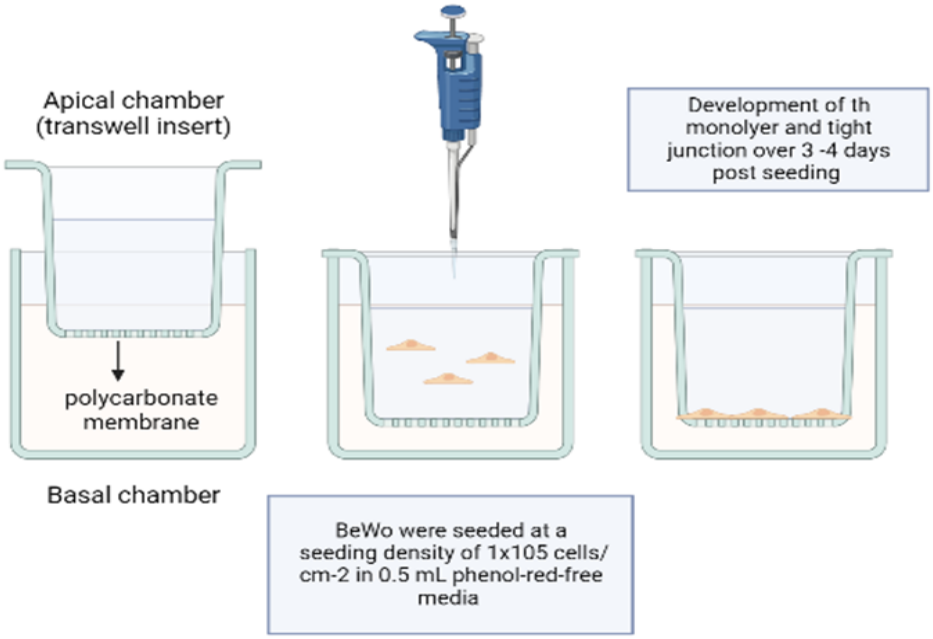


Figure 6.1 Graphical Summary of Transwell model setting up with BeWo cell lines.

Bewo cells were seeded in a polycarbonate transwell membrane at a seeding density of 1 x 10^5 cells/ cm^{-2} in a 0.5 ml phenol-red free media. Cells were allowed to grow for 3-4 days before testing for monolayer development. *Image created with BioRender.com.*

6.3.4 Characterization of monolayer formation and BeWo syncytial fusion

The development of a monolayer and characterization of BeWo syncytialization was assessed by both the transport of FITC-dextran (40 kDa; Sigma Aldrich, Gillingham, UK) across the barrier and with tight junction staining. Briefly, 10 µM FITC- dextran (40 kDa) was added to the apical chamber and incubated for 30 minutes at 37°C. A sample of 50 µl was then collected from the basal chamber and placed in triplicate in a 96 well plate. Samples withdrawn from the basal chamber were replaced with fresh media (50 µl). The fluorescence was measured at Ex. 465 nm/ Em. 510 nm. The fluorescence was evaluated against a standard curve to calculate the amount of FITC-dextran passing through the monolayer (Aengenheister et al., 2018b). The procedure was repeated daily until the fluorescence was negligible on day 4 post seeding (Figure 6.2 A) when BeWo syncytialization characterization and nanoparticle transport study were carried out. The small molecular weight Antipyrine (Sigma-Aldrich, Gillingham, UK) was used as a positive control (Figure 6.2 B) and was detected using Liquid chromatography (LC) (C-18 column), for the area under the curve integrated between wavelength ranges from 232 nm to 252 nm. The mobile phase consisted of 60 % (v/v) Acetonitrile and 40 % (v/v) water.

6.3.4.1 Fluorescence staining for barrier integrity

For the assessment of BeWo syncytial fusion and integrity of the cell barrier, the transwell membranes were cut on day 4 post seeding and placed on a glass slide, then fixed with 4 % (v/v) paraformaldehyde (Sigma Aldrich, Gillingham, UK). Membranes were then stained with syncytialization marker mouse anti-E-cadherin (Sigma Aldrich, Gillingham, UK) and rabbit anti-zona occludens-1 (ZO-1; Insight

Biotechnology Ltd, Wembley, Middlesex, UK) at a dilution of 1/100 for 1 hour. Secondary antibodies (dilution of 1/250); goat anti-mouse IgG Alexa Fluor 488 conjugate (Sigma Aldrich, Gillingham, UK) and Alexa Fluor 568 donkey Anti-Rabbit IgG antibody (BioLegend, London, UK) were added and incubated for 1 hour at room temperature. Vectorshield with DAPI (Vector Laboratories Ltd, Accent Park, Peterborough, UK) was used for membrane mounting (Figure 6.2 C). Confocal images were acquired using confocal microscopy UltraView spinning disk system (PerkinElmer) comprising CSU-X1 spinning disk head (Yokogawa) and Volocity software.

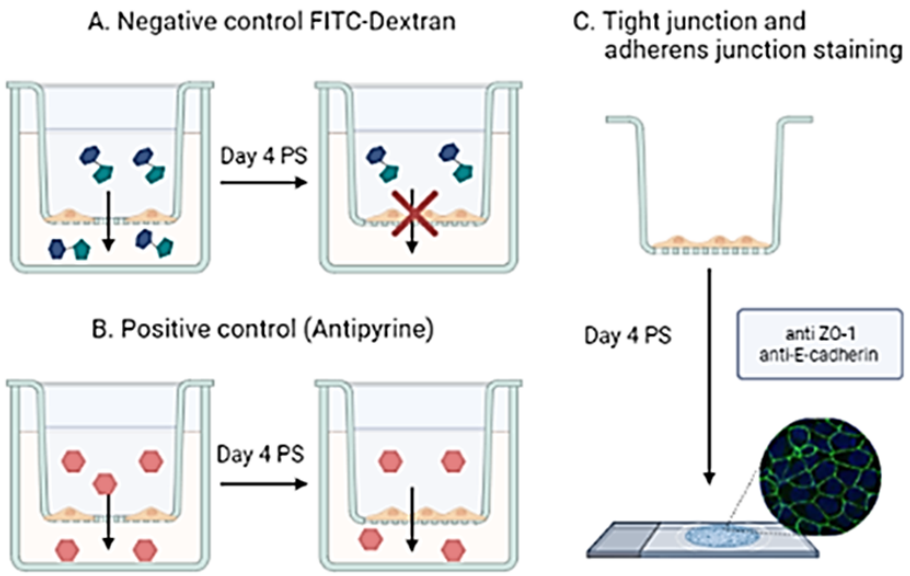


Figure 6.2 Graphical Summary of Characterization of monolayer formation and BeWo syncytial fusion.

(A) Transport of the negative control; FITC-Dextran (B) Transport of the positive control; Antipyrine (C) Tight junction ZO-1 and adherens junction E cadherin staining. Image created with BioRender.com.

6.3.5 Nanoparticles translocation across BeWo cell line

Assessment of the nanoparticle transport across BeWo was performed on day 4 post seeding (when FITC-dextran was not detected in the basal chamber) and the tight junction staining confirmed integrity of the barrier. Media from both chambers was removed and was replaced with 1.5 ml fresh media in the basal chamber and 0.5 ml nanoparticle suspension to the apical chamber. Briefly, nanoparticles of either (i) 250 µM of 50.12 ± 6.15 nm, 194.11 ± 9.51 nm, and 504.84 ± 10.91 nm MNP, or (ii) 250 µM of 47 nm, 200 nm or 490 nm polystyrene beads or (iii) 100 µM, 250 µM, or 1 mM of 50 nm, 200 nm or 500 nm MNP-PEG, suspended in a 0.5 mL phenol-red-free media was added in triplicate to the apical chamber (transwell inserts) containing BeWo cell barrier or acellular controls, and incubated at 37°C and 5 % CO_2. Antipyrine (100 µM) and FITC-dextran (5 µM) were used as a positive and negative controls respectively (Figure 6.3). At successive time points 100 µL from the basal chamber was transferred to a 96 well plate (and replaced with fresh media) to measure the absorbance at 540 nm to detect MNP/MNP-PEG against a standard calibration curve. Antipyrine was detected using LC (C-18 column) for area under the curve at wavelength ranges from 232 to 252 nm. The mobile phase consisted of 60 % (v/v) Acetonitrile and 40 % (v/v) water.

For each time point, the cumulative mass transport was calculated and corrected for the mass removed from the previous samples as follows: $\Delta Qn = Cn\,.Vb + \sum_{j=1}^{n-1} Vs.Cj$ where C_n is the nanoparticle concentration measured at time t_n, V_b is the volume of media added to the basal chamber (1.5 ml), V_s is sampling volume (100 µl) and the summation term represents the correction of the cumulative mass removed by sampling during the sampling period from t_n to t_{n-1}. Data was represented as the basolateral amount of the initial dose (ID) in %.

6.3.6 Statistical analysis

GraphPad Prism 8.0.2 (San Diego, California, USA) software was used for statistical analysis of the data. Data were compared using One-way Anova or t-test. Data are presented as mean ± SD, statistical significance was defined as $P < 0.05$

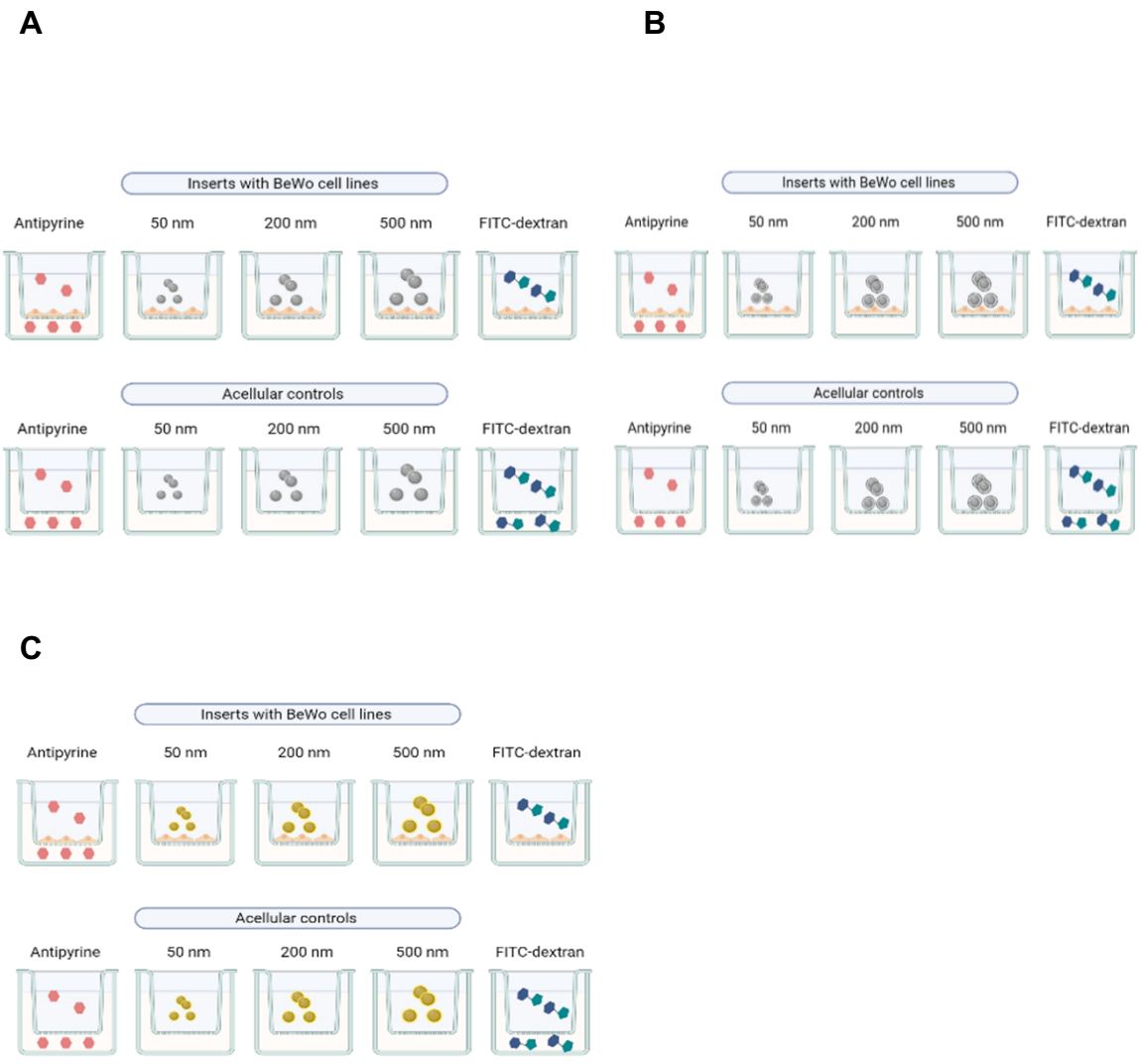


Figure 6.3 Graphical Summary of nanoparticle transportation across BeWo cell barrier.

Transport of 50 nm, 200 nm, or 500 nm (A) MNPs, (B) MNP-PEG or (C) polystyrene beads across BeWo cell barrier or acellular control alongside Antipyrine and FITC-dextran. Image created with BioRender.com.

6.4 Results

6.4.1 Secretion of hCG

The trophoblastic origin hormone hCG is considered as a marker of trophoblast differentiation. The release of hCG from BeWo upon induction of Forskolin was determined using ELISA. Levels of hCG in cell culture supernatant from BeWo cells supplemented with forskolin significantly increased with time of culture (Figure 6.4) indicating that BeWo cells have good physiological function.

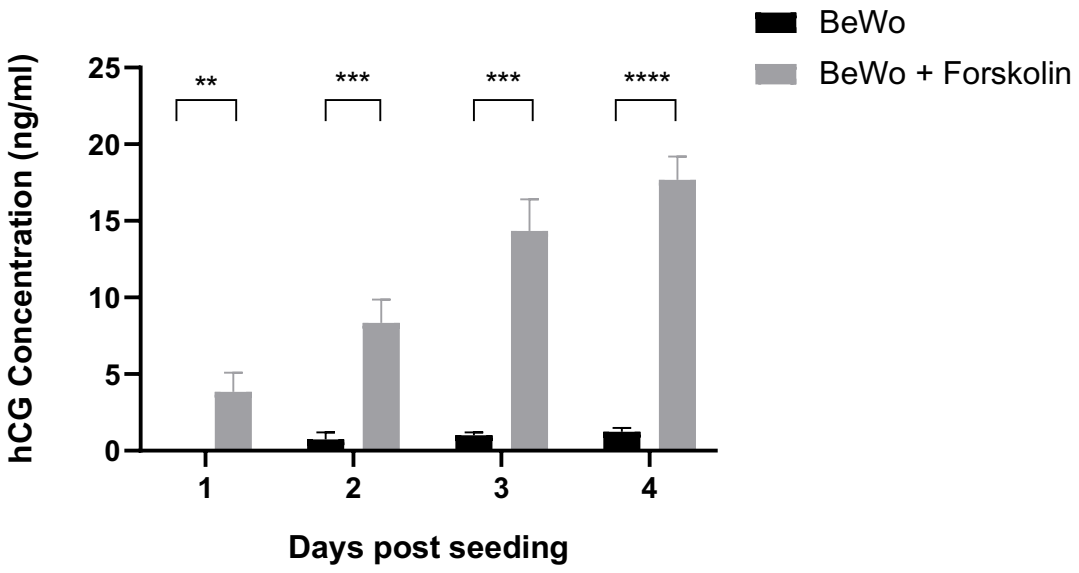


Figure 6.4 Level of hCG hormone in culture media of BeWo cells.

*hCG release from BeWo cells at days 1,2,3 and 4 post seeding determined by ELISA. Data represent mean ± SD (n=3 per treatment). **p ≤ 0.01, ***p ≤ 0.001*** ≤p 0.0001.*

6.4.2 Confirmation of monolayer formation and BeWo syncytial fusion in transwell model

Since spontaneous syncytial fusion rate is low, Forskolin was used to trigger BeWo cell fusion (Msheik et al., 2019). The development of BeWo monolayer and integrity within the transwell set-up was assessed by monitoring the transport of the large molecule FITC-Dextran (40 kDa) (Figure 6.2). The concentration of FITC-dextran detected in the basal chamber gradually decreased until it was negligible on day 4 post-seeding, indicating the formation of a confluent cell layer (Figure 6.5). To visualize the integrity of the cell barrier, cells were stained with tight junction protein ZO-1 and adherent junction protein E-cadherin on day 4 post seeding. Results show that only forskolin-treated BeWo cells were multinucleated, cell-to-cell fused trophoblasts while control BeWo cells treated with dimethyl sulfoxide DMSO failed to fuse (Figure 6.6 A and B).

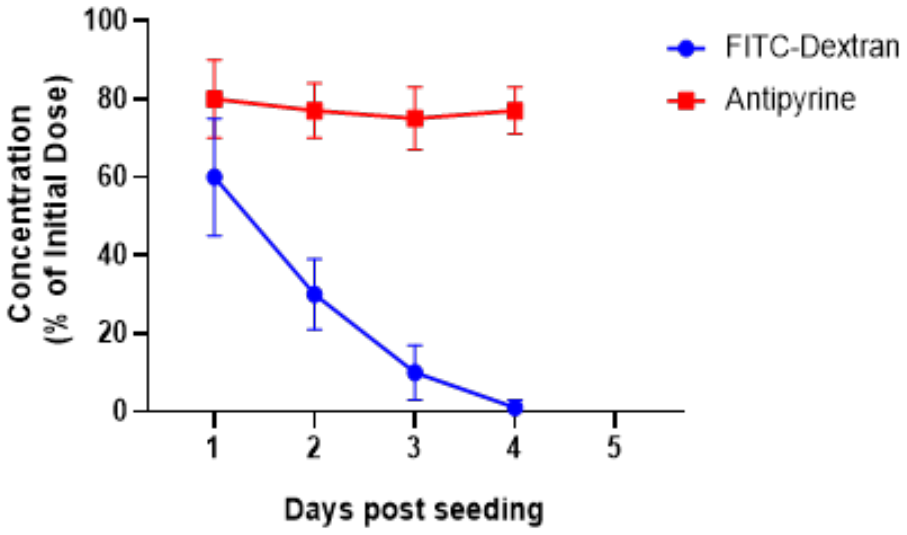


Figure 6.5 Confirmation of monolayer and BeWo syncytial fusion.

Transport of negative control FITC-Dextran (40 kDa) and positive control Antipyrine across BeWo cell layer.

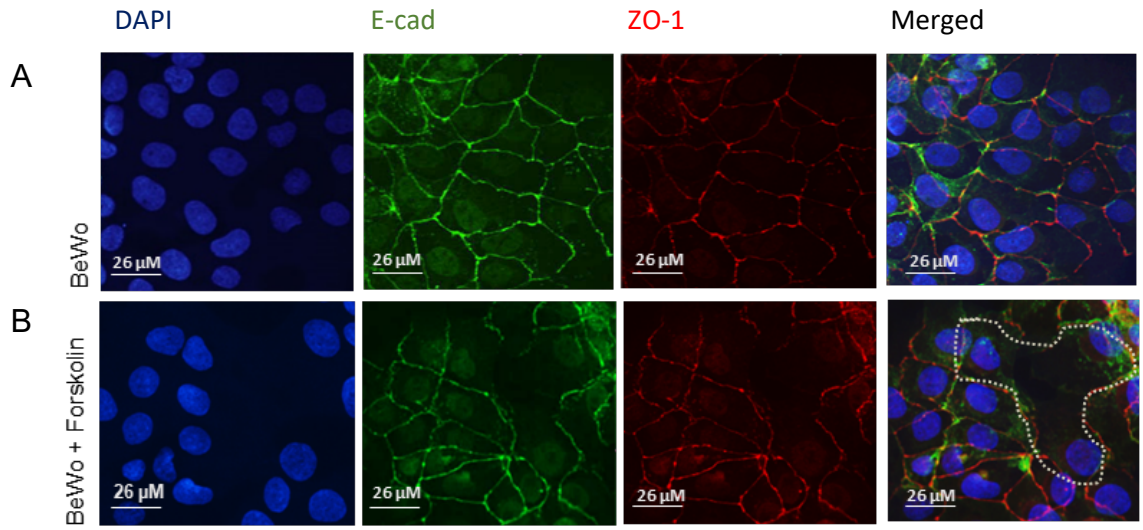


Figure 6.6 Fluorescence staining for barrier integrity; Confirmation of monolayer and BeWo syncytial fusion.

Projected series images of BeWo cell layers on the transwell membrane imaged by confocal microscopy after staining with E-cadherin (E-Cad; green), zona occludens-1 (ZO-1; red), and DAPI (blue) treated with (A) DMSO or (B) Forskolin. The dashed line represents area of cellular fusion (multinucleated) upon treatment with Forskolin which is known to enhance BeWo syncytial fusion. Data are representative of at least three different experiments. Images were acquired and analysed using Volocity software. Scale bar = 26 µm.

6.4.3 The passage of MNPs across BeWo cell layer in a transwell model is size dependence

Transport of melanin nanoparticles across the BeWo cell layer was carried out on day 4 post seeding after the confirmation of a confluent monolayer and BeWo syncytial fusion (Figure 6.6). To assess the cut off size of melanin nanoparticles; 50 nm, 200 nm, and 500 nm MNPs were used alongside the positive and negative controls Antipyrine and FITC-dextran (40 kDa). Figure 6.7 shows that the translocation of MNPs across BeWo is size dependent; while 50 nm particles

showed no difference in translocation across BeWo in comparison to the acellular control (Figure 6.7 C), 200 nm MNPs were significantly retained and 500 nm particles were completely blocked by the BeWo cell barrier. It was also found that around 4 % of the initial dose of 200 nm MNPs crossed the BeWo cell layer while 18 % crossed the acellular control (Figure 6.7 D). The 500 nm MNPs, however, were not detected in the basal chamber of the cellular insert with BeWo, but 10 % of the initial dose was able to cross the acellular control (Figure 6.7 E) suggesting it was completely blocked by the BeWo cell barrier.

6.4.4 Comparison of the passage of MNPs and polystyrene beads across BeWo cell barrier in a transwell model; effect of material

Transport of positive control polystyrene beads was carried out to validate the results. Polystyrene beads were used because they are easy to obtain and were found to cross the placenta (Huang et al., 2015; Wick et al., 2010). Approximately 31 %, 20 % and 16 % of the initial dose of 49 nm, 200 nm, and 490 nm diameter polystyrene beads respectively were detected in the basal chamber compared to 20 %, 2 % and 0 % of the initial dose of 50 nm, 200 nm, and 500 nm MNPs (Figure 6.8). The passage of 49 nm and 490 nm polystyrene beads across BeWo cell barrier are comparable to the literature where around 35 % and 40 % of the initial dose of 49 nm and 25 % of the initial dose of 490 nm polystyrene beads passed across BeWo cell barrier after 24 hours incubation (Aengenheister et al., 2018b; Rothbauer et al., 2017).

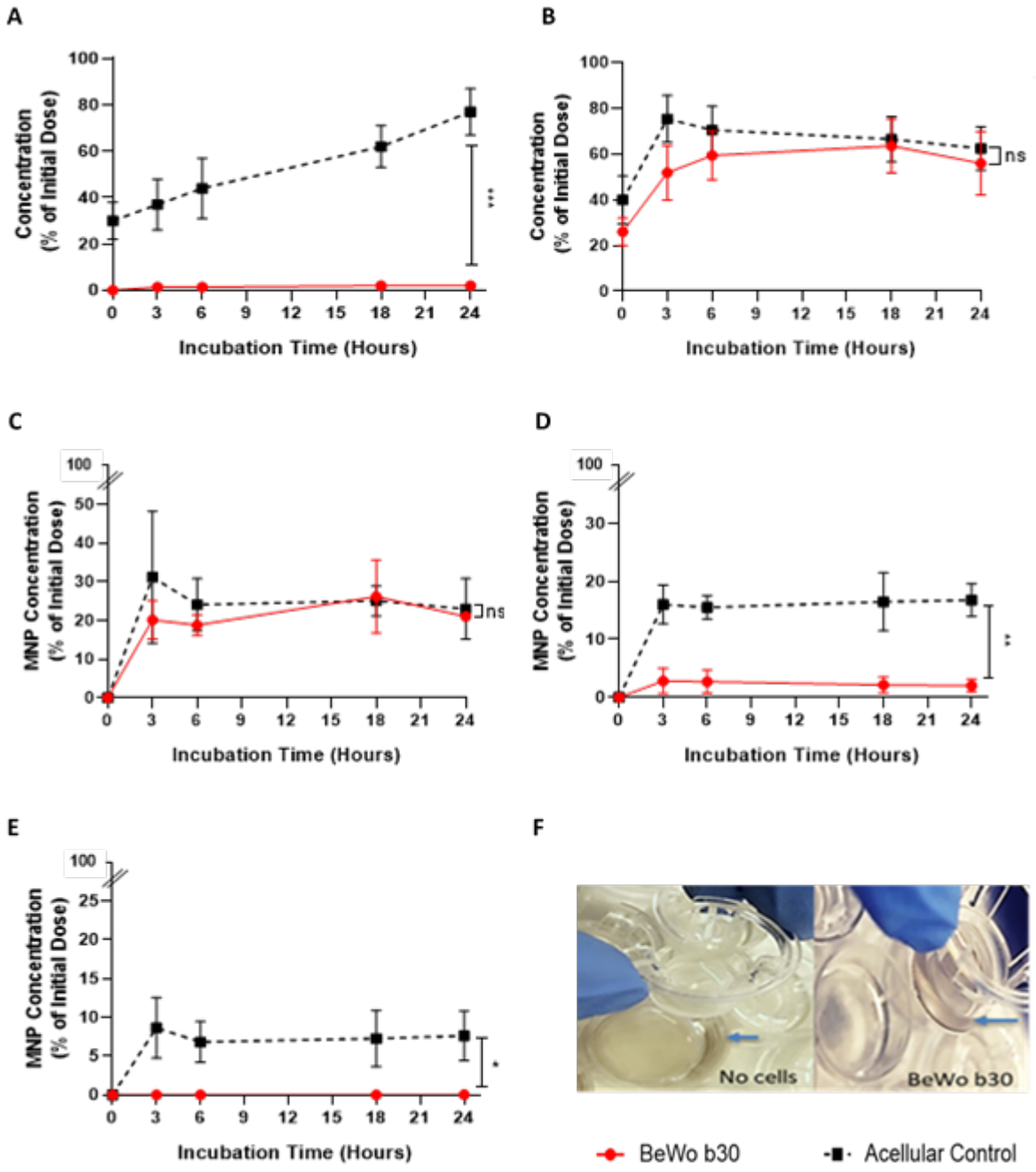


Figure 6.7 MNPs passage across BeWo cell barrier or acellular control in a transwell model.

*Transportation of (A) the negative control FITC-dextran 40kDa, (B) the positive control antipyrine (C) 50 nm MNP, (D) 200 nm MNP and (E) 500 nm MNP. (F) Transwell insert shows comparison of MNP across insert with BeWo cell barrier and acellular control. Data shows mean ± SD (n=3 per treatment). *p≤ 0.05, **p ≤ 0.01, ***p ≤ 0.001, ns; not significant.*

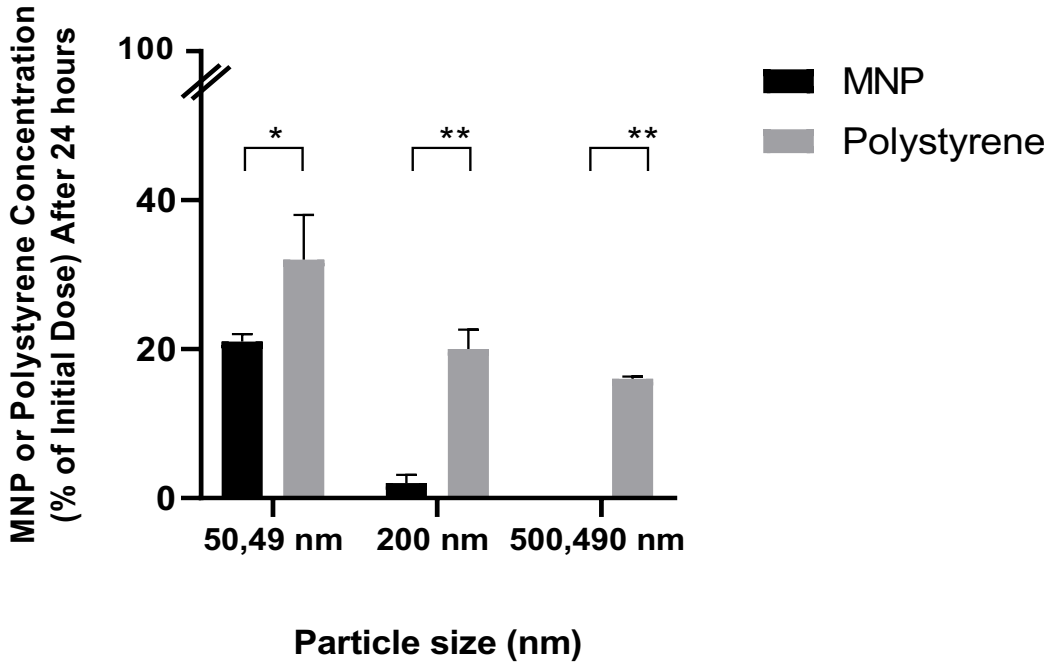


Figure 6.8 Comparison of the passage of MNPs and Polystyrene beads across BeWo cell barrier in a transwell model.

*Transportation of 50 nm, 200 nm, and 500 nm MNP or 49 nm, 200 nm, and 490 nm Polystyrene beads across BeWo cell barrier after 24 hours (n=3 per treatment). *p≤ 0.05, **p ≤ 0.01.*

6.4.5 PEGylation limits the passage of MNPs across BeWo cell layer in a transwell model

The passage of PEGylated MNPs across the BeWo cell barrier was tested to assess any changes due to the surface modification. It was observed that PEGylation limited the transport of the small particles (50 nm MNP-PEG) and completely restricted the transport of 200 nm and 500 nm MNP-PEG (Figure 6.9 A, B and C). While approximately 30 % of the initial dose of 50 nm MNPs was able to cross the

BeWo cell barrier, only around 15 % of the initial dose of PEGylated MNPs of the same size were detected in the basal chamber of the cellular insert with BeWo (Figure 6.7 C and Figure 6.9 A). On the other hand, around 25 %, 23 % and 20 % of the initial dose of 50 nm, 200 nm and 500 nm MNP-PEG respectively were detected across the acellular control membrane (Figure 6.9 A, B and C).

6.4.6 Increasing concentration has no effect on passage of MNP-PEG across BeWo cell barrier in a transwell model.

To test the effect of concentration on the passage of larger particles (200 nm and 500 nm diameter) across the BeWo cell barrier, 100 µM, 250 µM, or 1 mM of either 200 nm or 500 nm MNP-PEG was added to the apical chambers with either the BeWo barrier or acellular control on day 4 post seeding. It was shown that particles were not detected in the basal chamber of the cellular insert with a BeWo cell layer but were detected in the basal chamber of the acellular control. The concentration of particles in the basal chamber of the acellular control was significantly increased after increasing the initial dose (1 mM particles compared to the 250 µM particles). However, when increasing the initial dose to 1mM no particles were detected across the BeWo cell barrier suggesting that increasing the concentration had no effect on MNP-PEG passage or across the BeWo cell barrier (Figure 6.10).

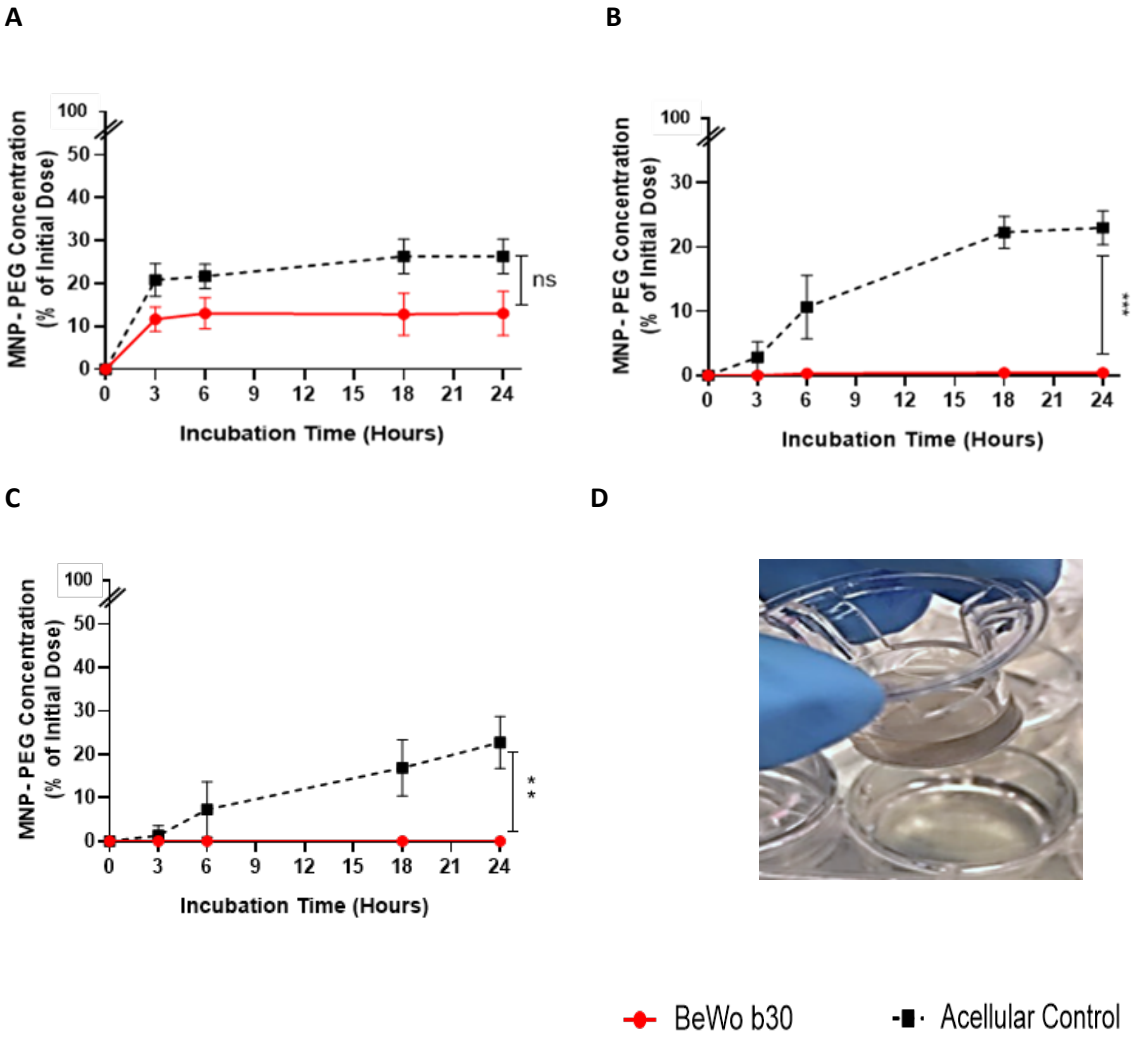


Figure 6.9 Passage of MNP-PEG across BeWo cell barrier or acellular control in a transwell model.

*Experiments were performed on day 4 post seeding. Passage of 100 µM of (A) 50 nm MNP-PEG, (B) 200 nm MNP-PEG and (C) 500 nm MNP-PEG across transwell insert with BeWo cell barrier or acellular control. (D) Transwell insert of MNP-PEG on BeWo cell barrier in the apical chamber. Data shows mean ± SD (n=3 per treatment). **p ≤ 0.01, ***p ≤ 0.001, ns; not significant.*

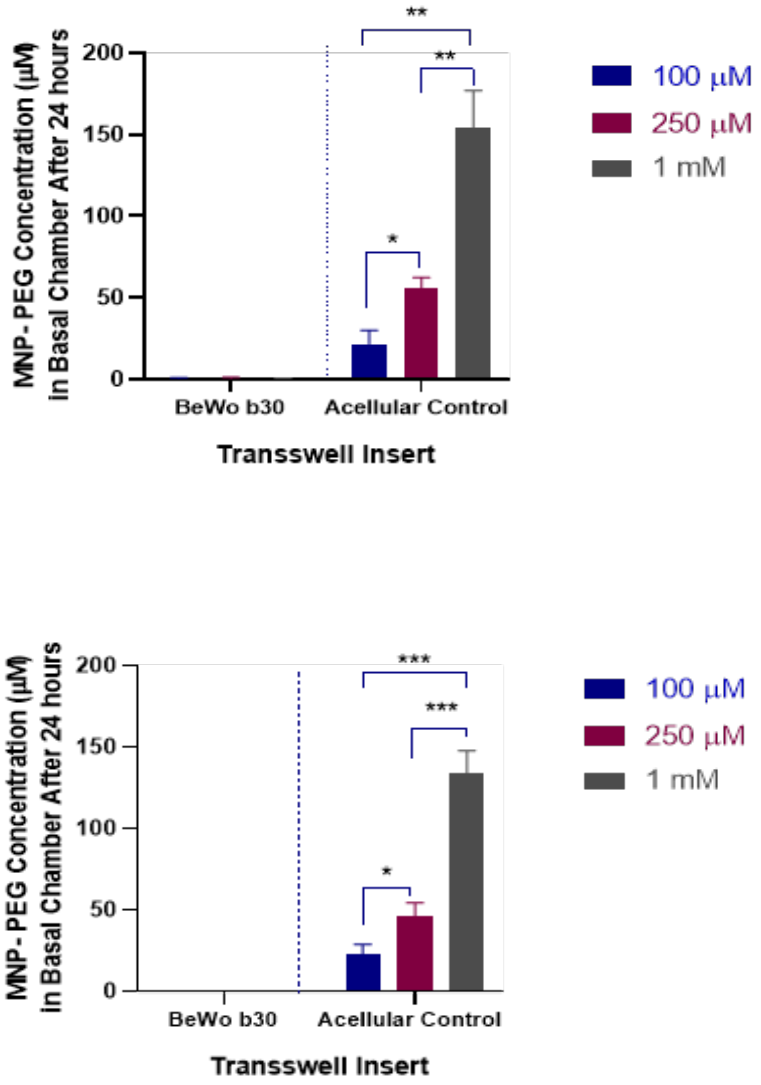


Figure 6.10 Effect of concentration on the passage of MNP-PEG across BeWo cell barrier or acellular control in a transwell model

*Passage of 100 µM, 250 µM and 1 mM of (top) 200 nm and (bottom) 500 nm MNP-PEG across BeWo monolayer on day 4 post seeding (n=3 per treatment). Data shows mean ± SD. *p≤ 0.05; **p ≤ 0.01; ***p ≤ 0.001.*

6.5 Discussion

In the previous chapters, synthesis of three differently sized melanin nanoparticles was successfully achieved and particles were further functionalized with PEG. Functional analysis was also tested for particle efficacy in chelating iron. The main aim of this chapter was to establish if any of the synthesized particles could be restricted from movement across an *in vitro* transwell model using the BeWo choriocarcinomic cell line. Interaction of nanoparticles with cells and tissues in general is determined by the particle characteristics and functionalization. It was found in the literature that movement of most nanoparticles across the placenta was mainly dependent on their diameter (Aengenheister et al., 2018b; Cornford et al., 2016; Huang et al., 2015; King and Muller, 2016; Myllynen et al., 2008; Poulsen et al., 2015; Semmler-Behnke et al., 2014; Wick et al., 2010; Yamashita et al., 2011). It was hypothesized that if melanin nanoparticles were designed with appropriate characteristics they could be restricted from movement across the placental barrier and safely used to treat the mother without harming the foetus. The main findings support this hypothesis; movement of melanin nanoparticles across the BeWo cell layer was heavily dependent on the size of the particles (Figure 6.7). Moreover, surface functionalization with PEG was also found to restrict movement of the particles across the BeWo cell barrier (Figure 6.9).

6.5.1 BeWo hormonal secretion, syncytial fusion, and integrity of monolayer

hCG is produced upon the differentiation from mono-nucleated to the syncytial state. To evaluate the basic physiological function of BeWo cells, secretion of hCG hormone was confirmed. hCG significantly increased with time in cell culture media

containing forskolin (Figure 6.4) which is known to increase hCG levels leading to the formation of a multinucleated state (Drwal et al., 2018; Rothbauer et al., 2017; Tang et al., 2018).

Although BeWo cells are a well-established *in vitro* model for transplacental transport, there are some discrepancies regarding the time taken to form a monolayer (between 4 and 6 days; (Cartwright et al., 2012). This also varies according to factors like type and size of the matrix used, seeding density, and passage number. Because cells grown on a transwell insert are not visible under the light microscope, assessment of the confluent layer formation was carried out by monitoring transport of the negative control FITC dextran which was negligible on day 4 post seeding (Figure 6.5). Assessment of a monolayer formation using high molecular weight molecules is well reported in the literature since Trans-epithelial electrical resistance (TEER) values can be poorly correlated with permeability and vary widely according to the pore size of the matrix and the type of apparatus, making it hard to define standard values (Aengenheister et al., 2018b; Cartwright et al., 2012; Liu et al., 1997; Rothbauer et al., 2017; Saunders, 2009; Tang et al., 2018). Nonetheless, beside the transfer decrease of the para-cellular marker FITC-dextran, visual confirmation of the barrier integrity with the tight junction staining on day 4 post seeding (Figure 6.6) added confidence to the robustness of the translocation study (Aengenheister et al., 2018b; Cartwright et al., 2012; Msheik et al., 2019; Rothbauer et al., 2017). Based on the results of cell morphology that suggested high integrity of the barrier as well as the transport of the negative control, the translocation study was carried out on day 4 post seeding; this was previously reported in the literature (Aengenheister et al., 2018b; Cartwright et al., 2012; Correia Carreira et al., 2015).

6.5.2 Transport of MNP across BeWo cell layer

In this chapter it was found that *in vitro* translocation of MNP across the BeWo cell barrier is highly dependent on their size. While small particles (50 nm) were able to breach the monolayer (Figure 6.7 C); 200 nm MNPs were partially blocked, and 500 nm MNPs did not cross the BeWo cell barrier at all (Figure 6.7 D and E). However, when polystyrene beads of similar sizes were applied, particles of all sizes were able to cross BeWo cell barrier with the smaller size being transferred at a higher rate in comparison to larger particles (Figure 6.8) suggesting that factors like chemical compositions and zeta potential play an important role on nanoparticle interaction with BeWo cells. Similar findings were previously reported using 50 nm and 100 nm fluorescent polystyrene latex fluoresbrite nanoparticles, where transport of 50 nm particles across a BeWo cell layer over 24 hours was four times higher compared to 100 nm particles (Cartwright et al., 2012) which further supports the validity of the transwell model. It was also noted that transport of Poly(lactic-co-glycolic acid) (PLGA) nanoparticles was decreased by half when their size increased to 196 nm compared to 143 nm (Lopalco et al., 2015).

Although animal models are not a good representation for human placenta, it gives an idea of systemic toxicity and the translocation pattern of nanoparticles in general. A size dependent pattern of nanoparticle penetration across the placental barrier has been reported in many *in vivo* studies. In a mice study using 70 nm, 300 nm and 1000 nm silica particles, only 70 nm particles were able to cross the placenta and accumulated in the foetal liver while larger particles were not observed in the placenta or foetus (Yamashita et al., 2011). Another study of gold nanoparticles of 1.4 nm, 18 nm and 80 nm through rat placenta in the third trimester found that about 3 % and 0.02 % of the initial dose of the 1.4 nm and 18 nm particles, respectively,

were able to cross the placenta but not the 80 nm particles (Semmler-Behnke et al., 2014). Since studies were carried out under different experimental conditions it is difficult to determine the threshold of maternal-foetal transfer for gold nanoparticles in rodents.

6.5.3 Effect of PEGylation on particle transport across BeWo

It was found that surface modification limited the transfer of the 50 nm MNPs and completely blocked 200 and 500 nm from passing across the BeWo cell barrier (figure 6.9). In previous studies, surface PEGylation was found to decrease placental transfer compared to non-PEGylated particles *in vivo* using quantum dots that were injected in the tail of pregnant mice (Chu et al., 2010). In an *ex vivo* human placenta, surface PEGylation of nanoparticles significantly decrease placental uptake and prevented translocation of liposomal doxorubicin across the human placenta (Parrott and DeSimone, 2012; Valero et al., 2017). The mechanism of the effect of PEGylation in reducing cellar interaction *in vitro* is not clear but could be due to the slight variation in the size or surface charge of the particles after PEGylation. In an *in vivo* administration however, PEGylation was found to diminish protein adsorption on the surface of the particles and the diameter as such (Kulvietis et al., 2011), both of these factors may affect particle interaction with the placenta.

6.5.4 Effect of concentration on particles transport across BeWo

Studying the effect of melanin nanoparticles concentration on particle transport across BeWo, it was demonstrated that higher concentrations of up to 1 mM had no effect on particle transport across a BeWo cell layer (figure 6.10). A similar pattern was previously reported with Fe_3O_4 nanoparticles where a concentration of 50 or 100 µg/ml had no significant difference in the translocation of the particles across a

BeWo cell barrier but was still detected with higher dose in the basal chamber of the acellular controls (Correia Carreira et al., 2015). This suggests that translocation of nanoparticles across the cellular barrier is mainly affected by factors associated with particle characteristics and not concentrations.

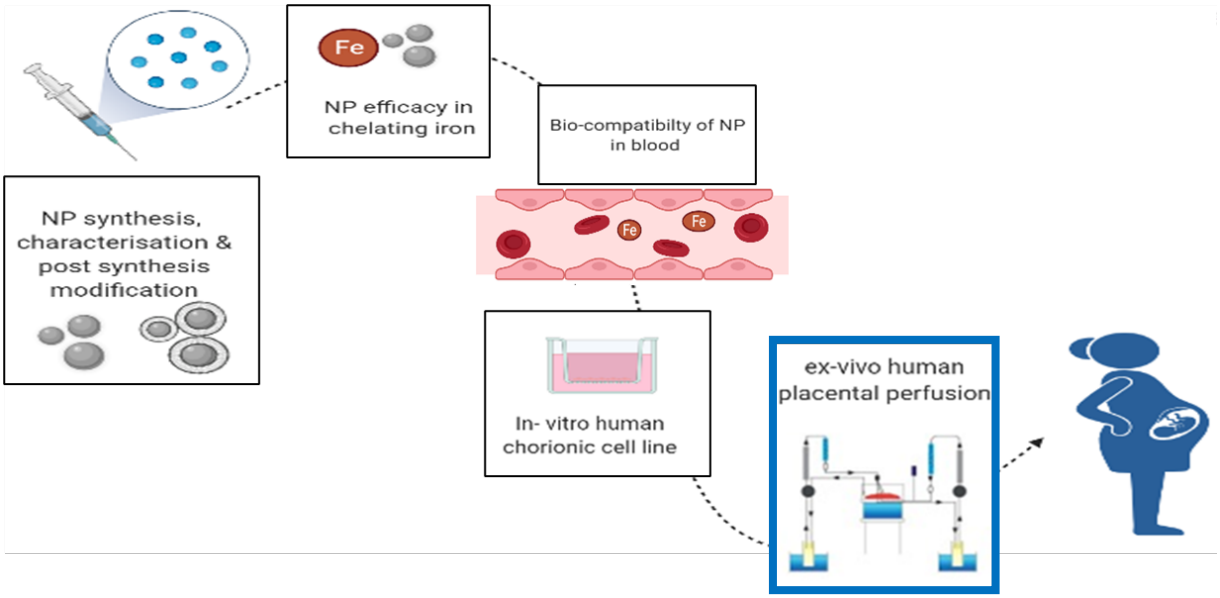
6.5.5 Strength and limitations

The *in vitro* transwell experiment with BeWo cells is a gold standard method in predicting transport of substances across the placenta *in vitro.* The *in vitro* model is more practical, but it does not represents inter-individual differences in terms of transport expressions such as P-glycoprotein which was found to be significantly variable on its expression on the apical membranes of term placentas (Nekhayeva et al., 2006). This issue can be addressed by using an *ex vivo* placental perfusion system. On the other hand, although the *ex vivo* dual lope placental perfusion is more representative of the *in vivo* situation, it is a challenging procedure that requires proximity to maternal wards and a critical set of criteria to ensure a successful perfusion (Burton et al., 2014; Karttunen et al., 2015). Thus, it was wise to implement transwell experiments with a BeWo cell barrier as an initial screening followed by an *ex vivo* placental perfusion on targeted particle size.

6.6 Summary

Results in this chapter support the hypothesis that translocation of melanin nanoparticles across a BeWo cell layer was mainly dependent on the particle size. The cut off size of particle transport across BeWo cell barrier was 200 nm PEGylated particles. Therefore, these were selected for the *ex vivo* human placental perfusion study in the next chapter.

Chapter 7. Investigation of melanin nanoparticle transport using an *ex vivo* human placental perfusion system



7.1 Abstract

Background Interaction of nanoparticles with the placental tissue is determined by particle characteristics and functionalization. It was found that particle size was the most significant factor for their interaction across the placenta.

Objectives The main aim of this chapter was to investigate the translocation of 200 nm MNP-PEG across the maternal foetal barrier in an *ex vivo* placental perfusion model.

Methods Placentae were collected after written consent from normal pregnancies delivered by caesarean section delivery, and immediately processed. After physical examination to define a suitable lobe the *ex vivo* dual lobe human placental perfusion system was started with a 30 minutes calibration. Testing of permeability and integrity of the barrier by monitoring the transfer of the small molecular weight Antipyrine and by leak of perfusion was then performed. This was followed by the administration of 200 nm MNP, MNP-PEG, or polystyrene beads for a duration of 6 hours perfusion. The criteria for successful perfusion included: volume loss of < 3 mL/hour, antipyrine equilibrium between maternal and foetal side within 3 hours and a foetal pH 7.2 to 7.4.

Results: Administered 200 nm melanin nanoparticles were not detected in foetal circulation after a 6 hours perfusion compared to the positive control polystyrene beads which were detected 60 minutes after administration. Viability of placental tissue was determined by the production of hCG which was not altered after 6 hours perfusion.

Conclusion: Melanin nanoparticles of 200 nm could be restricted from crossing the placenta in an *ex vivo* dual lobe human placental perfusion.

7.2 Introduction

7.2.1 Overview

In chapter 6, it was found that the cut off size of particle transport across a BeWo cell barrier was 200 nm PEGylated particles. In this chapter, 200 nm MNP and MNP-PEG were tested for their translocation across the placental barrier in an *ex vivo* human placental perfusion.

7.2.2 *Ex vivo* human placental perfusion

The *ex vivo* human placental model has been preferred in medicated drug testing during pregnancy and transfer across the placenta than the *in vivo* animal approach since it greater resembles human pregnancy (Pemathilaka et al., 2019). The *ex vivo* human placental perfusion technique was first described in 1967 (Panigel et al., 1967). The dual lobe perfusion system however, first described by Eaton and Oakey, 1994 (Eaton and Oakey, 1994) is the most commonly used method.

The *ex vivo* placental perfusion model enables study of aspects of placental function, including nutrient and drug transport and metabolism (Hutson et al., 2011), nanoparticle transport (Wick et al., 2010), antibodies, and viruses (Polliotti et al., 1996). The perfusion procedure has a high failure rate due to physical damage during delivery, presence of clots, and blocked or inaccessible vessels (Karttunen et al., 2015; Nishiguchi et al., 2019). Thus, to overcome these challenges, certain markers need to be considered.

7.2.3 Criteria for successful perfusion

To ensure a successful perfusion, intact foetal-maternal barrier, sufficient overlap between the two circulations, and viability and functionality of the placental tissue, needs to be achieved (Karttunen et al., 2015). The barrier integrity can be checked

by measuring the leak of perfusion media throughout perfusion (Miller et al., 1985; Myllynen et al., 2010; Wick et al., 2010). Transport of reference compounds has been used to ensure sufficient overlap between the maternal and foetal circulations such as; inulin, creatinine, glucose and Antipyrine (Karttunen et al., 2015; Myllynen et al., 2010; Schneider et al., 1972; Wick et al., 2010). Finally, either pH of the perfusion media, pressure in foetal circulation or hormonal synthesis can be used as parameters for biochemical functionality of the placental tissue (Karttunen et al., 2015; Wick et al., 2010).

7.2.4 Antipyrine

Antipyrine (also known as phenazone, phenazon, or anodynin) has been the most commonly used reference compound to confirm circulation overlap of perfused placenta (Karttunen et al., 2015; Myllynen et al., 2010; Wick et al., 2010). This is because of its low molecular weight (188.23 g/mol) and low protein binding that allows easy transport across the placenta in a short time without being metabolized or accumulate in the placental tissue (Karttunen et al., 2015; Schneider et al., 1972). Transport of antipyrine across the placenta is flow dependent by passive diffusion (Schneider et al., 1972).

7.2.5 Aim

The aim of this chapter was to investigate the effect of MNPs on placental function and tissue integrity, and to identify whether the 200 nm MNP-PEG, selected from results of the *in vitro* transwell model with BeWo cell barrier, could be restricted from transfer across the human placenta in an *ex vivo* perfusion model.

7.3 Materials and Methods

7.3.1 Physical examination

Placentae were collected after caesarean delivery (section 2.2) and delivered to the laboratory in warm Hanks's solution for immediate processing. Lobules suitable for perfusion were chosen based on physical examination of both the maternal and foetal side of the placenta. These are lobules that were intact, with no tissue perforation on either side of the placenta, and visible and accessible vessels (figure 7.1).

7.3.2 Perfusion media

Perfusion media for both maternal and foetal circulations consists of M199 phenol red-free cell culture media (Sigma Aldrich, Gillingham, UK) supplemented with 5 g Bovine Serum Albumin (BSA), 5000 U/L sodium Heparin (Sigma Aldrich, Gillingham, UK) and 10 mL antibiotic/antimycotic agent pH 7.4 (Sigma Aldrich, Gillingham, UK). Foetal media was also supplemented with 0.8 % (w/v) Dextran 20 (Sigma Aldrich, Gillingham, UK) to mimic the viscosity of foetal blood.

7.3.3 Perfusion equipment

Perfusion equipment included a perfusion chamber where a perfused placenta was placed in a perspex water jacket maintained at 37°C, two peristaltic pumps to adjust flow rate in each circulation, maternal and foetal reservoirs, water bath where medias are maintained at 37°C, and an oxygen tank to oxygenate maternal media with 95 % O_2 and 5 % CO_2, and six 1.7 mm foetal feeding tubes (Figure 7.2).

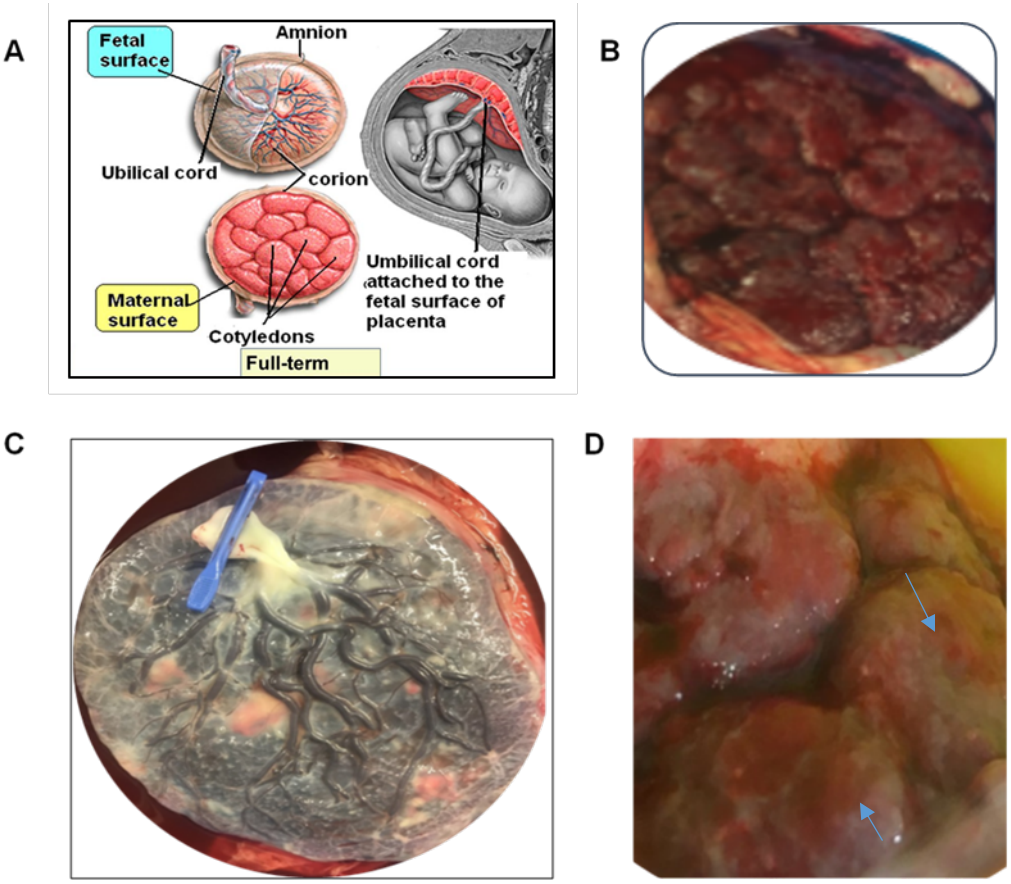


Figure 7.1 Physical examination of collected placentae.

(A) Illustration of the maternal and foetal side of the human placenta (B) Maternal side of a collected placental sample showing damaged lobules. (C) Foetal side of a collected placental sample showing visible vessels suitable for perfusion. (D) lobules from a collected placental sample suitable for perfusion.

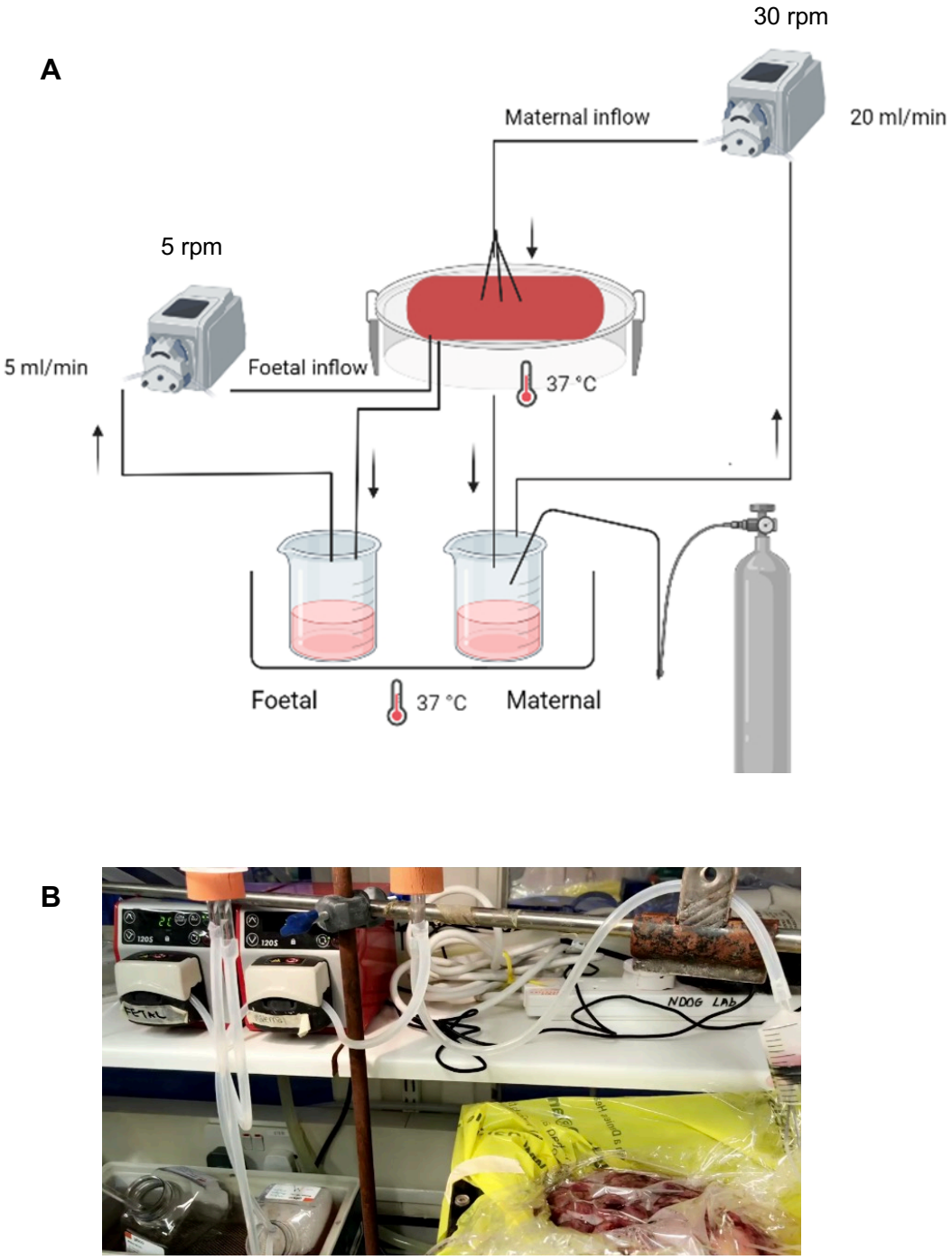


Figure 7.2 Placental perfusion system

(A) Diagram showing dual placental perfusion system whereby both the maternal and foetal circulation are perfused. Image created by Biorender. (B) Image represents a performed placental perfusion on one of the collected samples.

7.3.4 Perfusion procedure; setting up the system

An *ex vivo* dual lobe placental perfusion system was performed as previously described (Eaton and Oakey, 1994). Briefly, placentae were processed immediately by cannulating the artery and vein of an intact lobe (Figure 7.3 A) after selection by physical examination followed by the induction of foetal circulation at a rate of 5 ml/minute. The placenta was then inverted and placed inside a Perspex water jacked maintained at 37°. Perfusion of the maternal side was then inducted at a rate of 20 ml/minute through six foetal feeding tubes of 1.7 mm puncturing the maternal side of the identified lobe (Figure 7.3 B), and the circulation was started. Before adding the reference or study compounds, the perfusion was performed using either PBS or maternal and foetal media for 30 minutes with an open system for calibration and to wash RBCs, media was then discarded and replaced with fresh full media (600 ml). The perfusion circuit was closed before the induction of transportation experiment by ensuring the maternal perfusate flowed back to the maternal media bottle (Figure 7.2). Both perfusates were maintained at 37°C water bath.

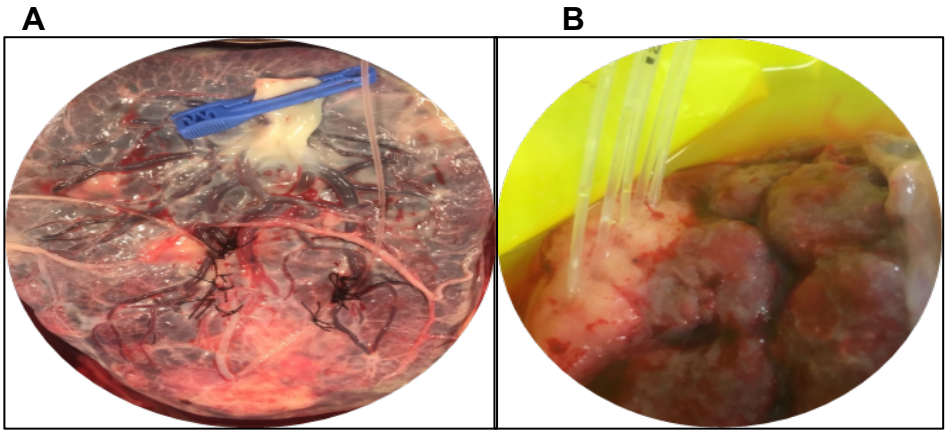


Figure 7.3 Cannulation of the perfused lobe.

(A) Image represents cannulation of artery and vein of the perfused lobe of a placental sample. (B) Image represents induction of the maternal circuit.

7.3.5 Nanoparticle transport

After closing the circuit, either 200 nm melanin or polystyrene nanoparticles were added to the maternal media. The perfusion was performed for 6 hours with equal starting volumes of maternal and foetal media. Maternal and foetal reservoirs (1 ml) were collected at each time point in separate tubes for analysis and centrifuged twice at 1500 g for 10 minutes at 4°C, followed by centrifugation at 10,000 g for 20 minutes to collect the particles. The concentration of nanoparticles in the maternal and foetal samples was determined by fluorescent quantification at Ex. 488 nm/ Em. 525 nm, against a standard calibration curve after correction for volume loss.

7.3.6 Permeability of the maternal-foetal barrier

The reference compound Antipyrine was used to assess the permeability, and to confirm overlap of the two circulations. Antipyrine was added to the maternal circuit, and maternal and foetal reservoir (300 µl) was collected after each time point into separate tubes. Concentration in reservoirs was measured by LC (C-18 column) of 232-252 nm wavelength and a mobile phase of 60 % (v/v) Acetonitrile and 40 % (v/v) water. The experiment was considered invalid if Antipyrine concentration did not reach equilibrium in the two circulations within 2 to 3 hours of perfusion.

7.3.7 Integrity of the maternal-foetal barrier

Integrity of the barrier was confirmed before starting the study and throughout the perfusion by continuously measuring the volume loss for each time point and by checking the pH of the perfusates. Leak of the perfusion was checked before adding the reference and study compounds, samples were discarded if the leak was more than the used limit value of 3 ml/h. Leaks were also checked at each time point

throughout the perfusion. The pH of the perfusate was always ensured to be between 7.2 and 7.4.

7.3.8 Viability of the placental tissue; hCG

Maintenance of placental function was assessed by measuring the production of hCG from placental tissue of a perfused lobe and control lobe using ELISA. hCG ratio was calculated as previously described (Wick et al., 2010); hCG = [(concentration after perfusion – concentration before perfusion) ÷ concentration before perfusion] x 100.

7.3.9 Criteria for a successful perfusion; checkpoints thought perfusion

A strict set of criteria were applied to consider perfusions of samples successful (Karttunen et al., 2015; Wick et al., 2010) and certain checkpoints were maintained throughout perfusion (Figure 7.4). Samples were only included if the leak of perfusion was < 3 mL/hour, Antipyrine concentration reached equilibrium between the maternal and foetal side within 2-3 hours, and a foetal pH of between 7.2 and 7.4 at all times.

7.3.10 Accumulation of melanin nanoparticles in placental tissue

Accumulation of melanin nanoparticles in the perfused lobe was analysed by measuring the fluorescence signal of the homogenate tissue as previously described (Ali et al., 2021). In brief, biopsies (1 g) from different depths of perfused lobes were homogenized in PBS (pH 7.4) at a concentration of 25 % (w/v) and shaken vigorously. The content of the tube (200 µl) was transferred to a 96 well plate and concentration was determined by fluorescent quantification at Ex. 488 nm/ Em. 525 nm, against a standard calibration curve.

7.3.11 Statistical analysis

GraphPad Prism 8.0.2 (San Diego, California, USA) software was used for statistical analysis of the data. Data were compared using One-way Anova or t-test. Data are presented as mean ± SD, statistical significance was defined as $P < 0.05$.

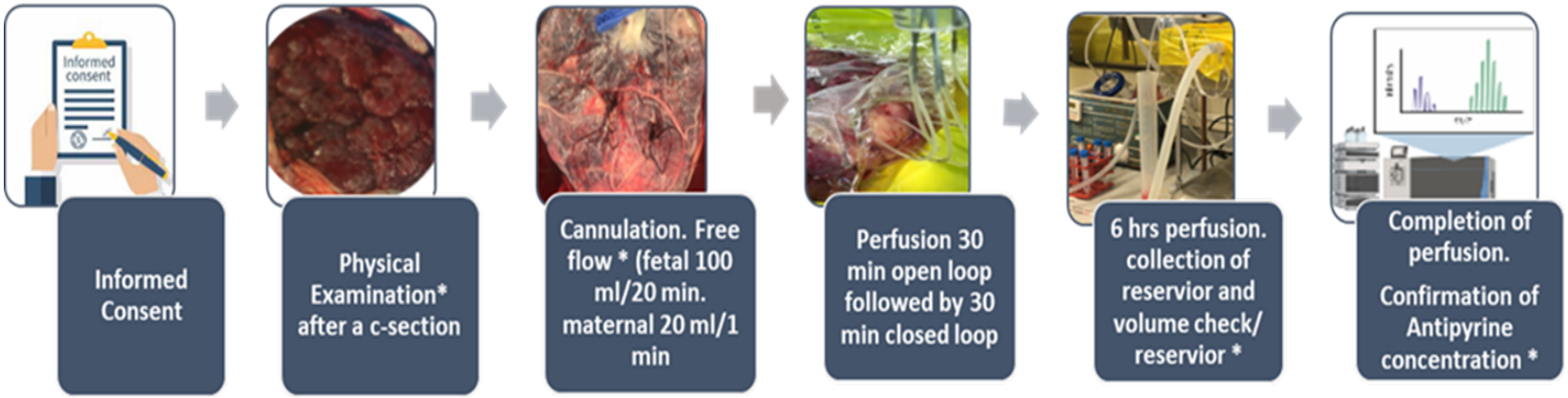


Figure 7.4 Workflow of the ex vivo placental perfusion and checkpoints to insure successful perfusions.

Stars represent checkpoints at each step to insure successful perfusion.

7.4 Results

7.4.1 Selection of successful perfusions

The *ex vivo* placental perfusion is considered a challenging procedure because placenta could be seriously damaged during delivery, and there is a risk of maternal-foetal leakage or blocked vessels (Karttunen et al., 2015). The success rate is between 30 % to 75 % depending on the reliability and strictness of the criteria used (Burton et al., 2014). The most common reported reason for failure is leaks or tears in tissue (Burton et al., 2014).

In this study, out of the 42 placental samples collected, only 34 placentae were selected for cannulation as no intact lobe was identified on the others. Which means the 8 placental samples failed to meet the first checkpoint. Out of the 34 cannulated placentae, 29 were able to meet the second checkpoint where circulation was successfully started. Perfusion was then performed for 30 minutes, at this stage 18 placentae were able to complete the perfusion for 6 hours as most placentae failed to meet the criteria; leak of less than 3 ml/h, maternal flow 20 ml/minutes, foetal flow 5 ml/minutes (Figure 7.5). The 18 samples that successfully met the criteria were included in the study.

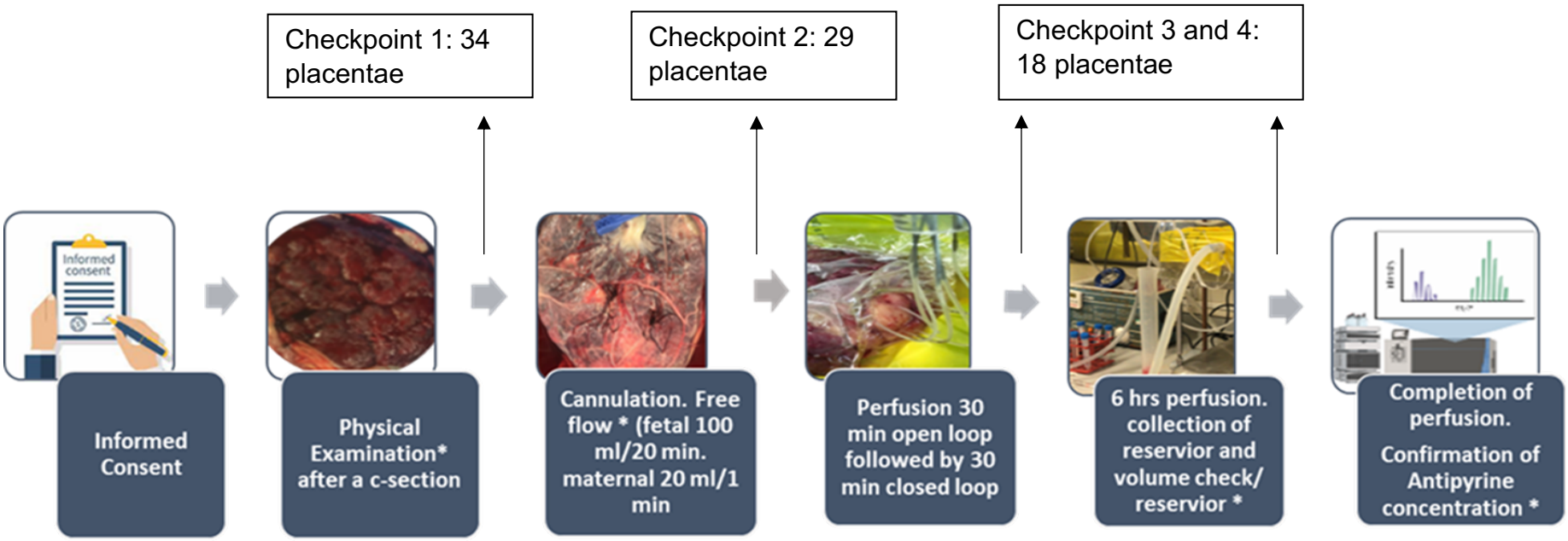


Figure 7.5 Selection of successful perfusions.

Stars represent checkpoints at each step to ensure successful perfusion; 18 out of 42 placentae were selected for the study.

7.4.2 Confirmation of successful perfusion

7.4.2.1 Permeability of the maternal-foetal barrier

Antipyrine is a small molecule that is known to easily cross the placenta in less than 3 hours. Antipyrine concentration in maternal and foetal perfusate was measured to ensure sufficient overlap between the two circulations which confirms the permeability of the maternal-foetal barrier (Karttunen et al., 2015; Myllynen et al., 2010; Wick et al., 2010). Data shows that the concentration of Antipyrine reached equilibrium within three hours of perfusion confirming a successful perfusion (Figure 7.6).

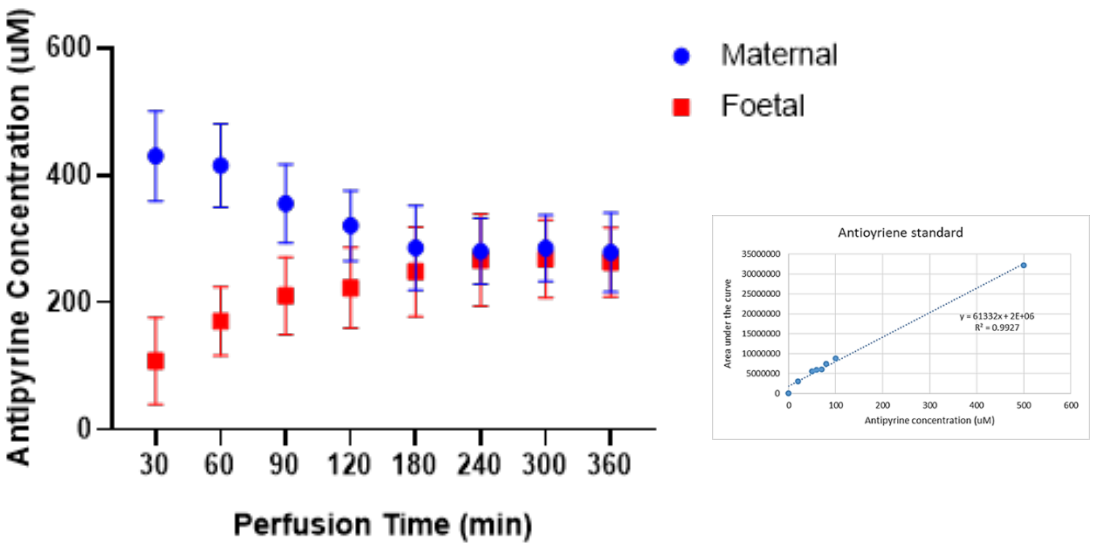


Figure 7.6 Permeability of the maternal-foetal barrier; measurement of Antipyrine concentration.

Graph shows the concentration of Antipyrine in maternal and foetal perfusate throughout 6 hours perfusion. Data represents mean ± SD, (n=6 per treatment).

7.4.2.2 Integrity of maternal- foetal barrier; volume loss

Leak of perfusate was checked throughout perfusion to ensure maintenance of barrier integrity (Karttunen et al., 2015). Samples included show volume loss of less than 3 ml/hr for 6 hours duration (Figure 7.7).

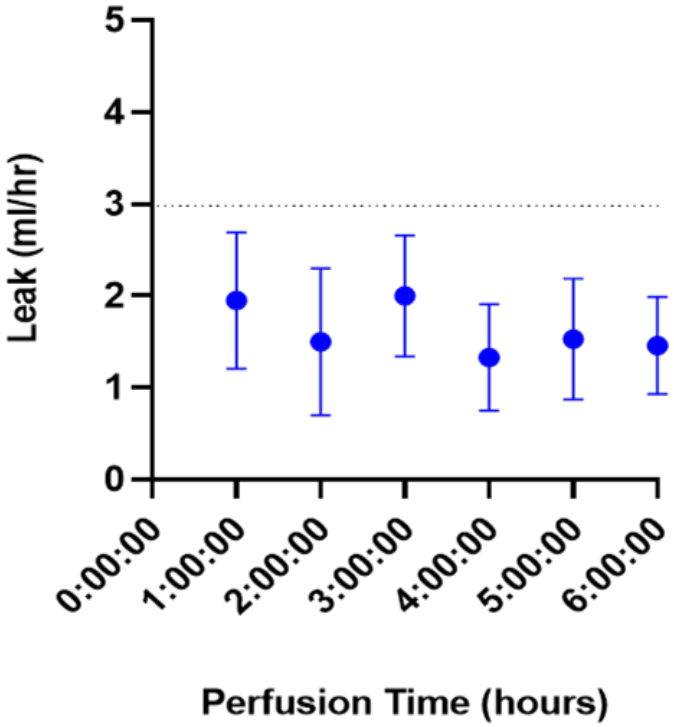


Figure 7.7 Integrity of the maternal-foetal barrier; measurement of volume loss throughout perfusion.

Graph shows the loss of volume before collecting reservoir at each time point throughout 6 hours perfusion. Data represents mean ± SD

7.4.3 Transport of melanin and polystyrene nanoparticles

Polystyrene nanoparticles (200 nm) were used to validate the method since it was found that a size of up to 240 nm could cross the maternal-foetal barrier in an *ex vivo* human placental perfusion (Wick et al., 2010). Results show that concentration of polystyrene nanoparticles was gradually decreased in the maternal perfusate, as soon as 60 minutes of administration. However, 200 nm MNP or MNP-PEG particles were not detected in the foetal circulation even after 6 hours of perfusion (Figure 7.8).

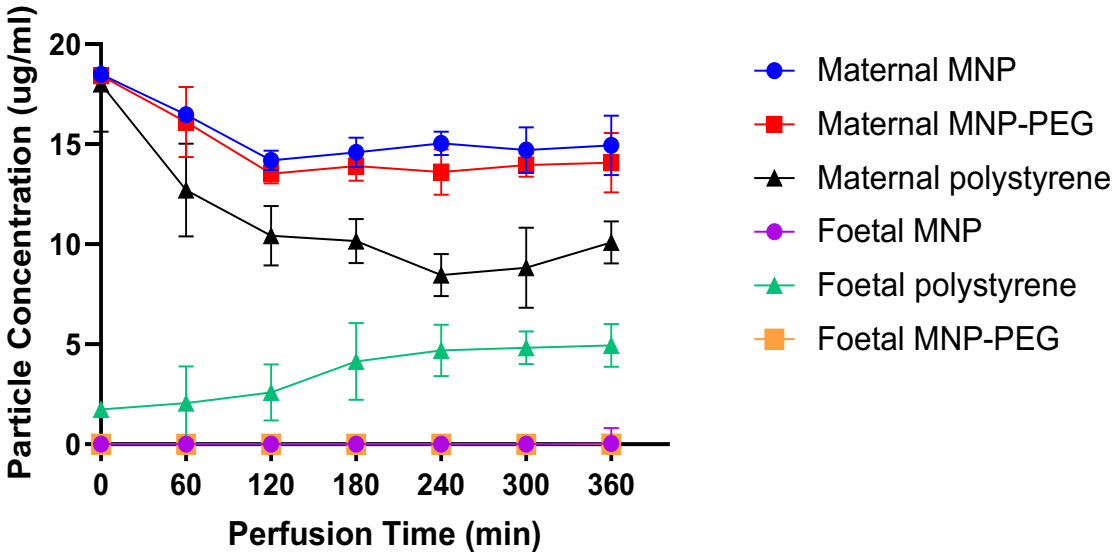


Figure 7.8 Trans-placental transport of melanin nanoparticles in an ex vivo human placental perfusion.

Graph shows concentration of 200 nm polystyrene, 200 nm MNP, and 200 nm MNP-PEG in maternal and foetal circulation. Data represents mean ± SD.

7.4.4 Viability of the placental tissue; hCG

Administration of polystyrene and melanin nanoparticles did not affect the viability of placental tissue in terms of the production of hCG as it was not altered after the administration (Figure 7.9). This also confirms the validity of the perfusion procedure.

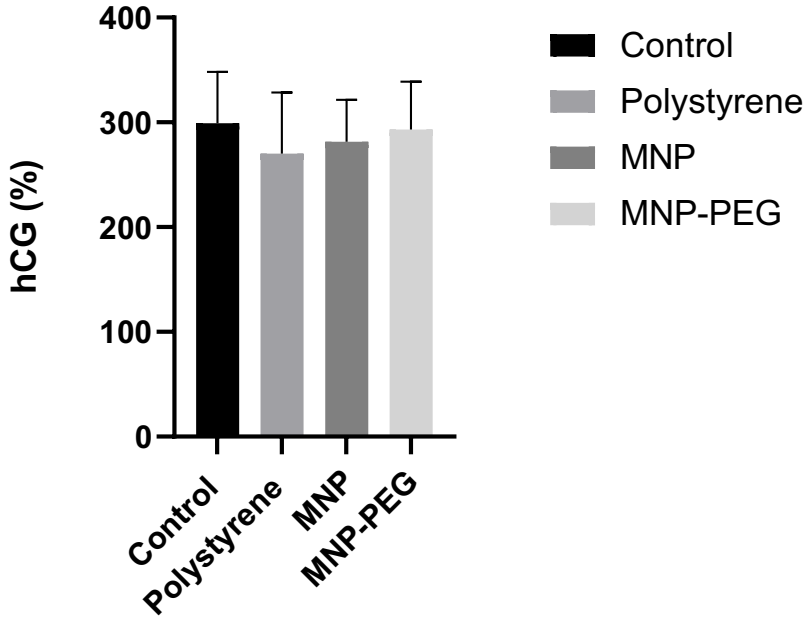


Figure 7.9 Viability of the placental tissue; hCG production.

Graph shows hCG production (%) after administration of polystyrene, MNP or MNP-PEG nanoparticles. Data represents mean ± SD (n=6). Data presented as hCG = [(concentration after perfusion – concentration before perfusion) ÷ concentration before perfusion] x 100.

7.4.5 Assessment of accumulation of melanin nanoparticles in the placental tissue

Biopsies were collected from the perfused lobe and homogenised to measure the fluorescent signal of the particles. No signals were detected in the collected tissues.

7.5 Discussion

This thesis aimed to determine whether melanin nanoparticles can be restricted from crossing the placenta and safely used to chelate iron during pregnancy. In this chapter, it was demonstrated that melanin nanoparticles of 200 nm and above did not cross the placenta after a duration of 6 hours *ex vivo* dual lobe human placental perfusion model (Figure 7.8). Experimental validity was determined by Antipyrine equilibrium (Figure 7.6) and low volume loss (Figure 7.7). The *ex vivo* placental model can only be performed on the third trimester placenta when the permeability of the barrier is possibly increased compared to early pregnancy (Kulvietis et al., 2011; Mori et al., 2007; van der Aa et al., 1998). Thus, this model can be considered as the worst case scenario of nanoparticle transport across the human placenta since it represents the most permeable stage of the placenta (Hutson et al., 2011), yet, 200 nm MNP were not detected in foetal circulation.

7.5.1 Validity, adequacy, and integrity of the perfusion

The energy charge of a placenta drops rapidly after delivery, but can be stabilized by cannulation and oxygenation (Burton et al., 2014). Therefore, the optimal conditions would be to process the placenta immediately after elective caesarean section delivery. Moreover, to ensure a proper experimental set up for a successful perfusion, adequacy and integrity of the barrier should be monitored during and after the experiment by monitoring the pH, oxygen levels, leakage, and adequate transfer of Antipyrine between maternal and foetal circulations. These parameters also normalize inter-placental variation (Burton et al., 2014; Hutson et al., 2011; Karttunen et al., 2015; Wick et al., 2010).

Antipyrine was used as a reference compound because it is a freely diffusible compound that does not bind to plasma proteins (Schneider et al., 1972). As Antipyrine crosses the placenta by passive diffusion, then, in theory, it's transfer is affected by the flow rate of the perfusion which has been set and confirmed. As a result, Antipyrine has easily crossed the placenta in all 6 samples and reached concentration equilibrium between maternal and foetal circulations within 3 to 4 hours as expected (Figure 7.6). In a comparative re-analysis of 126 *ex vivo* placental transfer of Antipyrine within and between laboratories Myllynen et al (2010) found that the maternal and foetal Antipyrine concentration were equal after 3 to 4 hours perfusion suggesting significant placental transfer (Myllynen et al., 2010). In other studies, equilibrium was within 2 to 3 hours (Karttunen et al., 2015; Wick et al., 2010). Since transfer of Antipyrine is not concentration dependent (Karttunen et al., 2015), this slight variation is probably due to ageing of the placenta which was found to reduce Antipyrine transfer (Karttunen et al., 2015), differences in the flow rate or variation of the surface area resulting from the suboptimal placing of the cannula.

A second parameter used to monitor the validity of perfusions was leak of perfusate for the integrity of the maternal foetal barrier. Significant volume loss (leak) during perfusion is an indication of a disintegrated barrier which is the most common reason for perfusion failure (Burton et al., 2014; Karttunen et al., 2015). It is agreed in the literature that a loss of between 2 and 4 ml/hour is typically accepted (Mathiesen et al., 2010). It was also reported that the negative marker FITC-dextran does not escape from foetal to maternal circulation if the leak is less than 3 ml/hour indicating the integrity of the barrier (Mathiesen et al., 2010). This finding supports the use of a leak of less than 3 ml/hour as an inclusion criteria for this study (Figure 7.7).

7.5.2 Transfer of nanoparticles across the placental barrier

Results from other groups using *ex vivo* human placenta suggested that size was an important factor of placental uptake, with most particles larger than 80 nm being excluded (King and Muller, 2016; Myllynen et al., 2008; Poulsen et al., 2015; Wick et al., 2010). Perfusion profiles obtained from particles smaller than 80 nm suggest that these small particles cross the barrier by diffusion. However, other characteristics of nanoparticles, such as the surface charge or chemical composition affect their interaction with the placental barrier. When polystyrene particles with diameter of 50, 80, 240 or 500 nm were applied to the *ex vivo* placental perfusion, particles with diameter up to 240 nm were able to cross the placental barrier, but the 500 nm particles were retained in the maternal circuit (Wick et al., 2010).

Surface modification is another factor that could affect particles interaction with the placental barrier. In a study of PEGylated gold particles with diameters of 10 and 30 nm, particles were not detected in foetal circulation after a 6 hours perfusion (Myllynen et al., 2008). In another study of PEGylated and carboxylated gold nanoparticles of 3 nm diameter, the PEGylated particles were able to cross the placenta but the carboxylated particles did not (Aengenheister et al., 2018a). In the current study, however, neither the 200 nm MNP or MNP-PEG was detected in foetal circulation after 6 hours (Figure 7.8). All these findings suggest that while the interaction of nanoparticles with the placenta is highly dependent on their size and/or their surface charge/chemistry, it is challenging to identify the contribution of an individual factor that affects this interaction.

7.5.3 Strength and limitations

The *ex vivo* human placental perfusion is the method of choice when evaluating the transfer of compounds across the human placenta and can predict the extent of placental transfer. The use of this model maintains the polarized nature of the placenta and represents the transfer process *in vivo* (Myllynen et al., 2010). Although it does not reflect the situation in early pregnancy (since only term placentas are perfused), term placentas are thinned and express fewer efflux transporters (Sun et al., 2006; Vähäkangas and Myllynen, 2006) which means that it may represent the highest exposure during gestation (Hutson et al., 2011). On the other hand, because of the complexity of the *ex vivo* perfusion system, many different criteria must be applied to ensure valid results. In this study, a set of critical inclusion criteria had been fulfilled (Figure 5.5). A limitation of this model is that it cannot fully represent the *in vivo* physiological conditions and overall pharmacokinetics including particle distribution, elimination, and protein binding, and their influence on particle transfer across the placenta.

Moreover, although no fluorescent signals of particle accumulation were detected in the homogenised tissue from the perfused lobe, a conclusion of MNP uptake cannot be driven from this finding, and a more robust method is needed to confirm particle uptake in the placental tissue which should be considered in future studies. Nonetheless, it was previously claimed that ambient black carbon particles accumulated in the foetal side of the human placenta after maternal exposure during pregnancy (Bové et al., 2019). However, it appears from the images that most particles were trapped in the syncytiotrophoblast layer which means it remained in the maternal side and did not reach the foetal side of the human placenta (Holder et al., 2021). Thus, understanding the biology and terminology of the foetal maternal

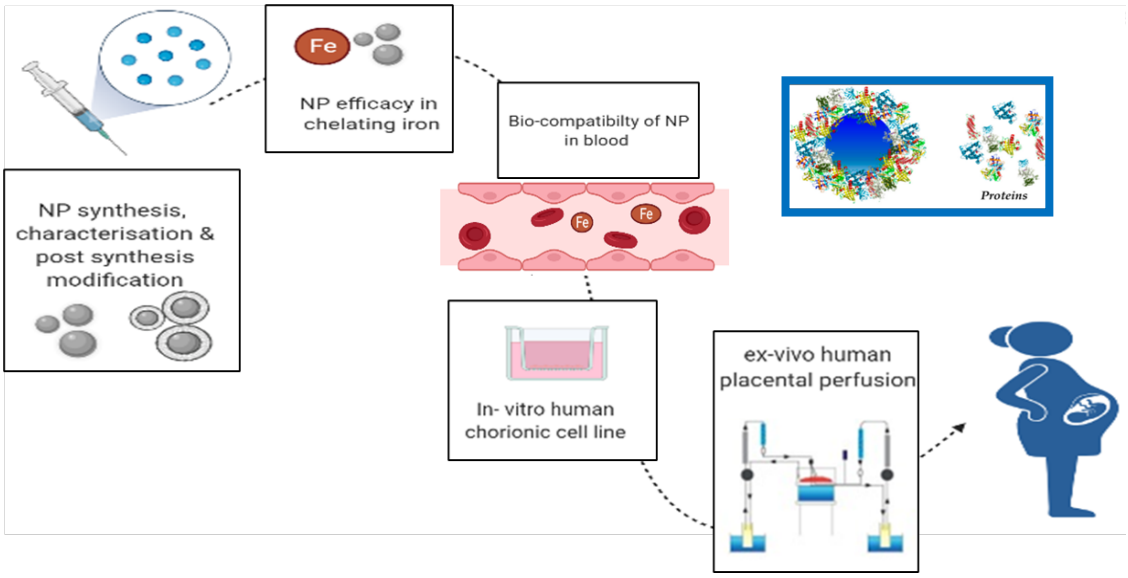
barrier then investigating the effect/toxicity of particles localization within this barrier on embryogenesis is far more important.

7.6 Conclusion

Together the findings of melanin nanoparticles transport across the perfused human placenta *ex vivo* and the *in vitro* transwell model using a BeWo cell barrier indicate the potential for particle restriction from movement across the placenta. In both models, 200 nm MNP-PEG was not detected in foetal circulation. The *in vitro* transwell experiments using a BeWo cell barrier shows high relevance to the data collected from the *ex vivo* experiments. Although data from the two models are similar, they are not identical due to technical differences between the two models including flow pattern, exposure time, and layers of the tissue separating the maternal and foetal circulations. BeWo cells only represent the trophoblastic layer while the *ex vivo* dual lobe placental perfusion contains the syncytiotrophoblast cell layer, connective tissue, and the foetal endothelium, which explains such differences. Both models, however, are considered as a valid tool to predict foetal exposure to harmful substance.

Although data derived from these models provides relevant information of placental exposure to melanin nanoparticles, for more complete information *in vivo* experiments would be more sophisticated and increasingly necessary for drug distribution and toxicity throughout the body before routine application in clinics.

Chapter 8. Investigating protein binding to melanin nanoparticles; formation of protein corona



8.1 Abstract

Background: It is known that when nanoparticles are introduced to the biological environment, due to their high surface energy, they adsorb protein to their surface forming a protein corona which can alter the nanoparticle identity and overall fate in the biological system. Size and composition of nanoparticle corona is determined by the particle characteristics as well as the protein profile of the surrounding environment.

Objectives: The aim of this chapter was to identify the extent and composition of the protein corona on both melanin and polystyrene nanoparticles from three different groups.

Methods: The nanoparticles were incubated with serum from healthy non-pregnant women (n=6), pregnant women (n=6), and women with beta thalassemia (n=4), and was assessed using SDS-PAGE and proteomics analysis.

Results: It was shown that the amount of protein adsorbed by the 50 nm particles was greater than the amount of protein adsorbed by either 200 nm or 500 nm particles. Proteomics analysis of the protein corona on the MNPs identified 43 significantly different proteins between the three serum groups. No proteins were identified as being significantly different between PEGylated and non-PEGylated particles.

Conclusion: Results may provide better understanding of particle behaviour *in vivo*. Further validation and further investigation are needed to provide deeper insights into therapeutic development.

8.2 Introduction

8.2.1 Overview

In chapter 7, an *ex vivo* human placental perfusion model was used to study the transfer of melanin nanoparticles across the placenta. However, transfer results from the e*x vivo* experiment could be over or underestimated simply because it does not fully represent overall physiological conditions *in vivo*. Although protein binding is not the most significant factor when the transfer of the particles is limited (as by the *ex vivo* results of melanin nanoparticles transfer), investigating protein binding to MNPs during pregnancy will help to understand their behaviour *in vivo* for safe and efficient applications.

8.2.2 Personalized (disease specific) corona

Disease state has a significant impact on the plasma environment and proteome profile. Thus, the concentration and conformation of plasma proteins can serve as biomarkers for specific disorders. This effect of disease status was studied on protein corona formation with various diseases and biological environments (Corbo et al., 2017; Hajipour et al., 2014; Hajipour et al., 2015). The term “personalized corona” was introduced by Hajipour et al (2014) based on their finding that synthetic polystyrene and silica nanoparticles incubated with human serum from different diseases and medical conditions (Figure 8.1) resulted in altered corona compositions (Hajipour et al., 2014). Therefore, it is important to track corona formation on different individuals for better understanding of their behaviour *in vivo*.

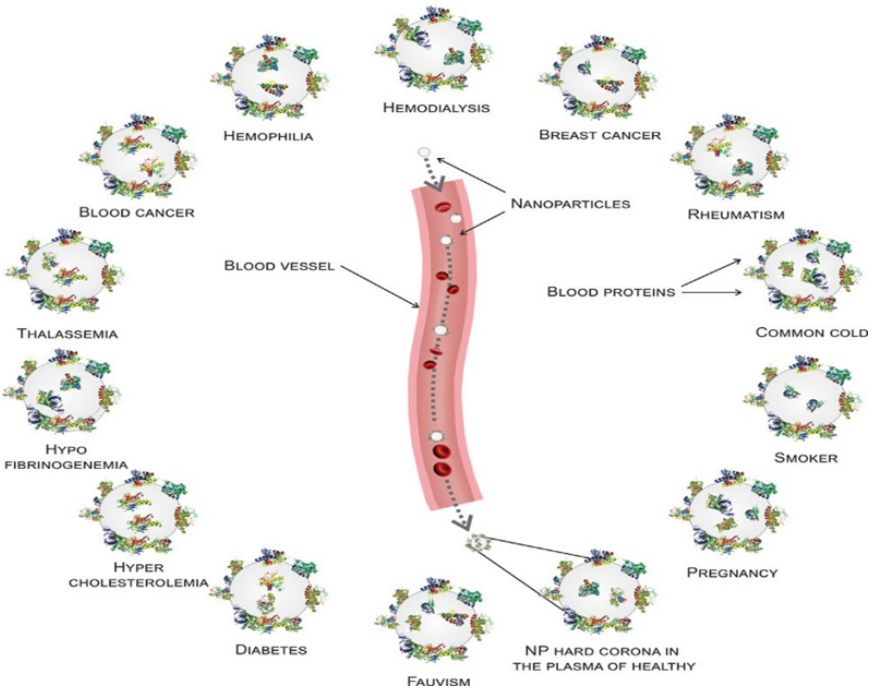


Figure 8.1 Schematic representation of personalized corona depending on serum profile of different conditions. (Hajipour et al., 2014)

8.2.3 Protein binding and drug transfer across the placenta

The two major plasma proteins responsible for binding to a majority of exogenously administered compounds are albumin and α1-acid glycoprotein (AAG) (Bteich, 2019). During pregnancy, the concentration of plasma proteins is altered compared to non-pregnant individuals and the concentration of these two proteins is also different between maternal and foetal plasma (Krauer et al., 1984; Zhao et al., 2021). This alteration can affect drug binding activity in the maternal circulation that may lead to an increase in the accumulation of drugs in foetal circulation (Nau et al., 1984).

The *ex vivo* human placental perfusion model occasionally been found to underestimate the foetal exposure to drugs that binds to albumin (e.g., oxcarbazepine, diazepam, valproic acid, or propylthiouracil) and to overestimate foetal exposure of drugs that binds to AGG (e.g., anaesthetics and propranolol)

compared to *in vivo* results (Hutson et al., 2011). The underlying mechanisms of these findings are not known. However, these data may suggest that protein binding to drugs can significantly impact their transfer across the placental barrier if the drug is actively transported. On the other hand, protein binding showed no significant contribution when the drug transfer across the placenta is limited. An *ex vivo* perfusion model was able to show limited transfer of these molecules with results closely reflecting the *in vivo* situation (Hutson et al., 2011).

8.2.4 Aims

The aims of this chapter were to identify the degree and composition of the protein corona after incubation with serum from three different groups: healthy non-pregnant women, healthy pregnant women, and women with beta thalassemia. Sodium dodecyl-sulfate polyacrylamide gel electrophoresis (SDS-PAGE) was performed, followed by a deep proteomic analysis and gene ontology analysis of identified clusters.

8.3 Materials and methods

8.3.1 Sample processing

Blood samples were collected after informed consent from healthy women, healthy pregnant women, and women with beta thalassemia (section 2.2). Samples were centrifuged at 2500 g for 5 min at 4 °C. The collected plasma was then diluted and incubated with 100 µL of 1 mM particle suspension (50 nm, 200 nm, or 500 nm MNP, MNP-PEG or polystyrene) for 1 hour at 37 °C. The samples were then centrifuged at 18,000 g for 30 minutes to obtain a pellet of 'Particle-Corona' complex. The pellet was then washed twice with 1 mL PBS and resuspended in 30 µl of 1 % (w/v) SDS for 1 hour to remove the adsorbed protein from the particle surfaces. The pellet was then centrifuged for 30 minutes at 30,000 g and the supernatant containing the proteins was collected for SDS-PAGE, zeta potential and proteomic analysis (Figure 8.2).

8.3.2 SDS-PAGE

Supernatant containing protein (100 µl) was collected and added to a mix containing sample buffer and reducing agent (Invitrogen) and heated for 5 minutes at 95 °C. SDS-PAGE gels were run at 200 V until the dye front reached the bottom, and then stained with Coomassie blue for 1 hour. The gel was then de-stained with a mixture of 5 % (v/v) methanol, 7.5 % (v/v) Acetic acid, and 87.5 % (v/v) H_2O.

8.3.3 Zeta potential

The zeta potential of the particles was measured before and after corona complex formation as previously described in chapter 3.

8.3.4 Proteomics analysis

Only 200 nm MNP, MNP-PEG and polystyrene (based on the *ex vivo* experiment) were used for the proteomic analysis.

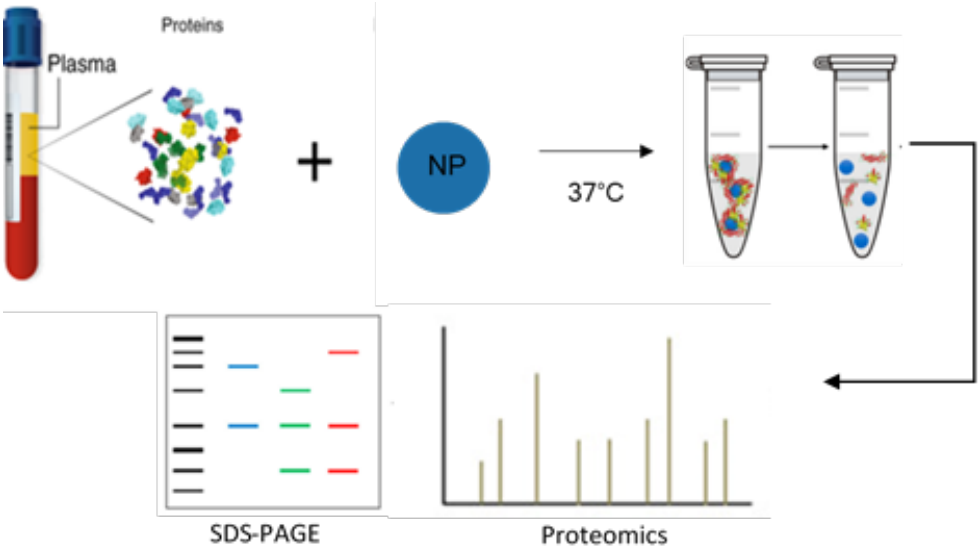


Figure 8.2 Graphical abstract for methods used in this chapter.

8.3.4.1 Sample protein digestion

Digestion was performed by technicians at the Oxford Target Discovery Institute using Suspension Traps (S-TRAP) micro columns digestion protocol (Protifi, Farmingdale, NY). Sample buffer was adjusted to a final concentration of 5 % SDS followed by a reduction/alkylation with 10 mM Tris Carboxy Ethyl Phosphene (TCEP)/ 50 mM Iodoacetamid (IAA) and were dissolved in a final concentration of 1.2 % phosphoric acid. Samples were then diluted (1:7) with 90 % MeOH and 100 mM Triethylammonium bicarbonate buffer (TEAB), loaded on a spin filter and centrifuged at 4000 x g and washed (4x) with 150 µl of 90 % MeOH before they were transferred to fresh 1.5 ml Eppendorf tubes for trypsin digestion (5 µg trypsin in 50 mM TEAB) at 37°C overnight. Then, samples were washed twice with 100 µl

of 0.1% Trifluoroacetic acid (TFA) and 100 of µl 50 % acetonitrile/ 0.1 % TFA and speedvac to dryness. Finally, samples were resuspended in 21 µl of 5 % DMSO and 5 % formic acid before loading for mass spectrometry (MS) analysis (injection volume = 1 µl).

8.3.4.2 Mass Spectrometry data-independent acquisition (DIA)

MS analysis was performed by the Target Discovery Institute MS laboratory led by Dr Roman Fischer (TDI, University of Oxford, UK). Peptides were resuspended in 5 % formic acid and 5 % DMSO and then trapped on an Acclaim PepMap 100 C18 HPLC Columns (300 µm x 5 mm, 5 µm particle size, Thermo Fisher Scientific) using solvent A (0.1 % Formic Acid in water) at a pressure of 60 bar and separated on an Ultimate 3000 UHPLC system (Thermo Fischer Scientific) coupled to a QExactive mass spectrometer (Thermo Fisher Scientific). The peptides were separated on an Easy Spray PepMap RSLC column (75 µm i.d. x 2 µm x 50 mm, 100 Å, Thermo Fisher) and then electro-sprayed directly into an QExactive mass spectrometer (Thermo Fisher Scientific) through an EASY-Spray nano-electrospray ion source (Thermo Fisher Scientific) using a linear gradient (length: 60 minutes, 5 % to 35 % solvent B (0.1 % formic acid in acetonitrile and 5 % dimethyl sulfoxide) at a flow rate of 250 nL/min. Raw data was acquired in the MS in a DIA mode. Full scan MS spectra were acquired in the Orbitrap Fusion Lumos and peaks were selected for Higher-energy C-trap dissociation (HCD) fragmentation at 28% of normalized collision energy (NCE) / stepped NCE. HCD spectra were also acquired in the Orbitrap (resolution 17500, AGC target 1e6, isolation window 20 m/z).

8.3.4.3 Proteomics data availability (data search)

Data search was performed by technicians at TDI Oxford. The data base used to identify proteins and peptides was UPR_Homo_sapiens _9606_ UP000005640_ 20200803.fasta. Settings were as follows: library-free search, deep learning-based spectra, Retention time prediction, maximum number of protease (trypsin) missed cleavages set to 1, PTMs: Carbamidomethyl (C), Oxidation (M). Data output were filtered by applying a 1 % False Discovery Rate (FDR) and Match Between Runs (MBR) was used. Data was handed over at this point and system biology analysis was then applied.

8.3.4.4 System biology analyses

Perseus version (2.0.6.0) (Max Planck Institute of Biochemistry, Germany) was used for quantitative analysis (Tyanova et al., 2016). The data were transformed (log2x), normalized, and proteins were then filtered such that they were detected in at least 70% of the replicate experiments ($n = 6$) and missing values were imputed from a normal distribution (width = 0.3 and shift = 1.8) in the total matrix mode based on the assumption that these proteins were below the detection limit. Enriched proteins were identified by either a t-test (volcano plots), or a one-way ANOVA-based multiple sample test with the number of randomizations set to 250 and the permutation-based FDR accepted equal or below 0.05 with technical replicates grouped for randomization (FDR-corrected p-value < 0.05 were considered statistically significant). Data was then filtered based on ANOVA significance to produce the heat maps. Subsequent Tukey's *post hoc* analysis with an accepted FDR value equal or below 0.05 was performed on all ANOVA significant results to identify and determine fold change differences in significant ($p < 0.05$) proteins across conditions.

8.3.4.5 Enriched ontology clustering

Functional annotations, including gene ontology (GO) enrichment among cluster enriched, differential genes, was computed and retrieved with the following ontology sources: GO biological processes and GO cellular component using Metascape (http://www.metascape.org) (Zhou et al., 2019), (http://geneontology.org) and (http://www.string-db.org). Significant terms (differences between the groups) were hierarchically clustered into a tree network with a similarity > 0.3 are connected by edges (the thickness of the edge represents the similarity score). Each term was represented by a circle node, the size of the node is proportional to the number of input genes that fell into that term and the colour represents its cluster. The network was visualised using Cytoscape (v3.1.2) (Cline et al., 2007). Functional protein association networks of identified proteins were created using STRING.

8.3.5 Statistical analysis

Zeta potential data analysis was performed using GraphPad Prism 8.0.2 (San Diego, California, USA) software. Data are presented as mean ± SD, statistical significance was defined as $P < 0.05$. Proteomics data analysis was performed as described in the methods section. FDR-corrected p-value < 0.05 were considered statistically significant. Data were compared using One-way Anova or t-test unless otherwise stated.

8.4 Results

8.4.1 Determination of protein corona formation using SDS-PAGE

SDS-PAGE shows fewer protein bands adsorbed onto the surface of the melanin nanoparticles compared to the surface of the polystyrene nanoparticles of the same particle size. Moreover, 50 nm MNPs adsorbed a wider variety of protein sizes than the larger particles 200 and 500 nm, but this was decreased with PEGylation. The composition of the protein corona found on the polystyrene particles was different among the three different patient groups, while almost similar protein sizes (40-55 kDa) were adsorbed onto the MNP and MNP-PEG irrespective of which patient group serum was used (Figure 8.3).

8.4.2 Zeta potential before and after particle incubation

When comparing the zeta potential before and after protein corona formation, a significant decrease in zeta potential was seen for the polystyrene-corona complex compared to before incubation with serum. However, no significant difference in zeta potential was found between MNP or MNP-PEG corona complexes compared to before incubation (Figure 8.4).

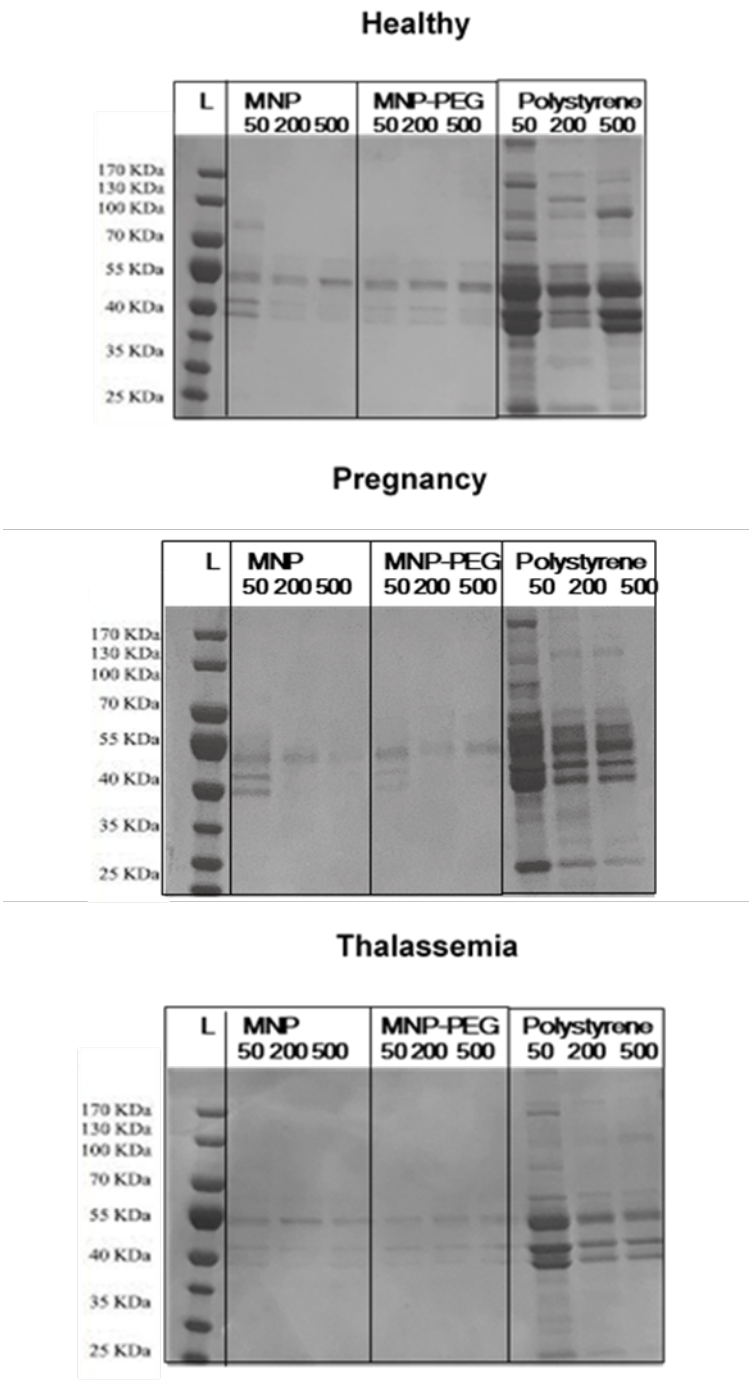


Figure 8.3 Formation of Protein corona; SDS-PAGE.

SDS-PAGE showing protein corona after incubation in serum from healthy, pregnant, or thalassemia women. Particles were 50 nm, 200 nm, or 500 nm, and either MNP, MNP-PEG, or Polystyrene. L = protein marker ladder. Data are representative of at least six different experiments on healthy and pregnant women, and four different experiments on thalassemia women.

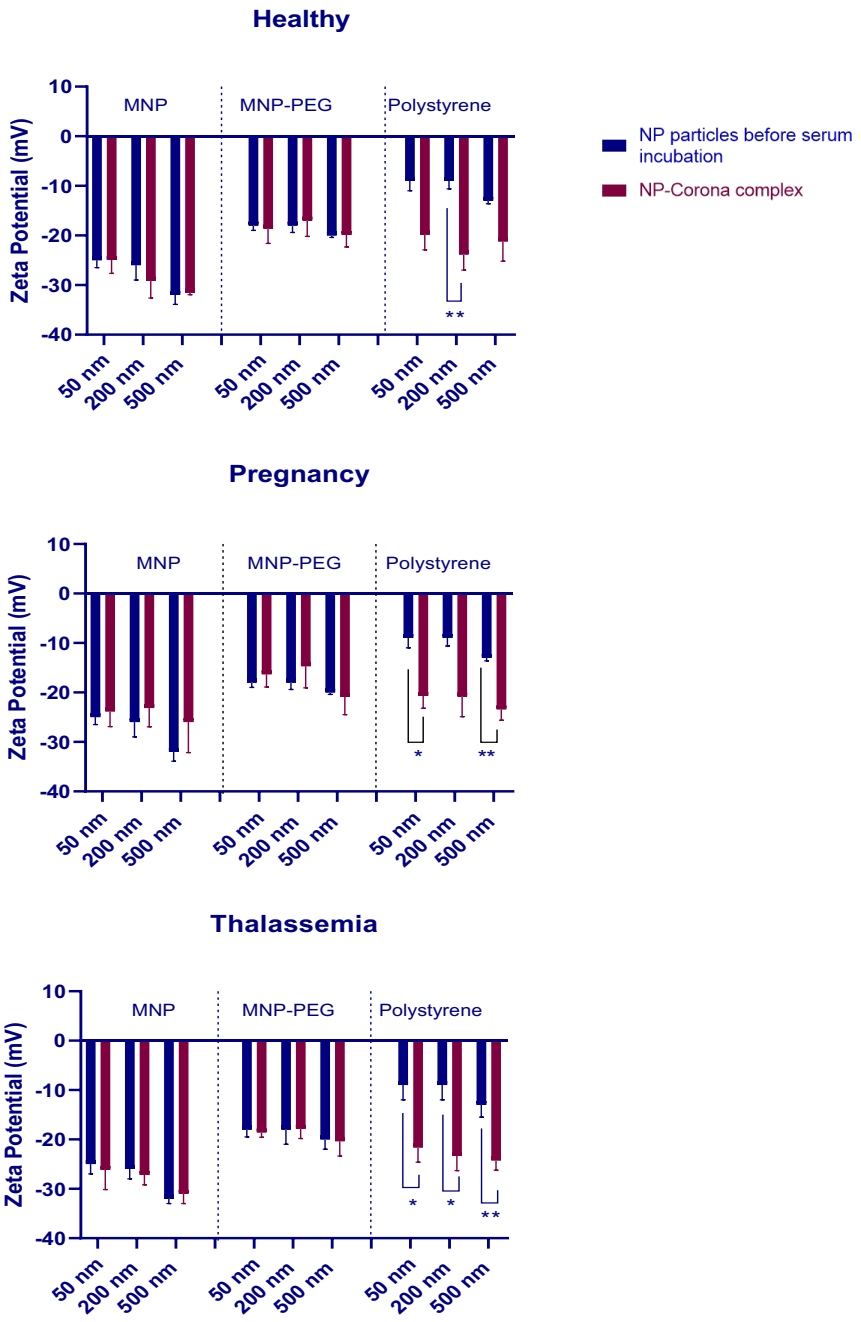


Figure 8.4 Zeta potential before and after corona formation.

*Graphs showing zeta potential before and after incubation in serum from healthy, pregnant, or thalassemia women. Particles were 50 nm, 200 nm, or 500 nm, and either MNP, MNP-PEG, or Polystyrene. Data are representative of at least six different experiments on healthy and pregnant women, and four different experiments on thalassemia women. Data shows mean ± SD. *p≤ 0.05; **p ≤ 0.01.*

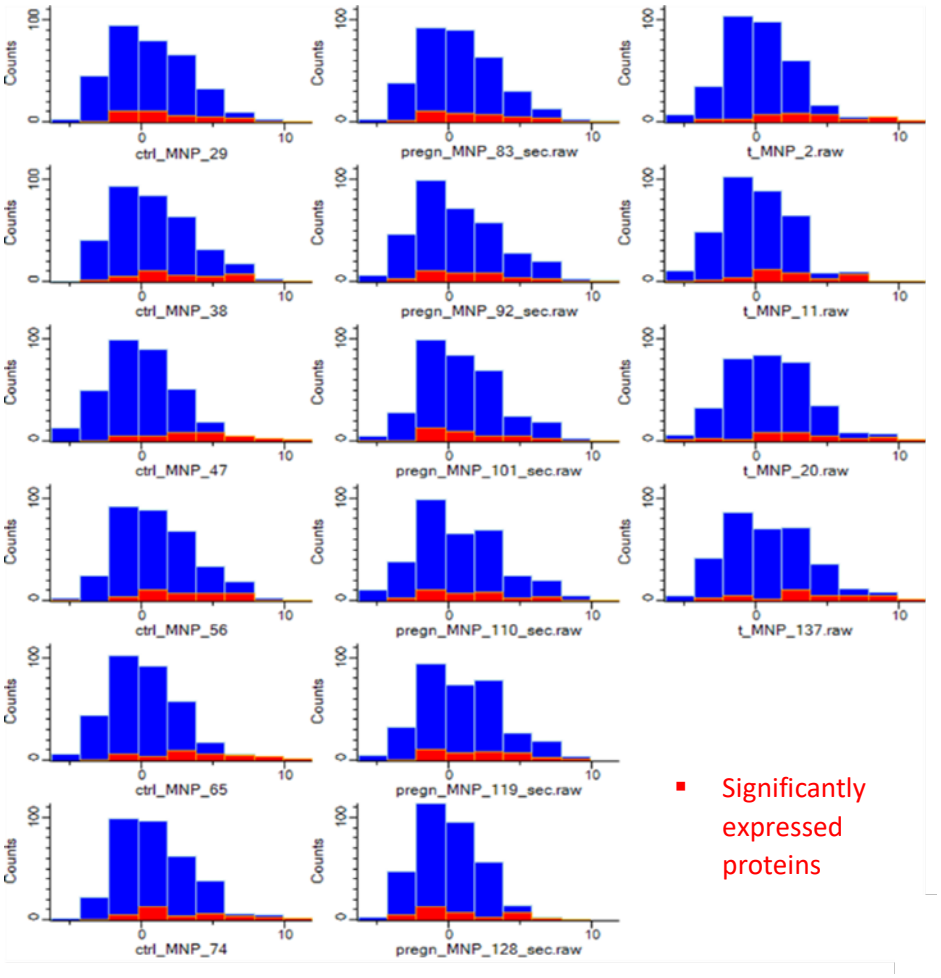
8.4.3 Proteomics analysis

8.4.3.1 Significant differences in MNP protein corona composition were seen with serum from the 3 different groups.

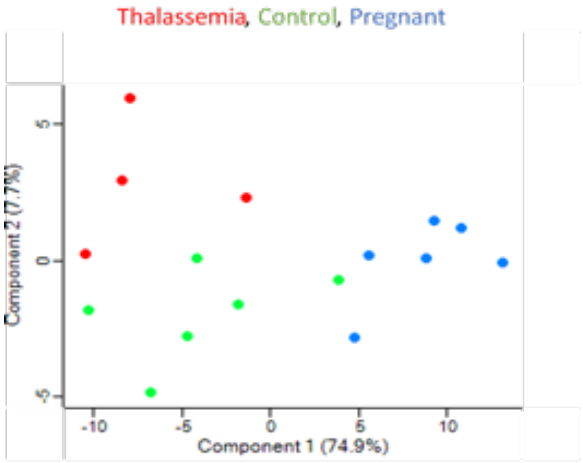
After normalization, missing values were imputed from a normal distribution based on the assumption that these proteins were below the detection limit. Figure 1 (appendix III) shows that missing data are low expression proteins.

Proteomic comparison of MNP corona identified 43 significantly enriched proteins attached to the particle surface according to the serum type (Figure 8.5 A and appendix III). The principal component analysis (PCA) plot indicated clear differences in the proteomics profile between the groups; and the thalassemia group was more closely clustered with the control group on the PC1 axis (Figure 8.5 B). The heatmap (Z-score) of the 43 significantly different proteins was then created with FDR <0.05 between the three groups and shows clear hierarchical clustering of the proteins attached to the MNP surface during pregnancy. After exclusion of keratin contamination, 7 downregulated proteins were identified in the pregnant group compared to the control and thalassemia groups, 8 upregulated proteins compared to the thalassemia group, and 4 upregulated proteins compared to the control group (Figure 8.5 C). The analysis of gene ontology using STRING revealed the top enriched cellular component to be melanosome, tertiary granule, collagen containing extracellular matrix, extracellular exosome, and extracellular space (Figure 8.6). The analysis of gene ontology using Metascape revealed the top enriched pathways being positive regulation of protein binding (log10(p) -5.91), and SARS -CoV-2-host interaction (log10(p) -4.79), (Figure 8.7).

A


Counts
ctrl_MNP_29
pregn_MNP_83_sec.raw
t_MNP_2.raw
ctrl_MNP_38
pregn_MNP_92_sec.raw
t_MNP_11.raw
ctrl_MNP_47
pregn_MNP_101_sec.raw
t_MNP_20.raw
ctrl_MNP_56
pregn_MNP_110_sec.raw
t_MNP_137.raw
ctrl_MNP_65
pregn_MNP_119_sec.raw
ctrl_MNP_74
pregn_MNP_128_sec.raw
Significantly expressed proteins

B


Thalassemia, Control, Pregnant
Component 2 (7.7%)
Component 1 (74.9%)

C

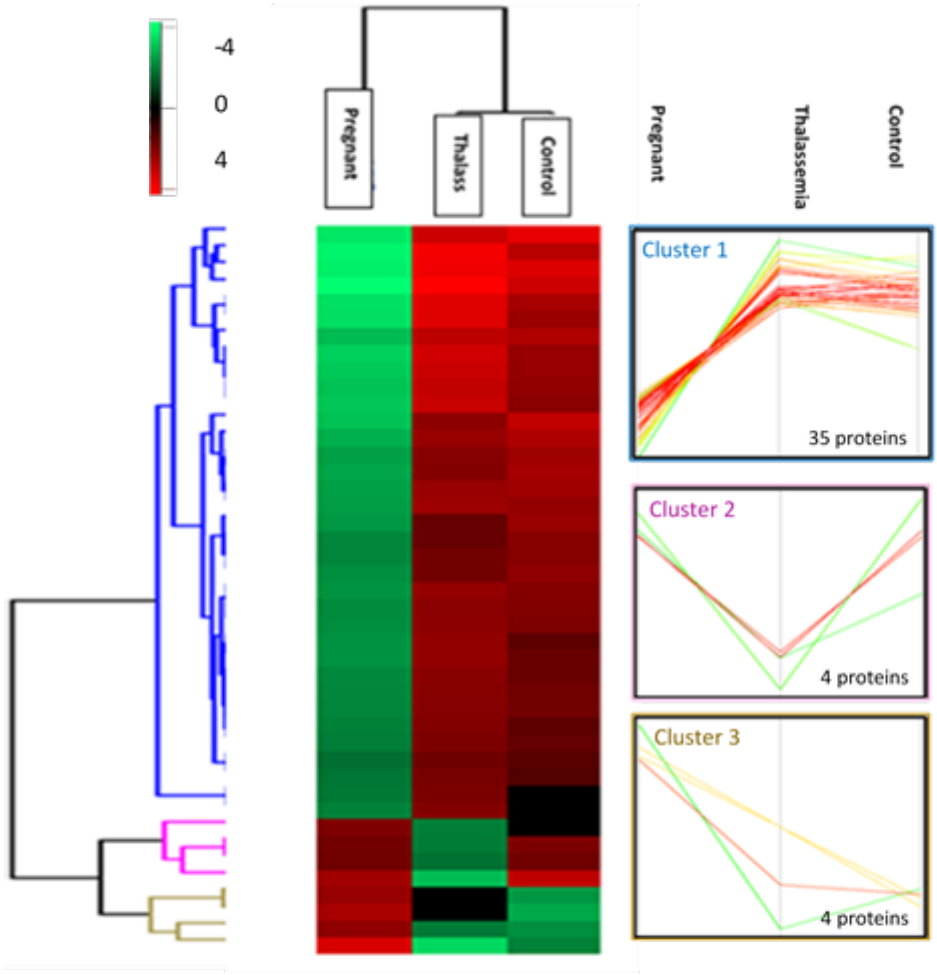
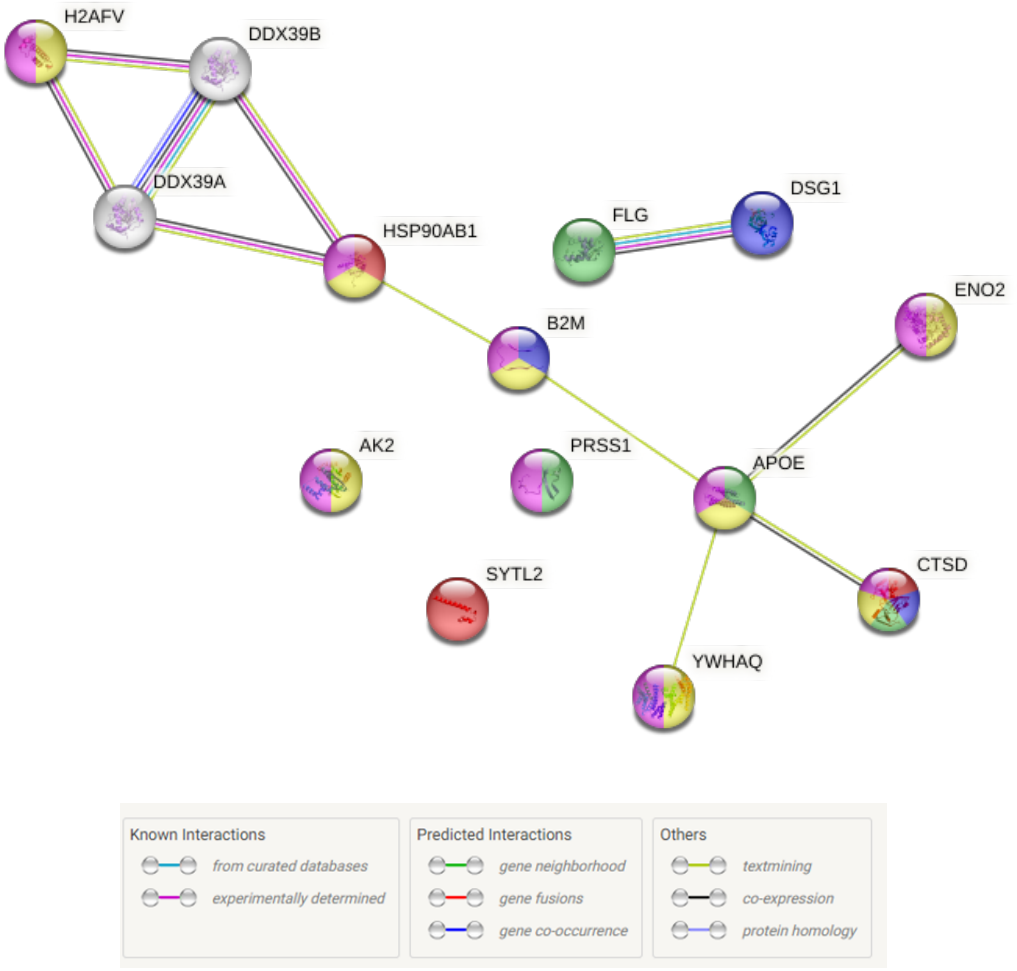


Figure 8.5 The effect of plasma alterations mediated by different groups; healthy, pregnant and thalassemia on the corona composition formed attached on the surface of MNPs.

(A) Histograms show significantly different proteins attached to MNPs surface on each group that passed a one-way ANOVA-based multiple-sample test for statistically significant enrichment (FDR ≤ 0.05), (red indicates high and green indicates low expression) (B) PCA plot shows clear proteomic profile differences between the 3 groups (FDR ≤ 0.05), (C) Heat map representation (Z-scores) of proteins that passed a one-way ANOVA-based multiple-sample test for statistically significant enrichment (FDR ≤ 0.05) followed by post hoc Tukey's test (FDR ≤ 0.05) to filter for significant enrichment proteins across conditions (healthy n=6, pregnancy n=6, thalassemia n=4).



	GO-term	description	Count in network	Strength	FDR
	GO:0042470	Melanosome	3 of 104	1.61	0.0498
	GO:0070820	Tertiary granule	3 of 164	1.41	0.0498
	GO:0062023	Collagen containing extracellular matrix	4 of 396	1.15	0.0498
	GO:0070062	Extracellular exosome	8 of 2099	0.73	0.0498
	GO:0005615	Extracellular space	9 of 3195	0.6	0.0498

Figure 8.7 Gene ontology cellular component enrichment analysis of MNP corona.

String™ interactive pathway analysis of proteins (n=14) with top rank GO cellular component pathways.

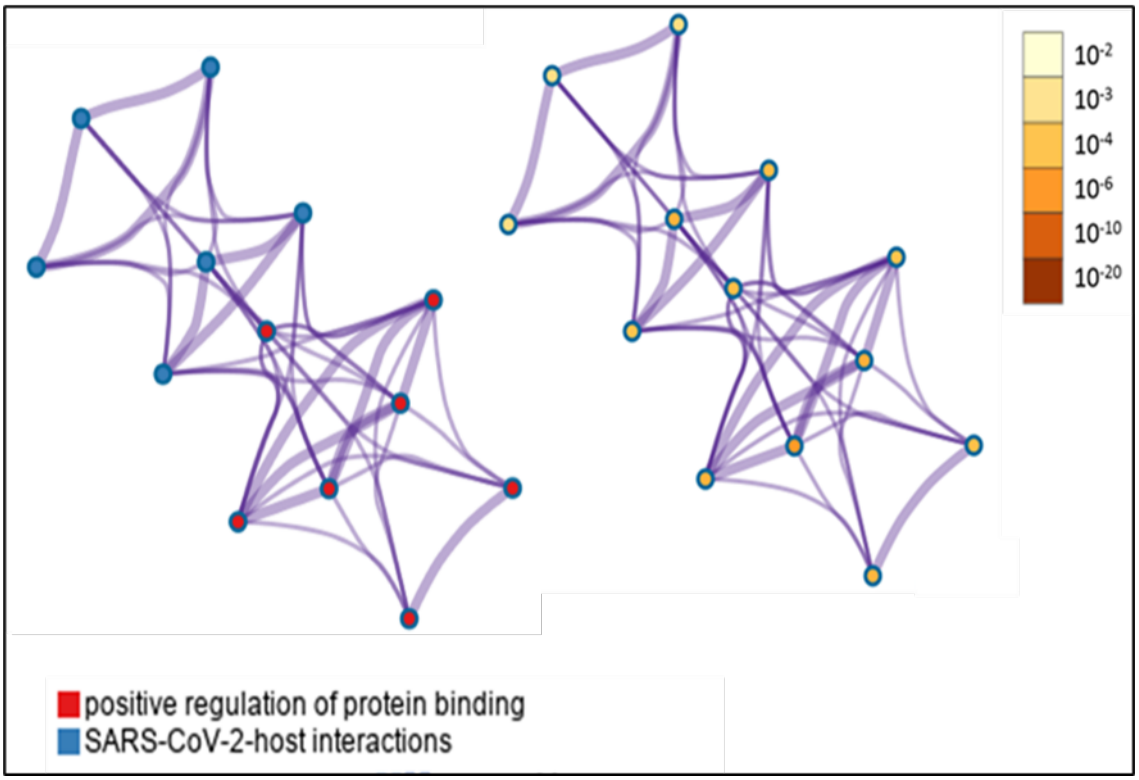


Figure 8.7 Gene ontology pathway and process enrichment analysis of MNP corona.

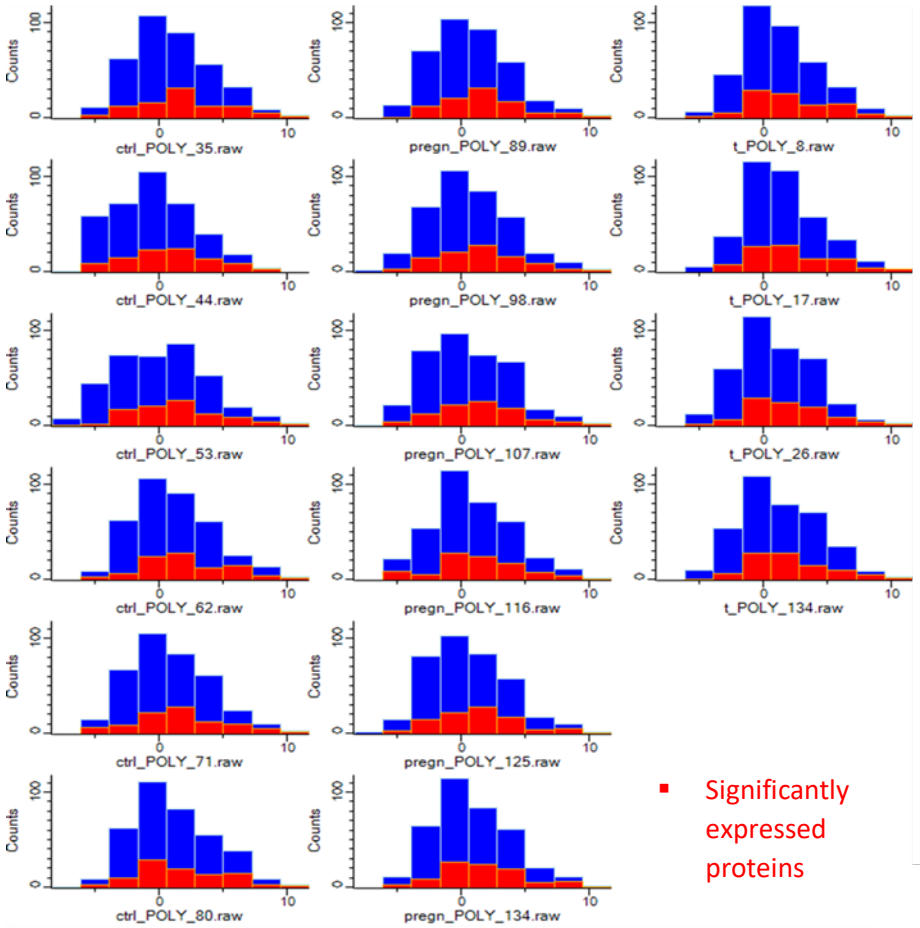
Significant and enriched terms hierarchically clustered into a tree network based on Kappa-statistical similarities among their gene memberships. The 0.3 kappa score was applied as the threshold to cast the tree into term clusters. Each term was represented by a circle node, the size of the node is proportional to number of input genes fell into that term and the colour represents its cluster. The network was visualised using Cytoscape (v3.1.2).

8.4.3.2 Significant differences in the composition of protein corona formed on the surface of polystyrene particles

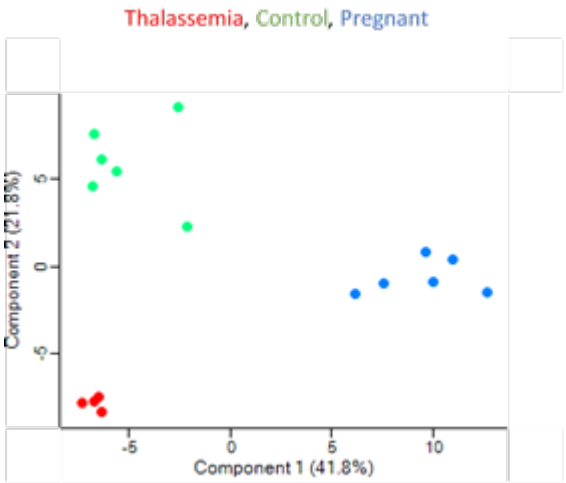
After normalization, missing values were imputed from a normal distribution based on the assumption that these proteins were below the detection limit. Figure 1 (appendix IV) shows that missing data are low expression proteins.

Proteomic comparison of the corona on polystyrene NPs identified 100 significantly enriched proteins attached to the particle surface according to the serum type (Figure 8.8 A and appendix IV). The PCA plot indicated a very clear proteomics profile separation between the groups; with the thalassemia group more closely clustered with the control group on the PC1 axis (Figure 8.8 B). A heatmap (Z-score) of the 100 significantly different proteins was then created with FDR <0.05 between the three groups and showed clear hierarchical clustering of the proteins attached to the polystyrene surface during pregnancy; 34 upregulated proteins and 66 downregulated proteins compared to the other groups (Figure 8.8 C). The analysis of gene ontology revealed the top 7 enriched pathways being the following: immune system process (log10(p) -5.71), adaptive immune response (log10(p) -40.75), complement activation (log10(p) -28.49), haemostasis (log10(p) -11.44), complement and coagulation (log10(p) -10.79), plasma lipoproteins particle clearance (log10(p) -10.62) and platelets degranulation (log10(p) -10.49) (Figure 8.8 C and Figure 8.9).

A


Counts
ctrl_POLY_35.raw
pregn_POLY_89.raw
t_POLY_8.raw
ctrl_POLY_44.raw
pregn_POLY_98.raw
t_POLY_17.raw
ctrl_POLY_53.raw
pregn_POLY_107.raw
t_POLY_26.raw
ctrl_POLY_62.raw
pregn_POLY_116.raw
t_POLY_134.raw
ctrl_POLY_71.raw
pregn_POLY_125.raw
ctrl_POLY_80.raw
pregn_POLY_134.raw
Significantly expressed proteins

B


Thalassemia, Control, Pregnant
Component 2 (21.8%)
Component 1 (41.8%)

C

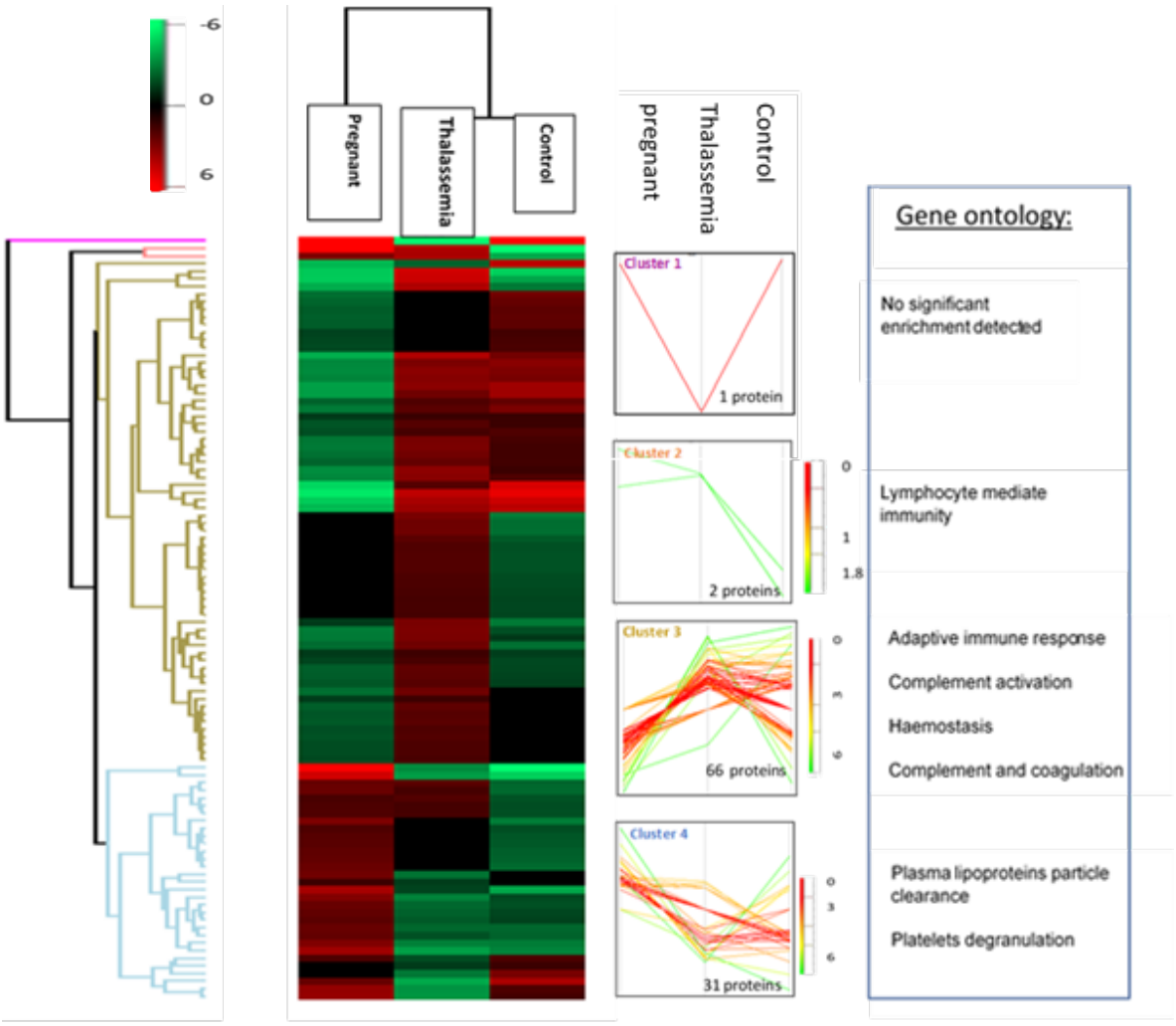


Figure 8.8. The effect of plasma alterations mediated by different groups; healthy, pregnant and thalassemia on the corona composition formed attached on the surface of polystyrene particle.

(A) Histograms show significantly different proteins attached to polystyrene particle surface on each group that passed a one-way ANOVA-based multiple-sample test for statistically significant enrichment (FDR ≤ 0.05), (red indicates high and green indicates low expression) (B) PCA plot shows clear proteomic profile differences between the 3 groups (FDR ≤ 0.05), (C) Heat map representation (Z-scores) of proteins and that passed a one-way ANOVA-based multiple-sample test for statistically significant enrichment (FDR≤ 0.05) followed by post hoc Tukey's test (FDR ≤ 0.05) to filter for significant enrichment proteins across conditions (healthy n=6, pregnancy n=6, thalassemia n=4).

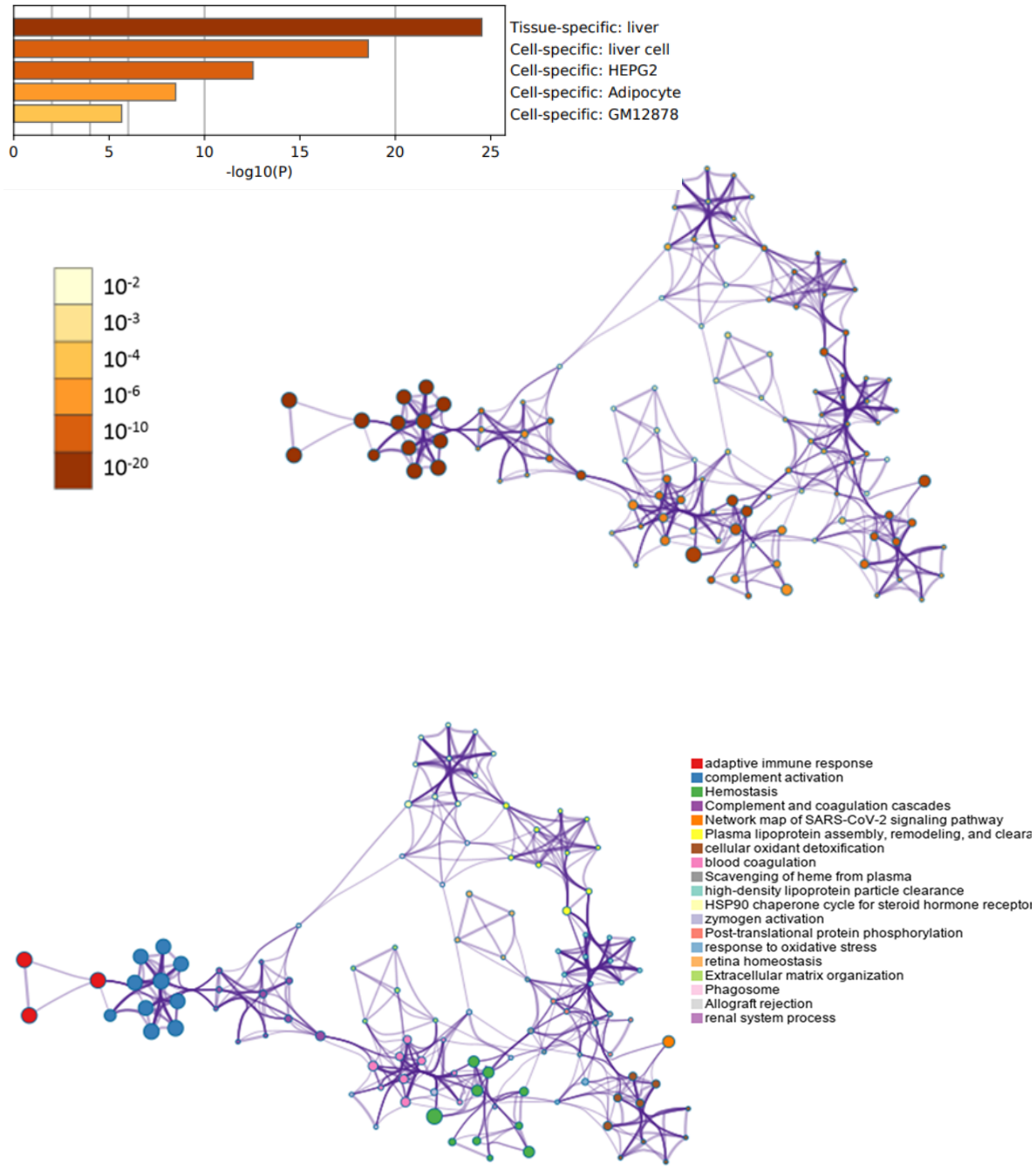


Figure 8.9 Gene ontology pathway and process enrichment analysis of polystyrene corona.

Significant and enriched terms hierarchically clustered into a tree network based on Kappa-statistical similarities among their gene memberships. The 0.3 kappa score was applied as the threshold to cast the tree into term clusters. Each term was represented by a circle node, the size of the node is proportional to number of input genes fell into that term and the colour represents its cluster. The network was visualised using Cytoscape (v3.1.2).

8.4.3.3. Effect of particles material on composition of the protein corona from the 3 serum groups

Comparison of corona composition on the surface of MNP and polystyrene particles revealed 302 differently enriched proteins between MNPs and polystyrene particles after incubation with serum from healthy control group, 255 from pregnancy, and 336 from thalassemia after a Student's t-test (FDR ≤0.05, S0: 0.1) (Figure 8.10).

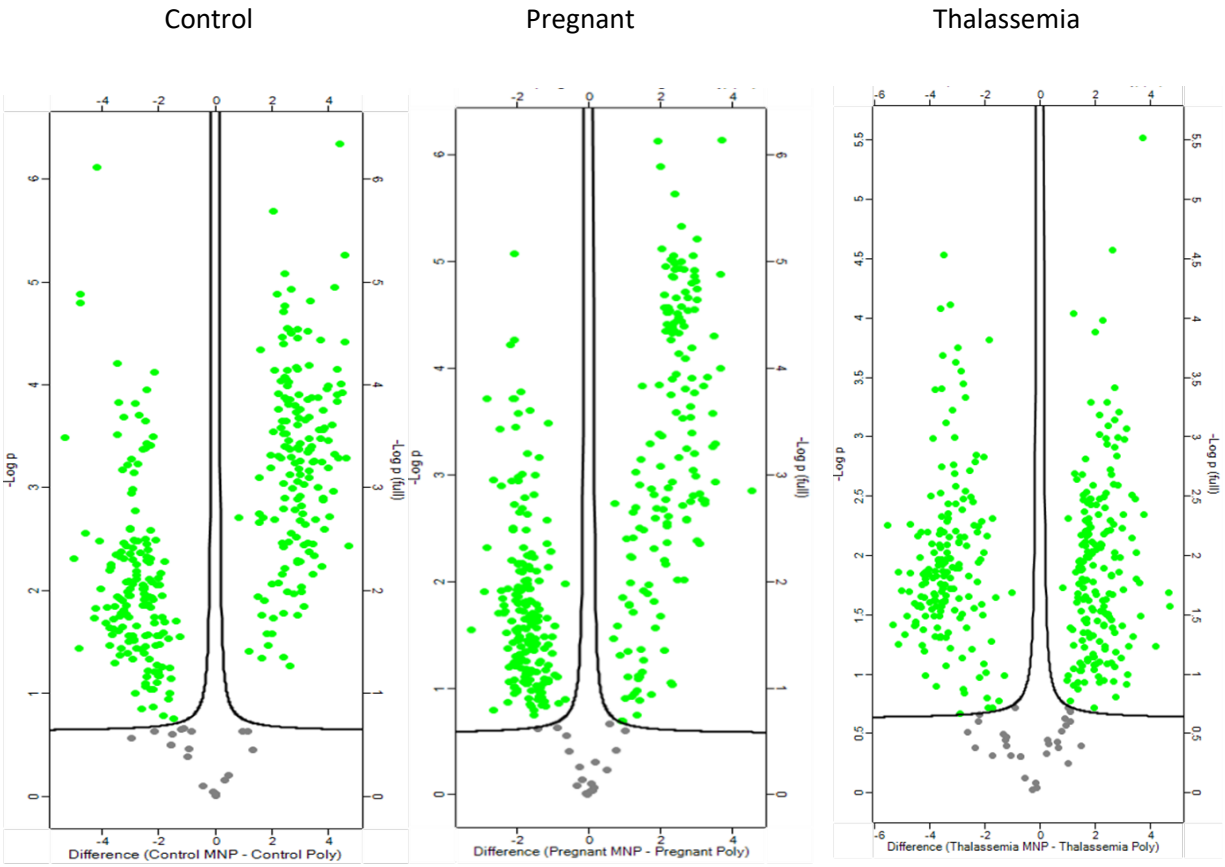


Figure 8.10 The effect of particle material on corona composition mediated by different groups; healthy, pregnant and thalassemia.

Volcano plots show the level of change (x axis (log2 scale)), and the level of significance (y axis (-log10(adjusted p-value)). The dots represent significantly enriched (green) and non-significantly enriched (grey) proteins between MNP and polystyrene particles in each group, after Student's t-test (FDR ≤0.05, S0: 0.1), (healthy n=6, pregnancy n=6, thalassemia n=4).

8.4.3. 4. Effect of PEGylation on composition of the protein corona from the 3 different serum groups

Comparison of corona composition between MNP and MNP-PEG showed no significant differences after incubation with serum from pregnant women or women with beta thalassemia after a Student's t-test (FDR ≤0.05, S0: 0.1) (Figure 8.11).

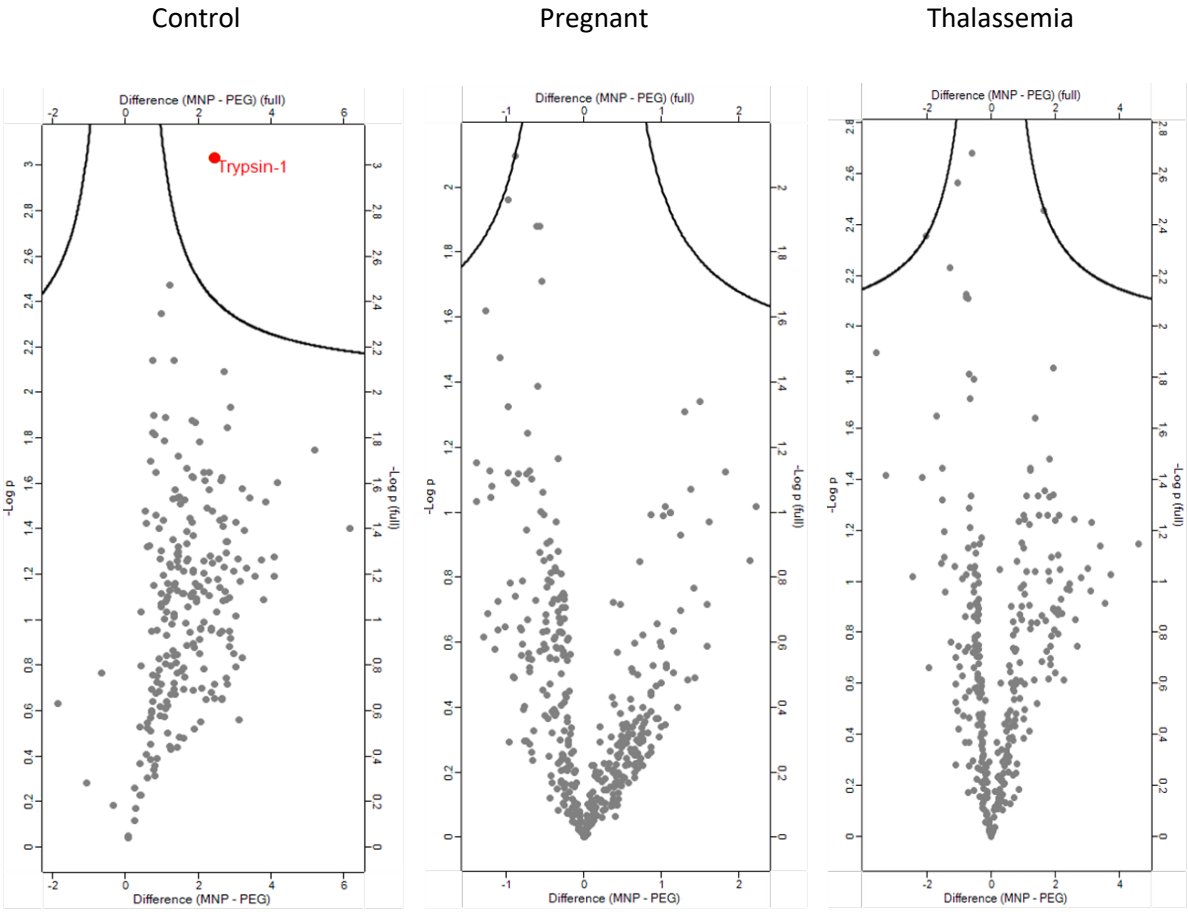


Figure 8.11 The effect of PEGylation on corona composition mediated by different groups; healthy, pregnant and thalassemia.

Volcano plots show the level of change (x axis (log2 scale)), and the level of significance (y axis (-log10(adjusted p-value)). The dots represent significantly enriched (red) and non-significantly enriched (grey) proteins between MNP and MNP-PEG in each group, after Student's t-test (FDR ≤0.05, S0: 0.1), (healthy n=6, pregnancy n=6, thalassemia n=4).

8.5 Discussion

It is known that when nanoparticles interact with biological materials, they can selectively adsorbed proteins to their surface forming a layer called the protein corona. The thickness and composition of the protein corona varies according to certain particle characteristics including particles size, charge, chemical composition, surface properties, shape, angle of curvature and dispersion (Aggarwal et al., 2009; Kharazian et al., 2016). It was shown from previous works using gold and polystyrene particles that more proteins were adsorbed on 30 nm than 50 nm gold particles (Dobrovolskaia et al., 2009) and 50 nm more than 100 nm polystyrene particles (Lundqvist et al., 2008). Results from our SDS-PAGE show a variation in protein corona between different particle sizes where smaller melanin and polystyrene nanoparticles (50 nm), adsorbed more proteins to their surface compared to larger 200 and 500 nm melanin particles (Figure 8.3). This could be due to the increased surface area to volume ratio of smaller particles.

Disease state has significant impact on the plasma environment and proteome profile. Effects of the state of health on protein corona formation have been studied in various diseases since the biological environment can vary according to disease condition (Hajipour et al., 2014). Our MS results show significant differences in protein corona composition between the three different groups: healthy non pregnant women, pregnant women, and women with beta thalassemia, in both types of particles (Figure 8.5 and Figure 8.8). Polystyrene particles, however, showed a greater distinction between the groups with 100 significant proteins compared to 43 significant proteins using melanin particles. Within these 100 significant proteins of polystyrene corona, albumin and five apolipoproteins were found in the corona composition after incubation with pregnant serum (Appendix III

cluster 4). Apolipoproteins are involved in the transportation of lipids, thus they are expected to affect intracellular trafficking, transport, and particle uptake into cells (Lundqvist et al., 2008). Albumin has been previously used to enhance nanoparticle uptake (Martins et al., 2018) and increased the caveolae-mediated endocytosis of 100 nm polystyrene particles (Wang et al., 2009). It was also found that binding of albumin, immunoglobulins, and apolipoproteins to polystyrene particles facilitates their transfer across the placenta in an *ex vivo* human placental perfusion system (Gruber et al., 2020).

Differences in gene ontology between the corona found on the melanin and polystyrene NPs may explain their behaviour *in vivo*. It was previously found that plain and modified (amine and carboxyl) polystyrene particles bound to immunoglobulins, apolipoproteins, complements, and coagulation factors (Lundqvist et al., 2008). Gene ontology results of the corona from polystyrene NPs revealed the top GO biological pathways: immune system process, adaptive immune response, complement activation, haemostasis, and complement and coagulation (Figure 8.9) in agreement with the literature. Gene ontology of cellular components can determine particle bio-distribution and clearance *in vivo* (Nel et al., 2009). While the GO cellular component enrichment analysis of the corona from melanin NPs was melanosome and extracellular matrix (Figure 8.6), the corona from polystyrene NPs was liver and adipocytes (Figure 8.9). One explanation could be due to the nature of melanin nanoparticles that resemble melanin structure in the body defined in the GO analysis. Another explanation could be that bio-inspired melanin particles mediate their biological identity with longer circulation time *in vivo*, whereas polystyrene nanoparticles are recognized as non-self and eliminated by liver cells. This could also explain the non-significant differences between

PEGylated and non-PEGylated melanin nanoparticles (Figure 8.11) since particle PEGylation is used to improve circulation time *in vivo* by limiting particles opsonization.

While these results give interesting indications of the differences in protein corona seen for the different NPs and disease states, definitive conclusions cannot be determined at this stage. Firstly, validation by Western blot is needed to confirm the results. Secondly, the underlying physiochemical principles of protein adsorption on a nanoparticle surface is not fully understood and determination of the protein corona is very challenging since corona formation is a very dynamic process and proteins are continually adsorbed and de-adsorbed with subsequent translocation *in vivo* (Monopoli et al., 2012). This leads to the question of whether their behaviour/ biodistribution *in vivo* would be determined by the original corona at the point of entry or by the modified corona formed after a subsequent movement in the body. Thirdly, it was found that the composition of the protein corona changed when incubated with different concentrations of serum and incubation times (Partikel et al., 2019). Therefore, whether the *ex situ* results reflect the situation *in vivo* will need to be further investigated.

8.5.1 Strength and limitations

This chapter investigated the size and identity of the differently enriched proteins adsorbed on the surface of melanin and polystyrene particles after incubation with serum from three different groups: healthy non-pregnant, pregnant and beta thalassemia. Detailed gene ontology enrichment analysis was then undertaken. However, due to disruptions caused by the Covid-19 pandemic and subsequent suspension to research facilities and limited access to sample collection , as well as demographic difficulties in collecting blood from women with beta thalassemia in

Oxford, sample collection was only completed a few months prior to submission. This was followed by technical problems within the MS service facility, such that raw data were only received a few weeks prior to submission. Therefore, proteins identified in the proteomic analysis have not yet been further validated.

8.6 Summary

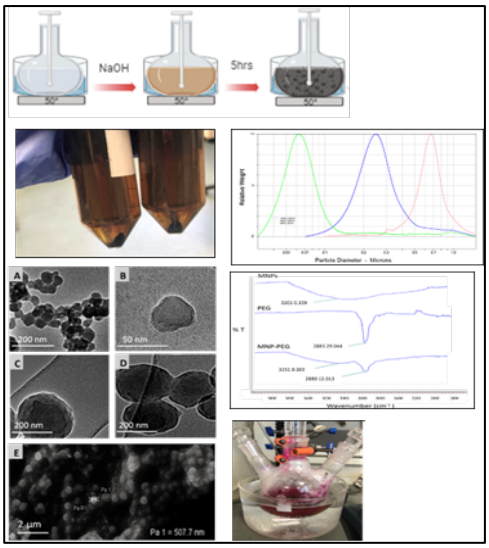
In this chapter, it was shown using SDS-PAGE and proteomics analysis that formation of a corona on melanin NPS is varied according to particle size and protein environment. Potential proteins and mechanisms associated with the corona on melanin and polystyrene NPs were also identified. PEGylation of MNPs shows no significant differences on corona composition. Validation and further investigation may provide further insights into therapeutic development.

Chapter 9. Conclusion and future perspectives

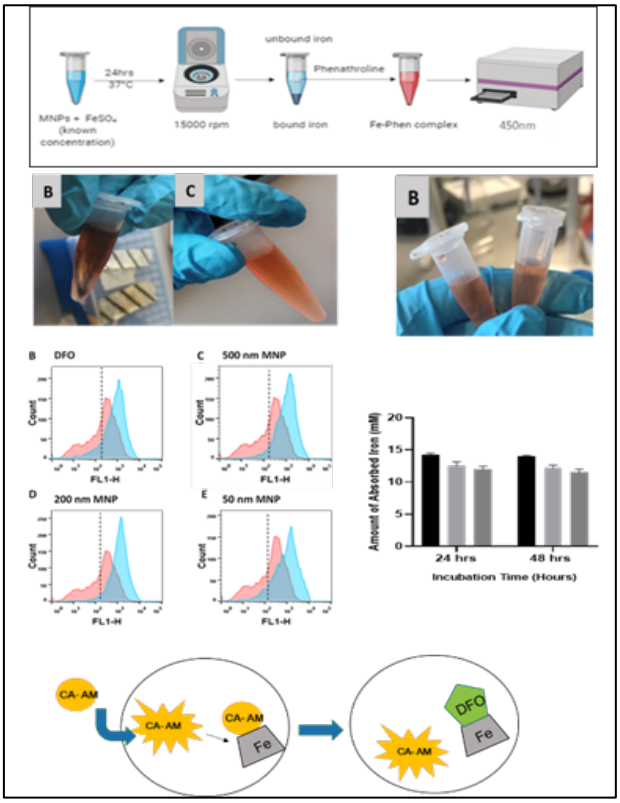
This thesis addressed the complicated and neglected challenge of treating thalassaemia during pregnancy in which a medication needs to be restricted from crossing the placenta while still preventing iron overload in the mother. The ongoing revolution in medicines for longstanding and emerging health challenges has largely failed pregnant women. The foundations of this project were based upon nanoparticles which can be designed to not cross the placenta and can provide a practical solution for this under-served group of the population. Through the work presented here, promising and novel findings have been made regarding i) the efficacy of melanin nanoparticles to chelate iron, ii) their biocompatibility with blood iii) their restriction from crossing the placenta with appropriate size, and iv) their behaviour with serum proteins from different patient groups.

9.1 Summary of the main finding of the thesis

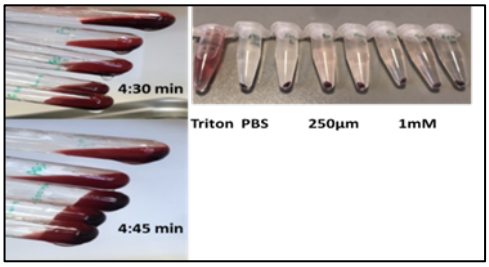
The key findings of the thesis are summarized in Figure 9.1.



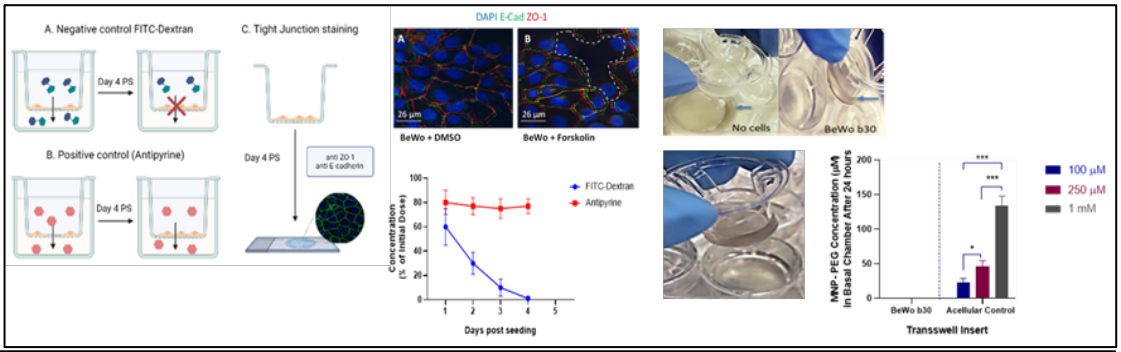
Chapter 3: Melanin nanoparticles 50 ± 10 nm, 200 ± 20 nm, and 500 ± 10 nm were synthesized with a zeta potential of - 26 ± 0.25 mV, -27 ± 1 mV, -32 ± 1 mV respectively. Particles were then imaged, PEGylated, and fluorescently labelled with Rhodamine B.



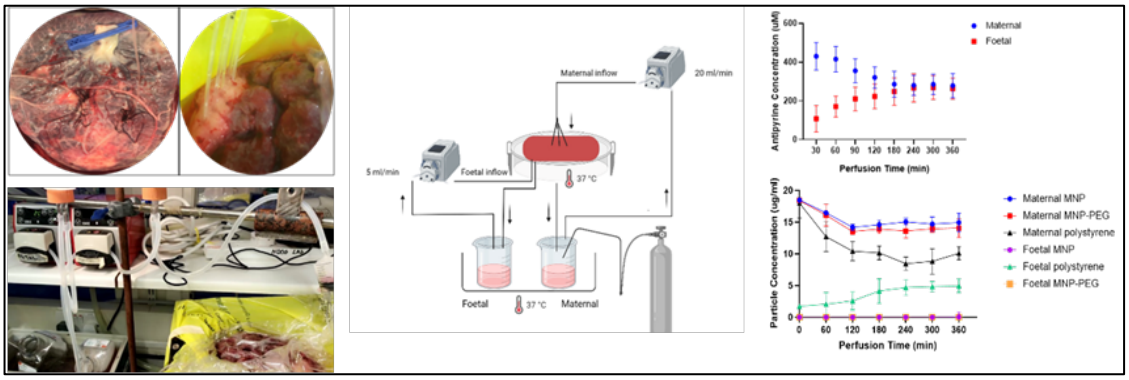
Chapter 4: The particles were found to effectively chelating iron with a maximum adsorption of 14 +/- 0.25 mM of iron/g of material, significantly more than the commonly used chelator DFO of the same concentration. Particles' PEGylation, did not affect their chelation efficacy. The particles were also found to reducing the LIP in HepG2 cell lines at relevant concentration.



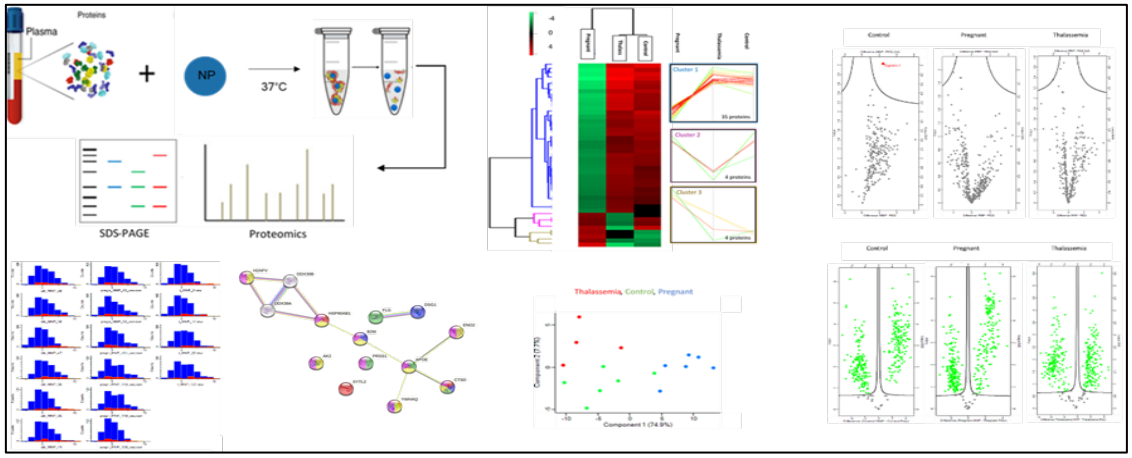
Chapter 5: 200 nm and 500 nm particles showed excellent compatibility with RBCs and there were no significant differences in clotting or prothrombin time in comparison to controls. PEGylation improved hemocompatibility of the 50 nm particles.



Chapter 6: The cut off size of particles restriction from movement across the barrier was 200 nm MNP-PEG. Surface modification with PEG had a significant effect on reducing translocations of the smaller particles (50 nm). Increasing concentration of the particles has no effect on their translocation across BeWo cells.



Chapter 7: Melanin nanoparticles of 200 nm could be restricted from crossing the placenta in an *ex vivo* dule lobe human placental perfusion. Viability of placental tissue was determined by the production of hCG which was not altered after 6 hours perfusion



Chapter 8: Formation of a corona on melanin NPS was varied according to particle size and protein environment. Proteomics analysis of the protein corona on the MNPs identified 43 significantly different proteins between the three serum groups. No proteins were identified as being significantly different between PEGylated and non-PEGylated particles.

Figure 9.1 Graphical summary of the key findings of the thesis.

9.2 Contribution to the field and clinical implications

Results in this thesis show that melanin nanoparticles may reduce the dosage and frequency of chelation therapy to be used in non-pregnant thalassemia compared with DFO. More importantly, MNPs may provide a safer option for iron chelation in pregnant thalassemia.

Conducting clinical trials in pregnancy raises many challenges due to concerns regarding the safety of both the mother and the foetus, particularly when testing novel therapies. For many years, pregnant women were largely excluded from clinical trials following the legacy of thalidomide and diethylstilbestrol. Furthermore, pregnant women have been recently categorized as vulnerable (Spencer et al., 2022), which contributes to inequality to the heath of these women and their unborn children (Fisk et al., 2011). The Covid-19 vaccination trial is a prominent example where pregnant women were first excluded before they were prioritised for the vaccination which could potentially save them from the severe complications of Covid-19 infection (Male, 2022). Because pregnant women are more susceptible to infections, an increased risk of more severe symptoms, hospitalization, intensive care unit admission, and mechanical ventilation have been reported in pregnant women compared with their non-pregnant counterparts. It was found that the infection induced perinatal complications including premature delivery, pre-eclampsia, stillbirth and maternal morbidity and mortality (Male, 2022). The mRNA/nanoparticles-based vaccines developed by Pfizer and Moderna were then tested in a large population of pregnant women without reports of unfavourable complications (Male, 2022) paving the way for more nanoparticles medications to be used in the future.

The exclusion of pregnant women from clinical trials has limited research on treatments developed specifically for pregnancy with only two drugs in the past 40 years being developed (Wise, 2022). There is a critical need for therapeutic research with innovative study designs that include pregnant and lactating women to fill the knowledge gaps regarding safe and effective therapeutics in these population. The findings here may accelerate research in safe and effective chelation therapeutics for pregnant and lactating women with β-thalassemia to reduce maternal and infant morbidity.

Additionally, melanin nanoparticles showed promising results in variety of biomedical applications including imaging and cancer treatment (Park et al., 2019). Several additional observations from this thesis suggest the safety of melanin nanoparticles, including their interaction with blood, serum proteins and human placenta.

To date more than 30 nanoparticles are clinically approved and applied in varies clinical applications (Anselmo and Mitragotri, 2021). The global administration of lipid nanoparticles in Covid-19 mRNA vaccines can be considered as a remarkable period for the field of nanomedicine, yet there is much to learn about their behaviour in vivo. Nanoparticle fate in the biological system is one of the most debatable aspects in the field. However, since particle characteristics determine their circulation time, optimising nanoparticle design to balance optimal clearance with the exposure duration required for their therapeutic needs is a feasible way to minimise toxicity. It was found that nanoparticles can be cleared by several routes depending on their size, material, and charge. Bio-inspired nanoparticles for example were found to degrade to low-molecular weight complexes that were then excreted by the kidneys (Longmire et al., 2008). Some particles may undergo

opsonization by serum proteins, glomerular filtration, or liver phagocytosis (Longmire et al., 2008). Thus, studies into particle-specific clearance is much needed. However, studies have shown that elimination of MNPs in iron overloaded mice were mainly by hepatic and renal system after around 16 to 17 hours of administration (Yan et al., 2016).

9.3 Experimental consideration

Nanoparticle interactions with the placenta are determined by factors that can be manipulated at the synthesis stage. In this thesis, it was hypothesized that a nanoparticle chelator with appropriate characteristics could be restricted from movement across the placenta, and safely used to treat the mother. Findings in this thesis support this hypothesis and can serve as a proof-of-concept for *in vitro* and *ex vivo* safety and efficacy of using melanin nanoparticles during pregnancy. Further experimental considerations must be undertaken before translating this basic research to clinical trials. The specific limitations associated with each set of experiments are discussed in detail and suggestions for improvements in each of the experimental chapters.

9.4 Impact of Covid-19 on this thesis

Disruptions caused by the Covid-19 pandemic substantially impacted the progression of this thesis. Due to laboratory closures and limited access to sample collection and research facilities including the TEM, deep analysis and imaging of particles taken up into the tissues of the perfused placentas could not be performed as planned, and proteins identified in the proteomic analysis could not be further validated.

9.5 Future perspectives and research directions

In this thesis, a library of melanin nanoparticles of three different sizes was synthesized, and their efficacy, safety and transplacental transport in an *in vitro* and *ex vivo* placental models examined. There is still much to learn however about their interaction with placental tissue and about their behaviour *in vivo*.

Potential proteins and mechanisms associated with MNP coronas in three different patient groups was identified. Validation of identified proteins with Western blot is needed as well as deep investigation of the corona to improve therapeutic development. Also, when analysing particle accumulation in the placental tissue, no fluorescent signals of the particle were detected in the homogenised tissue from the perfused lobe. In depth imaging analysis with larger sample sizes and deep TEM imaging analysis of all layers of the placental barrier would provide further insight into their interaction with the placental tissue.

Although MNP transport across the human placenta has been studied in this thesis, there are multiple factors that influence the individual response to medications. Physiological changes during pregnancy and variation in the activities of specific transports can affect the drug metabolism, distribution, transport, and excretion. Thus, understanding nanoparticle specific pharmacological properties; pharmacokinetics (PK; what the body does to a drug) and pharmacodynamics (PD; what the drug does to the body) may improve the efficacy of the treatment. Moreover, it will be important to study nanoparticle transport and activity with placenta in relation to specific gestational stages. However, due to practical and logistical reasons that limit pharmacological research in pregnant and lactating women, alternative approaches and research tools may help conducting maternal

pharmacological research. Computational simulation models have gained popularity in recent years particularly post-pandemic. Pharmacological modelling such as population pharmacokinetics and physiologically based pharmacokinetic (PBPK) modelling have been used to estimate drug activities in pregnant women. One example is the use of population pharmacokinetics modelling in estimation of oseltamivir activity in pregnant women with influenza infection (Pillai et al., 2015). These models are predictive and powerful in providing relevant information about optimal treatment that could help in designing smaller and safer clinical trials. Similar models could be applied to study the nanoparticle pharmacological activity during pregnancy.

Additionally, in this thesis, a combination of *in vitro* and *ex vivo* models allowed determination of the cut off size of particle restrictions from movement across the human placenta. However, indirect toxicity without direct passage of a medication has been previously reported using other types of particles and medications (Hawkins et al., 2018). This can be tested with a co-culture approach of transwell model using both BeWo and foetal cells. The model can also be applied with a three-dimensional culture model of spheroids or organoids to provide closer representation to study nanoparticle toxicity towards the foetus.

Another approach to combine the co-culturing methodology alongside mechanistic studies of nanoparticles would be to use microfluidic devices, such as a placentaon-chip model. Microengineering co-culture models of a placenta-on-chip can replicate the physiology and functionality of the placental barrier and the circulation of pharmaceutical intake between the mother and the foetus (Pemathilaka et al., 2019). Microfluidic devices may overcome technical difficulties of the ex-vivo perfusion to analyse the nanoparticles uptake and could be applied in future studies.

Finally, *in vivo* animal testing of drug pharmacodynamics and pharmacometrics will be an essential step in the *de novo* drug discovery and development process for the FDA approvals.

In the age of modern medicine many pregnancy complications could be avoided. Results presented in this thesis give hope to women with β-thalassemia to spend more time enjoying pregnancy and less worrying about avoidable risks that threaten them and their babies.

References

.

Aengenheister, L., Dietrich, D., Sadeghpour, A., Manser, P., Diener, L., Wichser, A., Karst, U., Wick, P., and Buerki-Thurnherr, T. (2018a). Gold nanoparticle distribution in advanced in vitro and ex vivo human placental barrier models. Journal of Nanobiotechnology *16*, 79.

Aengenheister, L., Keevend, K., Muoth, C., Schönenberger, R., Diener, L., Wick, P., and Buerki-Thurnherr, T. (2018b). An advanced human in vitro co-culture model for translocation studies across the placental barrier. Scientific Reports *8*, 5388.

Aggarwal, P., Hall, J.B., McLeland, C.B., Dobrovolskaia, M.A., and McNeil, S.E. (2009). Nanoparticle interaction with plasma proteins as it relates to particle biodistribution, biocompatibility and therapeutic efficacy. Adv Drug Deliv Rev *61*, 428-437.

Alexis, F., Pridgen, E., Molnar, L.K., and Farokhzad, O.C. (2008). Factors Affecting the Clearance and Biodistribution of Polymeric Nanoparticles. Molecular Pharmaceutics *5*, 505-515.

Ali, A., Zhang, Q., Dai, J., and Huang, X. (2003). Calcein as a fluorescent iron chemosensor for the determination of low molecular weight iron in biological fluids. Biometals *16*, 285-293.

Ali, H., Kalashnikova, I., White, M.A., Sherman, M., and Rytting, E. (2013). Preparation, characterization, and transport of dexamethasone-loaded polymeric nanoparticles across a human placental in vitro model. International Journal of Pharmaceutics *454*, 149-157.

Ali, S., Albekairi, N.A., Al-Enazy, S., Shah, M., Patrikeeva, S., Nanovskaya, T.N., Ahmed, M.S., and Rytting, E. (2021). Formulation effects on paclitaxel transfer and uptake in the human placenta. Nanomedicine: Nanotechnology, Biology and Medicine *33*, 102354.

Amin, D.R., Sugnaux, C., Lau, K.H.A., and Messersmith, P.B. (2017). Size Control and Fluorescence Labeling of Polydopamine Melanin-Mimetic Nanoparticles for Intracellular Imaging. Biomimetics (Basel) *2*.

Amin, K., and Dannenfelser, R.-M. (2006). In vitro hemolysis: Guidance for the pharmaceutical scientist. Journal of Pharmaceutical Sciences *95*, 1173-1176.

Audus, K.L. (1999). Controlling drug delivery across the placenta. European Journal of Pharmaceutical Sciences *8*, 161-165.

Bartczak, D., Muskens, O.L., Nitti, S., Sanchez-Elsner, T., Millar, T.M., and Kanaras, A.G. (2012). Interactions of human endothelial cells with gold nanoparticles of different morphologies. Small *8*, 122-130.

Borgna-Pignatti, C., Rugolotto, S., De Stefano, P., Zhao, H., Cappellini, M.D., Del Vecchio, G.C., Romeo, M.A., Forni, G.L., Gamberini, M.R., Ghilardi, R.*, et al.* (2004). Survival and complications in patients with thalassemia major treated with transfusion and deferoxamine. Haematologica *89*, 1187-1193.

Bové, H., Bongaerts, E., Slenders, E., Bijnens, E.M., Saenen, N.D., Gyselaers, W., Van Eyken, P., Plusquin, M., Roeffaers, M.B.J., Ameloot, M.*, et al.* (2019). Ambient black carbon particles reach the fetal side of human placenta. Nature Communications *10*, 3866.

Breuer, W., Shvartsman, M., and Cabantchik, Z.I. (2008). Intracellular labile iron. The International Journal of Biochemistry & Cell Biology *40*, 350-354.

Bteich, M. (2019). An overview of albumin and alpha-1-acid glycoprotein main characteristics: highlighting the roles of amino acids in binding kinetics and molecular interactions. Heliyon *5*, e02879.

Burton, G.J., Sebire, N.J., Myatt, L., Tannetta, D., Wang, Y.L., Sadovsky, Y., Staff, A.C., and Redman, C.W. (2014). Optimising sample collection for placental research. Placenta *35*, 9-22.

Caldas, M., Santos, A.C., Veiga, F., Rebelo, R., Reis, R.L., and Correlo, V.M. (2020). Melanin nanoparticles as a promising tool for biomedical applications – a review. Acta Biomaterialia *105*, 26-43.

Camaschella, C., and Cappellini, M.D. (1995). Thalassemia intermedia. Haematologica *80*, 58-68.

Cartwright, L., Poulsen, M.S., Nielsen, H.M., Pojana, G., Knudsen, L.E., Saunders, M., and Rytting, E. (2012). In vitro placental model optimization for nanoparticle transport studies. Int J Nanomedicine *7*, 497-510.
Cassinerio, E., Baldini, I.M., Alameddine, R.S., Marcon, A., Borroni, R., Ossola, W., Taher, A., and Cappellini, M.D. (2017). Pregnancy in patients with thalassemia major: a cohort study and conclusions for an adequate care management approach. Annals of Hematology *96*, 1015-1021.
Chen, X., Yan, Y., Müllner, M., van Koeverden, M.P., Noi, K.F., Zhu, W., and Caruso, F. (2014). Engineering Fluorescent Poly(dopamine) Capsules. Langmuir *30*, 2921-2925.
Chen, Z., Li, F., Liu, C., Guan, J., Hu, X., Du, G., Yao, X., Wu, J., and Tian, F. (2016). Blood clot initiation by mesoporous silica nanoparticles: dependence on pore size or particle size? Journal of Materials Chemistry B *4*, 7146-7154.
Chen, Z.A., Wu, S.H., Chen, P., Chen, Y.P., and Mou, C.Y. (2019). Critical Features for Mesoporous Silica Nanoparticles Encapsulated into Erythrocytes. ACS Appl Mater Interfaces *11*, 4790-4798.
Chithrani, B.D., Ghazani, A.A., and Chan, W.C.W. (2006). Determining the Size and Shape Dependence of Gold Nanoparticle Uptake into Mammalian Cells. Nano Letters *6*, 662-668.
Choy, M.Y., and Manyonda, I.T. (1998). The phagocytic activity of human first trimester extravillous trophoblast. Human Reproduction *13*, 2941-2949.
Chu, M., Wu, Q., Yang, H., Yuan, R., Hou, S., Yang, Y., Zou, Y., Xu, S., Xu, K., Ji, A.*, et al.* (2010). Transfer of Quantum Dots from Pregnant Mice to Pups Across the Placental Barrier. Small *6*, 670-678.
Chui, D.H., Fucharoen, S., and Chan, V. (2003). Hemoglobin H disease: not necessarily a benign disorder. Blood *101*, 791-800.
Cline, M.S., Smoot, M., Cerami, E., Kuchinsky, A., Landys, N., Workman, C., Christmas, R., Avila-Campilo, I., Creech, M., Gross, B.*, et al.* (2007). Integration of biological networks and gene expression data using Cytoscape. Nat Protoc *2*, 2366-2382.
Cohen, A.R., Galanello, R., Piga, A., De Sanctis, V., and Tricta, F. (2003). Safety and effectiveness of long-term therapy with the oral iron chelator deferiprone. Blood *102*, 1583-1587.
Colah, R., Gorakshakar, A., and Nadkarni, A. (2010). Global burden, distribution and prevention of β-thalassemias and hemoglobin E disorders. Expert Rev Hematol *3*, 103-117.
Corbo, C., Molinaro, R., Tabatabaei, M., Farokhzad, O.C., and Mahmoudi, M. (2017). Personalized protein corona on nanoparticles and its clinical implications. Biomaterials Science *5*, 378-387.
Cornford, E.M., Hyman, S., Cornford, M.E., Chytrova, G., Rhee, J., Suzuki, T., Yamagata, T., Yamakawa, K., Penichet, M.L., and Pardridge, W.M. (2016). Non-invasive gene targeting to the fetal brain after intravenous administration and transplacental transfer of plasmid DNA using PEGylated immunoliposomes. Journal of Drug Targeting *24*, 58-67.
Correia Carreira, S., Walker, L., Paul, K., and Saunders, M. (2015). The toxicity, transport and uptake of nanoparticles in the in vitro BeWo b30 placental cell barrier model used within NanoTEST. Nanotoxicology *9 Suppl 1*, 66-78.
Craparo, E.F., Musumeci, T., Bonaccorso, A., Pellitteri, R., Romeo, A., Naletova, I., Cucci, L.M., Cavallaro, G., and Satriano, C. (2021). mPEG-PLGA Nanoparticles Labelled with Loaded or Conjugated Rhodamine-B for Potential Nose-to-Brain Delivery. Pharmaceutics *13*.
Crichton, R. (2001). Pathophysiology of Iron Deficiency and Iron Overload in Man. In Inorganic Biochemistry of Iron Metabolism: From Molecular Mechanisms to Clinical Consequences, 2nd Edition, pp. 207-233.
d'Ischia, M., Napolitano, A., Pezzella, A., Meredith, P., and Sarna, T. (2009). Chemical and Structural Diversity in Eumelanins: Unexplored Bio-Optoelectronic Materials. Angewandte Chemie International Edition *48*, 3914-3921.
Danjou, F., Anni, F., and Galanello, R. (2011). Beta-thalassemia: from genotype to phenotype. Haematologica *96*, 1573-1575.

Diamantidis, M.D., Neokleous, N., Agapidou, A., Vetsiou, E., Manafas, A., Fotiou, P., and Vlachaki, E. (2016). Iron chelation therapy of transfusion-dependent β-thalassemia during pregnancy in the era of novel drugs: is deferasirox toxic? Int J Hematol *103*, 537-544.
Dobrovolskaia, M.A., Patri, A.K., Zheng, J., Clogston, J.D., Ayub, N., Aggarwal, P., Neun, B.W., Hall, J.B., and McNeil, S.E. (2009). Interaction of colloidal gold nanoparticles with human blood: effects on particle size and analysis of plasma protein binding profiles. Nanomedicine: Nanotechnology, Biology and Medicine *5*, 106-117.
Drwal, E., Rak, A., and Gregoraszczuk, E. (2018). Co-culture of JEG-3, BeWo and syncBeWo cell lines with adrenal H295R cell line: an alternative model for examining endocrine and metabolic properties of the fetoplacental unit. Cytotechnology *70*, 285-297.
Eaton, B.M., and Oakey, M.P. (1994). Sequential preparation of highly purified microvillous and basal syncytiotrophoblast membranes in substantial yield from a single term human placenta: inhibition of microvillous alkaline phosphatase activity by EDTA. Biochimica et Biophysica Acta (BBA) - Biomembranes *1193*, 85-92.
Enders, A.C., and Blankenship, T.N. (1999). Comparative placental structure. Adv Drug Deliv Rev *38*, 3-15.
Espósito, B.P., Epsztejn, S., Breuer, W., and Cabantchik, Z.I. (2002). A Review of Fluorescence Methods for Assessing Labile Iron in Cells and Biological Fluids. Analytical Biochemistry *304*, 1-18.
Fisk, N.M., McKee, M., and Atun, R. (2011). Relative and absolute addressability of global disease burden in maternal and perinatal health by investment in R&D. Trop Med Int Health *16*, 662-668.
García-Álvarez, R., and Vallet-Regí, M. (2021). Hard and Soft Protein Corona of Nanomaterials: Analysis and Relevance. Nanomaterials *11*, 888.
Gauster, M., and Huppertz, B. (2010). The paradox of caspase 8 in human villous trophoblast fusion. Placenta *31*, 82-88.
Gorbet, M.B., and Sefton, M.V. (2004). Biomaterial-associated thrombosis: roles of coagulation factors, complement, platelets and leukocytes. Biomaterials *25*, 5681-5703.
Grafmueller, S., Manser, P., Diener, L., Diener, P.A., Maeder-Althaus, X., Maurizi, L., Jochum, W., Krug, H.F., Buerki-Thurnherr, T., von Mandach, U.*, et al.* (2015). Bidirectional Transfer Study of Polystyrene Nanoparticles across the Placental Barrier in an ex Vivo Human Placental Perfusion Model. Environ Health Perspect *123*, 1280-1286.
Gref, R., Lück, M., Quellec, P., Marchand, M., Dellacherie, E., Harnisch, S., Blunk, T., and Müller, R.H. (2000). 'Stealth' corona-core nanoparticles surface modified by polyethylene glycol (PEG): influences of the corona (PEG chain length and surface density) and of the core composition on phagocytic uptake and plasma protein adsorption. Colloids and Surfaces B: Biointerfaces *18*, 301-313.
Gruber, M.M., Hirschmugl, B., Berger, N., Holter, M., Radulović, S., Leitinger, G., Liesinger, L., Berghold, A., Roblegg, E., Birner-Gruenberger, R.*, et al.* (2020). Plasma proteins facilitates placental transfer of polystyrene particles. Journal of Nanobiotechnology *18*, 128.
Guo, S., Shi, Y., Liang, Y., Liu, L., Sun, K., and Li, Y. (2021). Relationship and improvement strategies between drug nanocarrier characteristics and hemocompatibility: What can we learn from the literature. Asian J Pharm Sci *16*, 551-576.
Hajipour, M.J., Laurent, S., Aghaie, A., Rezaee, F., and Mahmoudi, M. (2014). Personalized protein coronas: a "key" factor at the nanobiointerface. Biomaterials Science *2*, 1210-1221.
Hajipour, M.J., Raheb, J., Akhavan, O., Arjmand, S., Mashinchian, O., Rahman, M., Abdolahad, M., Serpooshan, V., Laurent, S., and Mahmoudi, M. (2015). Personalized disease-specific protein corona influences the therapeutic impact of graphene oxide. Nanoscale *7*, 8978-8994.
Halim-Fikri, B.H., Lederer, C.W., Baig, A.A., Mat-Ghani, S.N.A., Syed-Hassan, S.R., Yusof, W., Abdul Rashid, D., Azman, N.F., Fucharoen, S., Panigoro, R.*, et al.* (2022). Global Globin Network Consensus Paper: Classification and Stratified Roadmaps for Improved Thalassaemia Care and Prevention in 32 Countries. J Pers Med *12*.

Hallaway, P.E., Eaton, J.W., Panter, S.S., and Hedlund, B.E. (1989). Modulation of deferoxamine toxicity and clearance by covalent attachment to biocompatible polymers. Proc Natl Acad Sci U S A *86*, 10108-10112.
Hamilton, J.L., and Kizhakkedathu, J.N. (2015). Polymeric nanocarriers for the treatment of systemic iron overload. Mol Cell Ther *3*, 3.
Hanscombe, O., Whyatt, D., Fraser, P., Yannoutsos, N., Greaves, D., Dillon, N., and Grosveld, F. (1991). Importance of globin gene order for correct developmental expression. Genes Dev *5*, 1387-1394.
Hawkins, S.J., Crompton, L.A., Sood, A., Saunders, M., Boyle, N.T., Buckley, A., Minogue, A.M., McComish, S.F., Jiménez-Moreno, N., Cordero-Llana, O*., et al.* (2018). Nanoparticle-induced neuronal toxicity across placental barriers is mediated by autophagy and dependent on astrocytes. Nature Nanotechnology *13*, 427-433.
He, Q., Zhang, J., Shi, J., Zhu, Z., Zhang, L., Bu, W., Guo, L., and Chen, Y. (2010). The effect of PEGylation of mesoporous silica nanoparticles on nonspecific binding of serum proteins and cellular responses. Biomaterials *31*, 1085-1092.
Herd, H., Daum, N., Jones, A.T., Huwer, H., Ghandehari, H., and Lehr, C.-M. (2013). Nanoparticle Geometry and Surface Orientation Influence Mode of Cellular Uptake. ACS Nano *7*, 1961-1973.
Hershko, C.A., Link, G., Konijn, A.M., and Cabantchik, Z.I. (2005). Objectives and Mechanism of Iron Chelation Therapy. Annals of the New York Academy of Sciences *1054*, 124-135.
Higgs, D.R., and Weatherall, D.J. (2009). The alpha thalassaemias. Cell Mol Life Sci *66*, 1154-1162.
Hoffbrand, A.V., Taher, A., and Cappellini, M.D. (2012). How I treat transfusional iron overload. Blood *120*, 3657-3669.
Holder, B., Aplin, J.D., Gomez-Lopez, N., Heazell, A.E.P., James, J.L., Jones, C.J.P., Jones, H., Lewis, R.M., Mor, G., Roberts, C.T*., et al.* (2021). 'Fetal side' of the placenta: anatomical mis-annotation of carbon particle 'transfer' across the human placenta. Nature Communications *12*, 7049.
Hong, L., and Simon, J.D. (2007). Current understanding of the binding sites, capacity, affinity, and biological significance of metals in melanin. J Phys Chem B *111*, 7938-7947.
Huang, J.-P., Hsieh, P.C.H., Chen, C.-Y., Wang, T.-Y., Chen, P.-C., Liu, C.-C., Chen, C.-C., and Chen, C.-P. (2015). Nanoparticles can cross mouse placenta and induce trophoblast apoptosis. Placenta *36*, 1433-1441.
Huang, Y., Li, Y., Hu, Z., Yue, X., Proetto, M.T., Jones, Y., and Gianneschi, N.C. (2017). Mimicking Melanosomes: Polydopamine Nanoparticles as Artificial Microparasols. ACS Cent Sci *3*, 564-569.
Hutson, J.R., Garcia-Bournissen, F., Davis, A., and Koren, G. (2011). The human placental perfusion model: a systematic review and development of a model to predict in vivo transfer of therapeutic drugs. Clin Pharmacol Ther *90*, 67-76.
ISO (2017). ISO 10993-4 : Biological evaluation of medical devices. Part 4: Selection of tests for interaction with blood.
Jiang, Y., Li, Y., Richard, C., Scherman, D., and Liu, Y. (2019). Hemocompatibility investigation and improvement of near-infrared persistent luminescent nanoparticle ZnGa2O4:Cr3+ by surface PEGylation. Journal of Materials Chemistry B *7*, 3796-3803.
Jones, C.J.P., and Fox, H. (1991). Ultrastructure of the normal human placenta. Electron Microscopy Reviews *4*, 129-178.
Ju, K.-Y., Lee, Y., Lee, S., Park, S.B., and Lee, J.-K. (2011). Bioinspired Polymerization of Dopamine to Generate Melanin-Like Nanoparticles Having an Excellent Free-Radical-Scavenging Property. Biomacromolecules *12*, 625-632.
Kang, H., Han, M., Xue, J., Baek, Y., Chang, J., Hu, S., Nam, H., Jo, M.J., El Fakhri, G., Hutchens, M.P*., et al.* (2019). Renal clearable nanochelators for iron overload therapy. Nature Communications *10*, 5134.
Karttunen, V., Sahlman, H., Repo, J.K., Woo, C.S., Myöhänen, K., Myllynen, P., and Vähäkangas, K.H. (2015). Criteria and challenges of the human placental perfusion – Data from a large series of perfusions. Toxicol In Vitro *29*, 1482-1491.

Kattamis, A., Forni, G.L., Aydinok, Y., and Viprakasit, V. (2020). Changing patterns in the epidemiology of β-thalassemia. European Journal of Haematology *105*, 692-703.
Kaur, I., Ellis, L.J., Romer, I., Tantra, R., Carriere, M., Allard, S., Mayne-L'Hermite, M., Minelli, C., Unger, W., Potthoff, A*., et al.* (2017). Dispersion of Nanomaterials in Aqueous Media: Towards Protocol Optimization. J Vis Exp.
Kharazian, B., Hadipour, N.L., and Ejtehadi, M.R. (2016). Understanding the nanoparticle–protein corona complexes using computational and experimental methods. The International Journal of Biochemistry & Cell Biology *75*, 162-174.
Kidd, R.D., Baker, H.M., Mathews, A.J., Brittain, T., and Baker, E.N. (2001). Oligomerization and ligand binding in a homotetrameric hemoglobin: two high-resolution crystal structures of hemoglobin Bart's (gamma(4)), a marker for alpha-thalassemia. Protein Sci *10*, 1739-1749.
King, A., and Muller, T. (2016). Using fluid-induced seismicity to infer permeability. ASEG Extended Abstracts *2016*, 1-5.
Kloet, S.K., Walczak, A.P., Louisse, J., van den Berg, H.H.J., Bouwmeester, H., Tromp, P., Fokkink, R.G., and Rietjens, I.M.C.M. (2015). Translocation of positively and negatively charged polystyrene nanoparticles in an in vitro placental model. Toxicology in Vitro *29*, 1701-1710.
Krauer, B., Dayer, P., and Anner, R. (1984). Changes in serum albumin and alpha 1-acid glycoprotein concentrations during pregnancy: an analysis of fetal-maternal pairs. Br J Obstet Gynaecol *91*, 875-881.
Krzyzaniak, J.F., Alvarez Núñez, F.A., Raymond, D.M., and Yalkowsky, S.H. (1997). Lysis of Human Red Blood Cells. 4. Comparison of in Vitro and in Vivo Hemolysis Data. Journal of Pharmaceutical Sciences *86*, 1215-1217.
Kulvietis, V., Zalgeviciene, V., Didziapetriene, J., and Rotomskis, R. (2011). Transport of Nanoparticles through the Placental Barrier. The Tohoku Journal of Experimental Medicine *225*, 225-234.
Kwiatkowski, J.L. (2011). Real-World Use of Iron Chelators. Hematology *2011*, 451-458.
LaPelusa A, D.H. (2022). Hemostasis. In: StatPearls [Internet] Treasure Island (FL): StatPearls Publishing; 2022 Jan-.
Levkovitz, R., Zaretsky, U., Gordon, Z., Jaffa, A.J., and Elad, D. (2013). In vitro simulation of placental transport: part I. Biological model of the placental barrier. Placenta *34*, 699-707.
Li, Q., Peterson, K.R., Fang, X., and Stamatoyannopoulos, G. (2002). Locus control regions. Blood *100*, 3077-3086.
Lin, J.H., Yu, C.J., Yang, Y.C., and Tseng, W.L. (2015). Formation of fluorescent polydopamine dots from hydroxyl radical-induced degradation of polydopamine nanoparticles. Phys Chem Chem Phys *17*, 15124-15130.
Lin, J.Y., and Fisher, D.E. (2007). Melanocyte biology and skin pigmentation. Nature *445*, 843-850.
Liu, F., Soares, M.J., and Audus, K.L. (1997). Permeability properties of monolayers of the human trophoblast cell line BeWo. Am J Physiol *273*, C1596-1604.
Liu, X., Ding, Y., Zhao, B., Liu, Y., Luo, S., Wu, J., Li, J., and Xiang, D. (2016a). In vitro and in vivo evaluation of puerarin-loaded PEGylated mesoporous silica nanoparticles. Drug Dev Ind Pharm *42*, 2031-2037.
Liu, Y., Ai, K., Liu, J., Deng, M., He, Y., and Lu, L. (2013). Dopamine-melanin colloidal nanospheres: an efficient near-infrared photothermal therapeutic agent for in vivo cancer therapy. Adv Mater *25*, 1353-1359.
Liu, Y., Ibricevic, A., Cohen, J.A., Cohen, J.L., Gunsten, S.P., Fréchet, J.M., Walter, M.J., Welch, M.J., and Brody, S.L. (2009). Impact of hydrogel nanoparticle size and functionalization on in vivo behavior for lung imaging and therapeutics. Mol Pharm *6*, 1891-1902.
Liu, Y., Tan, J., Thomas, A., Ou-Yang, D., and Muzykantov, V.R. (2012). The shape of things to come: importance of design in nanotechnology for drug delivery. Ther Deliv *3*, 181-194.
Liu, Z., Wang, Y., Purro, M., and Xiong, M.P. (2016b). Oxidation-Induced Degradable Nanogels for Iron Chelation. Sci Rep *6*, 20923.

Longmire, M., Choyke, P.L., and Kobayashi, H. (2008). Clearance properties of nano-sized particles and molecules as imaging agents: considerations and caveats. Nanomedicine (Lond) *3*, 703-717.
Lopalco, A., Ali, H., Denora, N., and Rytting, E. (2015). Oxcarbazepine-loaded polymeric nanoparticles: development and permeability studies across in vitro models of the blood-brain barrier and human placental trophoblast. Int J Nanomedicine *10*, 1985-1996.
Lunardi, C.N., Gomes, A.J., Rocha, F.S., De Tommaso, J., and Patience, G.S. (2021). Experimental methods in chemical engineering: Zeta potential. The Canadian Journal of Chemical Engineering *99*, 627-639.
Lundqvist, M., Stigler, J., Elia, G., Lynch, I., Cedervall, T., and Dawson, K.A. (2008). Nanoparticle size and surface properties determine the protein corona with possible implications for biological impacts. Proc Natl Acad Sci U S A *105*, 14265-14270.
Male, V. (2022). SARS-CoV-2 infection and COVID-19 vaccination in pregnancy. Nature Reviews Immunology *22*, 277-282.
Mariani, R., Trombini, P., Pozzi, M., and Piperno, A. (2009). Iron metabolism in thalassemia and sickle cell disease. Mediterranean journal of hematology and infectious diseases *1*, e2009006-e2009006.
Martins, J.P., D'Auria, R., Liu, D., Fontana, F., Ferreira, M.P.A., Correia, A., Kemell, M., Moslova, K., Mäkilä, E., Salonen, J*., et al.* (2018). Engineered Multifunctional Albumin-Decorated Porous Silicon Nanoparticles for FcRn Translocation of Insulin. Small *14*, 1800462.
Mathiesen, L., Mose, T., Mørck, T.J., Nielsen, J.K.S., Nielsen, L.K., Maroun, L.L., Dziegiel, M.H., Larsen, L.G., and Knudsen, L.E. (2010). Quality assessment of a placental perfusion protocol. Reproductive Toxicology *30*, 138-146.
McClatchey, A.K., Shield, A., Cheong, L.H., Ferguson, S.L., Cooper, G.M., and Kyle, G.J. (2018). Why does the need for medication become a barrier to breastfeeding? A narrative review. Women and Birth *31*, 362-366.
Mehta, K., Busbridge, M., Renshaw, D., Evans, R.W., Farnaud, S., and Patel, V.B. (2016). Characterization of hepcidin response to holotransferrin in novel recombinant TfR1 HepG2 cells. Blood Cells, Molecules, and Diseases *61*, 37-45.
Mehta, K.J., and Sharp, P.A. (2020). Iron elevates mesenchymal and metastatic biomarkers in HepG2 cells. Scientific Reports *10*, 21926.
Midgley, A.R., Pierce, G.B., Jr., Deneau, G.A., and Gosling, J.R. (1963). Morphogenesis of syncytiotrophoblast in vivo: an autoradiographic demonstration. Science *141*, 349-350.
Milani, S., Baldelli Bombelli, F., Pitek, A.S., Dawson, K.A., and Rädler, J. (2012). Reversible versus Irreversible Binding of Transferrin to Polystyrene Nanoparticles: Soft and Hard Corona. ACS Nano *6*, 2532-2541.
Miller, R.K., Wier, P.J., Maulik, D., and di Sant'Agnese, P.A. (1985). Human placenta in vitro: characterization during 12 h of dual perfusion. Contrib Gynecol Obstet *13*, 77-84.
Modell, B., Khan, M., and Darlison, M. (2000). Survival in β-thalassaemia major in the UK: data from the UK Thalassaemia Register. The Lancet *355*, 2051-2052.
Modell, B., Khan, M., Darlison, M., King, A., Layton, M., Old, J., Petrou, M., and Varnavides, L. (2001). A national register for surveillance of inherited disorders: beta thalassaemia in the United Kingdom. Bull World Health Organ *79*, 1006-1013.
Moe, A.J., Furesz, T.C., and Smith, C.H. (1994). Functional characterization of l-alanine transport in a placental choriocarcinoma cell line (BeWo). Placenta *15*, 797-802.
Monopoli, M.P., Åberg, C., Salvati, A., and Dawson, K.A. (2012). Biomolecular coronas provide the biological identity of nanosized materials. Nature Nanotechnology *7*, 779-786.
Mori, M., Ishikawa, G., Luo, S.-S., Mishima, T., Goto, T., Robinson, J.M., Matsubara, S., Takeshita, T., Kataoka, H., and Takizawa, T. (2007). The Cytotrophoblast Layer of Human Chorionic Villi Becomes Thinner but Maintains Its Structural Integrity During Gestation1. Biology of Reproduction *76*, 164-172.

Msheik, H., El Hayek, S., Bari, M.F., Azar, J., Abou-Kheir, W., Kobeissy, F., Vatish, M., and Daoud, G. (2019). Transcriptomic profiling of trophoblast fusion using BeWo and JEG-3 cell lines. Molecular Human Reproduction *25*, 811-824.
Muoth, C., Aengenheister, L., Kucki, M., Wick, P., and Buerki-Thurnherr, T. (2016). Nanoparticle transport across the placental barrier: pushing the field forward! Nanomedicine (Lond) *11*, 941-957.
Murphy, C.J., and Oudit, G.Y. (2010). Iron-overload cardiomyopathy: pathophysiology, diagnosis, and treatment. J Card Fail *16*, 888-900.
Myllynen, P., Mathiesen, L., Weimer, M., Annola, K., Immonen, E., Karttunen, V., Kummu, M., Mørck, T.J., Nielsen, J.K., Knudsen, L.E.*, et al.* (2010). Preliminary interlaboratory comparison of the ex vivo dual human placental perfusion system. Reprod Toxicol *30*, 94-102.
Myllynen, P.K., Loughran, M.J., Howard, C.V., Sormunen, R., Walsh, A.A., and Vähäkangas, K.H. (2008). Kinetics of gold nanoparticles in the human placenta. Reproductive Toxicology *26*, 130-137.
Nau, H., Helge, H., and Luck, W. (1984). Valproic acid in the perinatal period: Decreased maternal serum protein binding results in fetal accumulation and neonatal displacement of the drug and some metabolites. The Journal of Pediatrics *104*, 627-634.
Nekhayeva, I.A., Nanovskaya, T.N., Hankins, G.D., and Ahmed, M.S. (2006). Role of human placental efflux transporter P-glycoprotein in the transfer of buprenorphine, levo-alpha-acetylmethadol, and paclitaxel. Am J Perinatol *23*, 423-430.
Nel, A.E., Mädler, L., Velegol, D., Xia, T., Hoek, E.M.V., Somasundaran, P., Klaessig, F., Castranova, V., and Thompson, M. (2009). Understanding biophysicochemical interactions at the nano–bio interface. Nature Materials *8*, 543-557.
Nimtrakul, P., Tiyaboonchai, W., and Lamlertthon, S. (2019). Amphotericin B Loaded Nanostructured Lipid Carriers for Parenteral Delivery: Characterization, Antifungal and In vitro Toxicity Assessment. Curr Drug Deliv *16*, 645-653.
Nishiguchi, A., Gilmore, C., Sood, A., Matsusaki, M., Collett, G., Tannetta, D., Sargent, I.L., McGarvey, J., Halemani, N.D., Hanley, J.*, et al.* (2019). In vitro placenta barrier model using primary human trophoblasts, underlying connective tissue and vascular endothelium. Biomaterials *192*, 140-148.
Nourollahpour Shiadeh, M., Cassinerio, E., Modarres, M., Zareiyan, A., Hamzehgardeshi, Z., and Behboodi Moghadam, Z. (2020). Reproductive health issues in female patients with beta-thalassaemia major: a narrative literature review. Journal of Obstetrics and Gynaecology, 1-10.
Olivieri, N.F. (1999). The β-Thalassemias. New England Journal of Medicine *341*, 99-109.
Olivieri, N.F., Koren, G., Harris, J., Khattak, S., Freedman, M.H., Templeton, D.M., Bailey, J.D., and Reilly, B.J. (1992). Growth failure and bony changes induced by deferoxamine. Am J Pediatr Hematol Oncol *14*, 48-56.
Orendi, K., Gauster, M., Moser, G., Meiri, H., and Huppertz, B. (2010). The choriocarcinoma cell line BeWo: syncytial fusion and expression of syncytium-specific proteins. REPRODUCTION *140*, 759-766.
Orendi, K., Kivity, V., Sammar, M., Grimpel, Y., Gonen, R., Meiri, H., Lubzens, E., and Huppertz, B. (2011). Placental and trophoblastic in vitro models to study preventive and therapeutic agents for preeclampsia. Placenta *32 Suppl*, S49-54.
Origa, R. (2017). β-Thalassemia. Genetics in Medicine *19*, 609-619.
Origa, R., and Comitini, F. (2019). Pregnancy in Thalassemia. Mediterranean journal of hematology and infectious diseases *11*, e2019019-e2019019.
Panigel, M., Pascaud, M., and Brun, J.L. (1967). [Radioangiographic study of circulation in the villi and intervillous space of isolated human placental cotyledon kept viable by perfusion]. J Physiol (Paris) *59*, 277.
Park, J., Moon, H., and Hong, S. (2019). Recent advances in melanin-like nanomaterials in biomedical applications: a mini review. Biomaterials Research *23*, 24.

Parrott, M.C., and DeSimone, J.M. (2012). Relieving PEGylation. Nature Chemistry *4*, 13-14.
Partikel, K., Korte, R., Mulac, D., Humpf, H.-U., and Langer, K. (2019). Serum type and concentration both affect the protein-corona composition of PLGA nanoparticles. Beilstein J Nanotechnol *10*, 1002-1015.
Pattillo, R.A., and Gey, G.O. (1968). The establishment of a cell line of human hormone-synthesizing trophoblastic cells in vitro. Cancer Res *28*, 1231-1236.
Pemathilaka, R.L., Reynolds, D.E., and Hashemi, N.N. (2019). Drug transport across the human placenta: review of placenta-on-a-chip and previous approaches. Interface Focus *9*, 20190031.
Perring, J., Crawshay-Williams, F., Huang, C., and Townley, H.E. (2018). Bio-inspired melanin nanoparticles induce cancer cell death by iron adsorption. Journal of Materials Science: Materials in Medicine *29*, 181.
Petrakos, G., Andriopoulos, P., and Tsironi, M. (2016). Pregnancy in women with thalassemia: challenges and solutions. International journal of women's health *8*, 441-451.
Pillai, V.C., Han, K., Beigi, R.H., Hankins, G.D., Clark, S., Hebert, M.F., Easterling, T.R., Zajicek, A., Ren, Z., Caritis, S.N*., et al.* (2015). Population pharmacokinetics of oseltamivir in non-pregnant and pregnant women. Br J Clin Pharmacol *80*, 1042-1050.
Pinto, V.M., and Forni, G.L. (2020). Management of Iron Overload in Beta-Thalassemia Patients: Clinical Practice Update Based on Case Series. Int J Mol Sci *21*, 8771.
Pippard, M.J., Callender, S.T., Warner, G.T., and Weatherall, D.J. (1979). Iron absorption and loading in beta-thalassaemia intermedia. Lancet *2*, 819-821.
Polliotti, B.M., Holmes, R., Cornish, J.D., Hulsey, M., Keesling, S., Schwartz, D., Abramowsky, C.R., Huddleston, J., Panigel, M., and Nahmias, A.J. (1996). Long-term dual perfusion of isolated human placental lobules with improved oxygenation for infectious diseases research. Placenta *17*, 57-68.
Porter, J.B., Faherty, A., Stallibrass, L., Brookman, L., Hassan, I., and Howes, C. (1998). A Trial to Investigate the Relationship between DFO Pharmacokinetics and Metabolism and DFO-Related Toxicity. Annals of the New York Academy of Sciences *850*, 483-487.
Poulsen, M.S., Mose, T., Maroun, L.L., Mathiesen, L., Knudsen, L.E., and Rytting, E. (2015). Kinetics of silica nanoparticles in the human placenta. Nanotoxicology *9 Suppl 1*, 79-86.
Poulsen, M.S., Rytting, E., Mose, T., and Knudsen, L.E. (2009). Modeling placental transport: Correlation of in vitro BeWo cell permeability and ex vivo human placental perfusion. Toxicology in Vitro *23*, 1380-1386.
Rachmilewitz, E.A., and Giardina, P.J. (2011). How I treat thalassemia. Blood *118*, 3479-3488.
RCOG (2014). Management of Beta Thalassaemia in Pregnancy; Green-top Guideline No. 66

(Royal college of obstetricians and gynaecologists: Royal college of obstetricians and gynaecologists).
Ren, Z., Bremer, A.A., and Pawlyk, A.C. (2021). Drug development research in pregnant and lactating women. American Journal of Obstetrics and Gynecology *225*, 33-42.
Robson, S.C., Hunter, S., Boys, R.J., and Dunlop, W. (1989). Serial study of factors influencing changes in cardiac output during human pregnancy. Am J Physiol *256*, H1060-1065.
Robson, S.C., Hunter, S., Moore, M., and Dunlop, W. (1987). Haemodynamic changes during the puerperium: a Doppler and M-mode echocardiographic study. Br J Obstet Gynaecol *94*, 1028-1039.
Rossi, N.A., Mustafa, I., Jackson, J.K., Burt, H.M., Horte, S.A., Scott, M.D., and Kizhakkedathu, J.N. (2009). In vitro chelating, cytotoxicity, and blood compatibility of degradable poly(ethylene glycol)-based macromolecular iron chelators. Biomaterials *30*, 638-648.
Rote, N.S., Wei, B.R., Xu, C., and Luo, L. (2010). Caspase 8 and human villous cytotrophoblast differentiation. Placenta *31*, 89-96.
Rothbauer, M., Patel, N., Gondola, H., Siwetz, M., Huppertz, B., and Ertl, P. (2017). A comparative study of five physiological key parameters between four different human trophoblast-derived cell lines. Scientific Reports *7*, 5892.

Roumi, J.E., Moukhadder, H.M., Graziadei, G., Pennisi, M., Cappellini, M.D., and Taher, A.T. (2017). Pregnancy in β-thalassemia intermedia at two tertiary care centers in Lebanon and Italy: A follow-up report on fetal and maternal outcomes. American Journal of Hematology *92*, E96-E99.
Rubinchik-Stern, M., and Eyal, S. (2012). Drug Interactions at the Human Placenta: What is the Evidence? Frontiers in Pharmacology *3*.
Rund, D., and Rachmilewitz, E. (2005). Beta-thalassemia. N Engl J Med *353*, 1135-1146.
Rytting, E., and Audus, K.L. (2005). Novel Organic Cation Transporter 2-Mediated Carnitine Uptake in Placental Choriocarcinoma (BeWo) Cells. Journal of Pharmacology and Experimental Therapeutics *312*, 192-198.
Saffi, M., and Howard, N. (2015). Exploring the Effectiveness of Mandatory Premarital Screening and Genetic Counselling Programmes for β-Thalassaemia in the Middle East: A Scoping Review. Public Health Genomics *18*, 193-203.
Saunders, M. (2009). Transplacental transport of nanomaterials. Wiley Interdiscip Rev Nanomed Nanobiotechnol *1*, 671-684.
Sayani, F.A., and Kwiatkowski, J.L. (2015). Increasing prevalence of thalassemia in America: Implications for primary care. Ann Med *47*, 592-604.
Schmid, K.E., Davidson, W.S., Myatt, L., and Woollett, L.A. (2003). Transport of cholesterol across a BeWo cell monolayer: implications for net transport of sterol from maternal to fetal circulation. Journal of Lipid Research *44*, 1909-1918.
Schneider, H., Panigel, M., and Dancis, J. (1972). Transfer across the perfused human placenta of antipyrine, sodium and leucine. Am J Obstet Gynecol *114*, 822-828.
Scotet, V., Saliou, P., Uguen, M., L'Hostis, C., Merour, M.C., Triponey, C., Chanu, B., Nousbaum, J.B., Le Gac, G., and Ferec, C. (2018). Do pregnancies reduce iron overload in HFE hemochromatosis women? results from an observational prospective study. BMC Pregnancy Childbirth *18*, 53.
Semmler-Behnke, M., Lipka, J., Wenk, A., Hirn, S., Schäffler, M., Tian, F., Schmid, G., Oberdörster, G., and Kreyling, W.G. (2014). Size dependent translocation and fetal accumulation of gold nanoparticles from maternal blood in the rat. Part Fibre Toxicol *11*, 33.
Serre, C., Busuttil, V., and Botto, J.-M. (2018). Intrinsic and extrinsic regulation of human skin melanogenesis and pigmentation. International Journal of Cosmetic Science *40*, 328-347.
Shah, S.W., Zhao, H., Low, S.Y., McArdle, H.J., and Hundal, H.S. (1999). Characterization of Glucose Transport and Glucose Transporters in the Human Choriocarcinoma Cell Line, BeWo. Placenta *20*, 651-659.
Shangaris, P., Loukogeorgakis, S.P., Subramaniam, S., Flouri, C., Jackson, L.H., Wang, W., Blundell, M.P., Liu, S., Eaton, S., Bakhamis, N.*, et al.* (2019). In Utero Gene Therapy (IUGT) Using GLOBE Lentiviral Vector Phenotypically Corrects the Heterozygous Humanised Mouse Model and Its Progress Can Be Monitored Using MRI Techniques. Scientific Reports *9*, 11592.
Slominski, A., Tobin, D.J., Shibahara, S., and Wortsman, J. (2004). Melanin Pigmentation in Mammalian Skin and Its Hormonal Regulation. Physiological Reviews *84*, 1155-1228.
Soni, S. (2021). Gene Therapies for Transfusion-Dependent b-Thalassemia. Indian Pediatr *58*, 667-674.
Sorrentino, F., Maffei, L., Caprari, P., Cassetta, R., Dell'Anna, D., Materazzi, S., and Risoluti, R. (2020). Pregnancy in Thalassemia and Sickle Cell Disease: The Experience of an Italian Thalassemia Center. Frontiers in Molecular Biosciences *7*.
Spencer, R.N., Hecher, K., Norman, G., Marsal, K., Deprest, J., Flake, A., Figueras, F., Lees, C., Thornton, S., Beach, K.*, et al.* (2022). Development of standard definitions and grading for Maternal and Fetal Adverse Event Terminology. Prenatal Diagnosis *42*, 15-26.
Stephanou, C., Tamana, S., Minaidou, A., Papasavva, P., Kleanthous, M., and Kountouris, P. (2019). Genetic Modifiers at the Crossroads of Personalised Medicine for Haemoglobinopathies. J Clin Med *8*.

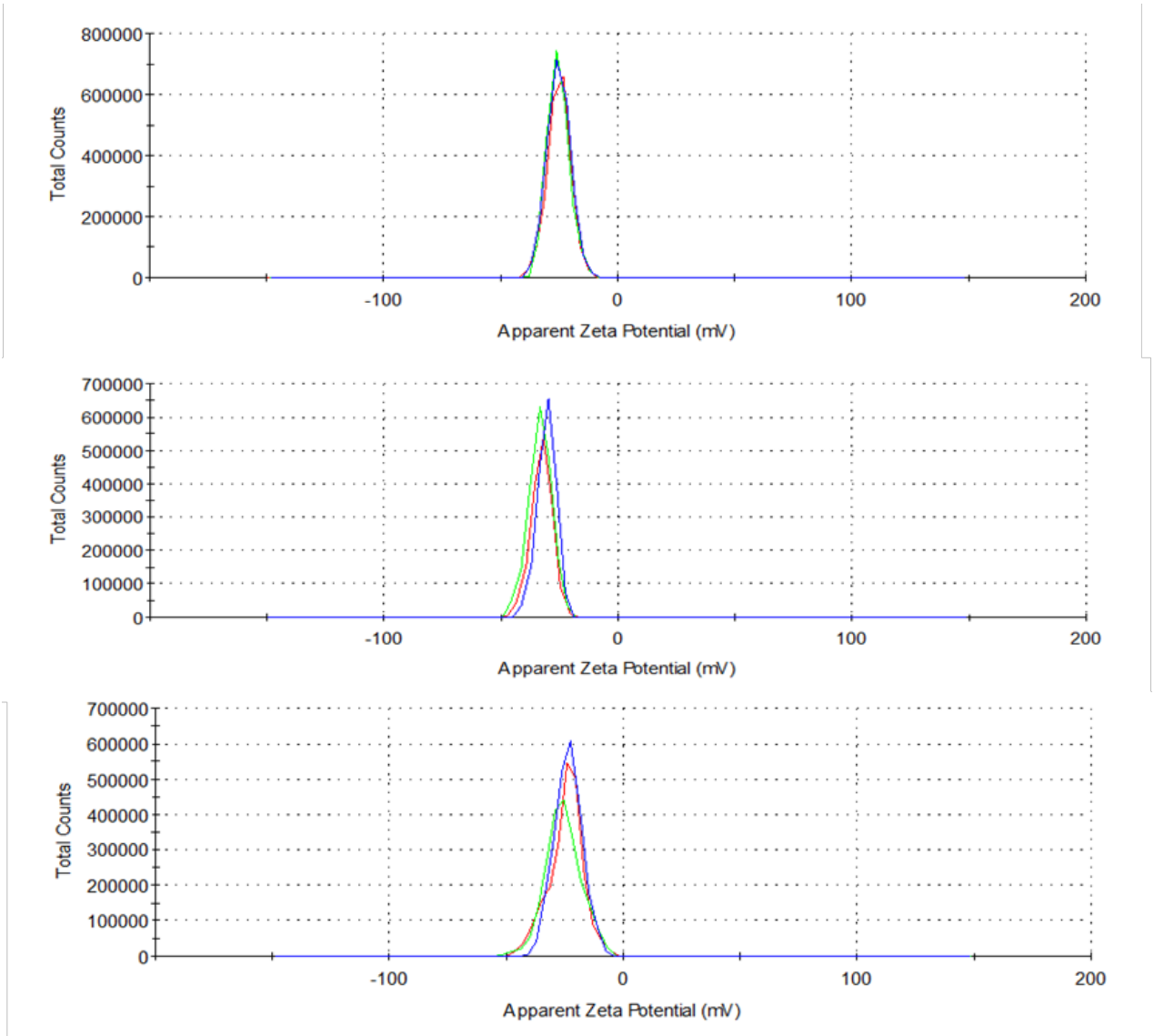
Suk, J.S., Xu, Q., Kim, N., Hanes, J., and Ensign, L.M. (2016). PEGylation as a strategy for improving nanoparticle-based drug and gene delivery. Adv Drug Deliv Rev *99*, 28-51.
Sun, M., Kingdom, J., Baczyk, D., Lye, S.J., Matthews, S.G., and Gibb, W. (2006). Expression of the multidrug resistance P-glycoprotein, (ABCB1 glycoprotein) in the human placenta decreases with advancing gestation. Placenta *27*, 602-609.
Svirshchevskaya, E.V., Zubareva, A.A., Boyko, A.A., Shustova, O.A., Grechikhina, M.V., Shagdarova, B.T., and Varlamov, V.P. (2016). Analysis of toxicity and biocompatibility of chitosan derivatives with different physico-chemical properties. Applied Biochemistry and Microbiology *52*, 483-490.
Syme, M.R., Paxton, J.W., and Keelan, J.A. (2004). Drug transfer and metabolism by the human placenta. Clin Pharmacokinet *43*, 487-514.
Takahashi, T., Utoguchi, N., Takara, A., Yamamoto, N., Nakanishi, T., Tanaka, K., Audus, K.L., and Watanabe, Y. (2001). Carrier-mediated Transport of Folic Acid in BeWo Cell Monolayers as a Model of the Human Trophoblast. Placenta *22*, 863-869.
Tang, H., Jiang, Z., He, H., Li, X., Hu, H., Zhang, N., Dai, Y., and Zhou, Z. (2018). Uptake and transport of pullulan acetate nanoparticles in the BeWo b30 placental barrier cell model. Int J Nanomedicine *13*, 4073-4082.
The Lancet Global, H. (2022). Homing in on haemoglobinopathies. The Lancet Global Health *10*, e1.
Thompson, A.A., Kim, H.-Y., Singer, S.T., Vichinsky, E., Eile, J., Yamashita, R., Giardina, P.J., Olivieri, N., Parmar, N., Trachtenberg, F.*, et al.* (2013). Pregnancy outcomes in women with thalassemia in North America and the United Kingdom. American journal of hematology *88*, 771-773.
Tyanova, S., Temu, T., Sinitcyn, P., Carlson, A., Hein, M.Y., Geiger, T., Mann, M., and Cox, J. (2016). The Perseus computational platform for comprehensive analysis of (prote)omics data. Nat Methods *13*, 731-740.
Urbán, P., Liptrott, N.J., and Bremer, S. (2019). Overview of the blood compatibility of nanomedicines: A trend analysis of in vitro and in vivo studies. WIREs Nanomedicine and Nanobiotechnology *11*, e1546.
Vähäkangas, K., and Myllynen, P. (2006). Experimental methods to study human transplacental exposure to genotoxic agents. Mutat Res *608*, 129-135.
Valero, L., Alhareth, K., Gil, S., Simasotchi, C., Roques, C., Scherman, D., Mignet, N., Fournier, T., and Andrieux, K. (2017). Assessment of dually labelled PEGylated liposomes transplacental passage and placental penetration using a combination of two ex-vivo human models: the dually perfused placenta and the suspended villous explants. International Journal of Pharmaceutics *532*, 729-737.
van der Aa, E.M., Copius Peereboom-Stegeman, J.H.J., Noordhoek, J., Gribnau, F.W.J., and Russel, F.G.M. (1998). Mechanisms of drug transfer across the human placenta. Pharmacy World and Science *20*, 139-148.
Vlachodimitropoulou, E., Chen, Y.-L., Garbowski, M., Koonyosying, P., Psaila, B., Sola-Visner, M., Cooper, N., Hider, R., and Porter, J. (2017). Eltrombopag: a powerful chelator of cellular or extracellular iron(III) alone or combined with a second chelator. Blood *130*, 1923-1933.
Vlachodimitropoulou, E., Thomas, A., Shah, F., and Kyei-Mensah, A. (2018). Pregnancy and iron status in β-thalassaemia major and intermedia: six years' experience in a North London Hospital. Journal of Obstetrics and Gynaecology *38*, 567-570.
Wang, J., and Pantopoulos, K. (2011). Regulation of cellular iron metabolism. Biochem J *434*, 365-381.
Wang, Y., Liu, Z., Lin, T.-M., Chanana, S., and Xiong, M.P. (2018). Nanogel-DFO conjugates as a model to investigate pharmacokinetics, biodistribution, and iron chelation in vivo. International journal of pharmaceutics *538*, 79-86.
Wang, Z., Tiruppathi, C., Minshall, R.D., and Malik, A.B. (2009). Size and Dynamics of Caveolae Studied Using Nanoparticles in Living Endothelial Cells. ACS Nano *3*, 4110-4116.

Way, B.A., Furesz, T.C., Schwarz, J.K., Moe, A.J., and Smith, C.H. (1998). Sodium-independent lysine uptake by the bewo choriocarcinoma cell line. Placenta *19*, 323-328.
Wice, B., Menton, D., Geuze, H., and Schwartz, A.L. (1990). Modulators of cyclic AMP metabolism induce syncytiotrophoblast formation in vitro. Exp Cell Res *186*, 306-316.
Wick, P., Malek, A., Manser, P., Meili, D., Maeder-Althaus, X., Diener, L., Diener, P.A., Zisch, A., Krug, H.F., and von Mandach, U. (2010). Barrier capacity of human placenta for nanosized materials. Environ Health Perspect *118*, 432-436.
Winter, W.E., Flax, S.D., and Harris, N.S. (2017). Coagulation Testing in the Core Laboratory. Lab Med *48*, 295-313.
Wise, J. (2022). Pregnant women should be included in clinical trials to improve outcomes, says commission. BMJ *377*, o1193.
Wu, T.-F., and Hong, J.-D. (2016). Synthesis of water-soluble dopamine–melanin for ultrasensitive and ultrafast humidity sensor. Sensors and Actuators B: Chemical *224*, 178-184.
Yamashita, K., Yoshioka, Y., Higashisaka, K., Mimura, K., Morishita, Y., Nozaki, M., Yoshida, T., Ogura, T., Nabeshi, H., Nagano, K.*, et al.* (2011). Silica and titanium dioxide nanoparticles cause pregnancy complications in mice. Nature Nanotechnology *6*, 321-328.
Yan, J., Ji, Y., Zhang, P., Lu, X., Fan, Q., Pan, D., Yang, R., Xu, Y., Wang, L., Zhang, L.*, et al.* (2016). Melanin nanoparticles as an endogenous agent for efficient iron overload therapy. J Mater Chem B *4*, 7233-7240.
Yang, H., Sun, C., Fan, Z., Tian, X., Yan, L., Du, L., Liu, Y., Chen, C., Liang, X.-j., Anderson, G.J.*, et al.* (2012). Effects of gestational age and surface modification on materno-fetal transfer of nanoparticles in murine pregnancy. Scientific Reports *2*, 847.
Yang R, M.L. (2022). Prothrombin Time. StatPearls Publishing.
Yoshida, T., Yoshioka, Y., Morishita, Y., Aoyama, M., Tochigi, S., Hirai, T., Tanaka, K., Nagano, K., Kamada, H., Tsunoda, S.-i.*, et al.* (2015). Protein corona changes mediated by surface modification of amorphous silica nanoparticles suppress acute toxicity and activation of intrinsic coagulation cascade in mice. Nanotechnology *26*, 245101.
Zeise, L., Murr, B.L., and Chedekel, M.R. (1992). Melanin standard method: particle description. Pigment Cell Res *5*, 132-142.
Zhang, B., Liang, R., Zheng, M., Cai, L., and Fan, X. (2019). Surface-Functionalized Nanoparticles as Efficient Tools in Targeted Therapy of Pregnancy Complications. Int J Mol Sci *20*, 3642.
Zhang, J., Tang, H., Liu, Z., and Chen, B. (2017). Effects of major parameters of nanoparticles on their physical and chemical properties and recent application of nanodrug delivery system in targeted chemotherapy. Int J Nanomedicine *12*, 8483-8493.
Zhang, P., Yue, Y., Pan, D., Yang, R., Xu, Y., Wang, L., Yan, J., Li, X., and Yang, M. (2016). Pharmacokinetics study of Zr-89-labeled melanin nanoparticle in iron-overload mice. Nucl Med Biol *43*, 529-533.
Zhang, R., Fan, Q., Yang, M., Cheng, K., Lu, X., Zhang, L., Huang, W., and Cheng, Z. (2015). Engineering Melanin Nanoparticles as an Efficient Drug-Delivery System for Imaging-Guided Chemotherapy. Adv Mater *27*, 5063-5069.
Zhang, X., Wang, S., Xu, L., Feng, L., Ji, Y., Tao, L., Li, S., and Wei, Y. (2012). Biocompatible polydopamine fluorescent organic nanoparticles: facile preparation and cell imaging. Nanoscale *4*, 5581-5584.
Zhao, J., and Stenzel, M.H. (2018). Entry of nanoparticles into cells: the importance of nanoparticle properties. Polymer Chemistry *9*, 259-272.
Zhao, S., Gockenbach, M., Grimstein, M., Sachs, H.C., Mirochnick, M., Struble, K., Belew, Y., Wang, J., Capparelli, E.V., Best, B.M.*, et al.* (2021). Characterization of Plasma Protein Alterations in Pregnant and Postpartum Individuals Living With HIV to Support Physiologically-Based Pharmacokinetic Model Development. Frontiers in Pediatrics *9*.

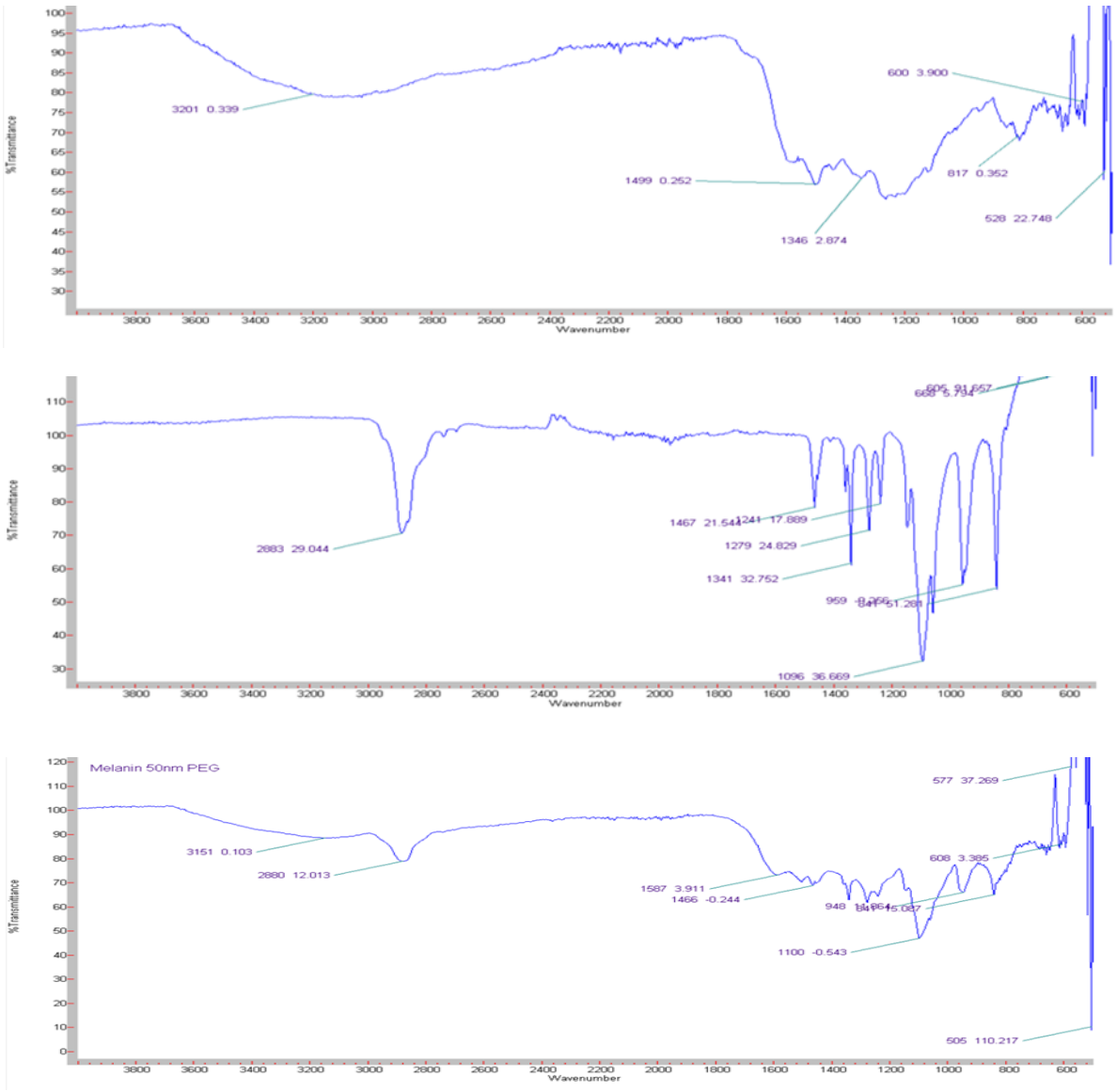
Zhou, Y., Zhou, B., Pache, L., Chang, M., Khodabakhshi, A.H., Tanaseichuk, O., Benner, C., and Chanda, S.K. (2019). Metascape provides a biologist-oriented resource for the analysis of systems-level datasets. Nature Communications *10*, 1523.

Appendix I

Melanin nanoparticles characteristics

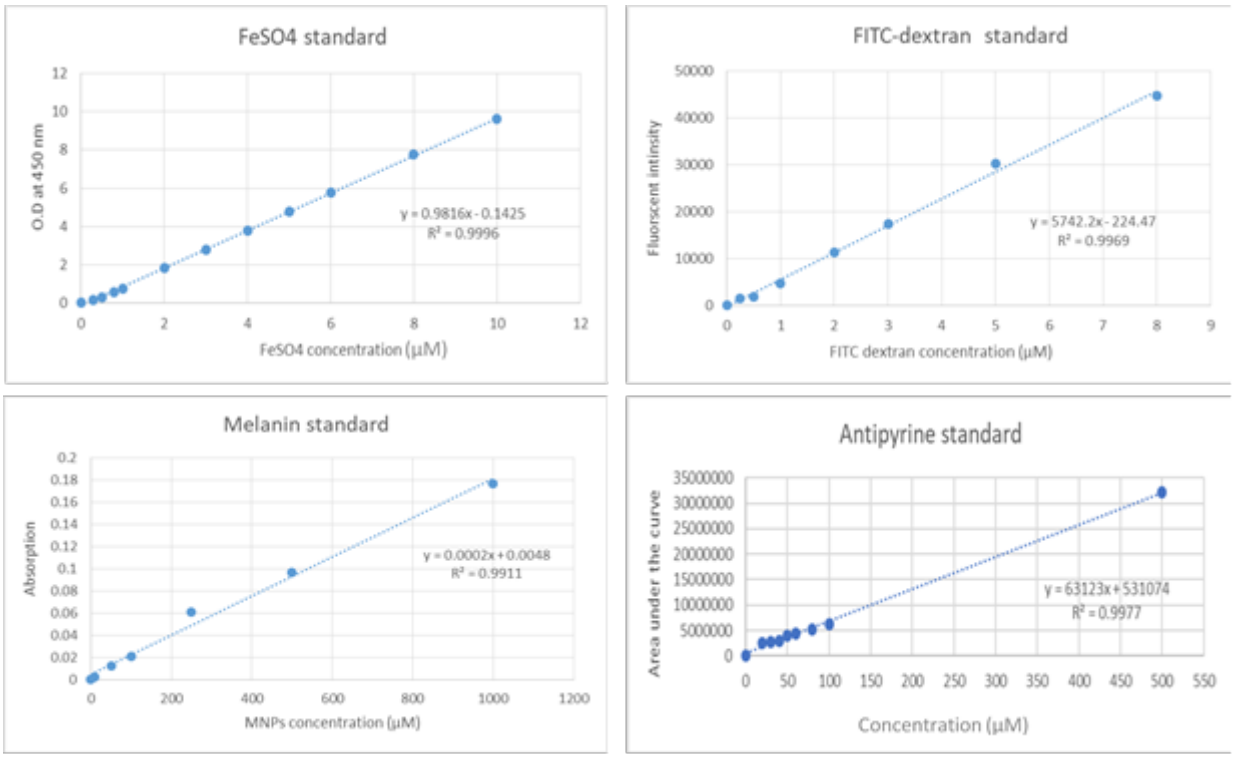


Zeta potential of melanin nanoparticles (3.4.3)

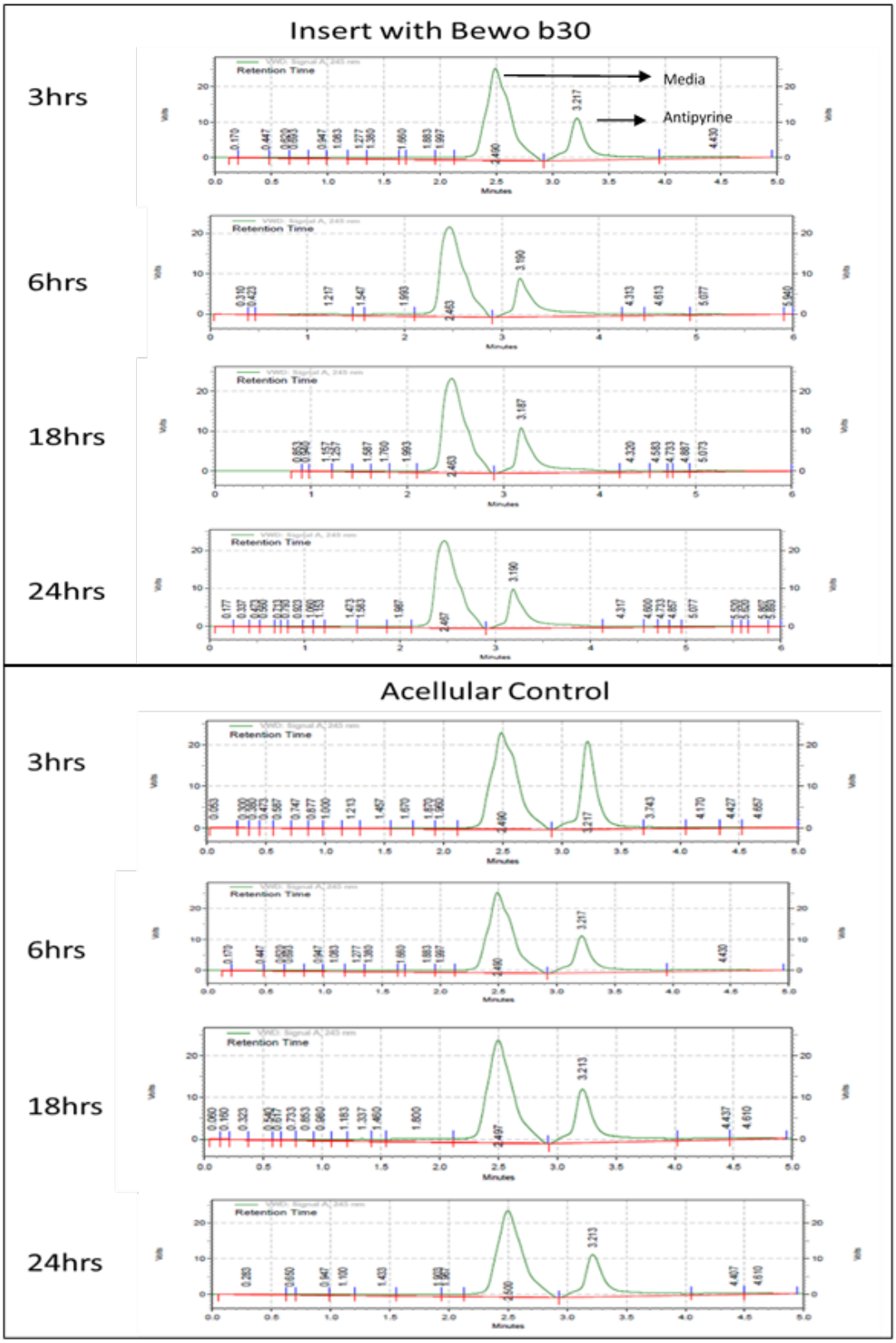


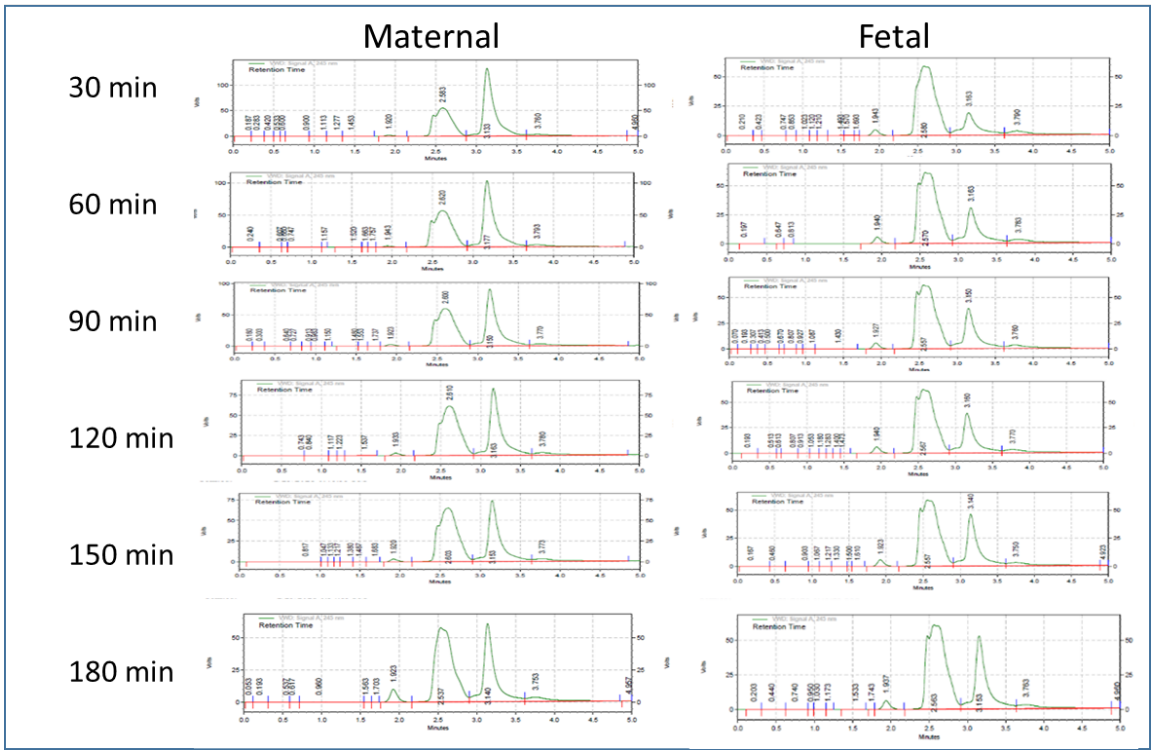
FTIR measurements of PEGylated melanin particles (3.4.6)

Appendix II

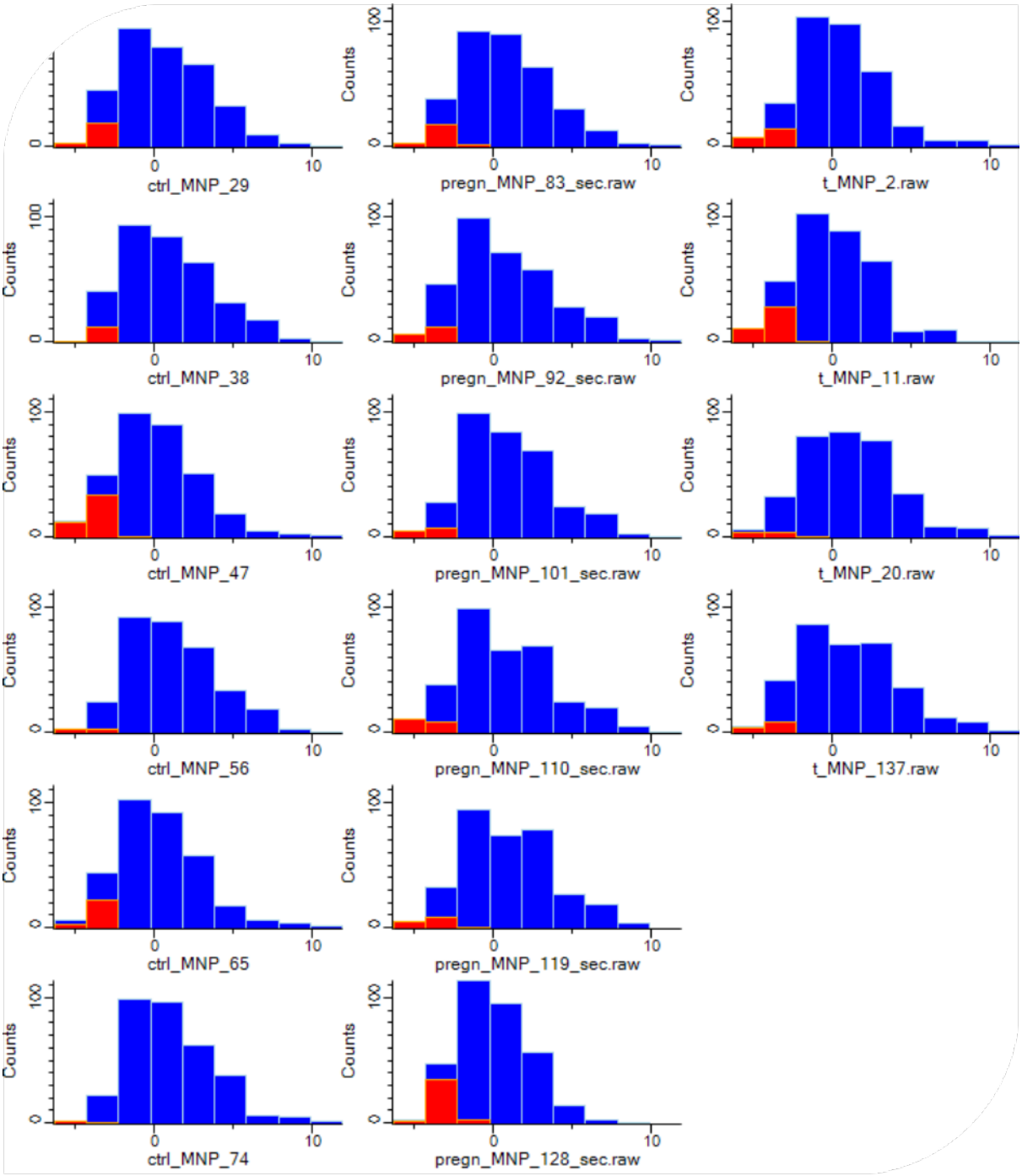


Standards calibration curves for $FeSO_4$, FITC-dextran, Melanin nanoparticles and Antipyrine.


Insert with Bewo b30
3hrs
6hrs
18hrs
24hrs
Media
Antipyrine
Retention Time
Minutes
Acellular Control
3hrs
6hrs
18hrs
24hrs
Retention Time
Minutes


Maternal
Fetal
30 min
60 min
90 min
120 min
150 min
180 min

Appendix III



Appendix 1 Figure 1. Data of the MNPs corona from the 3 different groups (healthy non-pregnant, pregnant and thalassemia) after replacing missing values from normal distribution. *Missing data are low expression proteins. Data are normally distributed.*

Gene list of MNPs corona from the 3 different groups (healthy non-pregnant, pregnant and thalassemia):

Gene Symbol (Cluster 1)	Description
DDX39A	DExD-box helicase 39A
DDX39B	DExD-box helicase 39B
KRT14	keratin 14
KRT10	keratin 10
KRT13	keratin 13
KRT16	keratin 16
KRT17	keratin 17
KRT18	keratin 18
KRT19	keratin 19
KRT12	keratin 12
KRT9	keratin 9
KRT6A	keratin 6A
KRT6B	keratin 6B
KRT1	keratin 1
KRT5	keratin 5
KRT79	keratin 79
KRT8	keratin 8
KRT3	keratin 3
KRT2	keratin 2
KRT4	keratin 4
KRT76	keratin 76
KRT77	keratin 77
CTSD	cathepsin D
PRSS1	serine protease 1
FLG	filaggrin
DSG1	desmoglein 1
KRT23	keratin 23

Gene Symbol (cluster 2)	Description
H2AZ2	H2A.Z variant histone 2
ENO2	enolase 2
YWHAQ	tyrosine 3-monooxygenase/tryptophan 5-monooxygenase activation protein theta
HSP90AB1	heat shock protein 90 alpha family class B member 1

Gene Symbol (cluster 3)	Description
APOE	apolipoprotein E
AK2	adenylate kinase 2
B2M	beta-2-microglobulin
SYTL2	synaptotagmin like 2

Appendix IV

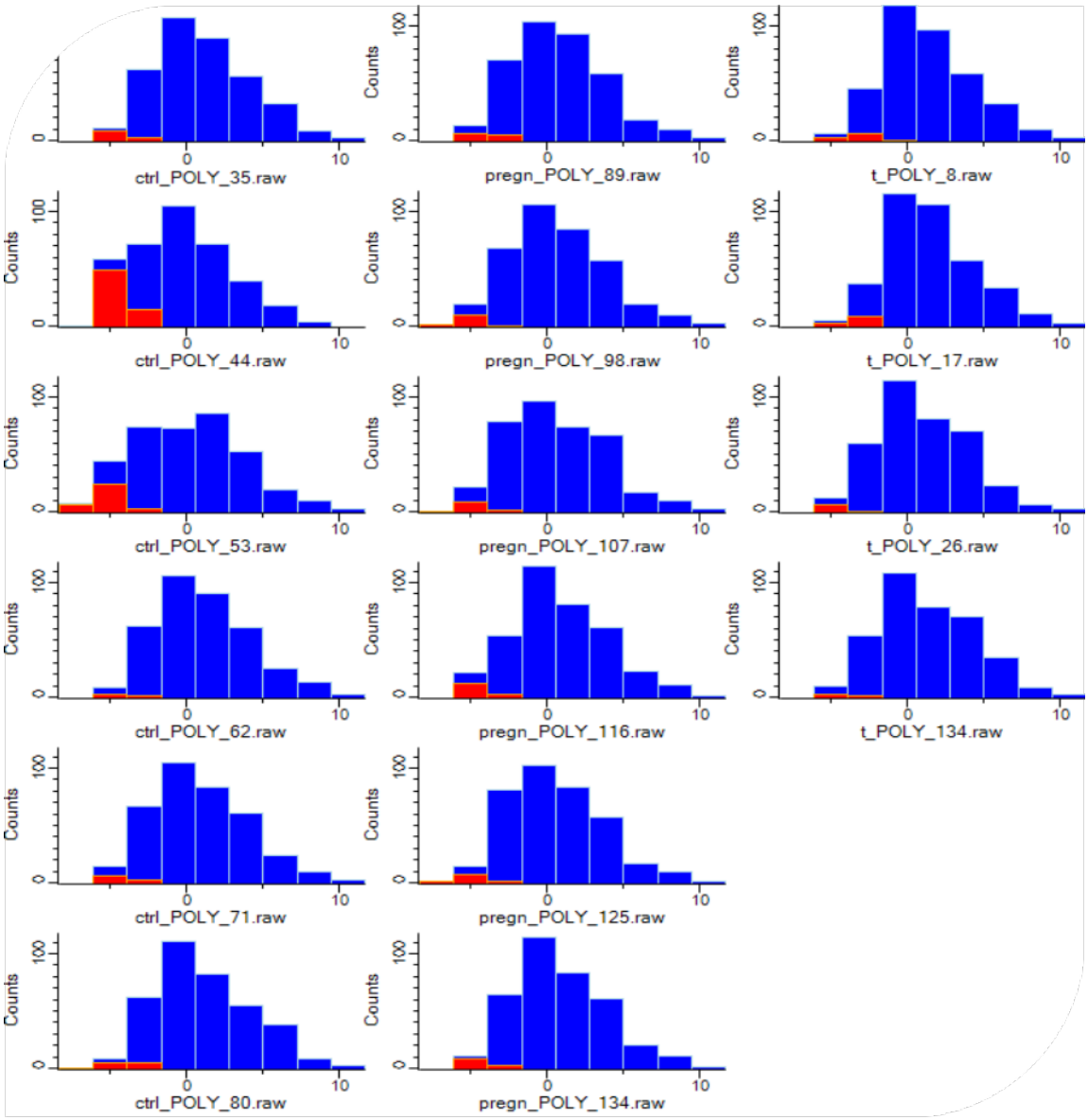


Figure 1. Data of the polystyrene corona from the 3 different groups (healthy non-pregnant, pregnant and thalassemia) after replacing missing values from normal distribution. *Missing data are low expression proteins. Data are normally distributed.*

Gene list of polystyrene corona from the 3 different groups (healthy non-pregnant, pregnant and thalassemia):

Gene Symbol (cluster 1)	Description
HPX	Hemopexin

Gene Symbol (cluster 2)	Description
IGHG3	Immunoglobulin heavy constant gamma 3
TUBB;TUBB4A;TUBB4B	Tubulin beta-4A chain

Genes Symbol (cluster 3)	Description
IGKV3-7	Probable non-functional immunoglobulin kappa variable 3-7
IGLV7-43;IGLV7-46	Immunoglobulin lambda variable 7-46
IGLV3-9	Immunoglobulin lambda variable 3-9
IGKV2D-29	Immunoglobulin kappa variable 2D-29
IGKV2-30;IGKV2D-29	Immunoglobulin kappa variable 2D-29
IGHV3OR16-12	Immunoglobulin heavy variable 3/OR16-12 (non-functional) (Fragment)
IGKV3-11;IGKV3D-11	Immunoglobulin kappa variable 3D-11
IGKV6D-21	Immunoglobulin kappa variable 6D-21
IGHV3-15	Immunoglobulin heavy variable 3-15
IGKV3D-20	Immunoglobulin kappa variable 3D-20
IGKV3-20;IGKV3D-20	Immunoglobulin kappa variable 3D-20
IGHV4-28	Immunoglobulin heavy variable 4-28
IGHV3-38	Probable non-functional immunoglobulin heavy variable 3-38
IGHV5-51	Immunoglobulin heavy variable 5-51
IGKV1-12;IGKV1-39;IGKV1D-12;IGKV1D-39	Immunoglobulin kappa variable 1-12
IGKV1D-33	Immunoglobulin kappa variable 1-33
IGHV3-72	Immunoglobulin heavy variable 3-72
IGLC7	Immunoglobulin lambda constant 7
IGLC3;IGLC6;IGLC7	Immunoglobulin lambda constant 7
IGLL5	Immunoglobulin lambda-like polypeptide 5
MASP2	Mannan-binding lectin serine protease 2
FCN3	Ficolin-3
C1R	Complement C1r subcomponent
CA1	Carbonic anhydrase 1
SERPINA3	Alpha-1-antichymotrypsin
A2M	Alpha-2-macroglobulin
A2M;PZP	Alpha-2-macroglobulin
IGKV1D-33	Immunoglobulin kappa variable 1D-33
IGKV1-39;IGKV1D-39	Immunoglobulin kappa variable 1-39
IGKV1-5	Immunoglobulin kappa variable 1-5
IGKV3-20	Immunoglobulin kappa variable 3-20

IGLV1-47	Immunoglobulin lambda variable 1-47
IGLV3-25	Immunoglobulin lambda variable 3-25
IGHV3-7	Immunoglobulin heavy variable 3-7
IGKC	Immunoglobulin kappa constant
IGHG1;IGHG4	Immunoglobulin heavy constant gamma 1
HBB;HBD;HBG1;HBG2	Hemoglobin subunit delta
APOH	Beta-2-glycoprotein 1
LRG1	Leucine-rich alpha-2-glycoprotein
ORM1	Alpha-1-acid glycoprotein 1
AHSG	Alpha-2-HS-glycoprotein
F11	Coagulation factor XI
IGLV7-43	Immunoglobulin lambda variable 7-43
APOD	Apolipoprotein D
IGHV4-34	Immunoglobulin heavy variable 4-34
PROS1	Vitamin K-dependent protein S
PRSS1	Trypsin-1
C1S	Complement C1s subcomponent
RPS27A;UBA52;UBB;UBC	Polyubiquitin-B
HSPA1A;HSPA1B;HSPA1L	Heat shock 70 kDa protein 1A
C7	Complement component C7
HSPA8	Heat shock cognate 71 kDa protein
ITGA6	Integrin alpha-6
AZGP1	Zinc-alpha-2-glycoprotein
PRDX2	Peroxiredoxin-2
COMP	Cartilage oligomeric matrix protein
SELENOP	Selenoprotein P
TUBA1B;TUBA1C	Tubulin alpha-1B chain
GSTO1	Glutathione S-transferase omega-1
IGLV3-21	Immunoglobulin lambda variable 3-21
DSG1	Desmoglein-1
PON3	Serum paraoxonase/lactonase 3
ACTBL2	Beta-actin-like protein 2
PROCR	Endothelial protein C receptor
CLEC11A	C-type lectin domain family 11 member A
GRIP1	Glutamate receptor-interacting protein 1

Genes Symbol (cluster 4)	Description
SERPINA1	Alpha-1-antitrypsin
IGKV1-13;IGKV1D-13	Immunoglobulin kappa variable 1D-13
ZNF528	Zinc finger protein 528
APOM	Apolipoprotein M
F13A1	Coagulation factor XIII A chain
HP	Haptoglobin
HP;HPR	Haptoglobin

SERPINA1	Alpha-1-antitrypsin
IGLV1-51	Immunoglobulin lambda variable 1-51
IGLV1-51	Immunoglobulin lambda variable 1-51
IGLV1-51	Immunoglobulin lambda variable 1-51
APOE	Apolipoprotein E
APOC1	Apolipoprotein C-I
APOC2	Apolipoprotein C-II
C9	Complement component C9
ALB	Albumin
GC	Vitamin D-binding protein
TF	Serotransferrin
VWF	von Willebrand factor
SHBG	Sex hormone-binding globulin
SERPINA7	Thyroxine-binding globulin
MRPL3	39S ribosomal protein L3, mitochondrial
ITIH1	Inter-alpha-trypsin inhibitor heavy chain H1
PZP	Pregnancy zone protein
FBLN1	Fibulin-1
SAA4	Serum amyloid A-4 protein
ITIH3	Inter-alpha-trypsin inhibitor heavy chain H3
AHNAK	Neuroblast differentiation-associated protein AHNAK
ANKRD30B	Ankyrin repeat domain-containing protein 30B
PCYOX1	Prenylcysteine oxidase 1
APOA1	Apolipoprotein A-I